Numerical studies of a fluid-filled precessing cylinder: a framework for the DRESDYN precession experiment

Von der Fakultät für Maschinenbau, Elektro- und Energiesysteme
der Brandenburgischen Technischen Universität Cottbus-Senftenberg

zur Erlangung des akademischen Grades eines
Doktors der Ingenieurwissenschaften (Dr.-Ing.)
genehmigte Dissertation
vorgelegt von
Master of Science (M. Sc.)

Federico Pizzi

geboren am 2. Mai 1991 in Pontedera (Italien)

Vorsitzender:	Prof. Dr. Christoph Egbers (BTU C-S)
Gutachter:	Apl. Prof. Dr. Uwe Harlander (BTU C-S)
Gutachter:	Prof. Dr. Andreas Tilgner (GAUG)
Gutachter:	Dr. Frank Stefani (HZDR)
Tag der mündlichen Prüfung:	7. Juni 2023

DOI: https://doi.org/10.26127/BTUOpen-6421

Abstract

Precession driven flows are believed to play a relevant role in planetary dynamics, such as in atmospheric phenomena, and as a complementary energy source for homogeneous dynamo action, i.e. the self-generation of planetary magnetic fields. Precessional motion occurs when a body rotates around an axis, which itself is rotating around another axis. The main influence of this forcing mechanism is a gyroscopic effect on the fluid flow which gives rise to a wavy dynamics even in the laminar regime. If the forcing magnitude is strong enough the flow goes through a series of phenomena such as instabilities, resonant interactions between waves, and transition to turbulence whose occurrence depends on the container shape and the nutation angle, i.e. the angle between the two axis. Numerical simulations and laboratory experiments have elucidated these phenomena demonstrating their complexity. Although many phenomena have a satisfactory explanation, others still remain elusive and merit further investigations. Great efforts have been devoted to the study of the small nutation angle regime (which is the natural configuration for geophysical applications) while a comprehensive analysis of the large angle regime for different precession ratios is still missing.
The interest in moderate to large forcing is particularly motivated by the need of theoretical supports for the upcoming DRESDYN (DREsden Sodium facility for DYNnamo and thermohydraulic studies) precession experiment, whose main purpose is to test the capability of a precessing fluid system to achieve a dynamo effect. Here, the possibility to generate a magnetic field is connected to the emergence of three large scale structures in the bulk flow: a directly forced standing wave, poloidal rolls reminiscent of Taylor vortices, and a geostrophic axisymmetric flow. The emergence of a geostrophic vortex is a hallmark of the precessing cylinder which is connected with the transition to turbulence. However the appearance of the poloidal vortices need to be clarified and characterized in the parameter space. Moreover the role and the behavior of boundary layers has not received great attention. These open questions represent the main motivations for the present work.

In order to analyze and investigate these points, in this thesis we use numerical simulations to study and understand the flow behavior in a fluid-filled precessing cylinder. We use two types of approaches: a global study to investigate large scale phenomena inside the precessing cylinder and the resulting magnetohydrodynamics behavior, and a local model to analyze and unveil the properties of turbulence forced by precession. In particular, in the context of the global approach, we study the role and the characteristics of the boundary layer developed both at the endwalls and at the sidewalls of the container. The endcaps give rise to an Ekman layer which is influenced by the poloidal flow emerging in the central region of the cylinder for an intermediate range of precession forcing, and the sidewall boundary layer reflects the transition of the bulk flow: while for weak forcing it is essentially an Ekman layer, it shows the properties of the so-called Stewartson layer once the bulk is dominated by the geostrophic columnar vortex. The results found in terms of instabilities (and possible turbulent states) are not restricted to our problem but are also paradigmatic features of atmospheric phenomena. Another focus is on the bulk flow behavior and its different responses with respect to the sense of motion: while prograde precession shows a steep transition to turbulence when increasing the forcing magnitude with a marked breakdown of the directly forced mode, retrograde precession presents a much smoother change. The precession angle plays also a crucial role in tuning the large scale structures. A related distinction has been found also for the dynamo action, which is more likely to occur for perpendicular and retrograde precession. Restricting our attention to the kinematic regime (where the equation of fluid motion and the magnetic field equation are decoupled) we characterized the dynamo action in dependence on nutation angle and precession strength.

Finally, with the aim to analyze the features of turbulent phenomena we characterize the precession driven turbulence as a complex scenario determined by the coexistence of geostrophic vortices (called also condensates), a typical feature of rotating turbulence prone to an inverse cascade of energy, and small scale 3D waves characterized by a direct energy cascade. We observe the interaction of these two structures as being governed by a clear hierarchy: the precession force injects energy mainly into 3D inertial waves which in turn feed the geostrophic vortices. This is a nonlinear effect of higher order since the weak nonlinear theory prohibits the interaction of inertial waves and geostrophic mode.

Kurzfassung

Präzessionsgetriebenen Strömungen wird eine wichtige Rolle in der Dynamik verschiedener planetarer Prozesse zugeschrieben, z. B. in atmosphärischen Phänomenen und als komplementäre Energiequelle für die Selbsterregung planetarer Magnetfelder durch den homogenen Dynamoeffekt. Eine Präzessionsbewegung tritt auf, wenn sich ein Körper um eine Achse dreht, die ihrerseits um eine andere Achse rotiert. In erster Linie bewirkt dieser Antriebsmechanismus einen gyroskopischen Effekt auf die Fluidströmung, der bereits im laminaren Regime eine wellenartige Dynamik hervorruft. Mit stärker werdendem Antrieb durchläuft die Strömung eine Reihe von Phänomenen wie Instabilitäten, resonante Wechselwirkungen zwischen Wellen und den Übergang zur Turbulenz, deren Auftreten von der Behälterform und dem Nutationswinkel, d. h. dem Winkel zwischen den beiden Achsen, abhängt. Numerische Simulationen und Laborexperimente haben diese Phänomene untersucht und ihre Komplexität aufgezeigt. Während für viele dieser Erscheinungen bereits eine zufriedenstellende Erklärung vorliegt, sind andere nach wie vor nur schlecht verstanden und bedürfen weiterer Untersuchungen. Das Hauptaugenmerk bisheriger Studien lag auf dem Fall kleiner Nutationswinkel, der die natürliche Konfiguration für geophysikalische Anwendungen darstellt. Eine umfassende Analyse des Falles großer Winkel für verschiedene Präzessionsverhältnisse stand bisher aus.
Das Interesse an mittleren bis starken Strömungsantrieben ist insbesondere durch den Bedarf an theoretischer Untersetzung des im Rahmen des Projektes DRESDYN (DREsden Sodium facility for DYNnamo and thermohydraulic studies) bevorstehenden Präzessionsexperiments motiviert. Dessen Hauptzweck besteht darin, die Fähigkeit eines präzedierenden Fluids zu testen, einen Dynamoeffekt zu bewirken. Diese Fähigkeit ist insbesondere mit dem Auftreten von drei großskaligen Strömungsstrukturen verknüpft: einer direkt erzwungenen stehenden Welle, einer poloidalen Wirbelstruktur, die an Taylor-Wirbel erinnert, und einer geostrophischen axialsymmetrischen Strömung. Die Entstehung eines solchen geostrophischen Strömungsanteils, der auch mit dem Übergang zur Turbulenz im Zusammenhang steht, ist typisch für den präzedierenden Zylinder. Jedoch stand eine eingehende Analyse dieses Effektes bisher aus. Desweiteren bedarf das Auftreten der poloidalen Wirbel einer weiteren Erklärung und Charakterisierung im Parameterraum. Auch haben die Rolle und das Verhalten von Grenzschichten präzedierender Strömungen bisher wenig Beachtung gefunden. Diese offenen Fragen bilden die Hauptmotivation für die vorliegende Arbeit.

In dieser Arbeit werden numerische Simulationen eingesetzt, um das Strömungsverhalten in einem flüssigkeitsgefüllten Präzessionszylinder zu untersuchen und zu verstehen. Dabei werden zwei Ansätze verfolgt: eine globale Modellierung, um großräumige Phänomene im Inneren des Präzessionszylinders und das daraus resultierende magnetohydrodynamische Verhalten zu untersuchen, und ein lokales Modell, um die Eigenschaften der durch die Präzession erzeugten Turbulenzstrukturen zu analysieren. Im Rahmen des globalen Modells untersuchen wir insbesondere die Rolle und die Eigenschaften der Grenzschichten, die sich an den Stirnwänden als auch an den Seitenwänden des Behälters entwickeln. An den Endkappen entsteht eine Ekman-Schicht, die von der poloidalen Strömung beeinflusst wird, welche sich in der zentralen Region des Zylinders bei mittleren Stärken des Präzessionsantriebs entwickelt. Die Grenzschicht an den Seitenwänden spiegelt hingegen den Übergang der Strömung wider: während sie bei schwachem Antrieb im Wesentlichen eine Ekman-Schicht ist, weist sie Eigenschaften der so genannten Stewartson-Schicht auf, sobald die Strömung von einem kolumnaren geostrophischen Wirbel dominiert wird. Die in Bezug auf Instabilitäten und mögliche turbulente Zustände gewonnenen Ergebnisse sind dabei nicht auf unser spezifisches Problem beschränkt, sondern weisen paradigmatische Merkmale atmosphärischer Phänomene auf. Ein weiterer Schwerpunkt liegt auf der Abhängigkeit und den unterschiedlichen Reaktionen der Strömung im Volumen von bzw. auf die Präzessionsrichtung: während prograde Präzession bei Erhöhung des Antriebs einen klaren Übergang zur Turbulenz mit einem deutlichen Zusammenbruch der direkt erzwungenen Mode zeigt, zeigt die retrograde Präzession einen wesentlich sanfteren Übergang. Dabei spielt der Präzessionswinkel ebenfalls eine entscheidende Rolle für die Einstellung der großräumigen Strukturen. Ein entsprechender Unterschied wurde auch für die Dynamowirkung gefunden, deren Auftreten bei senkrechter und retrograder Präzession wahrscheinlicher ist. Dabei beschränken wir uns auf das kinematische Regime (in dem die Gleichung für die Fluidbewegung von der Magnetfeldgleichung entkoppelt ist), um die Dynamowirkung in Abhängigkeit von Nutationswinkel und Präzessionsstärke zu charakterisieren.

Mit dem Ziel, die Eigenschaften turbulenter Phänomene zu analysieren, charakterisieren wir schließlich das komplexes Szenario der präzessionsgetriebenen Turbulenz. Dieses ist bestimmt durch die Koexistenz von geostrophischen Wirbeln (Kondensaten), einem typischen Merkmal rotierender Turbulenz, das zu einer inversen Energiekaskade neigt, und kleinskaligen 3D-Wellen, die durch eine direkte Energiekaskade gekennzeichnet sind. Es wird gezeigt, dass die Interaktion dieser beiden Strukturen durch eine klare Hierarchie bestimmt wird: der Präzessionsantrieb injiziert Energie hauptsächlich in die 3-dimensionalen Inertialwellen, die wiederum die geostrophischen Wirbel speisen. Da die schwach-nichtlineare Theorie die Wechselwirkung von Inertialwellen und geostrophischen Moden verbietet, muss dafür ein nichtlinearer Effekt höherer Ordnung verantwortlich sein.

Dedicato alle mie nonne
e alla memoria dei miei nonni

Contents

List of Figures

List of Tables

Nomenclature

Latin and Greek Letters

Symbol	**Meaning**	**Unit**
(x, y, z)	Cartesian coordinates	m
(r, φ, z)	Cylindrical coordinates	(m, rad, m)
t	Time	s
p	Pressure	$\mathrm{N\,m^{-2}}$
ρ	Mass density	$\mathrm{kg\,m^{-3}}$
ρ_e	Charge density	$\mathrm{C\,m^{-3}}$
μ	Dynamic viscosity	$\mathrm{kg\,m^{-1}\,s^{-1}}$
ν	Kinematic viscosity	$\mathrm{m^2\,s^{-1}}$
φ_{el}	Electric potential	V
ξ	Root of the dispersion relation	
q	Electric charge	C
e^-	Elementary charge	C
α	Nutation (precession) angle	degree
ϵ_0	Vacuum permittivity	$\mathrm{C\,V^{-1}\,m^{-1}}$
μ_0	Magnetic permeability	$\mathrm{N\,A^{-2}}$
σ	Electrical conductivity, magnetic field eigenvalue	$\mathrm{S\,m^{-1}}$, [−]
$u_z, u_r, u_\varphi,$	Vertical, radial and azimuthal flow velocity	$\mathrm{ms^{-1}}$
$\omega_z, \omega_r, \omega_\varphi,$	Vertical, radial and azimuthal vorticity	$\mathrm{s^{-1}}$
$B_z, B_r, B_\varphi,$	Vertical, radial and azimuthal magnetic field	T
g	Standard acceleration due to gravity	$\mathrm{m\,s^{-2}}$
η	Magnetic diffusivity/sidewall transformed coordinate	$\mathrm{m^2/s}$, m
R	Radius	m
D	Diameter, Dissipation	m, W

Symbol	Meaning	Unit
E	Energy	J
A	Injection term in local model	
H	Height	m
L	Length	m
(m, k, n)	Wave numbers (cylindrical)	$(\frac{1}{\mathrm{m}})$
(k_x, k_y, k_z)	Wave numbers in cartesian local model	$(\frac{1}{\mathrm{m}}, \frac{1}{\mathrm{m}}, \frac{1}{\mathrm{m}})$
$(k_{x,0}, k_{y,0}, k_{z,0})$	Constant wave numbers in cartesian local model	$(\frac{1}{\mathrm{m}}, \frac{1}{\mathrm{m}}, \frac{1}{\mathrm{m}})$
ω	Angular frequency	s^{-1}
ω_{mkn}	Inertial modes frequency	
Ω_c	Container (cylinder) angular velocity	s^{-1}
Ω_p	Precession (turntable) angular velocity	s^{-1}
f	Frequency	s^{-1}
T	Period	s
J	Bessel function in cylindrical coordinate	
δ	Boundary layer thickness	m
D	Total dissipation	$\mathrm{W\,m^{-3}\,kg^{-1}}$
O	Origin of the container	
$\mathcal{O}$	Order	
k	Wave number magnitude $\sqrt{k_x^2 + k_y^2 + k_z^2}$	$\frac{1}{\mathrm{m}}$
k_ω	Zeman Wave number	$\frac{1}{\mathrm{m}}$
f	Frequency	s^{-1}
$\overline{f}$	Fourier variable	
γ	growth rate of magnetic energy	
$\frac{1}{s}$		

Vector Quantities

Symbol	Meaning	Unit
$\boldsymbol{x}, \boldsymbol{r}$	Coordinate vector	m
$(\boldsymbol{x}, \boldsymbol{y}, \boldsymbol{z})$	Cartesian unit vectors	
$(\hat{\boldsymbol{r}}, \hat{\boldsymbol{\varphi}}, \hat{\boldsymbol{z}})$	Cylindrical unit vectors	
$\boldsymbol{u}$	Velocity vector	$\mathrm{m\,s^{-1}}$
$\overline{\boldsymbol{u}}$	Velocity vector in Fourier space	$\mathrm{m\,s^{-1}}$

Symbol	Meaning	Unit
$\boldsymbol{\omega}$	Vorticity	s^{-1}
$\boldsymbol{\Omega}_c$	Container angular velocity	s^{-1}
$\boldsymbol{\Omega}_p$	Precession (turntable) angular velocity	s^{-1}
$\boldsymbol{k}$	Wave vector in local model	$\frac{1}{\mathrm{m}}$
$\boldsymbol{e}$	Rate-of-strain tensor	s^{-1}
$\boldsymbol{E}$	Electric field	$\mathrm{V\,m}^{-1}$
$\boldsymbol{B}$	Magnetic field	T
$\boldsymbol{a}$	Vector potential	T m
$\boldsymbol{J}$	Current density	$\mathrm{A\,m}^{-2}$
$\boldsymbol{f}$	Acceleration due to volume forces	$\mathrm{m\,s}^{-2}$
$\boldsymbol{F}_L$	Lorentz force	N
$\boldsymbol{f}_L$	Lorentz force density	$\mathrm{N\,m}^{-3}$
$\boldsymbol{X}_0$	Container motion vector	m
$\boldsymbol{M}$	Matrix of the precession base flow	
$\boldsymbol{U}_b$	Precessing base flow	
$\boldsymbol{\varepsilon}(t)$	Precessing vector in local model	
$\boldsymbol{N}$	Nonlinear transfer	
$\boldsymbol{\Psi}$	Manifold in wave space	
$\boldsymbol{F}(\boldsymbol{k})$	Flux of energy in wave space	

Dimensionless Numbers

Number	Meaning
Re	Reynolds number
Rm	Magnetic Reynolds number
S	Interaction parameter
Po	Poincaré number
Po^c	Critical Poincaré number (precession ratio)
Po^o	Optimum Poincaré number for the dynamo action
Ek	Ekman number
Γ	Aspect ratio
Pm	Magnetic Prandtl number
Ro	Rossby number
Ro_f	Boundary layer Rossby number

Acronyms

Abbreviation	Meaning
2D	Two-dimensional
3D	Three-dimensional
UDV	Ultrasound Doppler Velocimetry
PIV	Particle Imaging Velocimetry
FM	Fluid Mechanics
ED	Electrodynamics
MHD	Magnetohydrodynamics
CFD	Computational Fluid Dynamics
NSEs	Navier-Stokes equations
MEs	Maxwell equations
HZDR	Helmholtz-Zentrum Dresden - Rossendorf
DNS	Direct Numerical Simulations
DRESDYN	DREsden Sodium facility for DYNamo and thermohydraulic studies
FFTW	Fast Fourier Transform in the West
BEM	Boundary Element Method
FVM	Finite Volume Method

1. Introduction

A l'alta fantasia qui mancò possa;
ma già volgeva il mio disio e 'l velle,
sì come rota ch'igualmente è mossa,
l'amor che move il sole e l'altre stelle.

Dante Alighieri, Paradiso, XXXIII

1.1. Geo- and astrophysical motivation

Magnetic fields are universal features in the universe which occur in all kinds of celestial bodies such as planets (e.g. Earth and Jupiter), stars like our Sun, and even galaxies (Rüdiger *et al.* (2013)). The evolution and spatial structure of geo- and astrophysical magnetic fields indicate that they went through a process of amplification followed by a self- sustaining mechanism due to internal dynamics (Rincon (2019)). Indeed if such mechanisms would not exist, the fossil magnetic fields of the early formation stage should have decayed over short time scales (as estimated by Weiss (2002) and Roberts & King

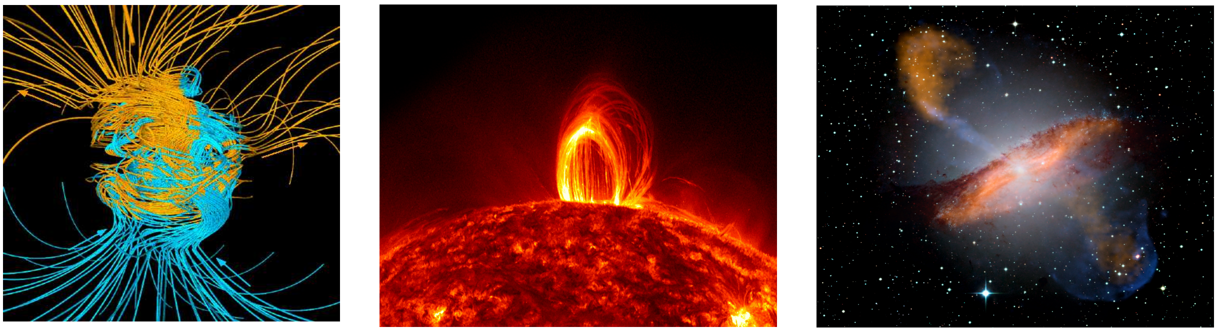

Figure 1.1. Various examples of celestial bodies characterized by dynamo action. Left: sketch of the geodynamo, 3D simulations from Glatzmaier & Roberts (1995) showing the Earth's magnetic field. Middle: solar phenomenon known as *coronal rain* (source Nasa (2013)). Right: galaxy Centaurus A observed by SOFIA (source Nasa (2021)).

(2013)). The fact that the Earth's interior has temperatures above the Curie threshold excludes the hypothesis that the geomagnetic field is caused by permanent magnetization. Therefore, it is commonly thought that the geomagnetic field is generated by fluid motions in the outer core and that its lifespan is around 3 billion years according with paleomagnetic observations (Tarduno *et al.* (2007)).

Another point which rules out the fossil-field hypothesis concerns the dynamical evolution and reversals of large-scale magnetic fields for quite short time scales in the order of a few thousand years (Rincon (2019)).

By now it is widely accepted that all magnetic fields in the universe are generated by the so called *dynamo process* referring to the capability of internal flows of electrically conducting fluids to bring about self-excitation of magnetic fields and electrical currents. The underlining physics is quite basic: a moving electrical medium exposed to a magnetic field induces an electromotive force (Faraday's law). This force generates an electric current (Ohm's law) associated with an amplified magnetic field (Ampère's law) (Rüdiger & Hollerbach (2004)). Self-excitation occurs when the amplification factor becomes infinite. The first application of this phenomenon to celestial bodies was given by Larmor (1919) to describe the solar magnetism. Even if the basic principle was technically realized in the 19th century (starting with Faraday (1832) and followed by the works of Jedlik, Hjorth, Siemens, Gramme, Pacinotti, Wheatstone all summarized in the work by Wilde (1867)), a proof that the dynamo process can actually work in homogeneous fluids was presented almost one century later by Herzenberg (1958) and Backus (1958).

Typical examples of celestial objects affected by dynamo action such as the Earth, the Sun and spiral galaxies are shown in Fig. 1.1.

The Earth's magnetic field presents peculiar features: (*i*) it is substantially dipolar (as observed in the first place by Glatzmaier & Roberts (1995), see Fig. 1.1); (*ii*) its dipole is closely aligned with the rotation axis. Moreover the field is not static and it goes through variations on different timescales. Among all these variations the most dramatic ones are *reversals*, i.e. switches of magnetic field polarity (Gubbins (1994), Merrill & McFadden (1994)). While the field reverses every few hundreds of thousand years irregularly (Merrill & McFadden (1999)), the duration of reversals can span 100 to 10000 years (Rüdiger & Hollerbach (2004)).

The main questions which raise from this picture are how the geomagnetic is generated and why it shows reversals. Regarding the first question, it is broadly believed that the major source for Earth's dynamo action is due to thermal and compositional buoyancy (Jones (2007), Landeau *et al.* (2022)). However a non- negligible amount of power can also rise from mechanisms tapping into the rotation energy of the Earth (Le Bars *et al.* (2015)). Since the energy budget might be tight for the convection driven geodynamo (Nimmo (2015)), a particular proposal regarding the cause of geodynamo was made by Bullard (1949) who indicated precession as a possible power source to generate the Earth's

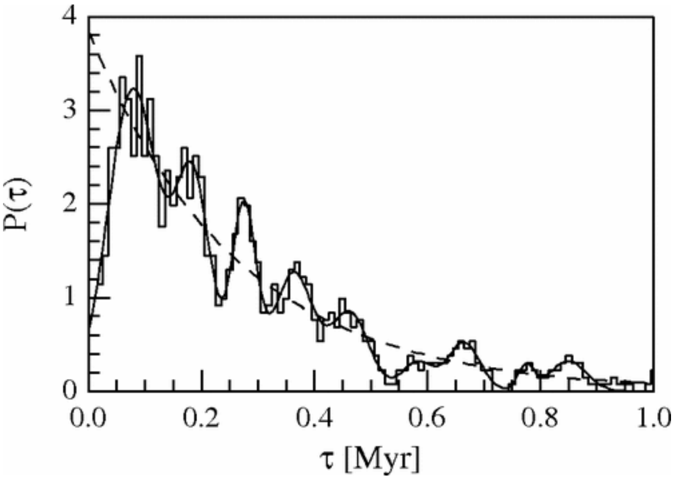

Figure 1.2. Probability density function of the Earth's magnetic field polarity time intervals from Consolini & De Michelis (2003). Note the different peaks at $\tau \approx n \times 95$ kyr, which points to a certain role of the Milankovitch cycle of Earth's orbit eccentricity.

magnetic field.

Mechanical forcing is not only an important candidate as a geodynamo source but also for explaining the geodynamo reversals. Indeed, orbital parameters' variations such as precession, obliquity and eccentricity are observed in the paleomagnetic measurements, suggesting in particular a connection between the ≈ 95 kyr Milankovitch cycle of the Earth's orbit eccentricity with the reversal statistics of the geomagnetic field. Fig. 1.2 replots a corresponding result of Consolini & De Michelis (2003) where the probability density of inter-reversal times shows maxima at multiples of the Milankovitch cycle of Earth's orbit eccentricity, indicating a stochastic resonance phenomenon.

1.2. Previous experimental dynamos

During the last decades, the interest in dynamo action has motivated several scientists to build complex experimental dynamo facilities in order to reproduce some features of cosmic magnetism. While technical dynamos (e.g. Siemens, Wheatstone) have a number of separated electrically conducting parts, cosmic dynamos work in almost homogeneous media. Although theoretical and numerical works have been successful in understanding many mechanisms, several problems remain unsolved. The geodynamo simulations are carried out in a zone of the parameter space far from the real one. This applies, in particular, to two governing parameters: the Reynolds number Re (the ratio of the Coriolis over the viscous force), or its inverse Ekman number Ek, and the magnetic Prandtl number Pm (the ratio of the magnetic diffusion time to the viscous diffusion time). The Earth's values are believed to be respectively of the order $Re \sim 10^{15}$ and $Pm \sim 10^{-6}$ while the state of the art of numerical simulations can achieve values as large as $Re \approx 10^7$ and as low as $Pm \approx 0.1$. The wide gap between real and numerical parameters is a problem for the reliability of the numerical results even if scaling laws are applied. The occurrence of turbulence is another problem due to the lack of validated models for fast rotating electrical conducting fluids. In view of those problems laboratory experiments are a complementary approach to improve our knowledge about the fluid flow behavior in the dynamo regime. Their first goal is then to confirm experimentally that hydromagnetic dynamos work at all. "Playing" with the experimental design can teach a lot about the specific roles of turbulence, boundary conditions, and different dynamo sources. The second point is related to a working hydromagnetic dynamo. Once self-excitation has occurred, one asks which process limits the exponential field growth and what is the mechanism of dynamo saturation. Recent laboratory dynamos comprise different mechanical installations to drive the flow such as propellers, guiding blades, external pumps. In general the fewer installations are present in the fluid, the more freedom has the flow to be modified and re-organized by the Lorentz forces. A most attractive mechanism to drive the flow and to avoid the use of mechanical part would be convection. However, it is very hard to achieve velocities sufficient for dynamo action in a purely convective way (Tilgner (2000)). Another point is the following: the self-excited magnetic field acts not only on the large scale flow, but it could also cause a back-reaction impacting the turbulence properties of the flow. This phenomenon is considered the most important one that dynamo experiments may help to understand, as they provide an interesting test-case for MHD turbulence models (Verma (2004)). An extreme case is the destabilizing role of magnetic field on the total flow. A paradigmatic example of this latter phenomenon is the magneto-rotational instability (MRI) (Rüdiger & Hollerbach (2004), Rincon (2019)). In principle dynamo experiments are suitable to observe similar instabilities in the presence of (self-excited or externally applied) magnetic fields. In addition to this, there is a large variety of wave phenomena to be studied in rotating magnetized flows.

One of the crucial concept of dynamo theory is the α-effect i.e. the induction of an electromotive force parallel to an applied magnetic field. It was actually observed by Max Steenbeck, through an apparatus, the α-box, consisting of two orthogonally interlaced copper channels through which sodium was pumped. The α-effect was clearly validated (Steenbeck *et al.* (1966), Steenbeck *et al.* (1967)) even if the flow had no local helicity.

In the following we discuss the main dynamo experiments that were carried out during the last decades:

- **Lowes-Wilkinson Dynamo**: Lowes and Wilkinson have carried out a long-term series of homogeneous dynamo experiments (Lowes & Wilkinson (1963), Lowes &

Wilkinson (1963), Wilkinson (1984)). The core idea of this kind of experiments had its roots in a 1958 paper by Herzenberg (1958) whose homogeneous dynamo consisted of two rotating small spheres embedded in a large sphere. The Lowes and Wilkinson dynamo is an apparatus with two rotating cylinders in a surrounding conductor. The success of this dynamo was due to the use of various magnetic materials (perminvar, mild steel, electrical iron) allowing a large magnetic Reynolds number. These experimental campaigns were characterized by the step-by-step improvements and also by the continuing comparison of the resulting field with geomagnetic features (Wilkinson (1984)). Starting with a simple geometry of the rotating cylinders which produced steady and oscillating magnetic fields, the design was made more sophisticated so that finally it permitted the observation of field reversals. This proved that a complex field behavior can result from comparatively simple patterns of velocity. The limits of this solid-body experiments were in the lack of possibility to investigate any non-trivial back-reactions of the Lorentz force on a fluid flow.

- **Riga dynamo**: Based on the concept of Ponomarenko's dynamo model (Ponomarenko (1973)) a series of experiments were carried out in St. Petersburg in 1986 (Gailitis *et al.* (1987)) which prepared the context for the Riga dynamo experiment. Several studies about promising dynamo configurations were conducted (Gailitis *et al.* (1976), Gailitis *et al.* (1980), Gailitis (1996a)) with specific focus on the onset at low magnetic Reynolds number. These works served as the basis for the design of the Riga dynamo, shown in Fig. 1.3. The first step was to optimize the main geometric relations, in particular the relations of the radius of each cylinder to each other and to the length of the system (Gailitis (1996b)). The experimental preparations were accompanied by extensive numerical simulations with the aim to optimize the flow profiles in terms of maximizing the helicity (Stefani *et al.* (1997)).
  Many experimental campaigns have been carried out between November 1999 and 2018 resulting in several achievements: the first recording of a self-exciting field in a liquid metal dynamo experiment (Gailitis *et al.* (2000)), observation of the saturated regime (Gailitis *et al.* (2001)), measurement of the radial magnetic field, pressure on the inner cylinder, Lorentz force, axial magnetic field (Gailitis *et al.* (2001b), Gailitis *et al.* (2002a) Gailitis *et al.* (2002b)). All the results were compared with the numerical outcomes of 2D simulations (Stefani *et al.* (1997)). The Lorentz force leads to a reduction of the differential rotation and hence to a deterioration of the dynamo capability of the flow. This self-consistent back-reaction model, which gives automatically a zero growth rate, can be assessed by the dependence of the resulting eigenfrequency and the axial structure of the field (Gailitis *et al.* (2001)). A summary of all the Riga experimental campaigns are reported in Gailitis *et al.*

(2018).

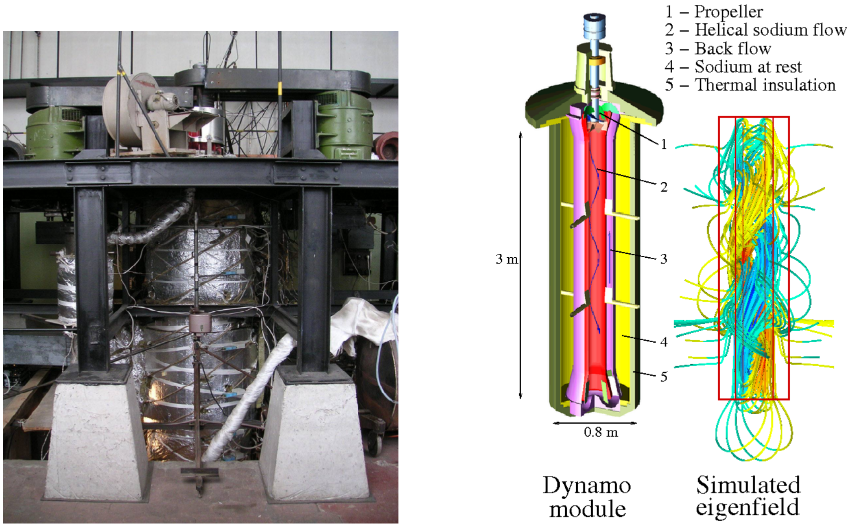

Figure 1.3. The Riga dynamo experiment. Left: photograph of the dynamo facility taken from Gailitis *et al.* (2018). Right: detailed sketch of the central dynamo module.

- **Karlsruhe dynamo**: A first idea for a Karlsruhe-type experiment can already be found in a paper by Gailitis (1967). The main concept was based on the replacement of real helical turbulence by pseudo-turbulence consisting of a large number of parallel channels with a helical flow inside. The seminal works by Roberts (1972) and Busse (1975) served then as the theoretical initiation of the Karlsruhe dynamo experiment, later designed and carried out by Stieglitz & Müller (2001) and Müller *et al.* (2002). This flow is characterized by an anisotropic α-effect that produces only electromotive forces in the horizontal direction. In the Karlsruhe configuration (see Fig. 1.4), the so called Roberts flow (Roberts (1972)) in each cell is replaced by a flow through two concentric channels. While in the central channel the flow is straight, in the outer channel it is forced by a spiral staircase in order to force a helical path. After having established the main configuration, the subsequent step was based on the maximization of α effect for a given power of the pumps. The result was a number of 52 spin generators, with a radius and a height of respectively 0.85 m and 0.7 m for the dynamo module.
  The Karlsruhe dynamo experiment has investigated several features such as its imperfect bifurcation behavior and properties of MHD turbulence (Müller *et al.* (2004)). The experimental data from the Karlsruhe experiment have been used in an attempt to distinguish between two different scaling laws of the geodynamo, with interesting outcomes for its power consumption (Christensen & Tilgner (2004)). From a theoretical point of view the investigation of the saturation mechanisms and their possible implication were addressed by Tilgner & Busse (2001).

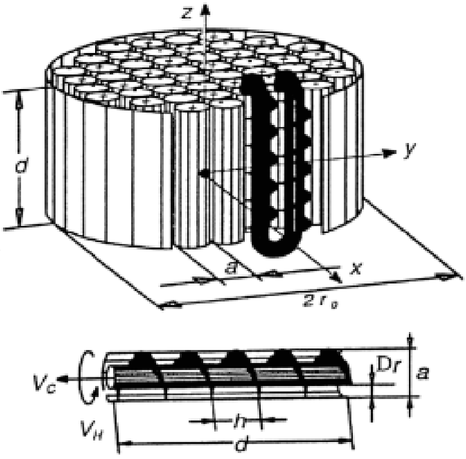

Figure 1.4. The Karlsruhe dynamo experiment (reproduced from Stieglitz & Müller (2001)). Sketch of the main module (top) and details of one of the spin generators (bottom).

- **Von-Kárman dynamo**: The von Kárman Sodium (VKS) dynamo experiment has been carried out at the CEA research center in Cadarache (France). The sodium flow is characterized by the so called $s2^+t2$ type (comprising two poloidal vortices directed inward in the equatorial plane, and two toroidal vortices) and it is produced by two disks situated at opposed end of a cylinder. The VKS 1 experiment was carried out with 50 liter of liquid sodium in a cylinder with diameter and height of 0.4 m, using two 75 kW motors at rotation rates up to 1500 rpm. The results of the VKS 1 experiments, including measured induction and turbulence data, have been published in Bourgoin *et al.* (2002) and Pétrélis *et al.* (2003). No self-excitation has been achieved, although remarkable deformations of applied magnetic fields have been measured. In a second version of this experiment (Berhanu *et al.* (2007), Monchaux *et al.* (2009)), VKS 2, the volume was extended to 100 l, and the available motor power can reach 300 kW. After this experimental upgrade, the VKS has shown not only a self-excitation of the magnetic field but also a myriad of other features such as oscillations, bursts and even reversals (Monchaux *et al.* (2009)). The “blemish” of this experiment consists in the necessity of using magnetic material for the disks, otherwise the dynamo action does not occur (Miralles *et al.* (2013)).

- **Other dynamo experiments**: other experimental facilities have provided many insights. For example the Madison dynamo, also characterized by a $s2^+t2$ flow (Nornberg *et al.* (2005)), the rotating torus experiment in Perm (Frick *et al.* (2002)), and the Sodium experiment in New Mexico (Colgate *et al.* (2002)).
  A particularly interesting laboratory facility is the Maryland Three Meter Geodynamo experiment which consists of a large spherical Couette container filled with water or with sodium for the MHD purposes. This set-up is able to achieve extreme

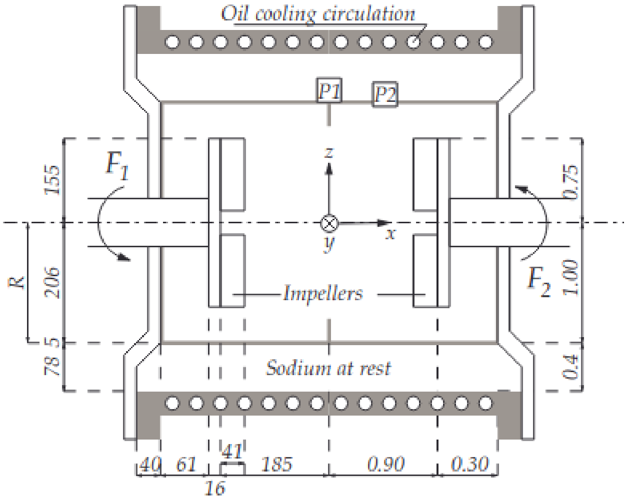

Figure 1.5. Schematic representation of von Karmán dynamo experiment (Monchaux *et al.* (2009)).

hydrodynamics regimes and even if the research group did not find yet a purely self-excited magnetic field, they collected a lot of knowledge regarding magneto-hydrodynamics phenomena imposing an axisymmetric magnetic field (Zimmerman *et al.* (2014)).

Based on Bullard's disk dynamo (Bullard (1949)), an interesting scenario was observed by Avalos-Zúñiga *et al.* (2017) in a homopolar disk dynamo experiment. This kind of facility contains the liquid metal in spiral coils and the resulting magnetic field is purely axial. In a recent work, Avalos-Zúñiga & Priede (2022) found a dramatic increase of magnetic field above certain rotation frequency. Once the magnetic field achieves the saturation whose value is more than two orders of magnitude of the background field the back reaction of electromagnetic torque slows down the disk rotation.

Characterized by a similar concept, the so called FURY dynamo experiment (Plunian & Alboussière (2021, 2022)) has shown the capability to achieve dynamo action exploiting only the differential rotation and using anisotropic electrical conductivity together with an anisotropic magnetic permeability. The result is a pseudo-axisymmetric (but with gaps in the copper) dynamo which from a theoretical point of view bypasses the anti-dynamo theorem proposed by Cowling (1933).

The experimental facilities described so far are characterized by constructional elements or mechanical moving parts which somehow differ from a celestial bodies. To go forward a non-invasive way to induce a flow motion potentially able to drive a dynamo action should be found. Among the forcing mechanisms particularly suitable is precession which has been discussed several times as a candidate source for the geodynamo. Indeed this kind of motion characterized by the change of orientation of the body's rotation axis,

was proposed by Bullard (1949) as power source for the magnetic field generation, and it has received special attention in the last decades. A series of studies were carried out in order to estimate the energetic amount required for the development of a magnetic field. Loper (1975) and Rochester *et al.* (1975) have shown that a purely laminar precessing flow cannot extract sufficient energy to convert into magnetic energy; however the scenario could be completely different for a turbulent precession driven flow which could dissipate a much higher order of magnitude of energy and possibly being able to sustain the geomagnetic field as claimed by Malkus (1968). Precessing-driven flows were therefore proposed as alternative or at least complementary energy sources for magnetic field self-excitation in the Earth's core (Malkus (1968), Vanyo (1991)), the ancient Moon (Dwyer *et al.* (2011), Noir & Cébron (2013), Cébron *et al.* (2019)), and even asteroids (Fu *et al.* (2012)). Numerical works have demonstrated that precession is able to generate a magnetic field in spherical shells (Tilgner (2005, 2007), Cébron *et al.* (2019)), full spheres (Lin *et al.* (2016)), spheroids (Wu & Roberts (2009)), cylinders (Nore *et al.* (2011), Cappanera *et al.* (2016), Giesecke *et al.* (2018)), and cubes (Krauze (2010), Goepfert & Tilgner (2016)). An amplification of an applied magnetic field by a factor of 3 has been observed previously in the precession experiment of Gans (1971).
The DRESDYN (DREsden Sodium facility for DYNamo and thermohydraulic studies) precession experiment (Stefani *et al.* (2012, 2015a)) is devoted to this purpose: verifying that the precession driven flow can achieve a self-generating dynamo. In the next Section 1.3 we will describe the upcoming experiment and all the auxiliary tools to tackle this problem.

1.3. The DRESDYN precession project: experiments and numerics

At Helmholtz-Zentrum Dresden-Rossendorf (HZDR) three main tools are used to scientifically address the problem of precession driven flows and its possibly dynamo action in cylindrical geometry:

- A large-scale dynamo precession machine.

- A 1:6 down-scaled water experiment.

- Direct Numerical Simulations.

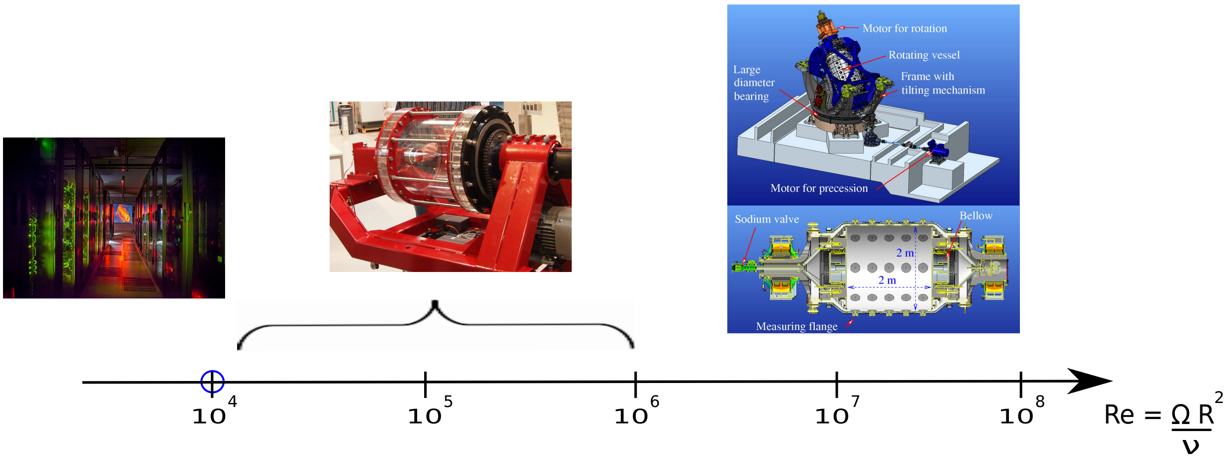

Figure 1.6. Scheme of the various fluid dynamics regimes of the various tools: (global) simulations till $Re \approx 10^4$; down-scaled water experiment for $10^4 \leq Re \leq 10^6$; and finally the dynamo experiment facility up to $Re \approx 10^8$.

The various Reynolds number regimes covered by the three different tools are shown in Fig. 1.6. As we can see from the schematic representation the simulations achieve $Re \approx 10^4$ which is, at the same time, the lower limit for the 1:6 down-scaled water experiment. This set-up runs up to $Re \approx 10^6$. The strongest regimes are covered by the large machine which works in a quite extreme fluid-dynamics condition.

1.3.1. The DRESDYN precession machine

The most ambitious device in the context of the DRESDYN project at HZDR is a precession-driven dynamo experiment (Stefani *et al.* (2012, 2015a,b)). The construction of this apparatus requires tremendous resources and efforts due to the challenges related to the building parts and the safety aspects. The “core” of the facility is the cylindrical

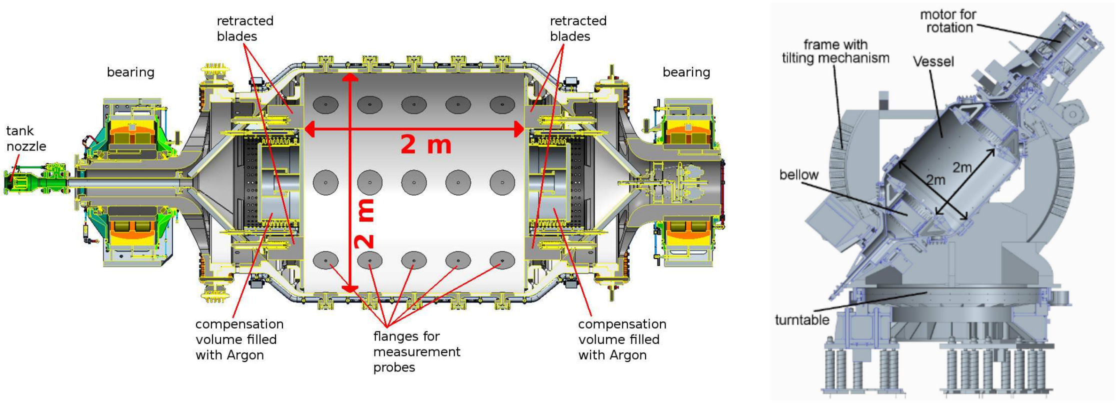

Figure 1.7. Representation of the cylindrical precessing vessel (left) and the tilting frame (right).

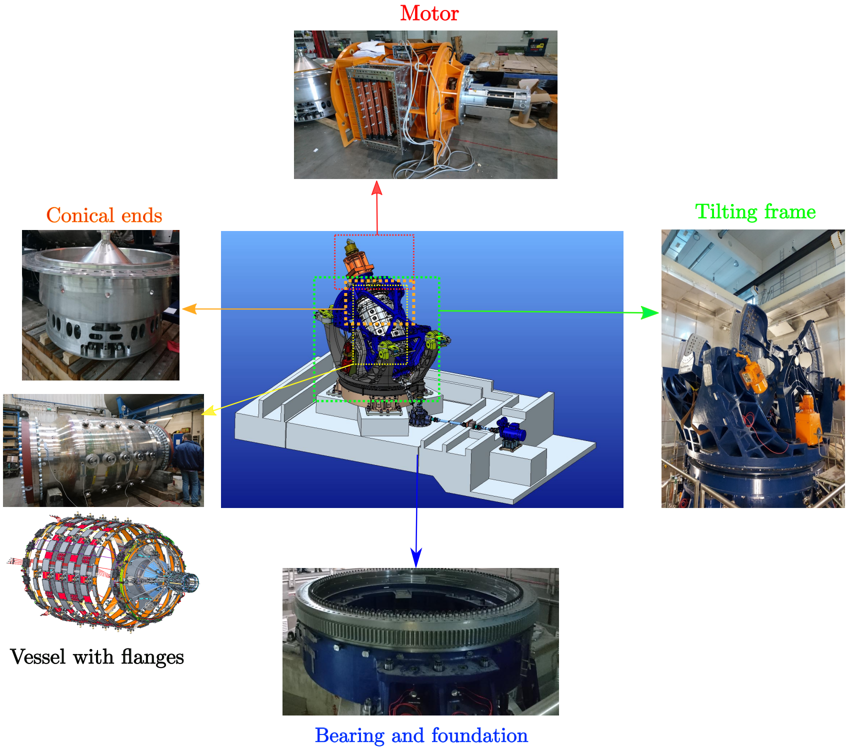

Figure 1.8. Scheme of the DRESDYN precession experiments with the main components (from Pizzi *et al.* (2022a)).

vessel of 1 m radius and 2 m height as shown in Fig. 1.7. This particular aspect ratio, $\Gamma = 2$, is believed to be very efficient for injecting the energy in the fluid flows. The shell of the cylindrical vessel is 3 cm thick since it must sustain a centrifugal pressure of 20 bar. As we can observe from the left panel of Fig. 1.8 there are 40 flanges mounted on the sidewall which contain the probes to measure the pressure. During the sodium experiment the pressure probes will be complemented by Hall sensors to measure the magnetic field. The other features of the machine are the achievable rotation, 10 Hz, and the precession frequency up to 1 Hz which is enough to cover both the laminar and the turbulent regime. The range of the tilt (nutation) angle runs between 45° and 90°. The change in the nutation angle is made possible through the tilting frame (Fig. 1.8) which comprises the pylons and the traverse.

The gyroscopic force emerging from the simultaneous rotation around two axes represents a serious challenge: the resulting torque exerted on the basement is 8×10^6 Nm, requiring a design of the basement standing on 7 pillars with a depth of 22 meters. The required power to rotate the cylinder is provided by an electric motor of 900 kW (as shown on the top panel of Fig. 1.8). An additional variation is possible by extending baffles on the two sides of the cylinder which are retracted during normal operation. The action of these baffles on the flow was recently studied by Wilbert *et al.* (2022).

1.3.2. The down-scaled water experiment

In order to provide detailed measurements of the flow behavior in dependence on the rotation rate (parameterized by the Reynolds number Re) and the precession strength Po, several experimental campaigns have been conducted at the 1:6 down water experiment (Herault *et al.* (2015, 2019), Kumar *et al.* (2023), Giesecke *et al.* (2018)).
The features of the cylindrical vessel are the following: a radius of 0.163 m and a height of 0.326 m with the same aspect ratio of 2 such as the large machine. The cylindrical shell is made by plexiglas so that a first qualitative flow visualization (see Fig. 1.10) is possible thanks to the water bubbles. The cylinder is driven by an asynchronous 3 kW motor via a transmission chain with the power being supplied by a slip ring. In Fig. 1.9(left) we can see the yellow rods whose function is to ensure the parallelism of the end caps of the cylinder. This structure is mounted on the turntable. To measure the flow field, ultrasonic transducers are placed at one end cap of the cylinder (1.9) and are connected with an ultrasound Doppler velocimeter. The transducers emit an ultrasonic pulse and receive echoes reflected from particles. The axial flow velocity is inferred from the Doppler shift of the recorded echoes. Previously obtained experimental results concerned the flow transition laminar/turbulent and a corresponding hysteretic cycle (Herault *et al.* (2015)), the detection of instabilities and detuning effects with the departure from solid body rotation (Herault *et al.* (2019)) and the detection of nonlinear large scale structure formed at certain precession ratios (Giesecke *et al.* (2018)). More recent experimental measurements have been shown to be in very good agreement with the numerical simulations (Giesecke *et al.* (2019), Kumar *et al.* (2023)). One of the most interesting observation is the transition between a laminar organized flow field to a chaotic one as shown in Fig. 1.10. For small forcing we see a characteristic S-shape while for increasing precession the flow becomes more and more chaotic with the air bubbles spread in the entire bulk region finally achieving a strong vortical behavior with turbulent

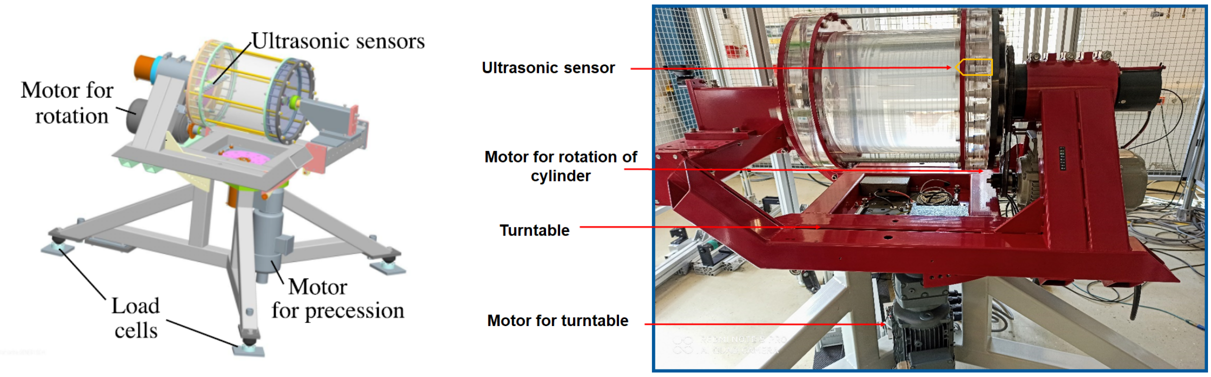

Figure 1.9. Down-scaled water experiment (as shown in Kumar *et al.* (2023)). Left: Sketch of the water experiment. Right: photography of the experiment with the description of the various components.

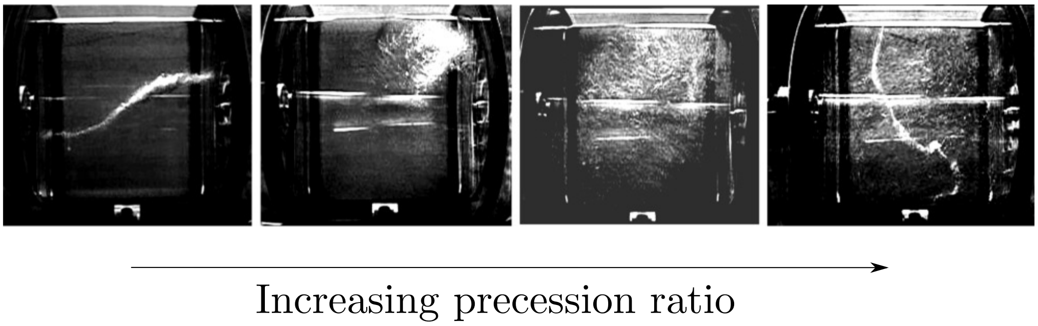

Figure 1.10. Flow observation taken from Herault *et al.* (2019). The nutation angle is fixed at 90° and the four panels show increasing precession ratio; left panel laminar with S-shape, then nonlinear regime and finally the chaotic turbulent state.

fluctuations. At the largest precession ratio a vertical column (aligned more or less with the precession axis) emerges.

1.4. Fluid dynamics of precession

Fluids enclosed in precessing cavities are important also outside the dynamo context. They characterize, e.g., the flow behavior in fuel tanks of rotating rockets (Stewartson (1959), Gans (1984)) and atmospheric large scale vortices, or the liquid part of planets interior (Le Bars *et al.* (2015), Cébron *et al.* (2019), Noir & Cébron (2013)). Quite generally the dynamics of the precessional forcing results from the continuous change of the orientation of the container rotation axis around a second one, the precession axis. Precession gives rise to complex three-dimensional flow structures originating from the interactions of free inertial modes (typical features of rotating fluids caused by the restoring effect of the Coriolis force), boundary layers and the base flow.

The pioneering work of Sloudsky (1895) and in particular Poincaré (1910), in which a precessing inviscid flow in a spheroidal cavity was mathematically described in terms of a uniform vorticity solution, started the field. Figure1.11 shows the main features of this *Poincaré flow* (known also as *tilt-over mode*): it is enclosed in a spheroidal cavity and the gyroscopic motion causes the tilt of the flow rotation axes, which from the container rotation vector migrates towards the precession vector increasing the precession strength. Moreover the fluid parcels tend to follow the elliptical streamlines in plane nearly perpendicular to the flow axes. If a resonant mechanism occurs then the flow undergoes the so called elliptical instability (Kerswell (2002)). The tilt of the fluid rotation axes has been confirmed by experimental observation such as the one shown in Fig. 1.11(b).

An extension of the Poincaré solution was developed by Busse (1968) who added viscous effects in boundary layers and weakly non-linear effects. A lot of interest has been devoted

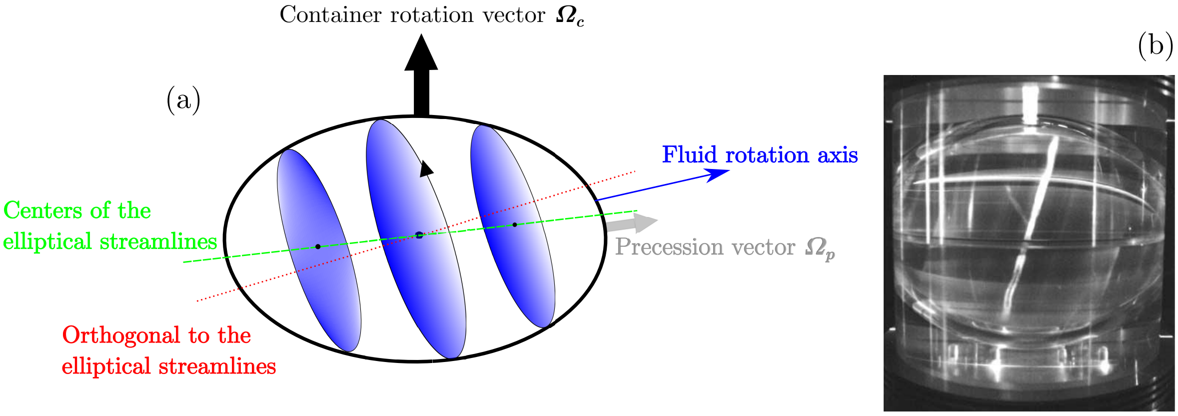

Figure 1.11. Features of the Poincaré flow. (a) Sketch of the Poincaré flow together with the various axes (adapted from Le Bars *et al.* (2015)). (b) Experimental observation of flow rotation axis in a spheroidal cavity reproduced from Noir *et al.* (2003).

to the cylindrical geometry which, even if it seems to be not suitable for geophysical applications, shows remarkable analogies in terms of flow transition (Herault *et al.* (2015)) with spheroids (Komoda & Goto (2019), Goto *et al.* (2014)) and ellipsoids (Burmann (2020)) while the spherical case is in some sense exceptional.

So far cylindrical geometry is the one that has been tested in terms of magnetic field amplification: Gans (1971) conducted experiments where he found an amplification of an external magnetic field by a factor of three. He also developed a linear hydromagnetic theory in cylindrical geometry.

The pure hydrodynamic problem of a precessing container represents a challenging issue due to the complexity of the flow field and the richness of its dynamics. In order to have an idea of the difficulties of the topic, Fig. 1.12 exhibits a summary of the various works done in the last decades. The phase diagram, Fig. 1.12(a), is defined in terms of the two major governing parameters: (i) the forcing term $Po\ \sin(\alpha)$ with Po being the precession magnitude (or Poincaré number), i.e the ratio of precession angular velocity over the container angular velocity, and α is the nutation angle; (ii) the Ekman number Re which quantifies the the viscous force with respect to the Coriolis force[1]. While it is clear that numerics and experiments are yet far from the planetary range, a lot of knowledge has been collected so far. Numerical works have investigated the role and subtle behavior of turbulence in several geometry such as cube (Fig. 1.12(b1)) and sphere (Fig. 1.12(b2)). In spheroid, see Fig. 1.12(b3), the chaotic flow is accompanied by the spin-up of the fluid axes which stays between the precession and the rotation axes, by contrast in cylindrical geometry the fluid flow is dominated by standing waves with unitary wave numbers as shown in Fig. 1.12(b4).

On the other side the experimental campaigns are able to achieve higher regimes due to the lack of computational limits. Therefore small-scale phenomena Fig. 1.12(c1), bulk

---

[1] In the present work we define the (global) Reynolds number as the inverse of the Ekman number.

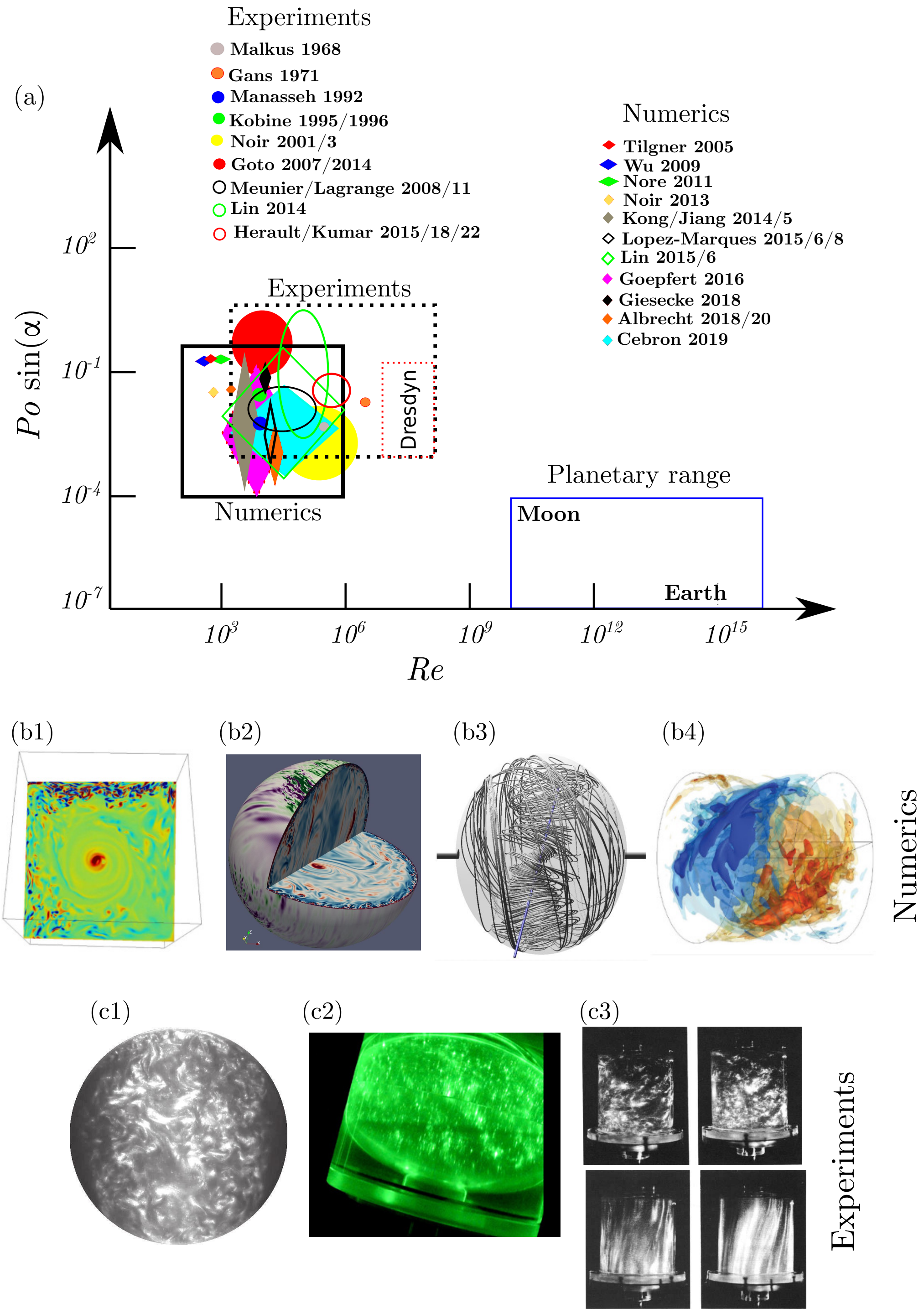

Figure 1.12. Summary of the precession driven flow results in literature. (a) Parameter space covered by numerical simulations, experimental investigations and planetary objects. (b1) Simulation in cubic geometry by Goepfert & Tilgner (2016); (b2) Simulation of turbulent geodynamo taken from Cébron *et al.* (2019); (b3) simulated fluid streamlines from Komoda & Goto (2019); (b4) contour of simulated precessing cylinder (Giesecke *et al.* (2018)). In the second row some experimental observation are shown: (c1) turbulence in precessing sphere taken from Horimoto & Goto (2018); (c2); PIV in spheroidal cavity by Nobili *et al.* (2021); (c3) several flow response categorized by Manasseh (1992).

instabilities Fig. 1.12(c2) and several pathway for transition to turbulence Fig. 1.12(c3) have been observed.

1.4.1. Precession driven flows in a fluid filled cylinder

The shape of the container plays a substantial role for the type of flow response. In the following we focus our attention on cylindrical geometry which is the topic of this thesis. In a cylinder, precessional forcing excites inertial modes (called Kelvin modes due to the first work by Kelvin (1880)) which become resonant if their frequency is equal to that of the forcing (Zhang & Liao (2017)). Therefore the flows show a non-trivial behavior already in the weakly forced regime being governed by a 3D flow field consisting of superimposition of inertial waves which are particularly excited when approaching the resonance condition. While outside the resonance the amplitudes of the inertial waves can be predicted by a linear-inviscid model (Greenspan (1968)), at resonance the viscosity must be taken into account in order to find the saturated amplitude. Various models have been proposed which include viscous effects (Gans (1970), Liao & Zhang (2012)) and even weakly non-linear interactions (Meunier *et al.* (2008), Gao *et al.* (2021)). A strong response of the fluid is typically observed in connection with the onset of instabilities, eventually leading to complex chaotic and/or turbulent flows as shown in Fig. 1.12(c3) (Manasseh (1992)). The resonance condition depends on the container aspect ratio (the ratio between radius and height); for example, when an inertial mode has a wavelength which matches the cylinder's height it becomes resonant (Greenspan (1968)). At resonance the flow is highly unstable, tending to degenerate into a state of chaotic and fine-scale motion called *resonant collapse* (McEwan (1970), Manasseh (1992)). Hysteresis phenomena, in terms of relaminarization-breakdown cycles, have been observed too (McEwan (1970), Manasseh (1992), Herault *et al.* (2015)) and several instability mechanisms were identified (Giesecke *et al.* (2015), Lagrange *et al.* (2011), Herault *et al.* (2019), Meunier *et al.* (2008)). A particularly interesting effect due to strong forcing action is the emergence of a geostrophic circulation which dominates the bulk flow behavior at large precession ratio. Geostrophic structures are well known in rotating flows with or without additional mechanical forcing and have been found in simulations and experiments that involve inertial waves such as libration (Favier *et al.* (2015), Le Reun *et al.* (2019)), tidal forcing (Barker & Lithwick (2013)) and the elliptical instability (Le Reun *et al.* (2017)). Geostrophic flows in strongly precessing cylinders have been observed in numerical studies (Giesecke *et al.* (2018), Kong *et al.* (2015), Jiang *et al.* (2014)) and experimentally by Kobine (1996) who proposed the centrifugal instability as the cause of the breakdown of inertial modes. A similar conclusion was drawn by Herault *et al.* (2019) in the context of the so-called *detuning effect*.

A possible scenario is that the collapse of directly forced inertial modes does not necessarily have to be complete, rather the growth of a centrifugal instability can develop independently. Another scenario (Zhang & Liao (2017), Greenspan (1969)) proposes that the axisymmetric part of the geostrophic circulation can be driven solely by non-linearity in viscous boundary layers formed on the cylinder endwalls (Manasseh (1992), Meunier *et al.* (2008), Liao & Zhang (2012)).

The focus of other experiments was on precession as an efficient mechanism to drive dynamo-prone flows without making use of any propellers or pumps (Léorat *et al.* (2003), Léorat (2006)).

This is the main background on which this Thesis is based on and in the next Section we will describe its outline.

1.5. Goals and structure of this Thesis

The general goal of a theoretical framework for experiments with fluid-filled precessing cylinders, in particular for the DRESDYN dynamo experiment, is to understand the various flow mechanisms. The specific problems to be attacked in this work are represented schematically in Fig. 1.13. They can be summarized as follows: (*i*) Understanding the flow behavior close to the wall and the role of boundary layers. (*ii*) Characterizing the flow response when changing the key governing parameters, i.e. container rotation, precession magnitude and the nutation angle. Connected to this point we want to find the best region in the phase space in order to trigger beneficial flow conditions for dynamo action. (*iii*) Verifying the capability of the flow to trigger dynamo action. (*iv*) Understanding the turbulence properties forced by precession.

The various points addressed above are complex topics by themselves and are strongly interrelated. The first challenge is to study them separately. The following bullet-points separate the various phenomena and indicate the respective chapters of the thesis:

- **Chapter 2** introduces the basic theoretical concepts underlying this work. Starting from the very basic governing equations of fluid mechanics and electrodynamics, we present the linear theory for precessing fluid flow and the explicit description of the inertial waves emerging in cylindrical geometry.

  The theoretical models are presented both for the global (i.e. the entire cylindrical domain) and the local model. For the latter we develop also the Fourier formulation used to work in spectral space for the turbulence studies.

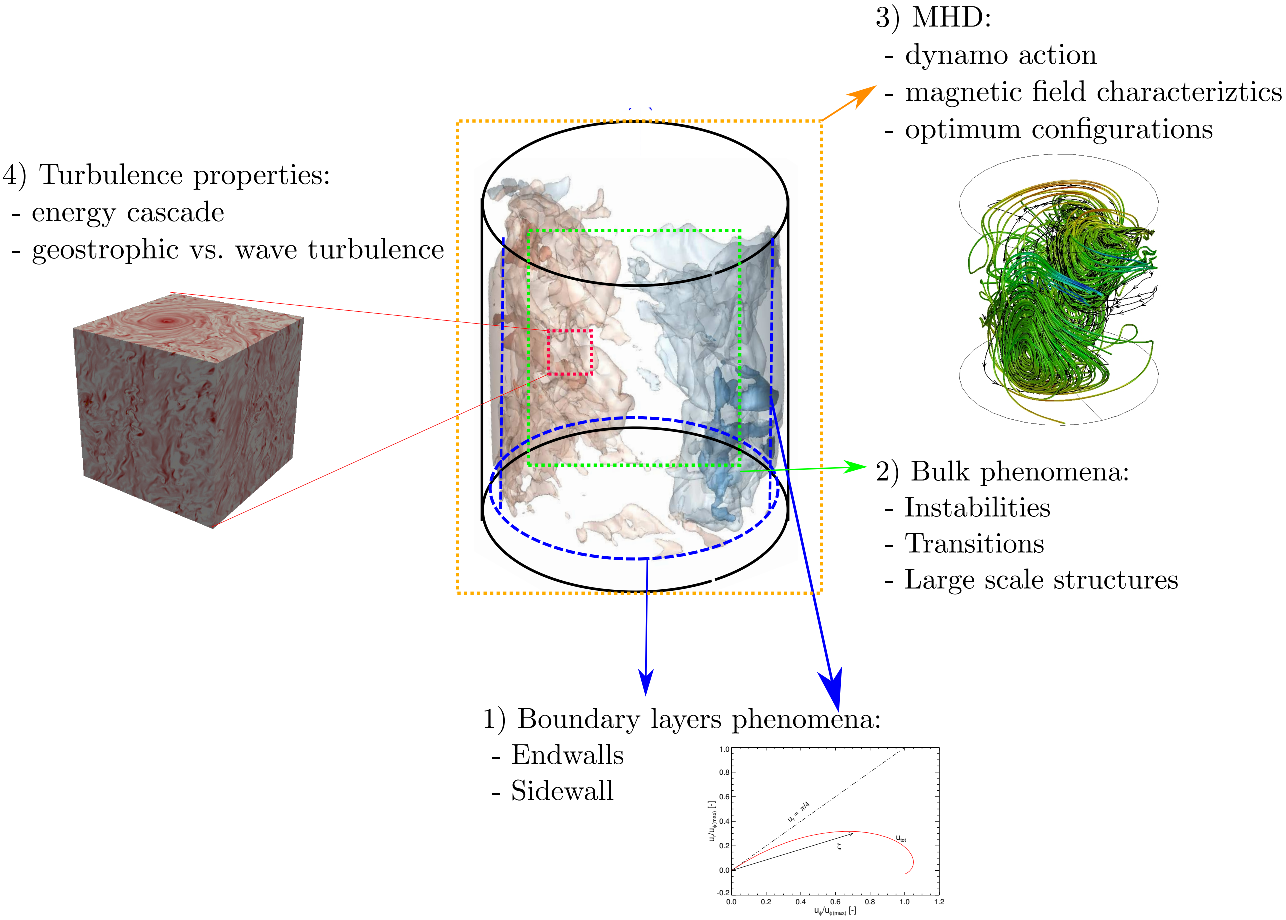

Figure 1.13. Summary of the topics addressed in the current thesis.

- **Wall phenomena: Boundary layers**

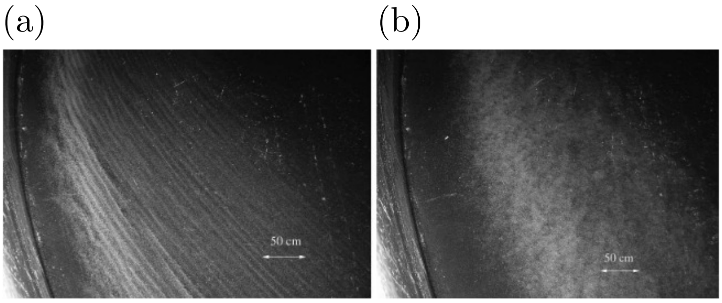

Figure 1.14. Experimental observation of the Ekman boundary layer by Sous *et al.* (2013). (a) Occurrence of the instabilities. (b) Fully turbulent layer.

The problem of boundary layers in cylindrical geometry is far from trivial due to the existence of two different types of walls: a flat boundary at the endcaps and a curved sidewall layer. Moreover the interactions between the bulk flow and the boundary layers are subtle. Precession, as a sub-category of rotational fluid dynamics, is known to develop so-called Ekman layers (when viscous forces are strong and balanced by the pressure gradients and Coriolis force). However up to present no investigation was carried out for the cylindrical geometry. The study of Ekman layers subjected to precession force may elucidate some mechanisms for the oceanographic and atmospheric fields such as the Ekman pumping mechanism or the emergence of cyclonic/anticyclonic vortices. It has been observed that the Ekman boundary layers are prone to instabilities and complex behavior in turbulence regime occurs (see Fig. 1.14).

Chapter 3 is concerned with the phenomena related to boundary layers in a precessing cylinder. We distinguish between the endwall layers, which are pure Ekman layers with some peculiarities, and sidewall layers. At low forcing the numerical results match well with the analytical theory. The increase of the forcing nonlinear effects cause peculiar interaction between the Ekman layer and the bulk flow only in certain range of precession magnitude for the endwall boundary layer. By contrast the sidewall boundary layer undergoes a subtle transition reflecting the changes in the bulk flow region. Furthermore, by making use of stress-free condition at the endcaps we are able to define a clear hierarchy between bulk and wall phenomena, discerning the various occurrences.

- **Impact of prograde/retrograde precession and the role of nutation angle**

Most studies (Manasseh (1992), Noir *et al.* (2001), Noir & Cébron (2013), Cébron *et al.* (2019), Albrecht *et al.* (2021)) have focused their attention on the retrograde motion (i.e when the rotation and precession vector rotates in opposite direction) due to the geophysical application. However one of the purposes of this thesis is to understand and show the difference of these two configurations. This topic deals specifically with the problem of forcing effects in fluid flows and what kind of bulk instabilities/large scales structures can emerge.

Chapter 4 investigates the flow response due to the prograde/retrograde type of precession motion and the role of the nutation angle. A stunning difference between prograde and retrograde precession occurs. The flow transition between laminar and turbulent state is steep only for the prograde motion which occurs together with a centrifugally unstable behavior. For particular combinations of the governing parameters a poloidal flow (resembling Taylor vortices) appears with different direction and magnitude when changing the nutation angle.

- **Dynamo action in precessing cylinder**

As already discussed precession could be a candidate mechanism to drive a homogeneous dynamo. The fluid flows should have enough helicity in order to trigger the self-excitation of the magnetic field. Several previous numerical works have observed precession driven dynamos. Here we focus on cylindrical geometry with a fixed aspect ratio to conduct a wide study changing the main governing parameters. Following the work of Giesecke *et al.* (2018) we make use of a kinematic dynamo model, by decoupling the flow field evolution from the magnetic field evolution, in order to discern if a particular flow configuration is able to self-generate the magnetic field at all. Even if our model is a simplified version in terms of the applied magnetic boundary condition and the lack of back-reaction we identify the optimum parameters to run the configuration.

Chapter 5 is the continuation of Chapter 4 where we use the fluid flow from the hydrodynamic simulations to check their capability to achieve dynamo action. In this work the investigation is based on the kinematic dynamo model, i.e. the magnetic field is supposed to have no back reaction on the fluid flows (no Lorentz force). In the first instance this approach allows to identify the beneficial flow structures to achieve the dynamo action by varying the governing parameters. We asses the best range of nutation angles to achieve a positive growth rate of the magnetic field. Moreover we find how the optimum precession (in terms of largest magnetic energy growth rate) ratio scales in terms of Reynolds number. The nutation angle controls not only the dynamo occurrence and growth rate but also the topology of the field.

- **Precession as a complex type of rotating turbulence**

The field of turbulence has a long history. The idea of *energy cascade* started with the intuition of Richardson (1922) which was then formalized by Kolmogorov (1941a), Kolmogorov (1941b) according to whom turbulence emerges as a composition of eddies of different sizes. The Kolmogorov turbulent cascade states that in turbulent flows the energy is mainly contained in large-scale eddies which are defined by small wavenumbers. The energy is transferred from the larger to the smallest scales passing through an intermediate region called inertial range, whereas the energy content scales as $k^{-5/3}$; this concept is shown in Fig. 1.15(a). Notice that at the largest wave numbers (Kolmogorov scale) the dissipation occurs in terms of a

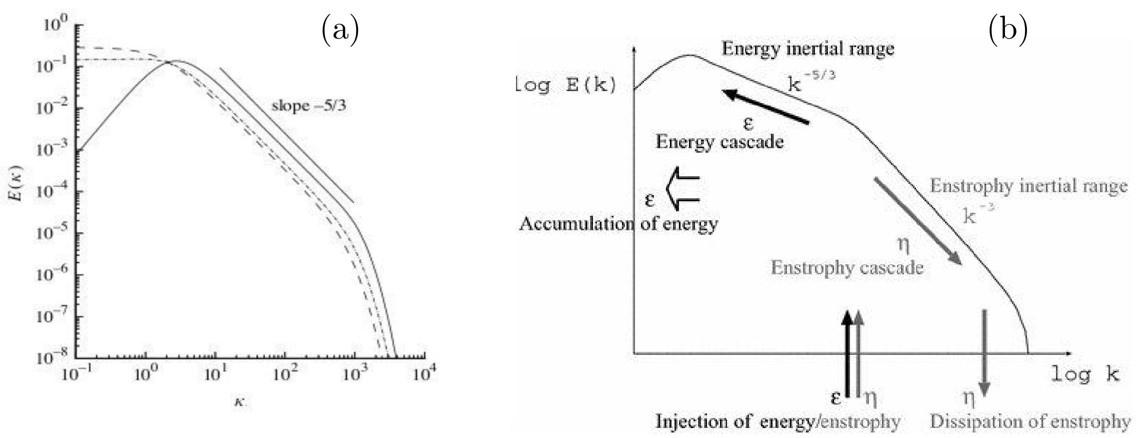

Figure 1.15. Difference between (a) 3D Kolmogorov from Pope (2000)) and (b) 2D energy turbulence energy spectra.

conversion of mechanical energy into thermal energy. In this range the turbulence structures tend to be isotropic.

This theory fails for all those phenomena dominated by rotation dynamics as they occur in astrophysical and geophysical bodies. The effects of rotation are relevant and can generate essentially two-dimensional flows, defined as quasi-geostrophic. However this anisotropic behavior does not occur at small scales where the influence of rotation is negligible. The main feature of rotating turbulence is that two quadratic invariant quantities are conserved independently: the total energy and the potential enstrophy (the vorticity intensity) which is related to the dissipation effects of turbulent kinetic energy (Rhines (1979), Biferale *et al.* (2016)). The results is that in astro/geophysical flows the cascade can be both direct and inverse making the final scenario complex as shown schematically in Fig. 1.15(b).

We investigate the precession driven flows under this point of view.

Chapter 6 is dedicated to the study of turbulence properties for fluid flows forced by precession. The main focus is on understanding the interplay between 2D vortices and 3D inertial wave turbulence which appear simultaneously. Consistently with these feature, we observe a split cascade, i.e. direct and inverse cascade. The precession ratio is responsible to inject energy in 3D waves while nonlinearities redistribute energy towards 2D structures.

- **Chapter 7** provides a summary of the present study and an outlook for future studies.

2. Theoretical background and numerical implementation

> *La filosofia [della natura] è scritta in questo grandissimo libro che continuamente ci sta aperto dinanzi a gli occhi (io dico l'universo), ma non si può intendere se prima non s'impara a intender la lingua, e conoscere i caratteri ne quali è scritto. Egli è scritto in lingua matematica...*
>
> Galileo Galilei, Il Saggiatore

In this Chapter, we introduce the governing equations of fluid mechanics and some well established theories in the context of rotating flows (Greenspan (1968), Tilgner (1998), Davidson (2013), Zhang & Liao (2017)). Then we present the fundamental equations of electrodynamics which, together with the equations of fluid motion, represent the theoretical keystone of magnetohydrodynamics (MHD). After that we discuss the theoretical base for the study of turbulence in Fourier space.

In the second part of this Chapter we describe the numerical methods adopted for this thesis.

2.1. Governing equations for rotating systems

According to the continuum hypothesis, velocity $\boldsymbol{U}(\boldsymbol{x}, t)$ and pressure fields $p(\boldsymbol{x}, t)$ are considered as continuous functions of the Eulerian space vector $\boldsymbol{x}$ and the time t which are defined on a subset of $\mathbb{R}^3$. The motion of viscous fluids is generally described by the Navier-Stokes equations (NSEs), which are the conservation laws for mass and momentum

(Newton's second law). The continuity equation describes the mass conservation:

$$\underbrace{\frac{\partial \rho}{\partial t}}_{\substack{\text{Temporal} \\ \text{variation}}} + \underbrace{\boldsymbol{\nabla} \cdot (\rho \boldsymbol{U})}_{\substack{\text{Spatial variation} \\ \text{of mass flux}}} = 0, \tag{2.1}$$

where $\rho(\boldsymbol{x}, t)$ denotes the density of the fluid. Equation (2.1) ensures that the temporal accumulation or loss of mass is equal to the net balance of the mass fluxes. Fluids are defined incompressible when there is no density variation and the continuity equation then simplifies to

$$\boldsymbol{\nabla} \cdot \boldsymbol{U} = 0, \tag{2.2}$$

stating that the velocity field must be solenoidal everywhere. When considering a fluid which undergoes rotation with a time-dependent angular velocity $\boldsymbol{\Omega}(t)$, there are different frames of reference that may be employed (Tilgner (1998)):

- rotating frame (r) → when the rotation axis is fixed in the fluid container;
- inertial frame (i) → non-rotating frame.

The relation between the time derivatives in the two frames is the following:

$$\left(\frac{\partial}{\partial t}\right)_i = \left(\frac{\partial}{\partial t}\right)_r + \boldsymbol{\Omega}\,(t) \times \ . \tag{2.3}$$

Applying Eq. (2.3) to the position vector $\boldsymbol{r}$ we obtain the relation:

$$\left(\frac{\partial \boldsymbol{r}}{\partial t}\right)_i = \left(\frac{\partial \boldsymbol{r}}{\partial t}\right)_r + \boldsymbol{\Omega}\,(t) \times \boldsymbol{r} \tag{2.4}$$

which can be expressed simply as $\boldsymbol{U}_i = \boldsymbol{U}_r + \boldsymbol{\Omega} \times \boldsymbol{r}$ i.e. the relation between the velocity $\boldsymbol{U}_r$ in rotating frame and the velocity $\boldsymbol{U}_i$ in the inertial frame. Then, applying again Eq. (2.3) to the velocity field we obtain

$$\left(\frac{\partial \boldsymbol{U}_i}{\partial t}\right)_i = \left[\frac{\partial\,(\boldsymbol{U}_r + \boldsymbol{\Omega}\,(t) \times \boldsymbol{r})}{\partial t}\right]_i = \left(\frac{\partial \boldsymbol{U}_r}{\partial t}\right)_i + \left(\frac{\partial \boldsymbol{\Omega}\,(t)}{\partial t}\right)_i \times \boldsymbol{r} + \boldsymbol{\Omega} \times \left(\frac{\partial \boldsymbol{r}}{\partial t}\right)_i \tag{2.5}$$

from which, after some algebra, we achieve the formulation

$$\left(\frac{\partial \boldsymbol{U}_i}{\partial t}\right)_i = \left(\frac{\boldsymbol{U}_r}{\partial t}\right)_r + 2\boldsymbol{\Omega}\,(t) \times \boldsymbol{U}_r + \left(\frac{\partial \boldsymbol{\Omega}\,(t)}{\partial t}\right)_i \times \boldsymbol{r} + \boldsymbol{\Omega}\,(t) \times (\boldsymbol{\Omega}\,(t) \times \boldsymbol{r}) \tag{2.6}$$

Eq. (2.6) connects the time evolution of the velocity in the inertial frame with that in the rotating frame.

2.1.1. The governing equations of precession fluid dynamics

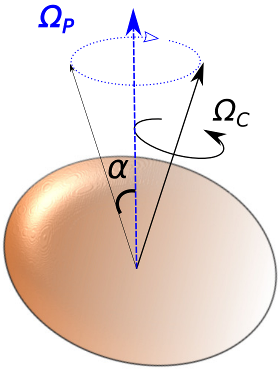

Figure 2.1. Sketch of a general precessing body with the container angular velocity $\mathbf{\Omega}_c$ and precessing angular velocity $\mathbf{\Omega}_p$. The prograde (retrograde) motion occurs when the container and precession vector have the same (opposite) sign.

We consider an incompressible homogeneous fluid enclosed in a generic body, driven solely by precession, in the (non-inertial) mantle frame as shown in Fig. 2.1. The resulting flow is described by the non dimensional Navier-Stokes equation (Albrecht *et al.* (2021)):

$$\frac{\partial \boldsymbol{U}}{\partial t} + \boldsymbol{U}\cdot\boldsymbol{\nabla}\boldsymbol{U} = -\boldsymbol{\nabla}P + \frac{1}{Re}\boldsymbol{\nabla}^2\boldsymbol{U} - 2\mathbf{\Omega}\times\boldsymbol{U} + \frac{d\mathbf{\Omega}}{dt}\times\boldsymbol{x}\,, \tag{2.7a}$$

$$\boldsymbol{\nabla}\cdot\boldsymbol{U} = 0\,. \tag{2.7b}$$

Here $\boldsymbol{U}$ is the velocity flow field, $\mathbf{\Omega} = \mathbf{\Omega}_{\boldsymbol{c}} + \mathbf{\Omega}_{\boldsymbol{p}}$ is the total rotation vector and $\boldsymbol{x}$ is the position vector with respect to the origin. P is the reduced pressure which includes the hydrostatic pressure and other gradient terms (including the centrifugal force) that do not change the dynamical behavior of the flow. The last two terms on the right-hand side are the Coriolis and the Poincaré force, respectively. In order to non-dimensionalize the Navier-Stokes equation we have used the radius R as length scale, $\mathit{\Omega}_c^{-1}$ as time scale and consequently $\rho(R\mathit{\Omega}_c)^2$ as the unit of pressure.

In order to close the problem it is necessary to define the boundary conditions. For a closed container, the realistic approach are no-slip conditions $\boldsymbol{U} = 0$ at all walls. The key parameters governing the hydrodynamics of precession flows are: (i) the Reynolds number Re (inverse of the Ekman number Ek) providing the ratio between Coriolis force and viscous force; (ii) the Poincaré number Po defined as the ratio of precession angular velocity to rotation angular velocity, and (*iii*) the geometry of the container which, in case of a cylinder, is the aspect ratio Γ:

$$Re = \frac{1}{Ek} = \frac{R^2\left(\Omega_c + \Omega_p \cos\alpha\right)}{\nu}, \quad Po = \frac{\Omega_p}{\Omega_c}, \quad \Gamma = \frac{H}{R}\,, \tag{2.8}$$

where ν denotes the kinematic viscosity. Another typical parameter of precession problem is the nutation angle i.e the angle between the angular and precession angular velocity vectors. It ranges between 0° and 90°.

2.1.2. Precession of a fluid-filled cylinder

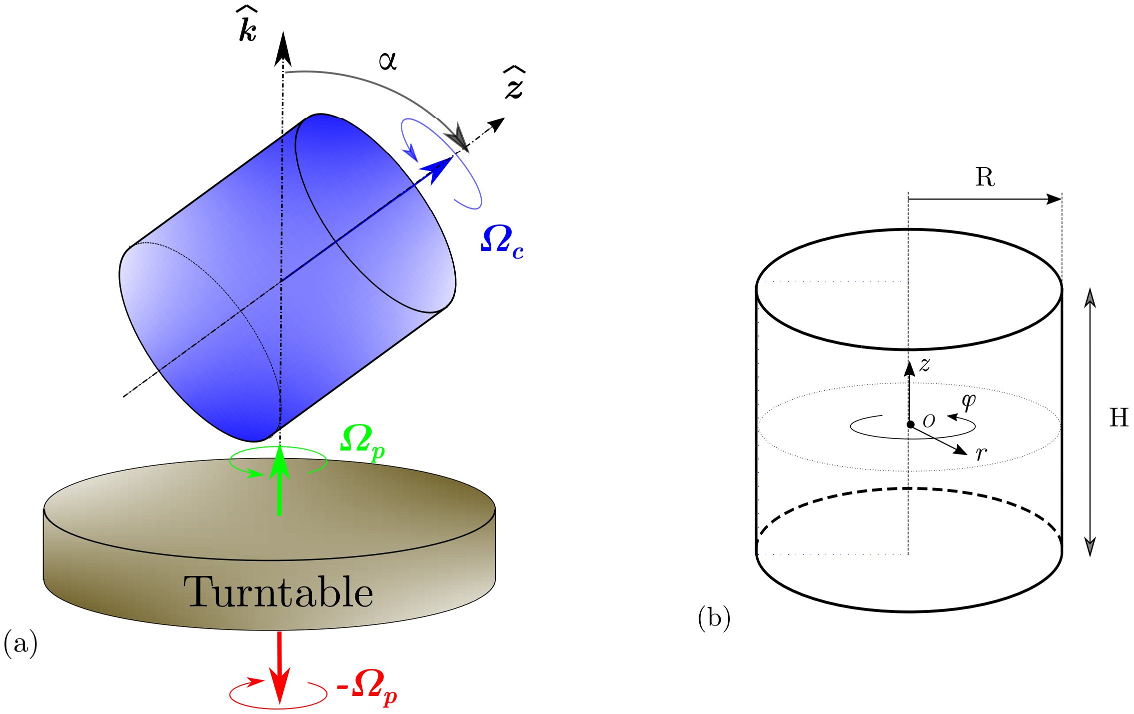

Figure 2.2. Schematic representation of the precessing cylinder as shown in Pizzi *et al.* (2021b). (a) Visualization of the cylinder with the rotation angular velocity $\boldsymbol{\Omega_c}$ and the precession angular velocity $\boldsymbol{\Omega_p}$ (prograde) or $-\boldsymbol{\Omega_p}$ (retrograde); α is the nutation angle that is measured from the precession axis $\hat{\boldsymbol{k}}$ to the cylinder axis $\hat{\boldsymbol{z}}$. (b) Cylinder body of radius R and height H. The origin O is located in the center of the cylinder with the cylindrical coordinate system (z, r, φ).

Now we specify the Navier-Stoles equation for the cylindrical geometry in the mantle frame:

$$\begin{aligned}\frac{\partial \boldsymbol{U}}{\partial t} + \boldsymbol{U}\cdot\boldsymbol{\nabla}\boldsymbol{U} = \quad & 2\left(\hat{\boldsymbol{z}} + Po\left[\hat{\boldsymbol{r}}\sin\alpha\cos\left(\varphi+t\right) - \hat{\boldsymbol{\varphi}}\sin\alpha\sin\left(\varphi+t\right) + \hat{\boldsymbol{z}}\cos\alpha\right]\right)\\ & -\boldsymbol{\nabla}P + \frac{1}{Re}\boldsymbol{\nabla}^2\boldsymbol{U} - 2\hat{\boldsymbol{z}}rPo\sin\alpha\cos\left(\varphi+t\right)\ ,\end{aligned} \tag{2.9}$$

with the last term of the right hand side being the Poincaré force. The cylindrical coordinates, fixed in the origin of the container O, are the axial (z), radial (r) and azimuthal (φ) ones, respectively, as shown in Fig. 2.2(b). The aspect ratio $\Gamma = H/R$ is fixed in experiment and so in simulations which can be chosen to meet the condition of resonance for various inertial modes, as will be explained in the subsection 2.1.4.

2.1.3. Linear models of precession hydrodynamics

In order to study the flow structures inside the cylindrical domain it is necessary to express them in an appropriate mathematical form. To do this we work with a simplified model. The inviscid linearized Navier-Stokes equation for precession is the simplified form of Eq. (2.9) with $Re \to \infty$ and without the advective term, i.e $\boldsymbol{u} \cdot \boldsymbol{\nabla} \boldsymbol{u} = 0$. We discuss the solutions by splitting the problem into a homogeneous and an inhomogeneous part. The homogeneous equation corresponds to the non-forced equation, describing a purely rotating flow:

$$\frac{\partial \boldsymbol{U}}{\partial t} + \boldsymbol{\nabla} P + 2\hat{\boldsymbol{z}} \times \boldsymbol{U} = 0. \tag{2.10}$$

For the linear inviscid model the corresponding boundary conditions reduce just to the free-slip, i.e., the normal velocities vanish at the wall:

$$\boldsymbol{U} \cdot \hat{\boldsymbol{n}} = 0, \quad \text{at} \quad r = 1, \quad z = \pm 1\,. \tag{2.11}$$

The solution of the linear Eq. (2.10) yields the eigenfunctions for rotating flows $\boldsymbol{U}_{mnk}(z, r, \varphi) e^{i\omega_{mkn}t}$ which are characterized by three integers (m, k, n) indicating azimuthal, axial and radial wave numbers, respectively. The explicit expression for U_{mkn} can be found in the subsection 2.1.4. The eigen-frequency ω_{mkn} is defined positive for a retrograde mode and negative for a prograde mode. This is in accordance with the sense of propagation of the waves in the rotating frame (Zhang & Liao (2017)). In order to calculate the flow amplitude that explicitly results from a given precessional forcing, one has to consider the inhomogeneous problem:

$$\frac{\partial \boldsymbol{U}}{\partial t} + \boldsymbol{\nabla} P + 2\hat{\boldsymbol{z}} \times \boldsymbol{U} = Real \left(\underbrace{Po \sin(\alpha)\; r\, e^{i\varphi + t} \hat{\boldsymbol{z}}}_{\boldsymbol{F}} \right). \tag{2.12}$$

Because the forcing has a structure $\boldsymbol{F} \propto e^{i\varphi}$, it allows solutions with $m = 1$. Then it is sufficient to assume

$$\boldsymbol{U} = \sum_k \sum_n a_{1kn} \boldsymbol{U}_{1kn} \left(z, r, \varphi\right) e^{i\omega_{1kn}t} \,. \tag{2.13}$$

The amplitudes a_{1kn} can be calculated using a projection approach (Manasseh (1994), Meunier *et al.* (2008)):

$$a_{1nk} = \frac{\int_V \boldsymbol{F} \cdot \boldsymbol{U}_{1nk}^* \, dV \;/\; \int_V \boldsymbol{U}_{1nk} \cdot \boldsymbol{U}_{1nk}^* \, dV}{i\left(1 - \mathit{\Omega}_c/\omega_{1nk}\right)} \,, \tag{2.14}$$

where the asterisk denotes the complex conjugate and V is the volume of the domain. The forcing term $\boldsymbol{F}$ on the right hand side of Eq. (2.12) is even in z, so it will project only on the modes whose vertical velocity is also even in z, requiring an odd axial wavenumber n (Manasseh (1992)). Because the precessional force is retrograde in the rotating frame, the prograde modes are never resonant with precession (Lin *et al.* (2014)).

2.1.4. Inertial modes in a rotating cylinder

Following the definition by Liao & Zhang (2012) we characterize the inertial modes (solutions of the Eq. 2.10) into three categories.

1. Inertial waves ($m \neq 0, k \neq 0, n \neq 0$):

$$\widehat{\boldsymbol{z}} \cdot \boldsymbol{U}_{mkn} = \quad -\frac{ik\pi}{\omega_{mkn}} J_m\left(\xi_{mkn} r\right) \sin\left(k\pi z/\Gamma\right) e^{im\varphi},$$

$$\begin{aligned}\widehat{\boldsymbol{r}} \cdot \boldsymbol{U}_{mkn} = \quad & -i\frac{\Gamma\xi_{mkn}}{4-\omega_{mkn}^2} \times \left[\left(1+\omega_{mkn}/2\right) J_{m-1}\left(\xi_{mkn} r\right)\right. \\ & \left. + \left(1-\omega_{mkn}/2\right) J_{m+1}\left(\xi_{mkn} r\right)\right] \times \cos\left(k\pi z/\Gamma\right) e^{im\varphi},\end{aligned} \tag{2.15a}$$

$$\begin{aligned}\widehat{\boldsymbol{\varphi}} \cdot \boldsymbol{U}_{mkn} = \quad & \frac{\Gamma\xi_{mkn}}{4-\omega_{mkn}^2} \times \left[\left(1+\omega_{mkn}/2\right) J_{m-1}\left(\xi_{mkn} r\right)\right. \\ & \left. - \left(1-\omega_{mkn}/2\right) J_{m+1}\left(\xi_{mkn} r\right)\right] \times \cos\left(k\pi z/\Gamma\right) e^{im\varphi},\end{aligned}$$

where J_m is the Bessel function of order m and ω_{mkn} is the frequency of the inviscid inertial modes which is calculated from

$$\omega_{mkn} = \pm 2 \times \left(1 + \left(\frac{\Gamma \xi_{mkn}}{k\pi}\right)^2\right)^{-1/2} , \tag{2.15}$$

$$\xi_{mnk} J_{m-1}\left(\xi_{mkn}\right) + \left(\pm\left(1 + \left(\frac{\Gamma \xi_{mkn}}{k\pi}\right)^2\right)^{1/2} - 1\right) \times m J_m\left(\xi_{mkn}\right) = 0 \, .$$

Among the infinite number of inertial waves the most important one for precessing cylinder is the $(1,1,1)$ mode which represents the gyroscopic motion resulting from the tendency of the fluid flow to align the flow rotation and the precession axis. Since in the inertial frame the rotation vector corresponds to the container axis, the flow develops its own axis in between the precession and the rotation vector. However, in contrast to the Poincaré-Busse theory (Busse (1968)) for spheroidal geometry, in a cylinder the flow rotation axis is not well defined, and acquires a non-trivial S-shaped structure (Giesecke *et al.* (2019), see for instance Fig. 1.10 left panel) so that a uniform vorticity approach is hardly possible.

2. Geostrophic modes $(m,0,n)$ (solutions of the Taylor-Proudman problem) which can be sub-divided into:
axisymmetric $(m=0)$ modes with

$$\widehat{\boldsymbol{z}} \cdot \boldsymbol{U}_{00n} = 0 \, ,$$

$$\widehat{\boldsymbol{r}} \cdot \boldsymbol{U}_{00n} = 0 \, , \tag{2.16}$$

$$\widehat{\boldsymbol{\varphi}} \cdot \boldsymbol{U}_{00n} = J_1\left(\xi_{00n} r\right) \quad \text{with} \quad J_1\left(\xi_{00n}\right) = 0$$

and non-axisymmetric $(m \neq 0)$ modes:

$$\widehat{\boldsymbol{z}} \cdot \boldsymbol{U}_{m0n} = 0,$$

$$\widehat{\boldsymbol{r}} \cdot \boldsymbol{U}_{m0n} = \frac{-im\Gamma}{2r} J_m\left(\xi_{m0n} r\right) e^{im\varphi}, \tag{2.17}$$

$$\widehat{\boldsymbol{\varphi}} \cdot \boldsymbol{U}_{m0n} = \frac{1}{2}\left[\Gamma\xi_{m0n} J_{m-1}\left(\xi_{m0n} r\right) - \frac{\Gamma m}{r} J_m\left(\xi_{m0n} r\right)\right] e^{im\varphi}.$$

The corresponding dispersion relation is

$$J_m\left(\xi_{m0n}\right) = 0.$$

3. Axisymmetric oscillations $(0, k, n)$ with $k \neq 0$. In contrast to the inertial waves' group, the axisymmetric oscillations present the following mathematical structure: the poloidal components U_z, U_r are purely imaginary, and the toroidal U_φ is purely real:

$$\begin{aligned}
\widehat{\boldsymbol{z}} \cdot \boldsymbol{U}_{0kn} = & \quad -i\,\frac{k\pi}{\omega_{0kn}} J_0\left(\xi_{0kn} r\right) \sin\left(k\pi z/\Gamma\right), \\
\widehat{\boldsymbol{r}} \cdot \boldsymbol{U}_{0kn} = & \quad -i\,\frac{\Gamma\omega_{0kn}\xi_{0kn}}{4-\omega_{0kn}^2} J_1\left(\xi_{0kn} r\right) \cos\left(k\pi z/\Gamma\right), \\
\widehat{\boldsymbol{\varphi}} \cdot \boldsymbol{U}_{0kn} = & \quad -\frac{\Gamma\xi_{0kn}}{4-\omega_{0kn}^2} J_1\left(\xi_{0kn} r\right) \cos\left(k\pi z/\Gamma\right).
\end{aligned} \tag{2.18}$$

Here ω_{0kn} is the frequency of the inviscid inertial modes which is calculated from

$$\omega_{0kn} = \pm 2 \times \left(1 + \left(\frac{\Gamma\xi_{0kn}}{k\pi}\right)^2\right)^{-1/2}$$

$$J_1\left(\xi_{0kn}\right) = 0 \quad \text{and} \quad \boldsymbol{U}_{0kn}\left(\omega_{0kn}\right) = \boldsymbol{U}_{0kn}^*\left(-\omega_{0kn}\right)\;.$$

The imaginary part (only U_z, U_r) comprises the axisymmetric double/quadruple roll structure (to be analyzed in more detail in sections 4.6, 4.7) which is the most promising "ingredient" for the occurrence of dynamo action. It is important to understand that this structure emerging in precessing driven flows is forced at the forcing frequency, therefore it has a vanishing frequency.

Due to the inviscid nature of the problem, the amplitude of the solution diverges at resonance due to the singularity in Eq. (2.14) when the container and the system frequencies are equal, i.e $\omega_{mnk} = 1$. The computation of the amplitude in the resonant case requires the consideration of viscous damping. Liao & Zhang (2012) describe an analytical procedure for the calculation of the full linear solution including viscosity in the bulk and in the boundary layer, which is valid on and off resonance. For weak precession the $(m,n,k) = (1,1,1)$ inertial mode is the dominant one, for which a simplified analysis was carried out by Gans (1970).

Figure 2.3 presents the 3D structures of the most prominent inertial modes occurring in a fluid filled precessing cylinder with aspect ratio $\Gamma = 2$: the central one is the directly forced mode caused by the gyroscopic effect on the fluid flow which dominates in the laminar regime, i.e for weak forcing. Once the precession ratio increases, the other two modes emerge due to the nonlinear phenomena enriching the dynamics of the flow. In particular the (0,0,1) mode resembles a columnar vortex which counteracts the solid body rotation while the (0,2,1) is a poloidal flow analogous to the Taylor vortices found in Taylor-Couette problem.

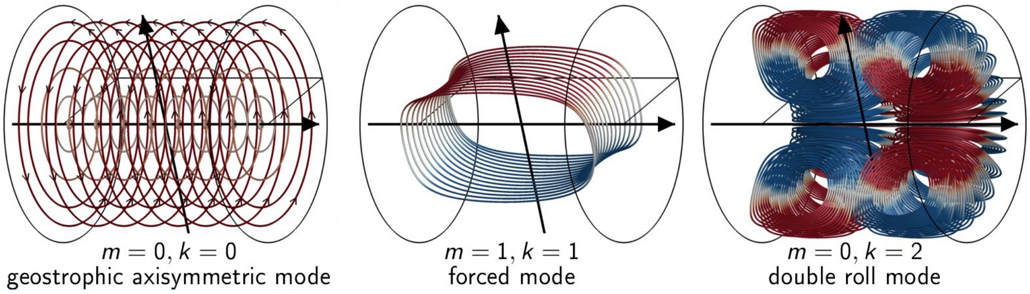

Figure 2.3. Three main flow structures emerging in a fluid-filled precessing cylinder.

2.2. A local model

In the geophysical and astrophysical context (Lesur & Longaretti (2005), Barker & Lithwick (2013), Le Reun *et al.* (2017)) the local approach is very common for simulations. Normally a Cartesian model can be considered as a small patch of the global domain which allows to focus on turbulent phenomena and to overcome computational limits such as large Reynolds number, boundary layers and geometry effects. A particular type of this approach, is the so called "shearing box" used to describe the dynamics of astrophysical discs (Hawley *et al.* (1995)).

The Eq. (2.9) describes the evolution of the total flow field $\boldsymbol{U}$. It incorporates the precessing base flow which in a local frame (co-rotating with the system, therefore it is in mantle frame) can be defined as (Mason & Kerswell (2002), Barker (2016))

$$\boldsymbol{U}_b = -2\,Po \begin{pmatrix} 0 & 0 & \sin(t) \\ 0 & 0 & \cos(t) \\ 0 & 0 & 0 \end{pmatrix} \begin{bmatrix} x \\ y \\ z \end{bmatrix} = M\,\boldsymbol{x}$$

and the perturbed flow field $\boldsymbol{u} = \boldsymbol{U} - \boldsymbol{U}_b$ for which the governing equation reads

$$\frac{\partial \boldsymbol{u}}{\partial t} + \boldsymbol{u} \cdot \boldsymbol{\nabla} \boldsymbol{u} = -\boldsymbol{\nabla} p + \frac{1}{Re} \boldsymbol{\nabla}^2 \boldsymbol{u} - 2\widehat{\boldsymbol{z}} \times \boldsymbol{u} - 2\boldsymbol{\varepsilon}(t) \times \boldsymbol{u} - M\boldsymbol{u} - M\boldsymbol{x} \cdot \nabla \boldsymbol{u}\,, \tag{2.19}$$

with $\boldsymbol{\varepsilon}(t) = Po\ (\cos(t), -\sin(t), 0)^T$ being the precession vector in the local frame. The flow field is confined in a triply periodic domain whose length is $L = 2\pi$.

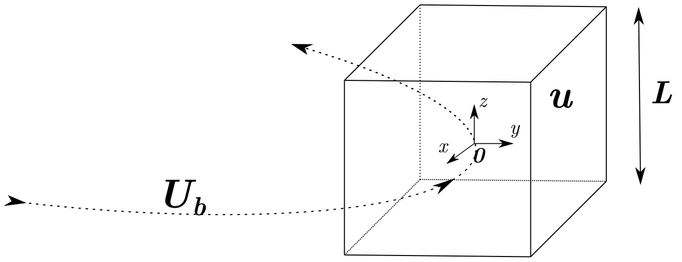

Figure 2.4. Sketch of the periodic cube with length L, subjected to the base flow $\boldsymbol{U_b}$. Inside the cube the (perturbed) flow velocity is $\boldsymbol{u}$.

2.2.1. Governing equations in Fourier space

Our goal is to perform the spectral analysis of precession-driven turbulence in Fourier (wavenumber $\boldsymbol{k}$-) space in order to understand dynamical processes (energy injection and nonlinear transfers) underlying its sustenance and evolution. To this end, following Barker & Lithwick (2013), Barker (2016), we decompose the perturbations into spatial Fourier harmonics (shearing waves) with time-dependent wavevector $\boldsymbol{k}(t)$,

$$f\,(\boldsymbol{r}, t) = \sum_{\boldsymbol{k}} \bar{f}\,(\boldsymbol{k}(t), t)\, e^{i\boldsymbol{k}(t)\cdot\boldsymbol{r}}, \tag{2.20}$$

where $f \equiv (\boldsymbol{u}, P)$ and their Fourier transforms are $\bar{f} \equiv (\bar{\boldsymbol{u}}, \bar{P})$. In the transformation (2.20), the wavevector of harmonics oscillates in time,

$$\boldsymbol{k}(t) = (k_{x0}, k_{y0}, k_{z0} + 2Po(-k_{x0}\cos(t) + k_{y0}\sin(t)))^T, \tag{2.21}$$

about its constant average value $\langle \boldsymbol{k}(t) \rangle = (k_{x0}, k_{y0}, k_{z0})$ due to the periodic time-variation of the basic precessional flow $\boldsymbol{U}_b$. Substituting Eq. (2.20) into Eq. (2.19) we obtain the following equation governing the evolution of spectral velocity $\bar{\boldsymbol{u}}$:

$$\frac{d\bar{\boldsymbol{u}}}{dt} = -i\boldsymbol{k}(t)\bar{P} - \frac{k^2}{Re}\bar{\boldsymbol{u}} - 2\boldsymbol{e}_z \times \bar{\boldsymbol{u}} - 2\boldsymbol{\varepsilon}\,(t) \times \bar{\boldsymbol{u}} - M(t)\bar{\boldsymbol{u}} + \boldsymbol{Q} \tag{2.22}$$

$$\boldsymbol{k}(t) \cdot \bar{\boldsymbol{u}} = 0. \tag{2.23}$$

Note that the wavevector $\boldsymbol{k}(t)$ as given by expression (2.21) satisfies the ordinary differential equation

$$\frac{d\boldsymbol{k}}{dt} = -M^T\boldsymbol{k} \tag{2.24}$$

and as a result the last term on the rhs of Eq. (2.19) related to the basic flow has disappeared when substituting Eq. (2.20) into it. The term $\boldsymbol{Q}(\boldsymbol{k},t)$ on the rhs of Eq. (2.22) represents the Fourier transform of the nonlinear advection term $\boldsymbol{u}\cdot\boldsymbol{\nabla u} = \nabla\cdot(\boldsymbol{uu})$ in the original Eq. (2.19) and is given by convolution (Mamatsashvili *et al.*, 2014, Buzzicotti *et al.*, 2018)

$$Q_m(\boldsymbol{k},t) = -i\sum_n\sum_{\boldsymbol{k}'} k_n\bar{u}_m(\boldsymbol{k}',t)\bar{u}_n(\boldsymbol{k}-\boldsymbol{k}',t)d^3\boldsymbol{k}', \tag{2.25}$$

where the indices (m,n) correspond alternatively to x,y,z. This term describes the net effect of nonlinear triadic interactions (transfers) among a harmonic $\boldsymbol{k}$ with two others $\boldsymbol{k}-\boldsymbol{k}'$ and $\boldsymbol{k}'$ and thus plays a key role in turbulence dynamics.

Multiplying both sides of Eq. (2.22) by the complex conjugate of spectral velocity $\bar{\boldsymbol{u}}^*$, the contribution from Coriolis force and part of the Poincaré force cancel out, since they do not do any work on the flow, $\bar{\boldsymbol{u}}\cdot(2\boldsymbol{e}_z\times\bar{\boldsymbol{u}} - 2\boldsymbol{\varepsilon}(t)\times\bar{\boldsymbol{u}}) = 0$, and as a result we obtain the equation for the (non-dimensional) spectral kinetic energy density $E = |\bar{\boldsymbol{u}}|^2/2$ in Fourier space as

$$\frac{dE}{dt} = \underbrace{-\frac{1}{2}\left[\bar{\boldsymbol{u}}^*\left(\boldsymbol{M}\bar{\boldsymbol{u}}\right) + \bar{\boldsymbol{u}}\left(\boldsymbol{M}\bar{\boldsymbol{u}}\right)^*\right]}_{injection} + \underbrace{\frac{1}{2}\left[\bar{\boldsymbol{u}}^*\boldsymbol{Q} + \bar{\boldsymbol{u}}\boldsymbol{Q}^*\right]}_{nonlinear\ transfer} - \underbrace{\frac{2k^2}{Re}E}_{dissipation}\ . \tag{2.26}$$

The pressure term also cancels out since $\bar{\boldsymbol{u}}^*\cdot\boldsymbol{k}(t)\bar{P} = 0$. Thus, the rhs of Eq. (2.26) contains three main terms:

- **Injection**

  $$A \equiv -\frac{1}{2}\left[\bar{\boldsymbol{u}}^*\left(\boldsymbol{M}\bar{\boldsymbol{u}}\right) + \bar{\boldsymbol{u}}\left(\boldsymbol{M}\bar{\boldsymbol{u}}\right)^*\right],$$

  which is of linear origin, being determined by the matrix $\boldsymbol{M}$, i.e., by the precessing background flow and describes energy exchange between the perturbations and that flow. If $A > 0$, kinetic energy is injected from the flow into the harmonics and hence they grow, which is basically due to precessional instability (Kerswell (1993), Mason & Kerswell (2002), Naing & Fukumoto (2011), Barker (2016)), whereas for $A < 0$ the harmonics give energy to the flow and decay.

- **Nonlinear transfer**

  $$NL \equiv \frac{1}{2}\left[\bar{\boldsymbol{u}}^*\boldsymbol{Q} + \bar{\boldsymbol{u}}\boldsymbol{Q}^*\right]$$

describes the transfer (cascade) of spectral kinetic energy among modes with different wavenumbers in Fourier space due to nonlinearity. The net effect of this term in the spectral energy budget summed over all wavenumbers is zero

$$\sum_{\boldsymbol{k}} NL(\boldsymbol{k}, t) = 0,$$

which follows from vanishing of the nonlinear advection term in the total kinetic energy equation integrated in physical space. Thus, the effect of the nonlinear term is to redistribute energy, that is injected by the total flow due to A, among harmonics while keeping the total spectral kinetic energy summed over all wavenumbers unchanged. Although the nonlinear transfers NL produce no net energy for perturbations, they play a central role in the turbulence dynamics together with the injection term A. The latter is thus the only source of new energy for perturbations drawn from the large reservoir of the background precessional flow. Due to this, below we focus on these two main dynamical terms – linear injection and nonlinear transfer functions, compute their spectra and analyze how they operate in Fourier space in the presence of precession instability using the tools of Ref. (Mamatsashvili *et al.*, 2014, 2016).

- **Viscous dissipation**

  $$D \equiv -\frac{2k^2}{Re}E$$

  is negative definite and describes the dissipation of kinetic energy due to viscosity.

2.3. The equations of electrodynamics

Classical electrodynamics is governed by Maxwell's equations. They comprise four partial differential equations that describe the relations of the electric $\boldsymbol{E}(\boldsymbol{x}, t)$ and the magnetic $\boldsymbol{B}(\boldsymbol{x}, t)$ field.

The following four equations (2.27a), (2.27c), (2.27b) and (2.27d) are referred to as the Maxwell equations where the currents and charge densities are denoted by $\boldsymbol{J}$, ρ_e, respectively:

$$\begin{cases} \boldsymbol{\nabla} \cdot \boldsymbol{E} = \dfrac{\rho_e}{\epsilon_0}, & (2.27a) \\ \boldsymbol{\nabla} \times \boldsymbol{E} = -\dfrac{\partial \boldsymbol{B}}{\partial t}, & (2.27b) \\ \boldsymbol{\nabla} \times \boldsymbol{B} = \mu_0 \left(\boldsymbol{J} + \epsilon_0 \dfrac{\partial \boldsymbol{E}}{\partial t} \right), & (2.27c) \\ \boldsymbol{\nabla} \cdot \boldsymbol{B} = 0. & (2.27d) \end{cases}$$

Several physical mechanisms emerge from Eq. (2.27): $\boldsymbol{E}$ fields can be generated by two different mechanisms: a static $\boldsymbol{E}$ field results from the distribution of electric charges, described via the total charge density ρ_e and the dielectric permittivity, ϵ_0, see Eq. (2.27a), i.e. Gauss' law. Moreover, an electric field can be induced by variations of accompanying magnetic fields $\boldsymbol{B}$, which is described by Faraday's law of induction, Eq. (2.27b). Similarly, magnetic fields are created by temporal variations of $\boldsymbol{E}$ and, more important for MHD, by currents. This is stated by the Ampère-Maxwell law, Eq. (2.27c), where μ_0 denotes the magnetic permeability, $\boldsymbol{J}$ is the electrical current density and the term $\epsilon_0 \partial \boldsymbol{E} / \partial t$ specifies the displacement currents. Finally, the impossibility of magnetic monopoles is formalized by Eq. (2.27d) stating that $\boldsymbol{B}$ must be solenoidal everywhere.

Moreover the current $\boldsymbol{J}$ is also induced by the electromagnetic fields. Ohm's law states that $\boldsymbol{J}$ is proportional to the force experienced by the free charges $\boldsymbol{J} = \sigma \boldsymbol{E}$, with σ being the electrical conductivity. For electrically conducting fluids Ohm's law must be reformulated in the frame of reference moving with the local velocity $\boldsymbol{u}_q$ of the conducting charges (Davidson, 2001),

$$\boldsymbol{J} = \sigma(\boldsymbol{E} + \boldsymbol{u}_q \times \boldsymbol{B}). \tag{2.28}$$

2.4. The equations of magnetohydrodynamics

The interaction between the motion of electrically conducting liquids with electromagnetic fields is described by merging the Navier-Stokes equations with the Maxwell equations. A particle with charge q, moving with the velocity $\boldsymbol{U}$, is subject to the electromagnetic force (Lorentz force) so that the total electromagnetic force becomes

$$\boldsymbol{F}_{EM} = \underbrace{q\boldsymbol{E}}_{Electrostatic force} + \underbrace{q\boldsymbol{U} \times \boldsymbol{B}}_{Lorentz force}. \tag{2.29}$$

Where the Hall effect has been neglected since we deal with the resistive (ideal) MHD. Notice that the Hall effect occurs in plasmas when there is a relative motion between electrons and ions in the presence of a magnetic field. The electrons are able to drift with the magnetic field while ions cannot. This results in the generation of an electric field that opposes the original current, leading to a phenomenon known as the Hall electric field. In MHD, the Hall effect becomes significant when the magnetic field is relatively strong, and the fluid has a high electrical conductivity (Davidson (2001)). Our problem consists of liquid metals with moderate magnetic fields therefore the simplification in Eq. (2.29) is universally accepted.

The electromagnetic force on a single charge q can be reformulated substituting $\rho_e = \sum q$ and $\boldsymbol{J} = \sum q\boldsymbol{u}_q$, giving the force density

$$\boldsymbol{f}_{EM} = \boldsymbol{f}_E + \boldsymbol{f}_L = \rho_e \boldsymbol{E} + \boldsymbol{J} \times \boldsymbol{B}. \tag{2.30}$$

When adding Eq. (2.30) into the Navier-Stokes equation we can make an important simplification for conducting fluids. Liquid metals, for example, exhibit usually high electrical conductivities of the order $\mathcal{O}(10^6\,\mathrm{S\,m^{-1}})$ providing a very fast charge balance. For typical conductors the so called relaxation time is in the order $\mathcal{O}(10^{-18}\,\mathrm{s})$ (Davidson (2001)) which is negligibly small in comparison to the flow's timescales. The result is that the influence of free charges ρ_e is insignificant and the Lorentz force in (Eq. (2.30)) is dominant:

$$\boldsymbol{f}_{EM} \approx \boldsymbol{f}_L = \boldsymbol{J} \times \boldsymbol{B}. \tag{2.31}$$

Another effect of charge conservation is that the current density must be solenoidal everywhere in the conducting metal and finally, the displacement currents are negligible, since in MHD approximation the flow velocity is much smaller than the speed of light $U \ll c$. Under these hypothesis, the Eqs. (2.32) plus the Eqs. (2.31) and (2.28) become

$$\begin{aligned}
&\boldsymbol{\nabla} \cdot \boldsymbol{J} = 0, && \boldsymbol{\nabla} \cdot \boldsymbol{B} = 0, && \text{(2.32a,b)}\\
&\boldsymbol{\nabla} \times \boldsymbol{E} = -\frac{\partial \boldsymbol{B}}{\partial t}, && \boldsymbol{\nabla} \times \boldsymbol{B} = \mu_0 \boldsymbol{J}, && \text{(2.32c,d)}\\
&\boldsymbol{f}_L = \boldsymbol{J} \times \boldsymbol{B}, && \boldsymbol{J} = \sigma(\boldsymbol{E} + \boldsymbol{U} \times \boldsymbol{B}). && \text{(2.32e,f)}
\end{aligned}$$

The behavior of $\boldsymbol{B}$ under the influence of $\boldsymbol{U}$ is governed by a transport equation for $\boldsymbol{B}$, called the *induction equation*, which can be derived by the combination of Ohm's law (2.32a), Ampère's law (2.32d) and Faraday's equation (2.32c):

$$\frac{\partial \boldsymbol{B}}{\partial t} = \underbrace{\boldsymbol{\nabla} \times (\boldsymbol{U} \times \boldsymbol{B})}_{advection} + \underbrace{\eta \nabla^2 \boldsymbol{B}}_{diffusion} \ . \tag{2.33}$$

Here, the magnetic diffusivity η is given by $\eta = (\mu_0 \sigma)^{-1}$ and plays an analogous role as the mechanical diffusivity (viscosity) in the momentum equation. The characteristic time for diffusion is $t \sim d_{\text{dif}}^2/(\eta)$ with d_{diff} being the diffusion length. The final (dimensionless) governing equations can be expressed as

$$\frac{\partial \boldsymbol{U}}{\partial t} + (\boldsymbol{U} \cdot \boldsymbol{\nabla})\boldsymbol{U} + \boldsymbol{\nabla} P - \frac{1}{Re}\nabla^2 \boldsymbol{U} - S(\boldsymbol{\nabla} \times \boldsymbol{B}) \times \boldsymbol{B} = 0, \tag{2.34}$$

$$\frac{\partial \boldsymbol{B}}{\partial t} - \boldsymbol{\nabla} \times (\boldsymbol{U} \times \boldsymbol{B}) - \frac{1}{Rm}\nabla^2 \boldsymbol{B} = 0. \tag{2.35}$$

They are fully characterized by three independent dimensionless numbers: the Reynolds number Re (previously described), the interaction parameter S, and the magnetic Reynolds number Rm, given as

$$S = \frac{B^2}{\mu_0 \rho U^2} \equiv \frac{\text{Lorentz forces}}{\text{Inertia forces}}, \tag{2.36}$$

$$Rm = \frac{Ul}{\eta} \equiv \frac{\text{Advection of } B}{\text{Diffusion of } B}. \tag{2.37}$$

Re and S appear in the momentum equation and determine the degree of turbulence and the importance of the Lorentz forces, respectively. Rm characterizes the induction effect. The magnetic Reynolds number is a most fundamental dimensionless number in MHD since it quantifies the overall impact of magnetic advection ($\sim$ magnetic induction) on the evolution of $\boldsymbol{B}$. In the limit $Rm \gg 1$, which is the typical range for plasmas, diffusion is negligible so that the propagation of $\boldsymbol{B}$ is given by the fluid motion $\boldsymbol{u}$. It can be shown that magnetic flux lines are then advected with the fluid flow, acting like elastic bands frozen into the conducting medium. The opposite limit $R_m \ll 1$ applies often in metallurgical MHD as, e.g. in liquid metal industrial applications.

2.5. Numerical methods

2.5.1. Global simulations

Usually the discussion of solutions in terms of inertial modes u_{mnk} with corresponding ω_{mnk}, the solution of the Navier-Stokes equation in the mantle frame, Eq. (2.9), comes along with some disadvantages when executing numerical simulations. In that reference system the dimensionless angular velocity due to precession, $\boldsymbol{\Omega}_p$, is time-dependent, and the directly forced inertial mode rotates with a frequency $-\Omega_c$ with respect to the observer, which complicates the computation of the base flow. By contrast, in the turntable frame of reference, the directly forced flow corresponds to a standing inertial wave, and the most obvious method to compute a base flow is a simple time-average.

The container frame is sometimes claimed to be a better numerical option due to the

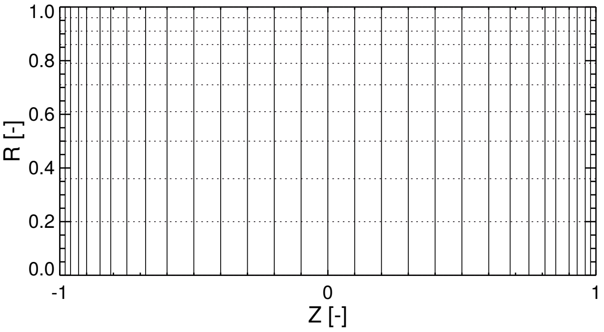

Figure 2.5. Representation of the dimensionless meridional semi-plane mesh using 300 quadrilateral elements. The elements are refined towards the boundaries in order to resolve the viscous boundary layer.

smaller velocity magnitude, allowing to reach lower values of Ek in the simulations (Tilgner (1998)). However this is strictly true only for weakly precessing flows, while in the strongly precessing regime we will show that the scaled velocities are of order $\propto O(1)$ in both reference frames. The governing equation in the turntable frame reads

$$\frac{\partial \boldsymbol{U}}{\partial t} + \boldsymbol{U} \cdot \boldsymbol{\nabla} \boldsymbol{U} = -\boldsymbol{\nabla} P + \frac{1}{Re} \boldsymbol{\nabla}^2 \boldsymbol{U} - 2\boldsymbol{\Omega}_p \times \boldsymbol{U}, \tag{2.38}$$

together with no-slip boundary conditions

$$U_\varphi = r\Omega_c, \quad U_r = 0 \quad \text{and} \quad U_z = 0\,, \tag{2.39}$$

and the time-independent precession vector $\mathbf{\Omega}_p$.
We utilize the DNS code SEMTEX (Blackburn *et al.* (2019)), which is based on the spectral element-Fourier method. We use 300 quadrilateral elements to mesh the meridional semi-plane with a refinement near the sidewall and the endwalls (Figure 2.5).

The meridional domain is defined by $r \in [0, 1]$ (radial range) and $z \in [-1, 1]$ (axial range) so that the aspect ratio is fixed to $\Gamma = H/R = 2$ and the dimensionless cylinder volume is $V = 2\pi$. Within each element a Lagrange interpolation polynomial of 7^{th} degree is employed. For the third dimension 128 azimuthal Fourier modes (which are equivalent to 256 spatial planes) are employed.

2.5.2. Numerical scheme for solving the induction equation

The induction equation described in Sec. 2.4 is solved using a finite-volume scheme. This code, described in detail in Giesecke *et al.* (2008), is characterized by the following algo-

rithm: first the induction equation in conservative form ($\partial_t \boldsymbol{B} + \boldsymbol{\nabla} \times \boldsymbol{E} = 0$) is solved to obtain the components of the magnetic field at time step $n+1$. Then the electric field for an intermediate step is obtained from an upwind scheme of the Riemann problem. Each time step is calculated by using the Courant-Friedrich-Lax criterion. One of the problems for polar coordinates is the treatment of the axis; in this case this problem is solved through the conditions imposed to the coefficient of each azimuthal mode of $\boldsymbol{B}$. The solenoidal condition on the magnetic field $\boldsymbol{\nabla} \cdot \boldsymbol{B} = 0$ is maintained due to the constraint transport mechanism when the initial field is divergence-free.
In our analysis we make use of the pseudo-vacuum conditions characterized by the zero tangential components of $\boldsymbol{B}$ at the wall. It has been observed in previous studies that this set-up decrease the threshold for the dynamo onset in between 15% (Stefani, unpublished) and 30% (Giesecke *et al.* (2010)).

2.5.3. Local patch

We solve Eq. (2.19) using the pseudo-spectral code SNOOPY (Lesur & Longaretti (2005)) which is a general-purpose code solving HD and MHD equations, including shear, rotation, weak compressibility, and several other physical effects. The Fourier transforms are computed using the FFTW3 library. Nonlinear terms are computed using a pseudo spectral algorithm with antialiasing 3/2-rule. The original version of the code has been modified by Barker (2016) to include precessional forcing and hence variables are decomposed in terms of shearing waves with periodically time-varying wavevector (Eq. 2.21) due to the basic shear flow $\boldsymbol{U}_b$ induced by precession. In this way, the shearing-periodic boundary conditions in the local computation domain (which are in fact fully periodic in the frame co-moving with the basic flow) are naturally satisfied in the code. The reliability of the precession implementation has been tested by Barker (2016) by comparing the growth rate of the precession instability from a liner-stability analysis (i.e switching off the nonlinear terms in Eq. 2.19) and the solution of the analytical model calculated by Kerswell (1993). The agreement is very good in a broad range of Po proving that the precession terms are well implemented (since they have linear nature). Further details regarding the resolution and the robustness of the results are shown in Appendix B.

3. Numerical studies for the $\alpha = 90^\circ$ case: bulk-phenomena and boundary layers

> *Com'è più difficile 'ntender l'opere di natura che un libro d'un poeta*
>
> Leonardo da Vinci, Appunti

3.1. Introduction

[1]Ekman boundary layers (named after Ekman (1905)) are typical features of rotating flows which are characterized by the balance between Coriolis and viscous forces. Ekman layers produce not only azimuthal velocity gradients near the end caps of a cavity, but they can also lead to the development of radial and axial velocity components depending on the net horizontal convergence/divergence values. Even if the radial and axial velocity flow velocities are small (Caldwell & Van Atta (1970)), they can cause a non-azimuthal circulation which eventually may generate large (but relatively weak) horizontal vortices (Coles & Van Atta (1966)).

The exchange of momentum between the fluid in the Ekman layer region and the surrounding fluid outside the boundary layer is a well known (and ubiquitous) phenomenon called Ekman pumping, which can lead to instabilities in the flow (Lilly (1966), Aelbrecht *et al.* (1999)). The early works were characterize by the use of the stability analysis in order to derive various thresholds for the onset of instabilities. These thresholds are given in terms of the Ekman boundary layer Reynolds number $Re_\delta = U_{\text{ref}}\delta_{Ek}/\nu$ with U_{ref} denoting the reference velocity outside the boundary layer, δ_{Ek} the thickness of the Ekman layer

---

[1] The present Chapter relies on the journal publication *Ekman boundary layers in a fluid filled precessing cylinder* Pizzi, Giesecke, & Stefani (2021a) © 2021 (with the permission of AIP Publishing).

and ν the kinematic viscosity of the fluid. For instance Faller & Kaylor (1966) and Lilly (1966) proposed two types of instability for laminar Ekman layers: a parallel instability (also called A-mode) appearing at $Re_\delta \approx 55$, and an inviscid instability (called B-mode) which appears around $Re_\delta \approx 115$. From a physical point of view, the A-mode instability consists of a series of rolls inclined with respect to the flow velocity outside the boundary layer. It vanishes at low Ekman numbers since it is of viscous type. The B-modes are called inviscid because of their maintenance at large Re_δ. Finally, the transition to a fully turbulent boundary layer is supposed to occur at $Re_\delta \approx 150$. The experimental work by Caldwell & Van Atta (1970) has confirmed A-mode instability by showing its spectral characteristics to be independent of Re_δ. Concerning the turbulent Ekman layer, the numerical simulations by Coleman *et al.* (1990) and Deusebio *et al.* (2014) showed that the mean velocity profiles and turbulent features, such as root mean square and stresses, do not strongly depart from those of turbulent non-rotating boundary layers. In turbulent convective phenomena, the role of Ekman layers seems to be essential; indeed King *et al.* (2009) observed that the system transition from thermally to rotationally dominated is controlled by the relative thickness of the thermal and mechanical (Ekman) boundary layers.

Several works have experimentally investigated the Ekman layers (Sous *et al.* (2013), Tatro & Mollo-Christensen (1967), Caldwell & Van Atta (1970), Caldwell *et al.* (1972)). Experimental facilities are naturally limited in scale by the size of the laboratory which goes along with a different impact of geometric effects when comparing, e.g., with atmospheric or planetary conditions. Notably, Sous *et al.* (2013) performed PIV in a big tank with a diameter of 13 m in order to emulate Ekman layers under atmospheric conditions. The aim of this Chapter is to extend and specify the characterization of Ekman boundary layers to the case of a fluid filled precessing cylinder. The main results will be the comparison of velocity profiles with analytical solutions and the scaling of the Ekman layer when increasing rotation and precession, respectively. We focus on a large nutation angle and a precession ratio far above the onset of primary instability in terms of a triadic resonance in order to approach the flow regime relevant for the DRESDYN dynamo experiment. Previous studies (Giesecke *et al.* (2018, 2019)) had revealed the key relevance of axisymmetric roll structures, showing up for certain precession ratios, to achieve dynamo action. While the emergence of these rolls was interpreted as the onset of a centrifugal instability, the complementary role of Ekman pumping in the endwall layers remains an open issue. It is here where the characterization of the Ekman layer, and its transition to turbulence, might play an important role in achieving the final goal to see dynamo action in a precession driven flow.

The rest of the Chapter is organized as follows: Section 3.2 further specifies the theory of precession driven flows in cylinders, followed by Section 2.5, which briefly describes the numerical method, the mesh discretization, and the parameter space explored with simulations. Section 3.3 is dedicated to the presentation of general results for precessing flows and their characterization through the decomposition into inertial modes which then are discussed in Section 3.4 together with the analysis of the geostrophic flow emerging in the strongly forced regime. The endwall Ekman layers are analyzed in Section 3.5 followed by the summary in Section 3.7.

3.2. Methods of analysis

Precession driven flows inside cylindrical vessels are dominated by a wave structure with azimuthal dependence $\propto e^{i\varphi}$ for moderate forcing (Manasseh (1994) and numerically Lagrange *et al.* (2011), Meunier *et al.* (2008)). However, for strong precession and at large nutation angle α axisymmetric and/or geostrophic contributions as well as inertial modes with $m \neq 1$ emerge. These contributions have been associated with the occurrence of various instabilities (Herault *et al.* (2019),Giesecke *et al.* (2018)) and are expected to impact the boundary layers in a non-negligible manner (Kong *et al.* (2014, 2015)). Therefore we need to discern the various flow structures present in the fluid flow. This goal is achieved through the expansion of the flow field in terms of the inertial modes with arbitrary wave numbers in the bulk plus the corresponding boundary layer flow $\boldsymbol{u}^{Bl}$. Following Kong *et al.* (2015) and Zhang & Liao (2017) the corresponding expansion reads:

$$\begin{aligned}\boldsymbol{u} \;=\; & \underbrace{\overbrace{\sum_{k=1}^{K} A_{00n}\,\boldsymbol{u}_{00n}\,(r)}^{\textbf{axisymmetric}} + \overbrace{\sum_{m=1}^{M}\sum_{n=1}^{N}\frac{1}{2}\left[A_{m0n}\,\boldsymbol{u}_{m0n}\,(r,\varphi)+c.c\right]}^{\textbf{non-axisymmetric}}}_{\textbf{Geostrophic}} \\ & + \underbrace{\sum_{k=1}^{K}\sum_{n=1}^{N}\frac{1}{2}\left[A_{0kn}\,\boldsymbol{u}_{0kn}\,(z,r)+c.c\right]}_{\textbf{axisymmetric}\quad\textbf{oscillation}} \\ & + \underbrace{\sum_{m=1}^{M}\sum_{k=1}^{K}\sum_{n=1}^{2N}\frac{1}{2}\left[A_{mkn}\,\boldsymbol{u}_{mkn}\,(z,r,\varphi)+c.c\right]}_{\textbf{inertial}\quad\textbf{waves}} + \boldsymbol{u}^{Bl}, \end{aligned} \tag{3.1}$$

where $c.c$ stands for complex conjugate and $\boldsymbol{u}_{mkn}$ are the eigenmodes given by Eqs. (1)-(2.16). The amplitudes A_{mkn} are computed by projecting the simulated flow field $\boldsymbol{u}$ on the eigenmodes:

$$A_{mkn} = \frac{2\,\int_V \boldsymbol{u}^{*}_{mkn}\cdot\boldsymbol{u}\,dV}{\left(\int_V \boldsymbol{u}_{mkn}\cdot\boldsymbol{u}^{*}_{mkn}\,dV\right)^{1/2}}\,. \tag{3.2}$$

This procedure allows to determine the strength of various contributions and to distinguish the interior bulk flow from the viscous boundary layer flow $\boldsymbol{u}^{Bl}$. Once we compute the amplitudes A_{mkn} for wave number triplets (m, k, n) it is possible to reconstruct the bulk flow, and to differentiate the boundary layer flow from the total one. The convergence of this method is shown in subsection 3.5.1 together with a comparison between numerical results and the analytical linear boundary layer expression.

Since our DNS solves the entire flow domain without focusing only on the boundary layer phenomena we face an intrinsic limit in the spatial resolution. Regarding the laminar (yet unstable) Ekman layer, Faller & Kaylor (1966) used the Ekman spiral computation as a reasonable criterion to check if the layer is well resolved. The Ekman spiral is the 2D projection of the vertical dependence of u_r and u_φ in the Ekman layer at the endcaps of the cylinder. This condition is fulfilled by our simulations since the velocity field evolves smoothly in the vertical direction inside the Ekman layer; this validation is described in detail in the next section 3.5.2.

In order to resolve the Kolmogorov scale in the sub-viscous layer in numerical simulations that involve fully turbulent Ekman layers, a grid resolution of at least 10 grid points is required (Deusebio *et al.* (2014), Coleman *et al.* (1990)). While we do not achieve this spatial resolution, our simulations remain far enough from the turbulence threshold (as shown below) so that a poorer resolution is well justified (Section 3.5.4), even for the smallest Ekman number ($Ek = 3.3 \times 10^{-5}$).

The simulations' initial conditions ($t = 0$) correspond to a pure solid-body rotation state with $u = [0, 0, r\mathit{\Omega}_c]^T$ ($\mathit{\Omega}_c$ is the cylinder angular velocity) with its corresponding kinetic energy density in dimensionless units

$$e_{sbr} = \frac{1}{V}\int_0^{2\pi} d\varphi \int_{-H/2}^{H/2} dz \int_0^R \frac{(\mathit{\Omega}_c r)^2}{2}\, r\, dr = 0.25\,. \tag{3.3}$$

The Ekman number varies in the range between $[10^{-3}, 3.3 \times 10^{-5}]$, and the Poincaré number in the range $[10^{-3}, 3 \times 10^{-1}]$. In this Chapter the focus lays on the $\alpha = 90°$ case. The parameter space of the various simulations is shown in Figure 3.1. Although the simulations are performed in the precessing frame of reference, all results will be presented and discussed in the mantle reference frame in which the inertial and geostrophic modes are well defined. In order to decrease the degree of freedom of the system we unify the Ekman and the Poincaré numbers to obtain a general forcing term (Liao & Zhang (2012), Kong *et al.* (2015)):

$$\epsilon = \frac{Po}{\sqrt{Ek}}\,. \tag{3.4}$$

which is included in the following range $3.16 \times 10^{-2} \leq \epsilon \leq 20$.

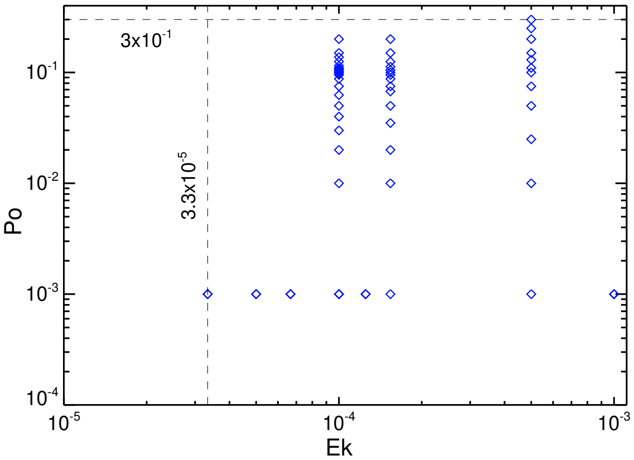

Figure 3.1. Parameter space of the performed simulations in terms of the two governing parameters: precession ratio Po and Ekman number Ek.

3.3. General flow features

A natural global diagnostic is the total kinetic energy of the fluid flow. We use the kinetic modal energy of azimuthal modes m, defined as

$$E_m = \frac{1}{2HR} \int_H \int_R \hat{\boldsymbol{u}}_m^* (z,r) \cdot \hat{\boldsymbol{u}}_m (z,r) \; r \, dr \, dz \, . \tag{3.5}$$

Here $\hat{\boldsymbol{u}}_m$ is the mode with azimuthal wave number m of the Fourier transform of the velocity field; the asterisk means complex conjugation. However, since the most dominant contribution originates from the directly driven flow $\propto \cos\varphi$ our first focus is on the Fourier mode corresponding to $m = 1$.

Typical results are shown in Figure 3.2. After a transition period whose duration varies with ϵ, the energy saturates in a statistically steady regime. In the weakly precessing regime (Fig. 3.2(a), red curve, $\epsilon = 10^{-1}$), the ultimate flow is stationary without fluctuations. The simple time-dependence goes along with a plain flow structure, as it is evident from the isosurfaces of the axial velocity component shown in Fig. 3.3(a). Increasing ϵ the kinetic energy begins to fluctuate. However, even for the largest ϵ considered, the variations remain sufficiently small to classify these states as statistically stationary. The onset of time-dependent solutions is connected with a rising complexity of the flow structure (Fig. 3.3). It is noteworthy that the energy of the $m = 1$ mode in the saturated state does not increase monotonically with ϵ. Figure 3.2(b) summarizes the results of the time-averaged $E_{m=1}$ in the statistically steady regime. We observe the presence of two regimes

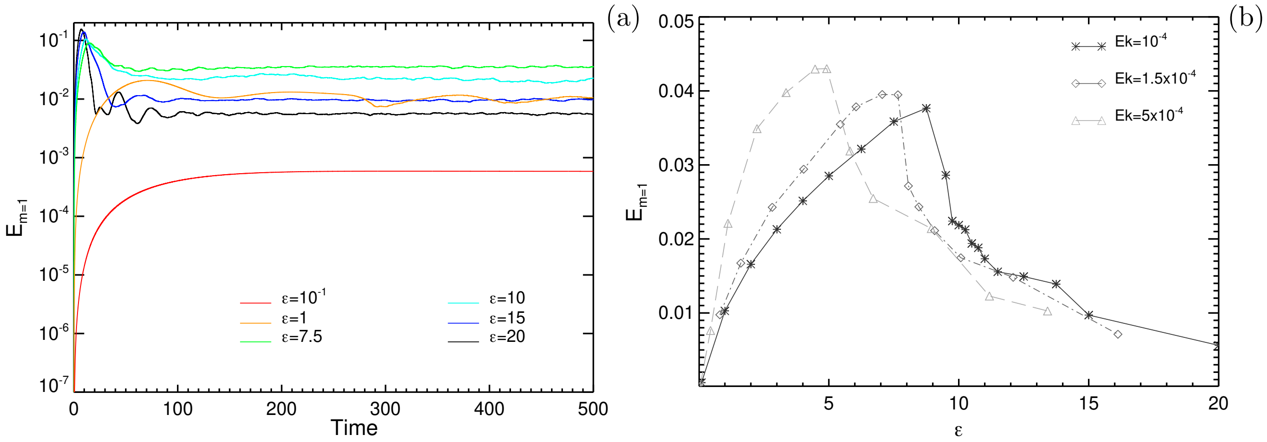

Figure 3.2. Main features of the modal energy of the first Fourier mode. (a) Time evolution of the kinetic energy $E_{m=1}$ contained in the first azimuthal wave number $m = 1$. (b) Time average in the statistically steady regime for all simulations. Note the abrupt change for $5 < \epsilon < 10$, depending on Ek.

that are distinguished by increasing or decreasing $E_{m=1}$. Moreover, at the maximum that separates the two regimes at a critical ϵ we see a rather abrupt transition corresponding to a significant reduction of the kinetic energy of the $m = 1$ inertial mode. For the range of parameters examined, the critical ϵ for the onset of the transition, indicated by the maximum of the $m = 1$ energy, is shifted to larger values with decreasing Ekman number and the width of the transitional regime becomes slightly narrower for decreasing Ek.

The corresponding 3D structure of the instantaneous velocity u_z is illustrated in Fig. 3.3 for various ϵ. With increasing ϵ the flow behavior becomes more complex with the occurrence of small-scale structures. However, for all the cases we see a clear presence of the $m = 1$ structure due to the precessional forcing. In addition, we see that for the largest ϵ the flow is more and more concentrated towards the sidewalls. As we will show in the next section 3.4, this is a result of the dominance of a geostrophic mode in the bulk which goes along with a local breakdown of the rotational motion finally leading to the weak axial flow (Fig. 3.3(d)).

3.4. Emergence of a geostrophic flow and its impact on the sidewall layer

In order to characterize the precession driven flow and to show the deviation from the simple configuration dominated by the forced mode, we apply the expansion into eigenfunctions according to Eqs. (3.1) and (3.2) which are then used to compute the contribu-

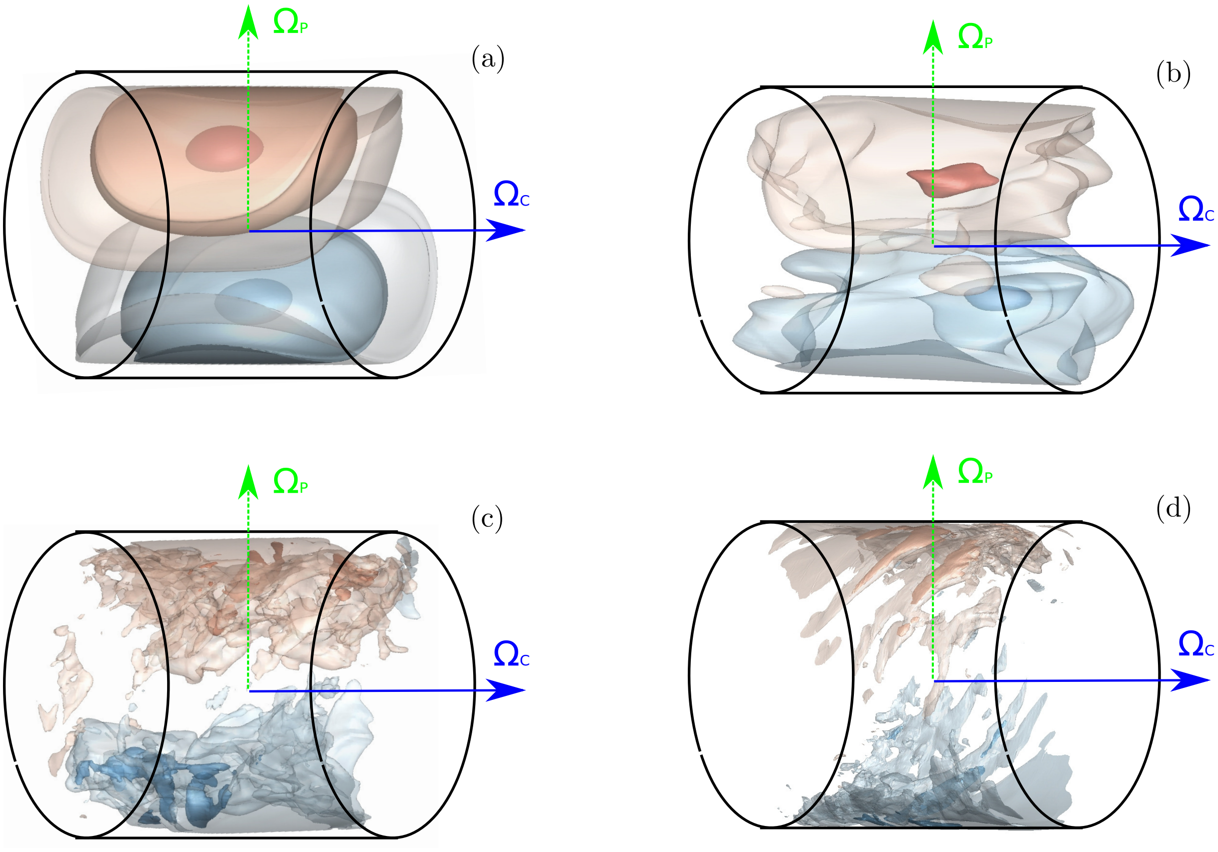

Figure 3.3. Isosurfaces of the instantaneous axial velocity u_z taken in the statistically steady regime at $t = 450$ (≈ 72 cylinder revolutions after the start of the simulations). (a) $\epsilon = 10^{-1}$, nested isosurfaces at 1%, 2.5%, 5%. (b) $\epsilon = 1$, nested isosurfaces at 10%, 25%, 50%; (c) $\epsilon = 10$, nested isosurfaces at 25%, 50%, 90%; (d) $\epsilon = 20$, nested isosurfaces at 25%, 50%, 90%. All percentages refer to the reference velocity $\Omega_c R$.

tions of various modes to the kinetic energy of the flow. We are mainly interested in the energy contained in the directly forced mode (Kong *et al.* (2015))

$$E_{111} = \frac{1}{2V}\left(\frac{|A_{111}|^2}{2}\right) , \tag{3.6}$$

and the energy of the geostrophic modes, which is defined as

$$E_{geo} = \frac{1}{2V}\left[\underbrace{\sum_{m>0}\sum_{n}\left(\frac{|A_{m0n}|^2}{2}\right)}_{E_{geo\,non-axi}} + \overbrace{\sum_{n}\left(|A_{00n}|^2\right)}^{E_{geo\,axi}}\right] , \tag{3.7}$$

with the absolute values of the amplitudes given by $|A_{mkn}|^2 = \Re e\,(A_{mkn})^2 + \Im\,(A_{mkn})^2$. The results are plotted in Fig. 3.4(a) for the three Ek numbers. Increasing the forcing ϵ, we find an increase of both contributions with the geostrophic energy becoming dominant between $\epsilon = 2.5$ and $\epsilon = 6.5$ (depending on Ek). With further increase of ϵ, the abrupt decrease of the energy of the directly driven $m = 1$ mode (as already discussed previously in Fig. 4b) goes along with a rather abrupt increase of the geostrophic energy. Finally the geostrophic energy becomes quite close to the energy of the initial solid body rotation (dashed lines at 0.25) for all cases, whereas the energy of the directly forced mode is more than two orders of magnitude smaller.

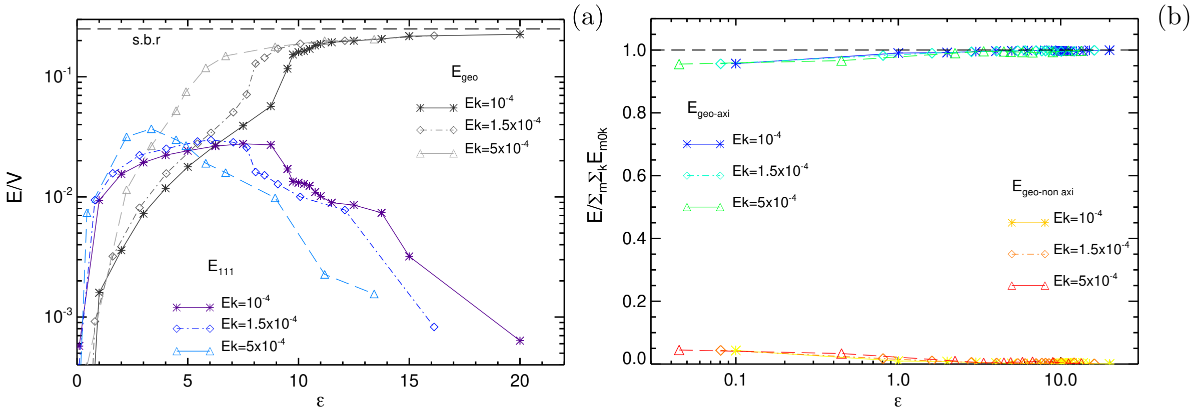

Figure 3.4. Impact of the forcing on the flow. (a) Comparison between the energy of the directly forced mode E_{111} and the geostrophic energy E_{geo}. The dashed black line represents the solid body rotation (s.b.r) energy density defined in Eq. (3.3). (b) Comparison of axisymmetric E_{axi} and non-axisymmetric $E_{non-axi}$ geostrophic energies as defined in Eq. (3.7).

In Fig. 3.4(b), we focus on the geostrophic modes, differentiating thereby the axisymmetric ($E_{geo-axi}$) and non-axisymmetric ($E_{non-axi}$) contributions. The results are consistent with previous numerical (Jiang *et al.* (2014), Kong *et al.* (2015)) and experimental (Kobine (1996)) studies and show that the geostrophic flow is substantially axisymmetric, i.e. dominated by $m = 0$. This behavior is distinctly different from that in the weak precessing case which was dominated by modes with $m = 1$ and $n = 1$.

Since the flow amplitude is concentrated on the mode with $m = 0$ and $n = 0$, the flow can be approximated as axisymmetric without significant axial dependence in the bulk region giving rise to a purely azimuthal circulation. In order to compute the corresponding geostrophic-axisymmetric flow contribution

$$U_g\left(r\right) = \sum_{k=1}^{K} A_{00k} \boldsymbol{u}_{00k}\left(r\right) \cdot \hat{\boldsymbol{\varphi}} \,. \tag{3.8}$$

we use $K = 29$ as summation limit for the radial wave numbers (as it is the maximum allowed for the solution of the dispersion relation for our radial mesh discretization).

Figure 3.5(a) shows the resulting radial profiles $U_g(r)$ for six different ϵ. In all cases U_g is oriented opposite to the rotation of the container, and for sufficiently large forcing U_g cancels the original solid-body rotation $\Omega_c r$ in the bulk (see e.g the purple and blue curves which are below the solid body rotation profile). Notice that U_g/r and its derivative

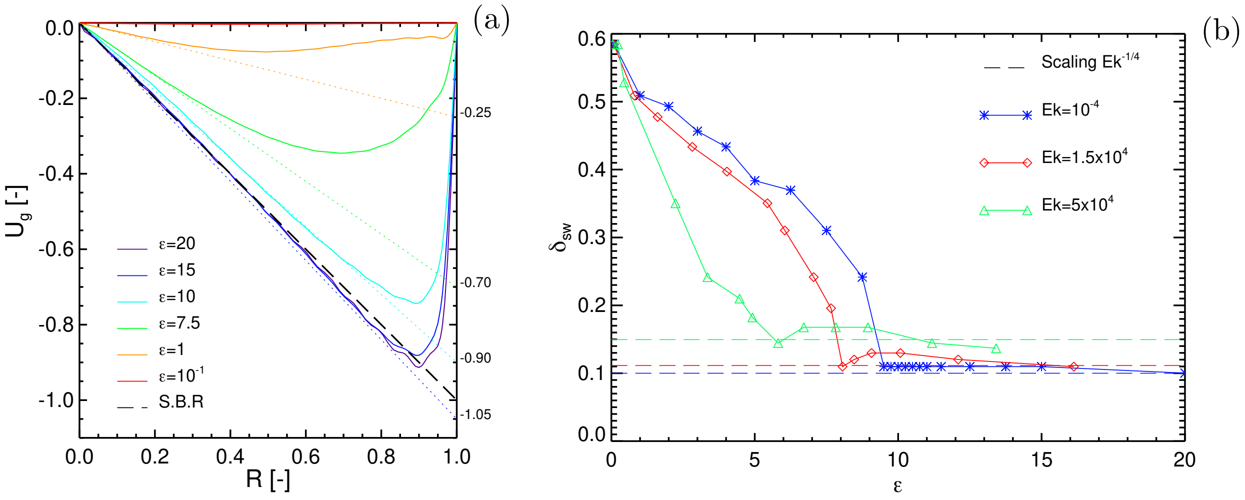

Figure 3.5. Axisymmetric-geostrophic flow. (a) Plot of the radial profile of the geostrophic axisymmetric flow $U_g(r)$ for different ϵ. The dotted lines represent the corresponding profiles $\Omega_g r$ with the angular velocity $\Omega_g = dU_g(r)/dr_{|r=0}$. The dashed line shows the solid body rotation profile. (b) Thickness of the sidewall boundary layer δ_{sw} developed by geostrophic flow and estimated using the location of the minimum of U_g.

dU_g/dr (whose summation represents the geostrophic vorticity) are negative and increase in magnitude with the forcing (see Fig. 3.5). The geostrophic axisymmetric mode is in close analogy with the anticyclonic geostrophic vortex emerging in a strongly librating ellipsoid (Le Reun *et al.* (2019)).

Note also the undulatory shape of the profiles which becomes more clearly visible at $\epsilon = 20$. This is not a result of an under-resolved numerical simulation, but an artifact of the limited radial wave number ($K = 29$) used for the decomposition; this means that the contributions of higher radial wave numbers increase for the largest ϵ.

According to Kong *et al.* (2015), we define the corresponding geostrophic angular velocity

$$\Omega_g = \frac{dU_g(r)}{dr}|_{r=0} \ , \tag{3.9}$$

and its rotation profiles $\Omega_g r$ are displayed by the dashed lines in Fig. 3.5(a). Note that Ω_g is aligned with the cylinder axis but with opposite direction due to the negative value of dU_g/dr. For weak forcing U_g remains small and the original rotation profile in the cylinder is hardly altered. Increasing ϵ, the geostrophic axisymmetric flow grows with the (minimum) peak of the radial profile of the rotation being shifting towards the sidewall. For sufficiently large ϵ we see no further change in the profile $\Omega_g r$, with Ω_g remaining around -1.05, which is slightly larger than the angular frequency of the container wall but in opposite direction indicating a kind of (anti-)super rotation. In these cases the strong modification of the radial profile of the time-averaged, total angular momentum (including solid body rotation) violates the Rayleigh criterion for centrifugal stability of rotating flows (Giesecke *et al.* (2018)). We will come back to this feature in Chapter 4.

Looking at the various profiles it is clear that in the proximity of the sidewall boundary ($R = 1$) a velocity gradient evolves, which increases with ϵ: this is a typical property of the axisymmetric-geostrophic modes which have to satisfy the no-slip condition on the lateral sidewall of the cylinder (see Eq. (2.16)). We use the minimum of U_g as the characteristic for the estimation of the thickness of the sidewall boundary layer δ_{sw} which gives the results as a function of ϵ shown in Figure 3.5(b). All curves have a similar tendency and are distinguished only by a shift with respect to ϵ. Similar to the breakdown of the kinetic energy of the $m = 1$ modes shown in Figure 3.2(a), we see a transition from a monotonic decrease of δ_{sw} to an asymptotic behavior above a critical ϵ (which again depends on Ek). In the asymptotic regime (i.e. for sufficiently large ϵ) the behavior is roughly in accordance with a scaling $\propto Ek^{1/4}$ as it would be expected for a Stewartson layer developed by a geostrophic flow on a vertical wall (Pedlosky (2008)). The transition occurs at the same ϵ where we see the drop of the energy of the $m = 1$ mode in Fig. 3.2(b) and the high branch of E_{geo} in Fig. 3.4(a) pointing out the involvement of the boundary layer for the bulk flow.

3.5. The endwall boundary layers

In this section, we analyze the properties of the endwall boundary layers and we check the thickness scaling in dependence of ϵ. Our main focus will be on strong forcing.

The no-slip boundary conditions imply a non-vanishing vertical gradient of the horizontal velocity field: $\partial_z u_r, \partial_z u_\varphi \neq 0$. These gradients cause the emergence of Ekman layers at the endwalls (Gans (1970), Zhang & Liao (2017), Meunier *et al.* (2008)) in which viscosity dominates and which provokes the saturation of the flow amplitude in the laminar regime. Moreover, the Ekman layers are responsible for the onset of a secondary flow in order to maintain the $\nabla \cdot \boldsymbol{u} = 0$ condition. Their presence is therefore intimately connected with the occurrence of Ekman pumping (Gans (1970)). The thickness of the laminar Ekman layer is known to scale as $\propto \sqrt{Ek}$ and consequently the transformed coordinate is defined as $\zeta = \pm(z \mp \Gamma/2)Ek^{-1/2}$.

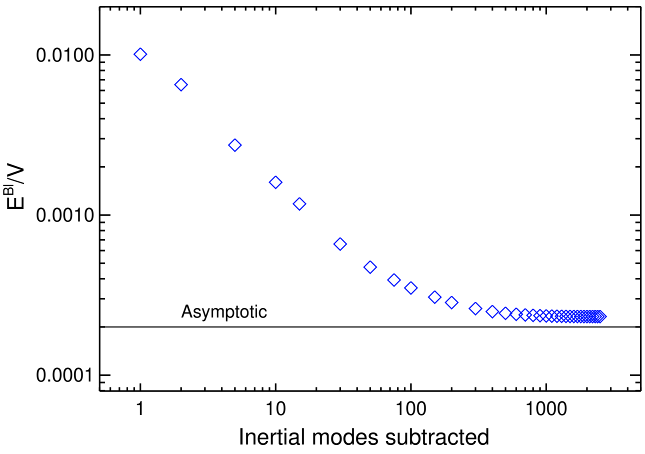

Figure 3.6. Convergence of the boundary layer energy E^{Bl} for the case $\epsilon = 10$ in dependence on the number of inertial modes applied for reconstruction of the bulk flow.

3.5.1. Truncation error for u^{Bl} and comparison with analytical model

First we check the convergence of the decomposition method (Eq. (3.1)) in terms of (volume-averaged) boundary layer energy defined as:

$$\frac{E^{Bl}}{V} = \frac{1}{V}\int_V \frac{(u_z^{Bl})^2 + (u_r^{Bl})^2 + (u_\varphi^{Bl})^2}{2}\, dV \; . \tag{3.10}$$

Figure 3.6 shows an asymptotic behavior for the interesting case $\epsilon = 10$ which exhibits the strongest dynamics. Since for all the computations we have subtracted at least 1000 modes to obtain the boundary layer flow field, we can conclude that the resulting u^{Bl} is reasonably well defined.

To enforce the validation of the filtered u^{Bl} we compare it with the linear analytical velocity profile as described by Gans (1970):

$$u_r^{Bl} = \pm A i e^{i\varphi}\left(\frac{\xi J_0(\xi r)e^{\zeta/\delta_1}}{2} + \frac{\xi J_2(\xi r)e^{\zeta/\delta_2}}{6}\right),$$

$$u_\varphi^{Bl} = \pm A e^{i\varphi}\left(-\frac{\xi J_0(\xi r)e^{\zeta/\delta_1}}{2} + \frac{\xi J_2(\xi r)e^{\zeta/\delta_2}}{6}\right)\,, \tag{3.11}$$

with A being the amplitude of the $(1,1,1)$ mode for the resonant cylinder

$$A = \frac{\epsilon\left(\xi^2 J_1\left(\xi\right)\right)^{-1}}{\left[\delta_2\left(3+\xi^2+6\sqrt{3}\left(1+\pi^2/4\right)\right) - 3\delta_1\left(3+\xi^2\right)\right]}\,, \tag{3.12}$$

and

$$\delta_1 = \frac{1+i}{\sqrt{2}} \quad \text{and} \quad \delta_2 = \frac{1-i}{\sqrt{6}} \,. \tag{3.13}$$

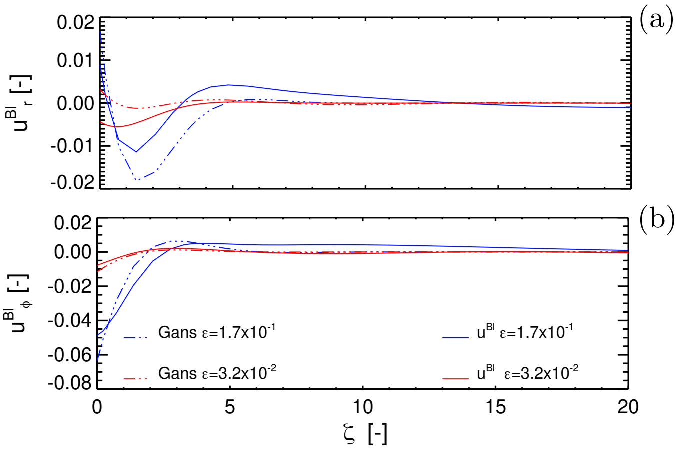

Figure 3.7. Comparison between the bottom endwall Ekman layer described by analytical theory (Equation (3.11) and the DNS filtered boundary layer $\boldsymbol{u}^{Bl}$ for two ϵ. (a) radial flow; (b) azimuthal flow, plotted against the transformed coordinate ζ.

The results are presented in Figure 3.7 for $\epsilon = 3.2 \times 10^{-2}$ (red curves) and $\epsilon = 1.7 \times 10^{-1}$ (blue curves) at the bottom endwall. The transformation coordinate ζ stretches the vertical coordinate in dependence on Ek, so that finally the peaks for the two Ek have a similar distance from the wall. Again we have rather good agreement between analytical and numerical solutions.

3.5.2. Ekman spiral

The Ekman spiral reflects the axial dependence of radial and azimuthal velocities inside the Ekman layers (Greenspan (1968), Deusebio *et al.* (2014)). It is shown in the inset plot of Fig. 3.8(a) taken at $\varphi \approx \pi$ for the bottom cylinder endwall. The variation of ϵ also impacts the characteristics of the Ekman spiral approaching, at the origin, an angle of $\approx 25°$. Interestingly, Caldwell & Van Atta (1970) and Caldwell *et al.* (1972) had reported similar values for the Ekman layers across the first instability.

For the lowest ϵ the slope at the origin is very close to the ideal value $\pi/4$ (see inset plot), consistent with the ideal Ekman layer theory. In Fig. 3.8(b) the Ekman spiral evolves with the azimuthal coordinate because of the dominant role of the first azimuthal wave number $m = 1$. The "rotation" of the spirals with the azimuthal coordinate results from the three-dimensional structure of the velocity field. Physically, this distribution along φ impacts the vortical behavior of the flow: the axial component of the vorticity in

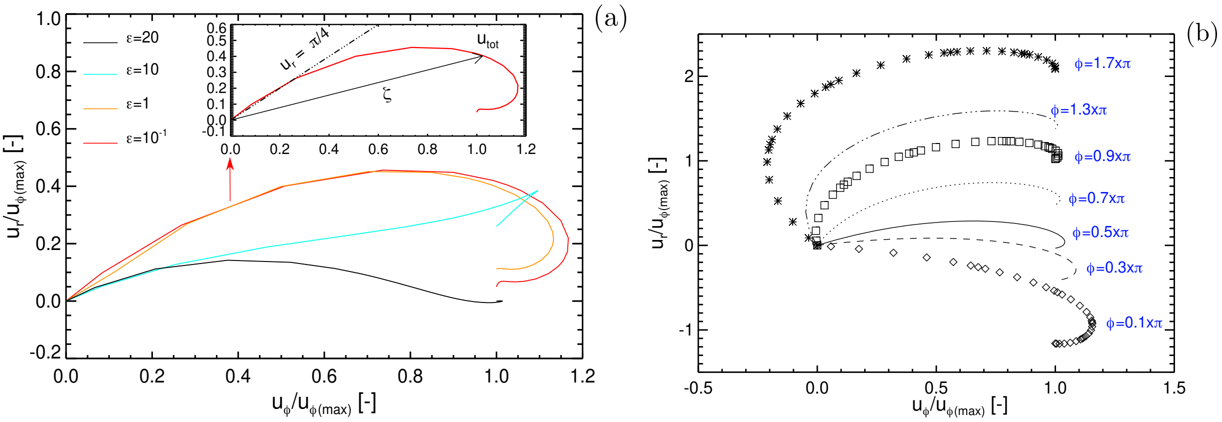

Figure 3.8. Ekman spiral at $r = 0.5R$ for the bottom endwall. (a) Impact of the forcing term ϵ on the spiral. Inset plot focus on the weakest case together with the spiral features (Greenspan (1968)) ζ and origin slope. (b) Plot of the azimuthal evolution of various spirals using velocity data at different azimuthal angles. The precession rotates this structure due to the dominance of the $m = 1$ mode.

cylindrical coordinates reads

$$\hat{\boldsymbol{z}} \cdot (\boldsymbol{\nabla} \times \boldsymbol{u}) = \left(\frac{\partial u_\varphi}{\partial r} - \frac{1}{r} \frac{\partial u_r}{\partial \varphi} + \frac{u_\varphi}{r} \right) , \tag{3.14}$$

from which it is clear that the azimuthal dependence due to the term $\propto \partial u_r / \partial \varphi$ could cause a modification with respect to the pure rotating flow.

3.5.3. Ekman layer thickness estimation for small ϵ

We determine the thickness of the Ekman boundary layer δ_{Bl} using the first peak of the radial velocity u_r and u_r^{Bl} adjacent to the wall which provides a suitable reference in case of rotating flows (Tatro & Mollo-Christensen, 1967). Figure 3.9 presents the radial velocity close to the bottom endwall for several small ϵ. We have selected the maximum profile at the bottom endcaps, which is comprised in between $275° \leq \varphi \leq 302°$ (from smallest to largest Ekman number). Figure 3.9(a) presents the total radial flow field which fulfills the no-slip condition at $z = 0$ and the maxima in this case are marked with square symbols. The second plot, Figure 3.9(b), shows u_r^{Bl} with the respective maxima marked by triangles. Note how the velocity gradient increases with ϵ. Collecting the velocity peaks of the curves in Fig. 3.9(a) and (b) we determine the scaling of the thickness of the Ekman layer. Figure 3.9(c) shows δ_{Bl} against the respective Ekman numbers (and ϵ) where both approaches provide almost identical results, which are in good agreement with the theoretical scaling law $\propto \sqrt{Ek}$ (solid black curve).

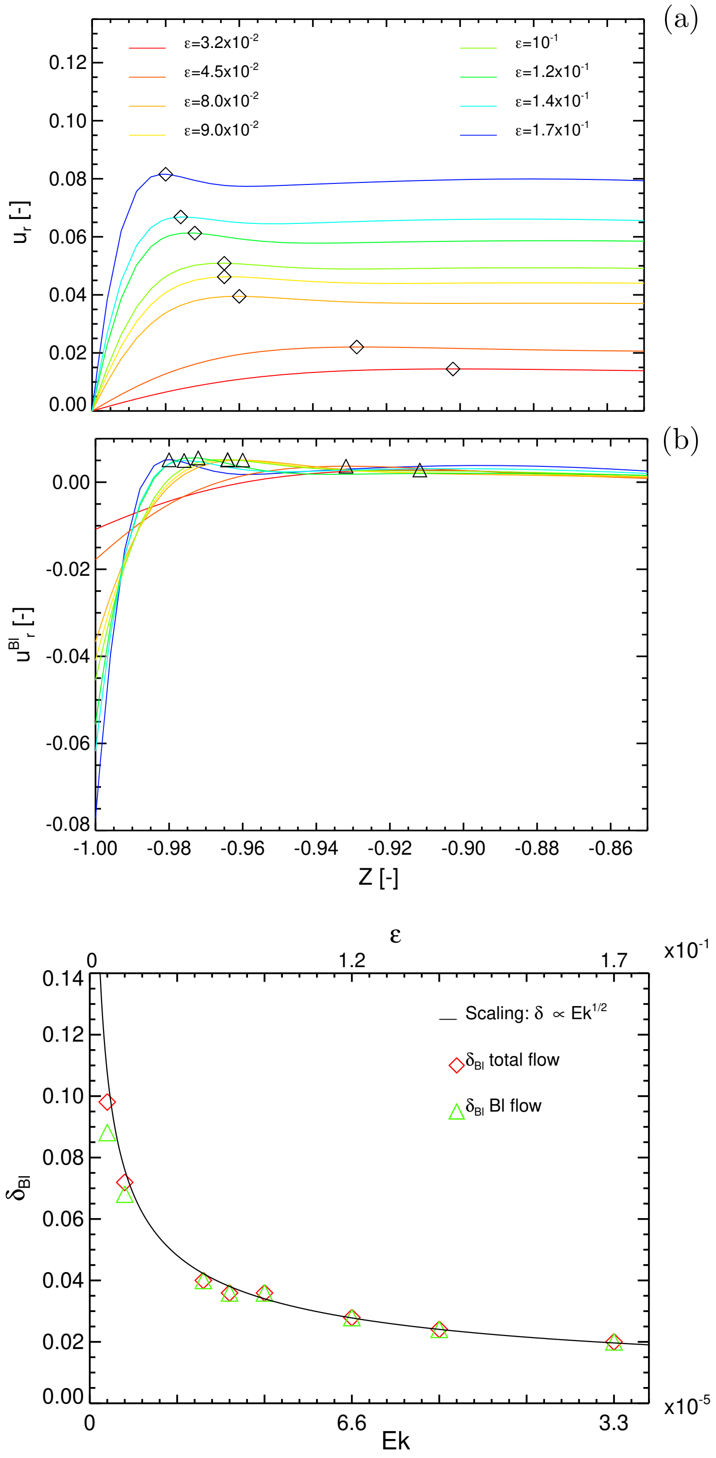

Figure 3.9. Plots of the time averaged radial velocity of the bottom endwall Ekman layer for various ϵ in the weak regime. (a): u_r with the respective maxima used for the determination of δ_{Bl} marked by diamond symbols; (b): boundary layer flow field u_r^{Bl} again with the respective maxima marked by triangle symbols. (c) Plot of the scaling law (solid curve) for the thickness of the laminar Ekman layer compared with the results from our simulation: total flow (red squares); boundary layer flow (green triangles).

3.5.4. Impact of the forcing term ϵ

The main goal of this part is to study the impact of ϵ on the bottom Ekman layer. Figure 3.10 presents the spatial structure of the azimuthal (left column) and radial flow components (right column) for three increasing ϵ at the height of $z = -1 + \sqrt{Ek}$.

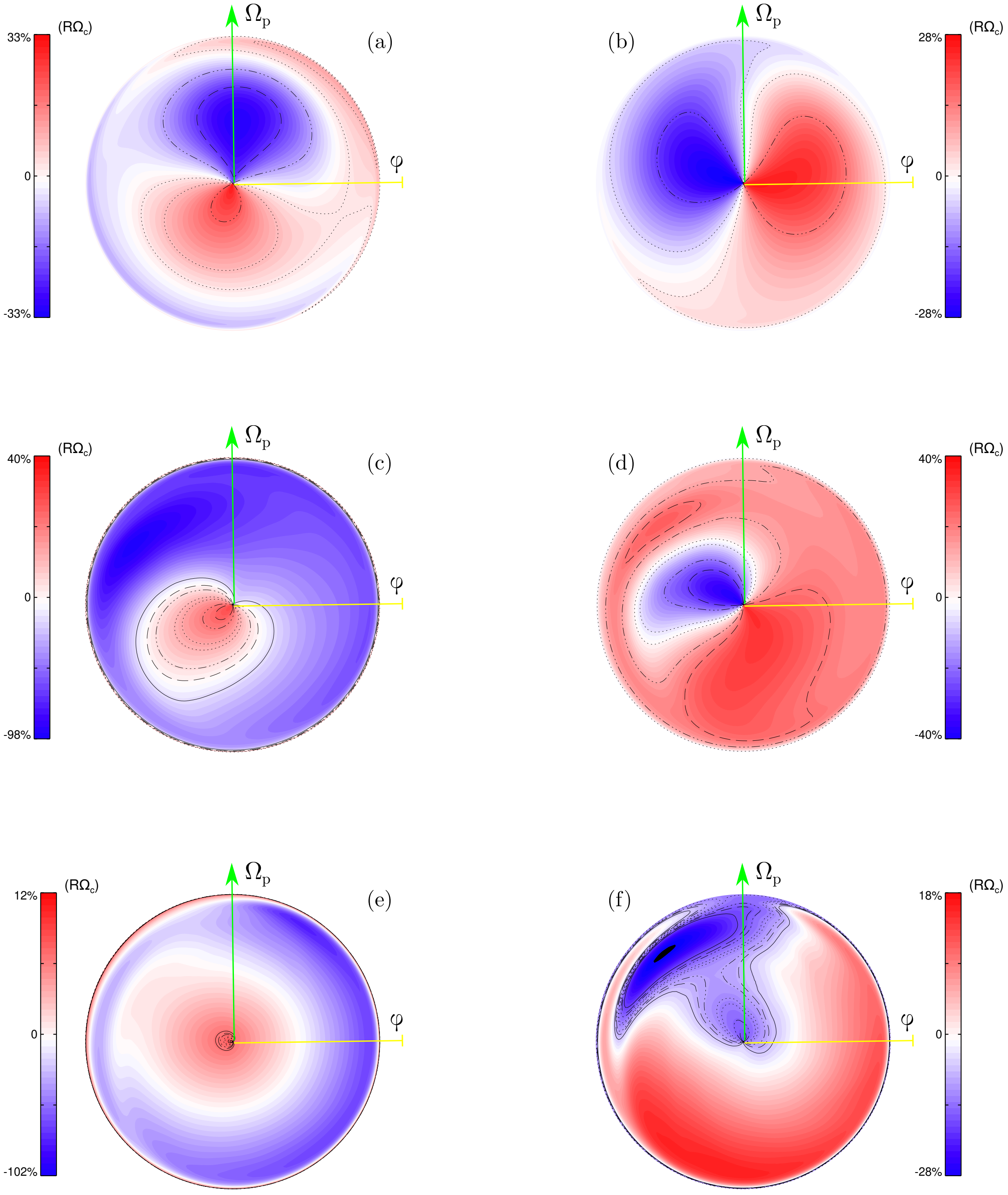

Figure 3.10. Polar contours of the time-averaged azimuthal u_φ (left column) and radial u_r (right column) velocity, both taken at $z = -1 + \sqrt{Ek}$ ($\zeta = 1$). From top to bottom: $\epsilon = 1$; $\epsilon = 10$; $\epsilon = 20$. Main features: u_φ shows transition from non-axisymmetric pattern (dominated by $m = 1$) to axisymmetric $m = 0$ whose magnitude is similar but with a direction opposite to the solid body velocity. The radial velocity u_r shows a phase shift $\approx -30°$ between $\epsilon = 1$ and $\epsilon = 10$. The green axis represents the precession axis and the yellow axis coincides with $\varphi = 0$.

The case $\epsilon = 1$ (Fig. 3.10(a),(b)) still shows the clear $m = 1$ structure, consistent with the analytical solution (as expressed in Eq. (1)) in concordance with the fact that this case is in the region dominated by E_{111}, see Fig. 3.4(a).
For larger ϵ, the flow reflects the change of the structure in the bulk (recall the dominance of the geostrophic axisymmetric flow) and u_φ becomes increasingly axisymmetric (Fig. 3.10(c),(e)), and oriented opposite to the rotation of the cylinder. As already evidenced in the previous section, for growing ϵ, the boundary layer flow is dominated by the azimuthal component, which becomes predominantly axisymmetric. In contrast, the radial component retains its prevailing non-axisymmetric character. Note also the significant change of the phase orientation when increasing ϵ (Fig. 3.10(b),(d),(f)). The dominant positive part of u_r in Figure 3.10(d) reveals a stronger radial flow towards the sidewalls, which will be investigated more in detail later.
As previously, we use the peak of the radial boundary layer velocity u_r^{Bl} closest to the bottom endwall to estimate the Ekman layer thickness. However, in contrast to the case of small ϵ, we remove the radial and azimuthal dependence by averaging in r and φ, a procedure that is all the more justified as the bulk inviscid flow is largely axisymmetric in the examined range of parameters. The resulting boundary layer thickness δ_{Bl} is shown in Fig. 3.11(a). We find that roughly the thickness follows the scaling $\propto Ek^{-1/2}$ as found for small ϵ. Considerable exceptions by means of an increase of the thickness by up to 30 to 40 percent occur exactly in the regime where we also find the breakdown of the forced mode (i.e. the drop of the energy E_{111}) and the sudden increase of the geostrophic-axisymmetric flow.

This enhanced thickness is connected with an increased suction of fluid into the Ekman layer which we calculate from an integration of the vertical velocity across the Ekman layer:

$$w = \frac{1}{\delta_{Bl}} \int_{-1}^{-1+\delta_{Bl}} \langle u_z \rangle_{r,\varphi} \, dz \; . \tag{3.15}$$

The results are presented in Fig. 3.11(b) and show that the largest w occurs in the same range of ϵ as the (local) maximum of δ_{Bl}. For smaller Ek we see a similar behavior, although with a narrowing of the peak. The previous results are also directly reflected in the profiles of the radial and axial velocity components, as shown close to the boundary in Fig. 3.12(a,b) for the cases with $Ek = 1 \times 10^{-4}$. Figure 3.12(a) shows the radial flow, Fig. 3.12(b) the residual $u_r - u_r^{Bl}$, and Fig. 3.12(c) the corresponding axial velocity (always space averaged in azimuthal and radial direction). While the peak magnitude of the velocity profiles clearly depends on the forcing term, its location with respect to the endwall does hardly change with ϵ. The only exception is u_r around $\epsilon = 10$ (green curve) which does not follow the general behavior. The green curve in Fig. 3.12(a),(b) indi-

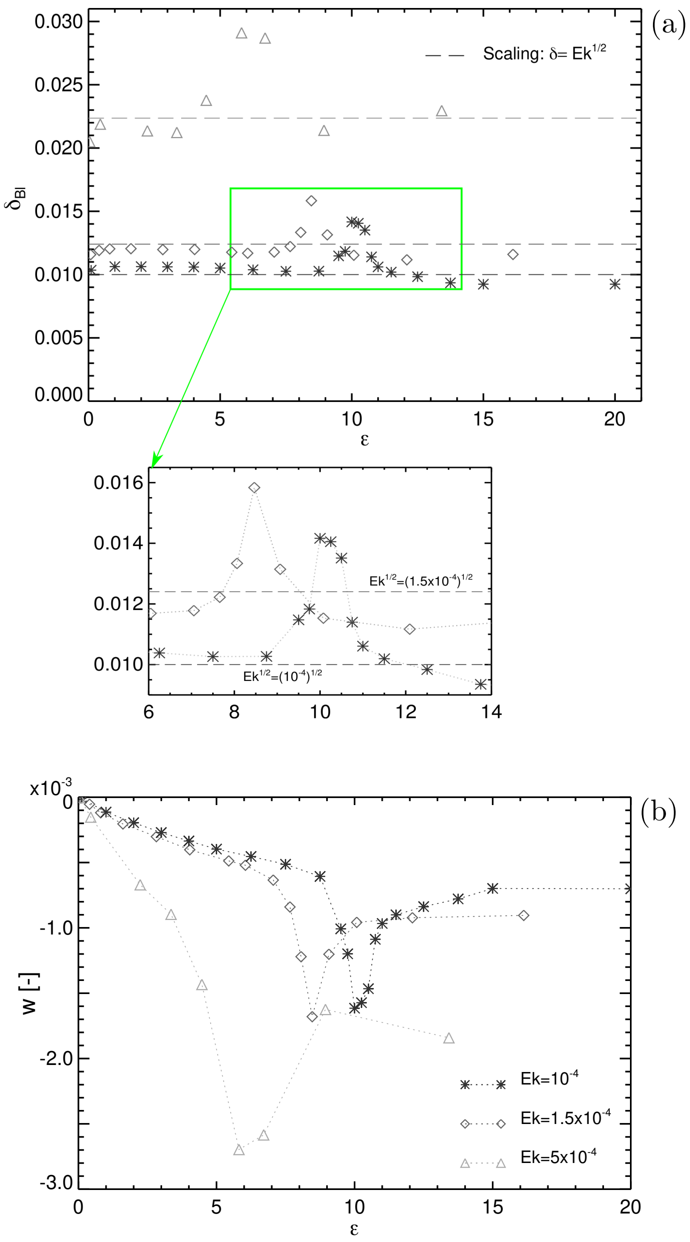

Figure 3.11. The influence of ϵ on the Ekman layer. (a) Plot of the thickness δ_{Bl} of the bottom Ekman layer as a function of the forcing term. The horizontal dashed line represent the theoretical scaling law $\propto \sqrt{Ek}$. The zoom plot shows a focus on the cases $Ek = 1.5 \times 10^{-4}$ and $Ek = 10^{-4}$ with the striking peak around $\epsilon \approx 8.5$ and $\epsilon \approx 10$. (b) Plot of the integrated vertical flow advection w defined in Eq. (3.15) as a function of the forcing term ϵ.

cates a larger positive radial flow representing a strong flow ejection towards the cylinder sidewalls. Furthermore, the total flow (top plot) exhibits a smoother structure without clear maximum and the residual part remains largely different from zero in contrast to the other cases. The horizontally averaged axial velocity $\langle u_z \rangle_{r,\varphi}$ of the $\epsilon = 10$ case presents the largest axial flow into the Ekman layer in Fig. 3.12(c).

Putting together the results of Fig. 3.11, and 3.12 we can assume that around $\epsilon \approx 10$ a stronger Ekman suction (negative vertical flow) occurs jointly with an enhanced radial

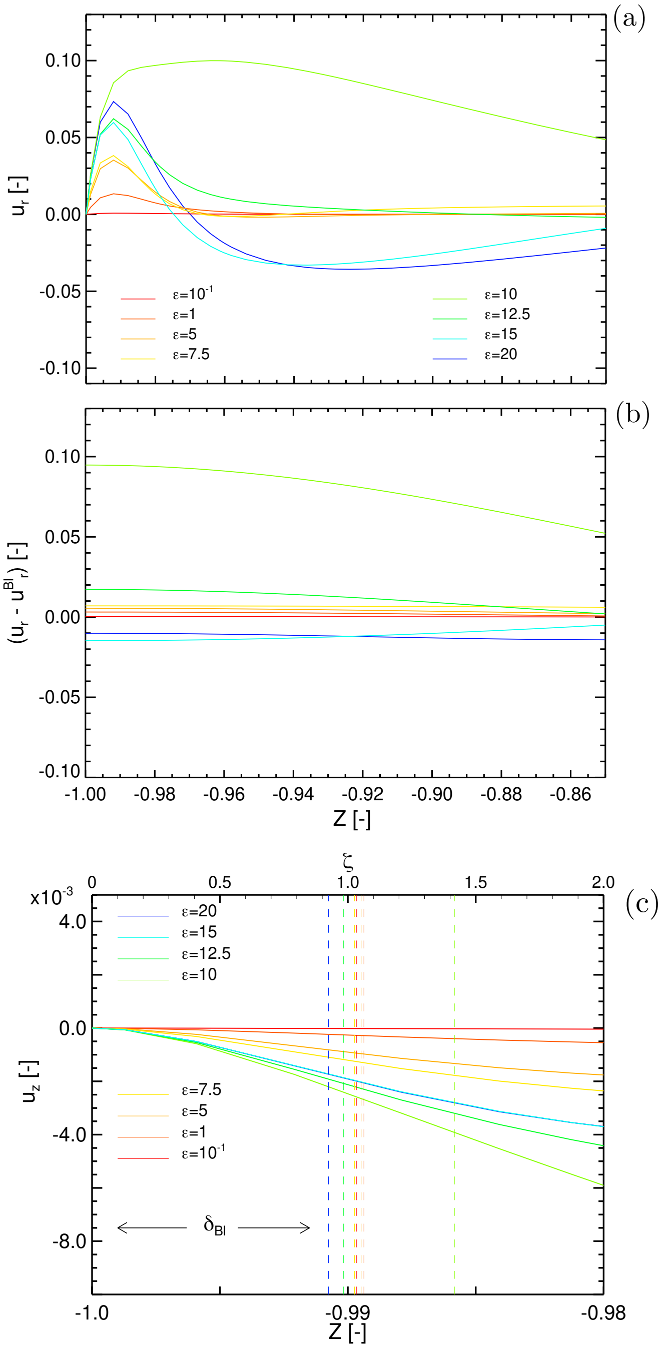

Figure 3.12. Plots of the velocities inside the bottom endwall Ekman layer, averaged in time and over radial and azimuthal coordinate. (a) Radial velocity: $\langle u_r \rangle_{r,\varphi}$; (b) residual flow $\langle u_r \rangle_{r,\varphi} - \langle u_r^{Bl} \rangle_{r,\varphi}$; (c) Axial velocity $\langle u_z \rangle_{r,\varphi}$.

outward flow (radial pumping). Interestingly, this observation is consistent with the general mechanism for nonlinear Ekman layers if only the geostrophic flow above the layer is anticyclonic (Sansón, 2001, Benthuysen & Thomas, 2012, Pedlosky, 2008). This is indeed the case here since the axisymmetric-geostrophic velocity $U_g(r)$ is oppositely directed to Ω_c, so that its axial vorticity is negative, as described in Section 3.4.

3.5.5. Computation of Re_δ and Ekman layer instabilities

In order to evaluate the stability of the Ekman layers, we define the usual Ekman boundary layer Reynolds number according to Coleman *et al.* (1990), Deusebio *et al.* (2014), Sous *et al.* (2013), Tatro & Mollo-Christensen (1967), Caldwell & Van Atta (1970) as

$$Re_\delta = \frac{\delta_{Ek} U_{ref}}{\nu} \quad \text{with} \quad \delta_{Ek} = \sqrt{Ek}\, R\,. \tag{3.16}$$

Here, the reference velocity U_{ref} is the velocity at the edge of the Ekman layers, which is usually defined as the magnitude of the geostrophic wind horizontal to the surface. Since for the entire range of ϵ simulated here, the geostrophic flow is essentially axisymmetric (Fig. 3.4(b)), we calculate the reference velocity in the following way:

$$U_{ref} = |\boldsymbol{\Omega}_g \times \hat{\boldsymbol{r}}|_{r=R} = |\boldsymbol{\Omega}_g| R\,, \tag{3.17}$$

with the rotation vector of the geostrophic flow $\boldsymbol{\Omega_g}$ as defined in Section 3.4. The linear stability analysis of the Ekman layer is known to provide two types of instabilities: the first instability occurs at $Re_\delta \approx 55$ and is characterized by a spiral roll structure (corresponding to class A in Caldwell & Van Atta (1970)). The second instability occurs at $Re_\delta \approx 115$ and is called "inviscid instability" (corresponding to class B). Fully turbulent Ekman layers emerge beyond $Re_\delta = 150$. In accordance with previous studies (Sous *et al.*, 2013, Deusebio *et al.*, 2014, Caldwell & Van Atta, 1970, Coleman *et al.*, 1990, Tatro & Mollo-Christensen, 1967) we use the ideal scaling law for the laminar regime $\delta_{Ek} \propto \sqrt{Ek}$ which in our case underestimates the thickness in the critical ranges where δ_{Bl} shows a local increase (Fig. 3.11). The results are presented in Fig. 3.13 where both instability thresholds are indicated as dashed horizontal lines. The tendency of the three curves confirms the emphasized role of the previously identified critical ϵ, here in relation with the transition from a monotonic increase of Re_δ to an asymptotic behavior independent of ϵ (but not independent of Ek). Only the curves for $Ek = 1.5{\times}10^{-4}$ and $Ek = 10^{-4}$ surpass the threshold of the first instability. For $Ek = 10^{-4}$ we find a saturation around $Re_\delta \approx 100$ for $\epsilon > 13$, hence neither the second instability nor a fully turbulent state are realized in the Ekman layers for all cases simulated in this study. The weakly pronounced maximum around the transitional regime indicates that in this regime the Ekman layer is closest to the threshold of the B-mode instability. Despite that in Fig. 3.13 the independent variable is the forcing parameter ϵ, it is obvious that Re_δ is a function of both, Po and Ek and the emergence of turbulent boundary layers would require sufficiently fast rotation as well as sufficiently strong precession. In order to estimate the threshold at which parameter we may expect fully turbulent endwall Ekman layers, we linearly extrapolate the largest Po cases. The linear extrapolations presented in Fig. 3.14 show that the threshold to

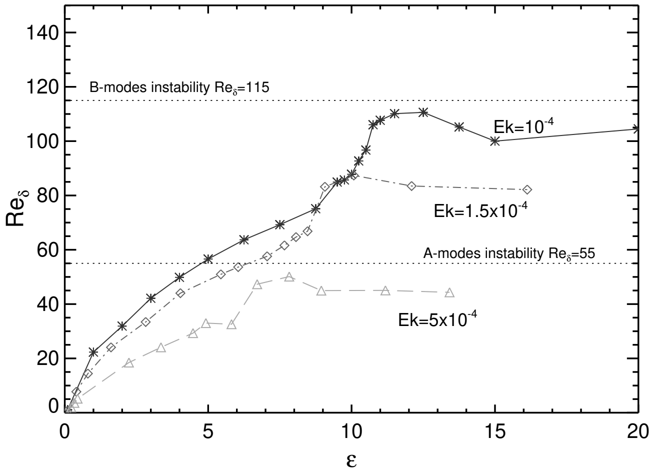

Figure 3.13. Plot of the Ekman boundary layer Reynolds number Re_δ as a function of the forcing ϵ. Horizontal dashed lines represent the two types of instabilities predicted by stability theory.

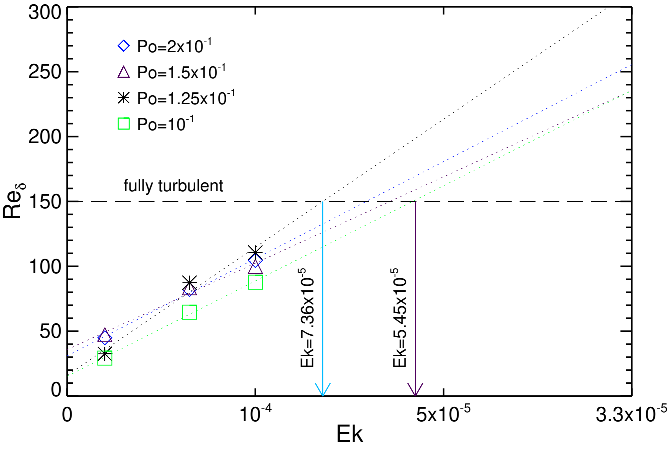

Figure 3.14. Linear extrapolation of Re_δ for the onset of turbulent Ekman layer and the corresponding expected range of Ek.

turbulent boundary layers is crossed in the range $5.5 \times 10^{-5} < Ek < 7.4 \times 10^{-5}$ which is out of the range of our numerical capacities but it is well in the range obtained in the 1:6 down-scaled water experiment, and of course also in the range of the DRESDYN experiment.

3.5.6. Boundary layers Rossby number

Usually, rotating flows in the laboratory are considerably impacted by curvature effects because of the *small* scale of the experimental devices, which is quite in contrast to planetary or atmospheric flows, essentially less vortical as stated by Sous *et al.* (2013).

Being dominated by strong (and radially dependent) azimuthal circulation at large enough forcing, our precessing flow exhibits this difference, too. We can quantify this departure in terms of the vortical Rossby number $Ro_t = U_g/(rf)$ (Sous *et al.* (2013)) where f is the standard Coriolis parameter $f = 2\Omega_c$ (Coleman *et al.* (1990), Deusebio *et al.* (2014), Sous *et al.* (2013)), which represents the background flow vorticity. For $\epsilon > 1$, Ro_t is in between $[-0.2, -0.5]$ with the negative values reflecting the anticyclonic behavior. Specifying the concept to the Ekman layer, we apply the method used by Sous *et al.* (2013) to define the friction Rossby number for azimuthal flows

$$Ro_f = \frac{u_\tau^2}{f'\nu}, \quad \text{with} \quad f' = f + \frac{U_g(r)}{r} + \frac{dU_g(r)}{dr}\,, \tag{3.18}$$

where the friction velocity is defined as

$$u_\tau = \sqrt{\nu \frac{\partial \langle u_\varphi \rangle_\varphi}{\partial z}|_{z=-1}}\,, \tag{3.19}$$

with the azimuthal velocity averaged in φ. In Eq. (3.18) the term f', called modified Coriolis parameter (Sous *et al.*, 2013), includes f and $U_g/r + dU_g/dr$ which is the vorticity modification due to the emergence of the geostrophic current. The ratio U_g/u_τ, the inverse of the wall drag coefficient, is a useful quantity in both laminar and turbulent Ekman layers (Csanady, 1967, Coleman *et al.*, 1990). The laminar theory for the atmospheric boundary layer (see Sous *et al.* (2013)) predicts a linear dependence of the geostrophic flow according to $U_g/u_\tau = (2 \times Ro_f)^{1/2}$ and the transition to a turbulent Ekman layer is expected to take place at $Ro_f^{1/2} > 10$.

We compute Ro_f at the peak of U_g so that the radial derivative dU_g/dr is zero. Figure 3.15(a) summarizes the outcome: we find a saturation for $\epsilon > 9$ for all cases, which may be linked with the corresponding saturation of the dominant E_{geo} in Fig. 3.4(a). In particular the threshold for the emergence of turbulent Ekman layers, i.e. $Ro_f^{1/2} > 10$, is never reached. Accordingly, we find that the velocity ratio U_g/u_τ is mostly linear in dependence on $Ro_f^{1/2}$ (Fig. 3.15(b)), as it is expected from the laminar theory of atmospheric boundary layers (Sous *et al.* (2013)). Some minor departures emerge for large precession ratio. These departures could be caused by the influence of the sidewall boundary layer since the radius corresponding to the maximum of U_g arises close to the sidewall in these cases (see Fig. 3.5).

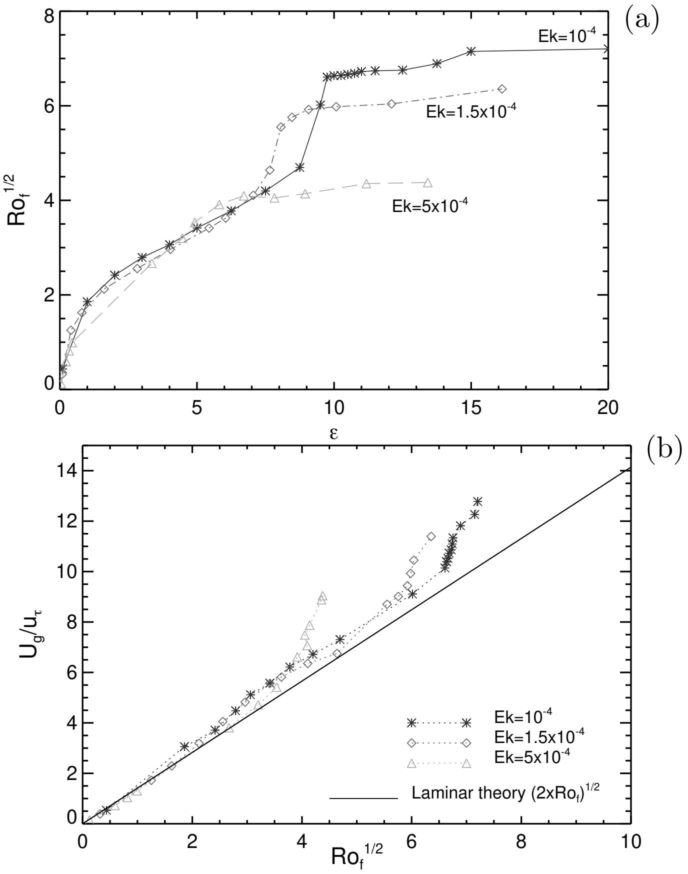

Figure 3.15. (a) $Ro_f^{1/2}$ against ϵ. (b) Plot of the velocity ratio U_g/u_τ as a function of the frictional Rossby number at $r = r(min(U_g))$. The solid line shows the laminar theory as described in Sous *et al.* (2013).

3.5.7. Law of the wall and statistical features

Finally we substantiate the previous results by applying classical time-averaged statistical quantities. A typical method to study turbulent boundary layers is the *law of the wall*. It states that at a fixed point the average velocity of a turbulent flow is proportional to the logarithm of the distance from that point to the wall (respectively boundary). More precisely, in the turbulent regime the boundary layers develop different regions characterized by the scaled coordinate $y^+ = zu_\tau/\nu$. Two layers are formed: (i) a viscous sublayer for $y^+ < 5$ where the viscous stresses are dominant with respect to the Reynolds shear stresses. In this region the scaled velocity $u^+ = u_\varphi/u_\tau$ follows the law $u^+ = y^+$; (ii) an outer layer with a logarithmic profile $u^+ = 1/k \ln(y^+) + B$. Here, $k = 0.41$ is the von Kármán constant and $B \approx 5.2$ the so-called log-law constant (Pope (2000)), which was inferred from experiments and which weakly depends on the specific type of the flow problem.

In Fig. 3.16(a) we plot the law of the wall for a radius r corresponding to the minimum peak of U_g (see Fig. 3.5(a)). Obviously, the logarithmic profile, indicated by the black

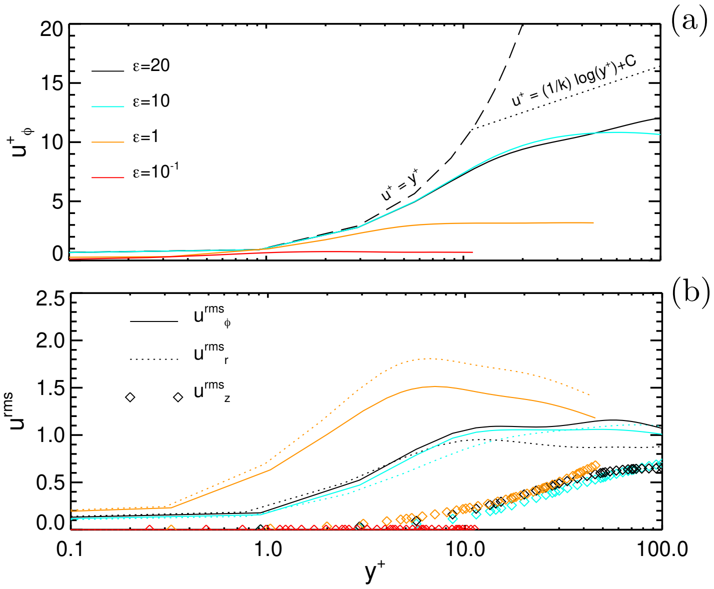

Figure 3.16. Impact of the forcing term ϵ on the mean statistical features of the Ekman layer. (a) Law of the wall and, (b) normalized root mean square velocity u^{rms}.

dotted line, is not achieved for any of the considered profiles. The flow velocity follows the viscous law $y^+ = u^+$ close to the wall but then remains significantly lower than, although parallel to, the log-law. For larger ϵ the scaled velocity profile u^+ continues until larger values of y^+; the reason is that at large ϵ the friction velocity u_τ increases causing the "dilatation" of y^+. We thus conclude that $y^+ = f(\epsilon)$. The evident growth of the profiles with the forcing term ϵ indicates that an increase in ϵ may result in a generation of a fully turbulent Ekman layer, consistently with the prediction in Fig. 3.14.

To assess the role of statistical fluctuations in the Ekman layer, we calculate the azimuthally averaged root mean square velocities u^{rms} normalized with u_τ:

$$u_j^{rms} = \frac{\sqrt{\langle u'_j u'_j \rangle}}{u_\tau} \ , \quad \text{with} \quad j = z, r, \varphi \tag{3.20}$$

where $u'_j = u_j - \langle u_j \rangle$ is the velocity fluctuation obtained by Reynolds decomposition. Since the subscripts are the same, $\langle u'_j u'_j \rangle$ represents the diagonal (isotropic) term of the Reynolds stress tensor. Figure 3.16(b) shows the typical features of wall bounded flows: streamwise u_φ^{rms} (solid lines) and spanwise u_r^{rms} (dashed lines) components of the flow field are larger than the vertical one u_z^{rms} (diamond lines). The peaks of u_φ^{rms} and u_r^{rms} are located around $y^+ \approx 5 \ldots 10$. However for the largest ϵ the values remain large with a second peak for $y^+ = 60$ which which points out the presence of significant fluctuations also in the bulk region.

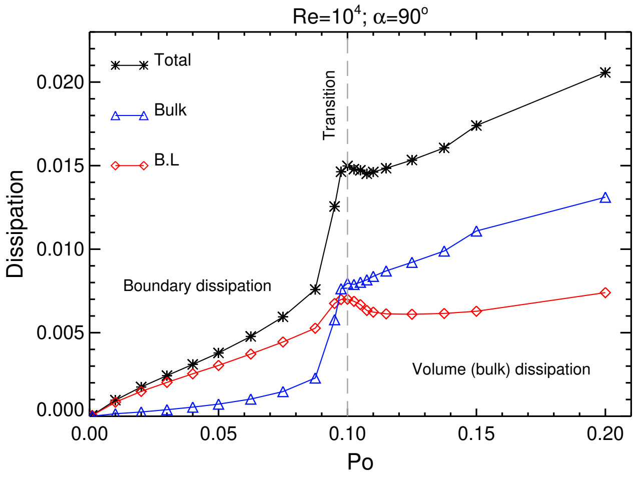

Figure 3.17. Plot of the time-averaged dissipations (defined in terms of enstrophy) as a function of the precession ratio split between the boundary layers and the bulk contributions. We fix the Reynolds number and the nutation angle.

3.6. Disentangling the bulk flow and boundary layers

Up to this point we have observed several phenomena in which boundary layers and the bulk flows interact. However we were not yet able to distinguish the hierarchical relations between them. For instance the axial flux together with the increase of radial velocity and endwall Ekman layer thickness in a certain range of the precession ratio, shown in Fig. 3.11- 3.12, could be due to a resonance-like behavior of the layer itself or to the flow injection inside the layer by bulk poloidal vortices (which will be fully analyzed in Section 4.6). Moreover, following the theorem proposed by Greenspan (1969), it is conjectured that the emergence of the geostrophic flow could be generated by nonlinearity in the endwall boundary layers (Zhang & Liao, 2017, Meunier *et al.*, 2008). The main purpose of this Section is to clarify these points.

First, we split the bulk and the boundary layers making use of the decomposition method (Eq. 3.1) and then analyzing the time-averaged dissipations defined in terms of enstrophy i.e: $\text{Dissipation}_{BL} = |\boldsymbol{\nabla} \times \boldsymbol{u}^{BL}|^2$ and $\text{Dissipation}_{Bulk} = |\boldsymbol{\nabla} \times \boldsymbol{u}_{mkn}|^2$. In order to achieve a high precision we use (m, k, n) up to $(10, 10, 12)$ which should be enough to separate the bulk velocity $\boldsymbol{u}_{m,k,n}$ and the boundary layer velocity $\boldsymbol{u}^{BL}$. The results are shown in Fig. 3.17 where we select the maximum Reynolds number (minimum Ekman number) analyzed in our global simulations. It is clearly shown that the flow transition, i.e. the jump around $Po \approx 0.10$, is mainly due to the bulk flow while the boundary layers present only a little bump. It is interesting to observe the shift between a region dominated by the boundary layer dissipation (corresponding to the laminar regime) and a region dominated by bulk dissipation. In the low Po range the dissipations are indeed due to the viscosity in the boundary layers consistent with the prediction of analytical theories (Gans (1970),

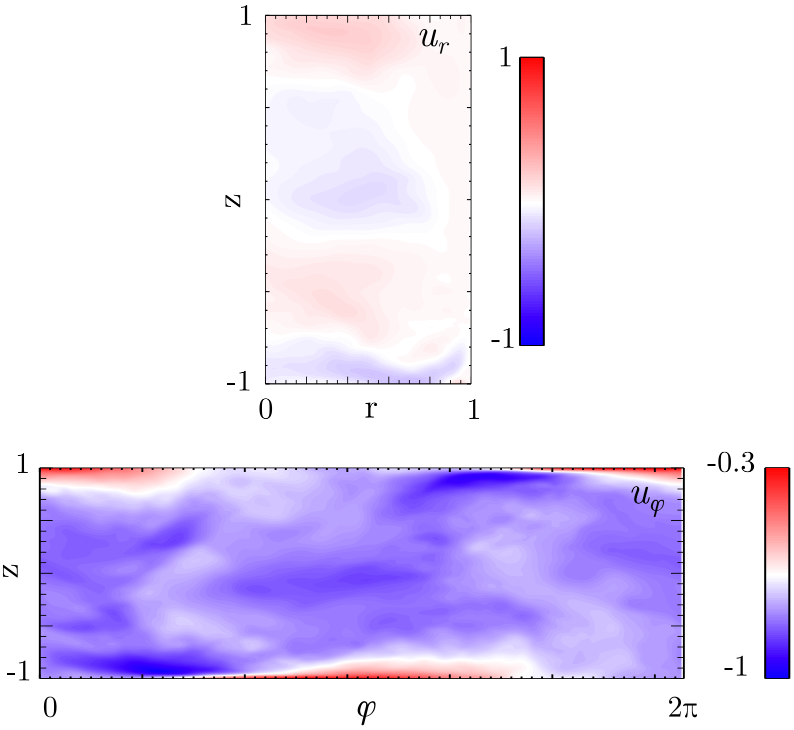

Figure 3.18. Contour plots of the radial and azimuthal velocities for the stress-free endwalls boundary condition for $Re = 6500$, $Po = 0.20$ and $\alpha = 90°$. Top panel shows the radial velocity u_r in the meridional semi-plane at $\varphi = \pi$. Bottom plot shows the azimuthal velocity in a cylindrical envelope taken at middle radius $r = 0.5$.

Meunier *et al.* (2008)). By contrast, at large Po the volume-bulk dissipation becomes dominant, a clear hallmark of turbulent behavior. This is a first indication that the increase of the precession ratio impacts mainly the bulk phenomena which dominates the transition of the total flow field; however in order to substantiate this claim we should be able to conduct a sensitivity analysis, i.e. to analyze one entity at a time.

The capabilities of numerical experiments allow to perform that study by 'switching off' the endwall boundary layers so we can establish if the bulk phenomena (emergence of geostrophic flow, transition to turbulence and rising of poloidal vortices) occur independently from the endwall Ekman layers.

We perform simulations with free stress boundary condition at the endcaps which specifically means to use the non-penetrating condition (wall normal velocity equal to zero) plus the vanishing normal derivative of the tangential components: formally

$$u_z = 0\,;\; \frac{\partial u_r}{\partial z} = \frac{\partial u_\varphi}{\partial z} = 0, \quad \text{at} \quad z = \pm 1\,. \tag{3.21}$$

In mathematical terms we use a Dirichlet condition for the axial velocity and a Neumann condition for the radial and azimuthal velocities. The result is that this 'artificial' set-up allows to simulate the flow field without the standard no-slip conditions and so the viscous boundary layer at the cylinder endcaps.

We start by showing in Fig. 3.18 the contours of the radial and azimuthal velocity in order to check the tangential flow behavior close to the endwalls. We select two different views: for the radial velocity u_r we plot a meridional-semiplane while for the azimuthal velocity u_φ we present a cylindrical envelope, i.e. a plane $[z, \varphi]$ taken at the middle radius $r = 0.5$. We observe several features. First of all the radial and azimuthal velocities do not vanish at the endwalls evidencing that there are no boundary layers there. Another interesting fact is that the radial velocity is very small in magnitude in the bulk region while the azimuthal one is strongly negative (notice that this analysis is in the container frame of reference), both clear indications of the dominance of axisymmetric-geostrophic circulation.
We generalize and quantify the results by computing the energies of the various modes (as done for the no-slip case in Sec. 3.4). The results are shown in Fig. 3.19 for two different Reynolds numbers. The flow transition found in the 'realistic' configuration (no-slip conditions) is observed also here for stress-free conditions in the same range of the precession ratios, $Po \approx 0.10$, with similar values. Notice that the solid black curve, the geostrophic-axysimmetric energy for $Re = 6500$ ($Ek = 1.5 \times 10^4$), is almost the same as the one shown in Fig. 3.4. Moreover also for stress-free conditions we see a drop of the directly forced mode for both Reynolds numbers.
The third interesting quantity, shown in the zoomed panel, is the energy of double poloidal vortices e_{02}, which again does not present significant differences with respect to the no-slip boundary condition cases (as it will be shown in the following Chapter 4, Fig. 4.4). Therefore the poloidal flow emerges regardless of the endwall layers. We can conclude that the behaviors observed for $Po \approx 0.1$ (corresponding to the forcing parameter $\epsilon \approx 10$ in Fig. 3.11- 3.12) are not related to wall-phenomena such as resonant Ekman layer but rather to the inflow from the bulk. In order to show the dominance of geostrophic flow even for the stress-free conditions, we show in Fig. 3.20 the contours of the axial velocity. In the top plot, the central region of the equatorial plane presents almost vanishing axial velocity such as in the meridional semiplane (bottom). The final results that we show in Fig. 3.21 is connected with the emergence and dominance of the geostrophic circulation which counteracts the solid body rotation: the radial distribution of the angular momentum, again for $Re = 6500$ and $Re = 8000$. For the larger Po the angular momentum, averaged both in $[z, \varphi]$, is negative meaning that the flow counteracts the container rotation.

In this Section we have shown that the main features of flows enclosed in precessing cylinders are bulk-related and they are not caused by nonlinear viscous mechanisms. Those main bulk structures impact the endwall and sidewall boundary layers.

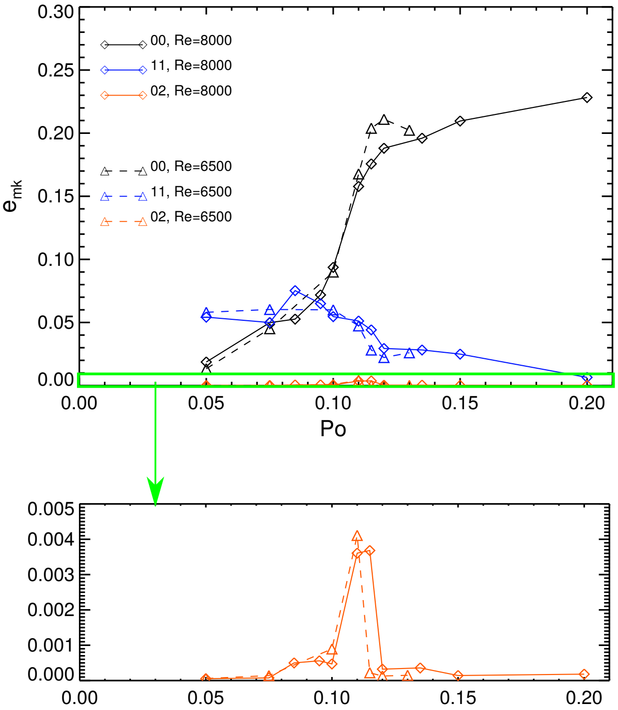

Figure 3.19. Plot of the energy of the main inertial modes for stress-free endwalls for two different Reynolds number $Re = 6500$ and $Re = 8000$. Top panel shows $e_{11} = \sum_n E_{11n}$ and $e_{00} = \sum_n E_{00n}$ as functions of the precession ratio while the bottom panel shows $e_{02} = \sum_n E_{02n}$.

3.7. Summary

In this Chapter we investigated numerically the fluid flow in a precessing cylinder with a special focus on the Ekman boundary layers and its interaction with the bulk flow in the moderate and strongly forced regime. In that regimes, we find deviations from the linear theory together with a significant modifications of the base flow in terms of an axisymmetric geostrophic mode whose rotation is opposite to that of the container. The transition of the bulk flow from a three-dimensional non-axisymmetric base flow to a geostrophic axisymmetric pattern is reflected in the scaling of both the sidewall boundary layers and the Ekman boundary layers on top and bottom of the cylinder. We use the peak of the radial boundary layer flow that is closest to the wall to determine the thickness of the Ekman layer δ_{Bl}, which essentially scales $\propto \sqrt{Ek}$ as it is the case in in the viscous theory of Gans (1970) or Zhang & Liao (2017). We find that the Ekman layers surpass the threshold of the first instability (class A) and show an increase in the thickness together with a marked vertical flow advection inside the boundary layer. This phenomenon occurs in a limited range of the forcing magnitude. Fully turbulent Ekman layers are not found, due to numerical restrictions in our simulations, which limit the range of achievable regimes. For this reason an estimation by extrapolation has been done.

The results of this chapter can be used as a basis in the context of the DRESDYN preces-

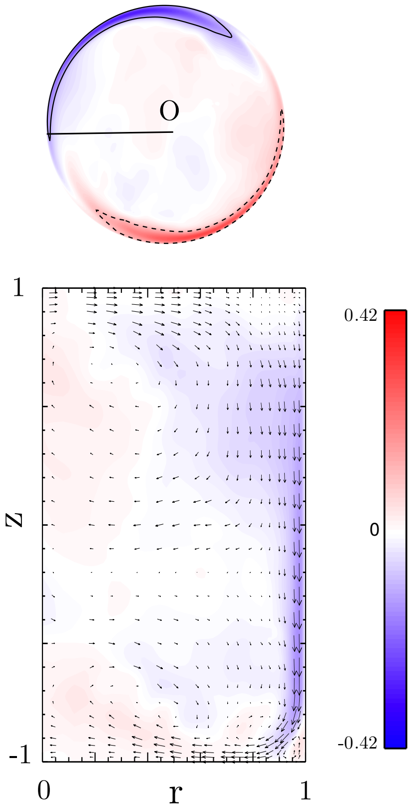

Figure 3.20. Contour plots of the axial velocity for the stress-free endwalls boundary condition for $Re = 6500$, $Po = 0.20$ and $\alpha = 90°$. Top panel shows the equatorial plane $z = 0$ with the origin of the cylinder O and the solid line represents the azimuthal location of the meridional semiplane shown the bottom panel. The color represents the u_z showing clearly that the center of the cylinder has vanishing axial flow. In the meridional contour the vectors represents the u_r, u_z flow field where it is clearly visible the double rolls.

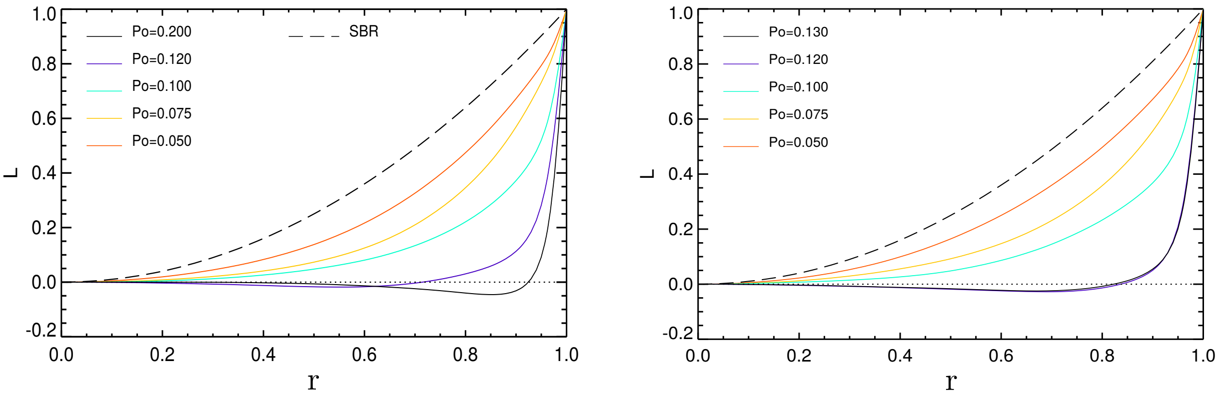

Figure 3.21. Radial distribution of the angular momentum for the stress free endwalls boundary conditions. Left plot shows the $Re = 6500$ cases and right plot the $Re = 8000$ cases.

sion experiment and the down-scaled water experiment. The properties of the boundary layers analyzed here can be extrapolated to the regime of the experiments: for weak forcing the scaling the Ekman layers developed on the endwalls should stay laminar indicating a thickness proportional to $\sim Ek^{-1/2}$. Since the radius of the small water experiment is 0.163 m while for the upcoming DRESDYN vessel is 1 m we can deduce a thickness of 0.15 mm for the former and 0.1 mm for the latter at their maximum rotation regime, i.e. at the smallest Ekman number. This feature is significant for the big machine since this thickness is significantly smaller than the roughness of the surface of the endcaps. Instead turbulent Ekman layers on the endcaps should be developing for large forcing with a thickness larger than for the laminar case.

Our results indicate that the region suitable for a possible dynamo action is between the class A and B instability.

Concomitantly to the breakdown of the directly forced flow and the rise of the geostrophic current, an increase of thickness of the sidewall boundary layers should occur. Again using the scaling law verified in this chapter, the transition from Ekman to Stewartson may be very clear in particular in the dynamo experiment since the thickness changes from $\delta_{sw} \sim Ek^{-1/2}$ to $\delta_{sw} \sim Ek^{-1/4}$.

4. Prograde and retrograde precession and the role of the nutation angle

> *Quando si attribuisca questo gran moto al cielo, bisogna di necessità farlo contrario a i moti particolari di tutti gli orbi de i pianeti, de i quali ciascheduno senza controversia ha il movimento suo proprio da occidente verso oriente, e questo assai piacevole e moderato, e convien poi fargli rapire in contrario, cioè da oriente in occidente, da questo rapidissimo moto diurno;*
>
> Galileo Galilei, Dialogo sopra i due massimi sistemi del mondo

4.1. Context and motivation

[1] In the previous Chapter 3 we have restricted our attention to the so called symmetric precession, i.e., the case of an orthogonal nutation angle. However, the flow responses in precessing driven cavities should depend quite generally on the forcing which comprises the precession strength and the nutation angle whose effect is not widely investigated. For example, geophysical studies deal mainly with retrograde motion (rotation and precession

---

[1] The present chapter relies on the journal publication *Prograde and retrograde precession of a fluid-filled cylinder* by Pizzi, Giesecke, Šimkanin, & Stefani (2021b) © 2021 (with the permission of IOP Publishing).

are opposite) and small nutation angle. The impact of the angle is not a trivial topic: while in the analytical theory both the linear (Liao & Zhang, 2012, Gans, 1970) and the weakly nonlinear cases (Meunier *et al.*, 2008, Gao *et al.*, 2021) tend to unify the precession ratio with the nutation angle forming a general forcing parameter. However in the strong forcing regime the scenario may be more subtle than that. In fact, as shown by Lopez & Marques (2016), the sole change of α causes completely different flow responses which are not predictable a priori. Consistently with these findings, experimental works have observed very different phenomena for different values of α: at low nutation angles the flow tends to undergo small-scale instabilities and a complex pathway to turbulence, such as the resonant collapse (Manasseh (1992)). Instead at large nutation angle large-scale structures occur together with more clear transitions dominated by geostrophic columnar vortices (Kong *et al.* (2015), Jiang *et al.* (2014), Pizzi *et al.* (2021a)).
So far, most studies of fluid-filled precessing cylinders, focused on the impact of Reynolds number and/or precession ratio, were carried out for small nutation angles. While for cylindrical geometry the prograde precession (i.e. when the projection of the container and the turntable rotation have the same sign) (Meunier *et al.* (2008), Kong *et al.* (2015), Jiang *et al.* (2014), Manasseh (1992)) and retrograde (Albrecht *et al.* (2021), Marques & Lopez (2015), Lopez & Marques (2018)) precession were investigated separately, a direct comparison between these two motions is still elusive. The present numerical investigation aims at assessing the role of prograde and/or retrograde motion for comparably large nutation angles for the future large scale precession experiment in frame of the DRESDYN project. In particular, we will extend the work of Giesecke *et al.* (2018, 2019) where precession ratios for efficient dynamo action were studied only for perpendicular nutation angle, by identifying the most promising parameters in terms of nutation angle and prograde or retrograde precession. The main idea is that the optimum range is characterized by the emergence of axisymmetric large-scale rolls which resemble the $s2^{+}t1$ flow structure studied in a spherical kinematic dynamo model by Dudley & James (1989) and in a cylindrical model by Xu *et al.* (2008).

The rest of the chapter is organized as follows: in Section 4.2 is described the phase space investigated in the present Chapter. The Section 4.3 is dedicated to the comparison of analytical and numerical results for weak forcing. The results concerning the different flow responses for varying nutation angles and prograde and retrograde motion in terms of inertial modes and flow structures are presented in Section 4.4. The stability of the flow is analyzed in detail in Section 4.5, and the poloidal structures emerging for certain precession ratios are discussed in Section 4.6. All results of this Chapter are summarized, together with their implications, in Section 4.8.

4.2. Investigated parameters

The parameter space to be investigated in this Chapter is the following: the Reynolds number varies in the range $[5\times10^2, 10^4]$ and the Poincaré number in the range $\pm[10^{-3}, 3.5\times 10^{-1}]$. The nutation angles are $\alpha = 60^\circ$, $\alpha = 75^\circ$ (in Sec. 4.3 we show results also for some other angles), both for prograde and retrograde precession, and $\alpha = 90^\circ$ for which there is no difference between prograde and retrograde precession. The aspect ratio will be fixed at $\Gamma = 2$ which is quite close to the resonance point $\Gamma = 1.989$ of the first inertial mode with $(m, n, k) = (1, 1, 1)$. A summary of all simulations in the parameter space (Re, Po) will later be shown in the stability diagram of Fig. 4.7(a).

Although the simulations are performed in the turntable frame of reference, almost all results will be presented and discussed in the mantle frame in which the inertial and geostrophic modes are more intuitive (the only exception are the plots of the angular momentum and the Rayleigh criterion shown in Figs. 4.5, 4.7).

In this Chapter we make also use of the projection of the DNS flow field onto a basis given by inertial modes (discussed in 3.2).

4.3. Comparison with analytical theory at low forcing

We focus on the mode $(1, 1, 1)$ which represents a gyroscopic motion resulting from the tendency of the fluid flow to align the flow rotation with the precession axis. We should, however, point out that it is not the same behavior as for the Poincaré flow since in the cylinder the presence of the endcaps influences the fluid rotation axis not allowing a uniform vorticity solution. The mode $(1, 1, 1)$ belongs to the inertial wave group described in subsection 2.1.4. We investigate the flow behavior with respect to the nutation angle α for a range between $[30^\circ, 90^\circ]$ for prograde and retrograde cases. In Fig. 4.1(a) the axial velocity for the forced mode u_z^{11} is shown to increase in magnitude with α. For prograde motion it is always larger than for the corresponding retrograde motion. The dominance of the first radial wave number $n = 1$ is clearly visible since all profiles have the typical shape of the first order Bessel function (diamond-black curve) whose argument is the first root of the dispersion relation $\xi_{111} = 2.7346$ confirming that the $(1, 1, 1)$ mode is substantially dominant for low Po. Next, we analyze the behavior of the directly forced mode's amplitude in terms of magnitude and phase. Fig. 4.1(b) shows the phase $\psi = \arctan(\Im(A_{111})/\Re(A_{111}))$ vs α for two different Reynolds numbers. The increase in the nutation angle provokes a phase shift quite pronounced for the prograde profiles (blue and green curve) while the retrograde profiles are much flatter indicating minor changes in the orientation of the flow structure. This features seem to be rather independent of Re. Then, we focus on the amplitude defining the scaled value as $a_{111} = |A_{111}|/(\sqrt{Re}|Po|\sin\alpha)$ and compare them with the analytical viscous solution close to resonance (Liao & Zhang (2012)). In Fig. 4.1(c) the results are shown: our numerical results have smaller values than the analytical viscous theory. Only the prograde case for $Re = 3500$ is close and parallel to the analytical model for $\alpha < 30°$. The reason for this quantitative discrepancy is due to the fact that our results are beyond the limit of validity for the analytical model, i.e $\epsilon \sin\alpha < O(1)$.

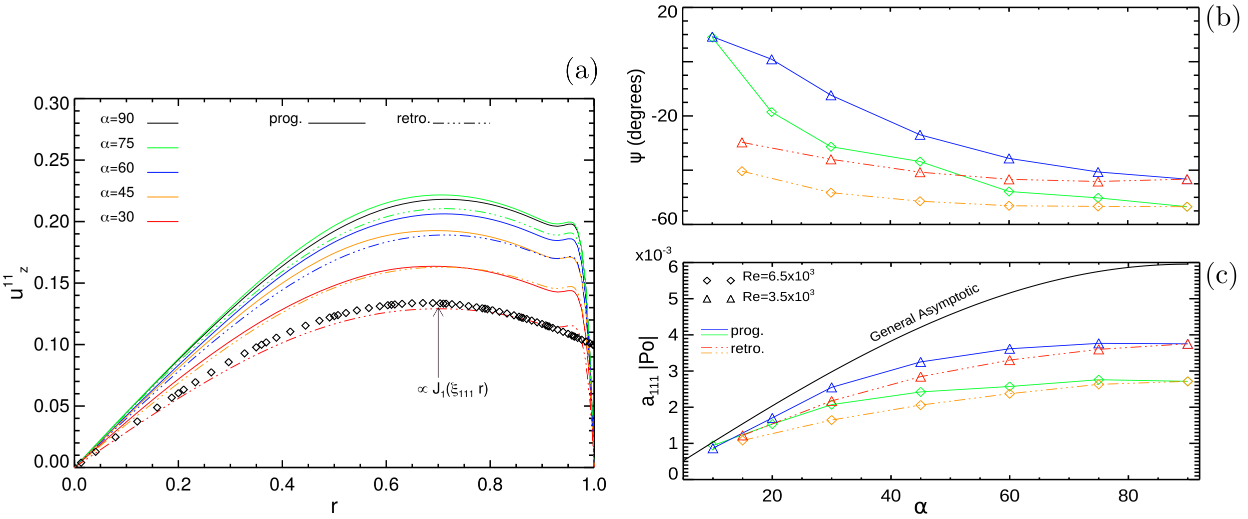

Figure 4.1. Analysis of the directly forced mode $(1, 1, 1)$. (a) Plot at $z = 0$ of the radial profile of axial velocity u_z^{11} for $Re = 6500$, $Po = 0.010$ and several nutation angles. Black diamond curve shows the Bessel function profile for the first radial wave number. (b) Plot of the phase of $(1, 1, 1)$ mode vs. nutation angle for two Reynolds numbers (symbols). (c) Comparison between the general asymptotic theory by Liao & Zhang (2012) with our numerical results as a function of the nutation angle.

The final result of this Section is presented in Fig. 4.2 where the scaled amplitude $a_{111} = A_{111}/(\sqrt{Re}Po\sin(\alpha))$ of the directly forced mode is plotted as a function of the aspect ratio Γ. The dotted horizontal line represents the amplitude calculated by using the simplified model of Gans (1970); the dashed line shows the inviscid theory which diverges at of the first resonant aspect ratio $\Gamma = 1.989$. Finally the blue line shows the linear asymptotic model by Liao & Zhang (2012). As we can observe our simulations (diamonds) agree well with the analytical model for small nutation angle, while they show a growing difference when increasing α. Since the simulated cases are for a fixed precession ratio, $Po = 0.1$, and $Re = 3500$ (orange diamonds) and $Re = 6500$ (green diamonds), this result shows that it is the nutation angle that causes the deviation from the linear model.

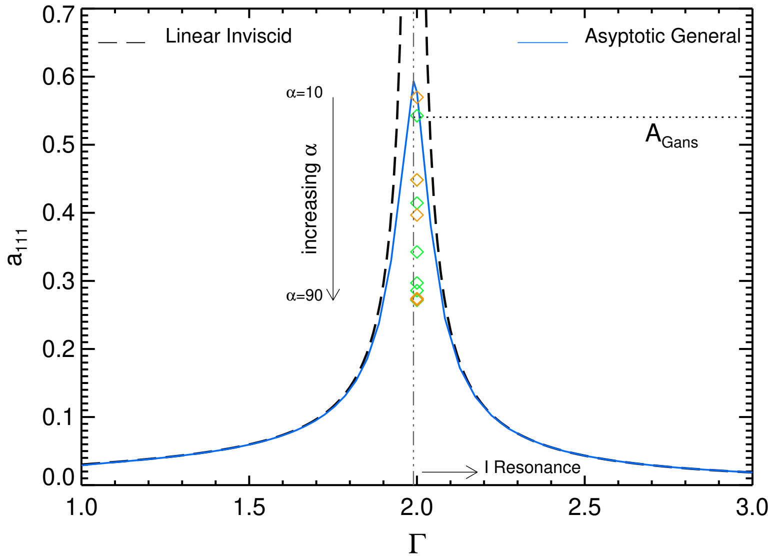

Figure 4.2. Comparison between DNS and analytical theory of the scaled directly forced mode amplitude a_{111}.

4.4. Impact of precession on the base flow

It is well-known that a precession-driven flow in cylindrical geometry changes with increasing forcing due to the emergence of an axisymmetric azimuthal flow and the related modification of the non-axisymmetric poloidal flow (Meunier *et al.*, 2008, Kong *et al.*, 2014, 2015, Jiang *et al.*, 2014). Here we focus on the specific influence of the nutation angle on this behavior.

In Fig. 4.3, we show the time-averaged axial velocity u_z which is a good representative of the base state. The three selected configurations $\alpha = 60°(p)$, $\alpha = 90°$ and $\alpha = 60°(r)$, as examples for prograde, perpendicular and retrograde precession, respond in different ways to the increase of the precession ratio Po. Only the prograde and the perpendicular cases show a reduction of the axial flow to negligible values inside the bulk region whose extension increases with the precession ratio. By contrast, the retrograde case (bottom row) remains essentially unchanged in magnitude and shape, but with counterclockwise phase shift from low to large Po.

For the smallest precession ratio $Po = 0.010$ (left column) the 3 configurations appear very similar. The flow magnitude is quite weak and the three-dimensional structures (indicated by the ± 0.15 levels) are symmetrical with respect to φ (the shape for $\alpha = 90°$ is a little more elongated). The plots for $Po = 0.100$ (central column) prove that in the bulk u_z vanishes at lower Po for prograde precession. Finally, at $Po = 0.200$, u_z is confined close to the sidewall for $\alpha = 60°(p)$ and $\alpha = 90°$, with this region being thinner for the latter case.

In order to quantify the flow response, we investigate the energy densities of the main inertial modes in dependence on the precession ratio. We define the energy densities of the geostrophic-axisymmetric, the directly forced mode and the solid body rotation energy (as reference) as follows:

$$e_{00} = \frac{1}{2V}\sum_{n} |A_{00n}|^2 \ , \quad e_{11} = \frac{1}{2V}\sum_{n} \frac{|A_{11n}|^2}{2} \ , \quad e_{sbr} = \frac{1}{2V}\int_V (\Omega_c r)^2 \, dV \ . \tag{4.1}$$

The energies for the axisymmetric-poloidal structures are:

$$e_{02} = \frac{1}{2V}\sum_{n} (\Im A_{02n})^2 \ , \quad e_{0k} = \frac{1}{2V}\sum_{n} (\Im A_{0kn})^2 \ , \tag{4.2}$$

with $\Im$ denoting the imaginary part (see subsection 2.1.4 for descriptions of this type of inertial modes which are called axisymmetric oscillations (Liao & Zhang, 2012, Zhang & Liao, 2017)).

Figure 4.4 shows the energies as defined in Eqs. (4.1) and (4.2) versus the precession ratio Po. The differences between different nutation angles (and prograde/retrograde precession) become stronger with increasing Po. The prograde and $\alpha = 90°$ cases display an abrupt transition from a state with low energy in the geostrophic axisymmetric mode (low state) to a state with high energy (high state). The retrograde cases (orange and red curves) reveal a much smoother increase of e_{00} whose final level is lower than for the prograde counterparts (Fig. 4.4(a)). While in the low state region (for $Po < 0.075$) the prograde curves are almost overlapping, from the transition onward to the maximum precession ratio they diverge, e.g., the blue and green curves ($\alpha = 60°$ and $\alpha = 75°$) show the jump at lower Po with the saturated levels differing by approximately 10%. Interestingly, the linear increase of the $\alpha = 90°$ case in the strong precession regime indicates the growth of the geostrophic azimuthal circulation which illustrates why the axial velocity contour (in Fig. 4.3) is so thin and concentrated close to the sidewall boundary for $Po = 0.200$. This is consistent with the outcome of Kong *et al.* (2015) who found that the larger the nutation angle the larger the bulk region that is occupied by the geostrophic-axisymmetric flow. The behavior of the forced mode energy e_{11} is closely related to that of e_{00}. In Fig. 4.4(b) the prograde curves increase until $Po \approx 0.08$ followed by a sharp breakdown of more than 60%. We notice two particular aspects: (i) the breakdown occurs at the same Po as does the jump of e_{00}; (ii) the smaller the angle the earlier the transition occurs. After the breakdown the curves for $\alpha = 60°, 75°$ remain flat, while the curve for $\alpha = 90°$ continues to decrease. In accordance with the linear increase of e_{00} as discussed above, the two retrograde curves do not show any sharp transition.

Closely related to the breakdown of e_{11} for the prograde and perpendicular cases, and the weaker decrease of e_{11} for the retrograde case, we observe energy peaks for the poloidal modes. Fig. 4.4(c) shows $e_{02} = f(Po)$ which is the energy associated with the axisymmetric vortex structure in the cylinder's meridional semi-plane (see also Fig. 4.8). The nutation angle and the prograde or retrograde configuration are decisive in this respect. The largest value of e_{02}, as found for the case $\alpha = 75°$ (r), is almost 50% larger than for $\alpha = 90°$ (and more than double than those of the other cases). It has a maximum around $Po = 0.130$ with a remarkably wide range of $\Delta\, Po \approx 0.020$. By contrast, the $\alpha = 60°$ (r) case (orange curve) shows the smallest magnitude whose maximum values are situated at still larger values of Po. Quite generally, the peaks for the retrograde profiles are shifted to larger precession ratios compared to the prograde ones. The prograde and perpendicular precession show curves with similar values for $Po < 0.090$ but while $\alpha = 90°$ has a clear peak followed by a steep decrease, the other cases remain at non-negligible level of e_{02}. Similar features are shown by the complementary part of the poloidal energy $\sum_{k\neq 2} e_{0k}$, Fig. 4.4(d), where $\alpha = 90°$ and $\alpha = 75°$ retrograde have the peak at the same Po as e_{02}. If we sum up the energies contained in the inertial modes considered in Fig. 4.4 we obtain that, for prograde and perpendicular precession, their summation contributes more than 90% of the total energy of the flow, whereas the summation for the retrograde cases stays around 60%. This fact indicates that the prograde precession is essentially characterized by these inertial modes while the retrograde cases are characterized by a more complex flow structure. However, other contributions of inertial modes are outside the scope of the present work because they are seemed less relevant for possible dynamo action.

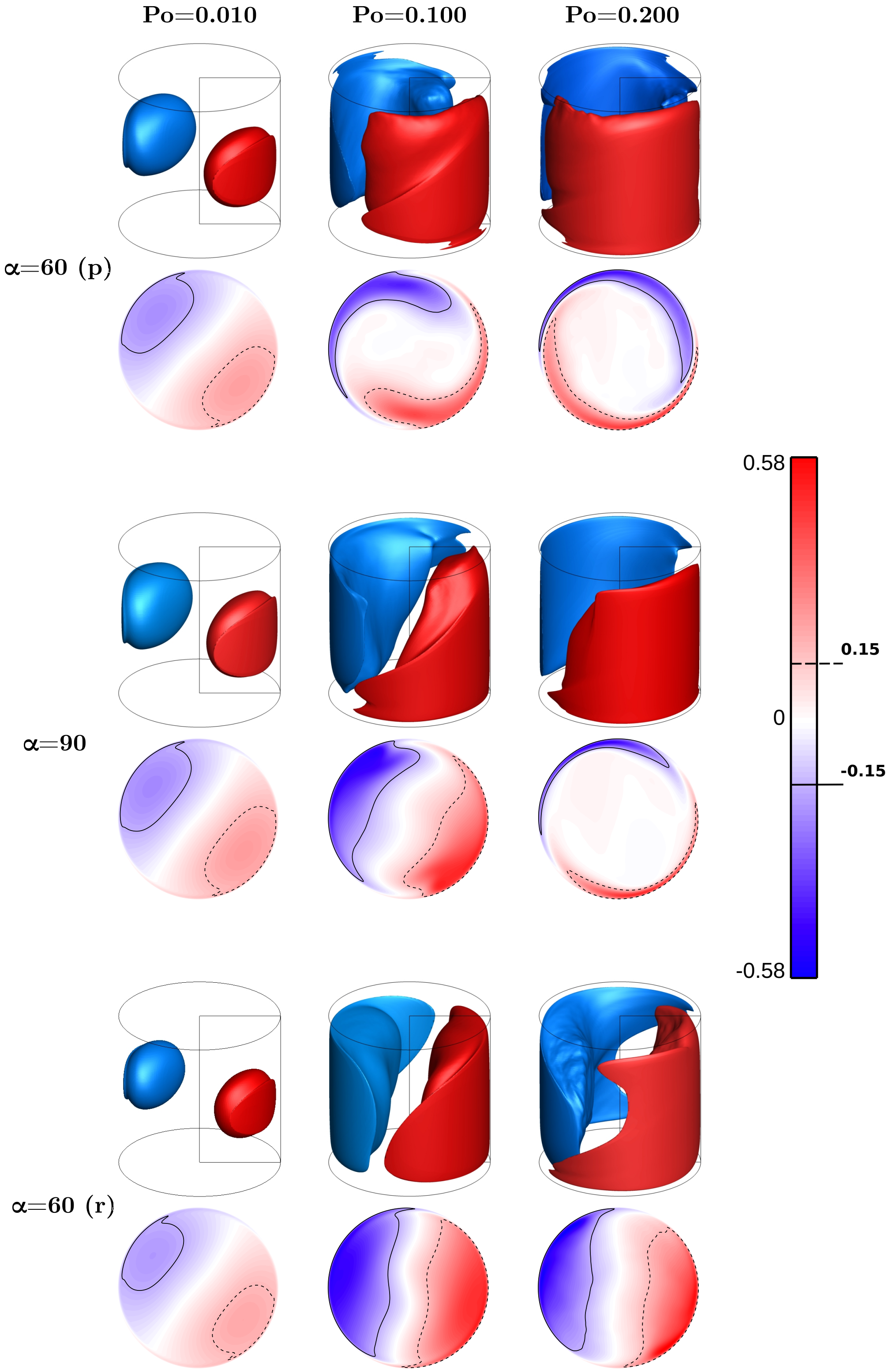

Figure 4.3. Flow structures for prograde, perpendicular and retrograde precession. 3d isosurfaces and 2d contours (at $z = 0$) of the time averaged axial velocity u_z for $Re = 6500$ and three representative precession ratios $Po = 0.010$, $Po = 0.100$, $Po = 0.200$ (from left to right). From top to bottom: prograde $\alpha = 60°(p)$; perpendicular $\alpha = 90°$; retrograde $\alpha = 60°(r)$. In the equatorial 2d polar plane 100 equispaced levels are shown; the isosurfaces are drawn at levels ± 0.15, and the meridional semiplanes of cylinder frame represent $\varphi = 0$.

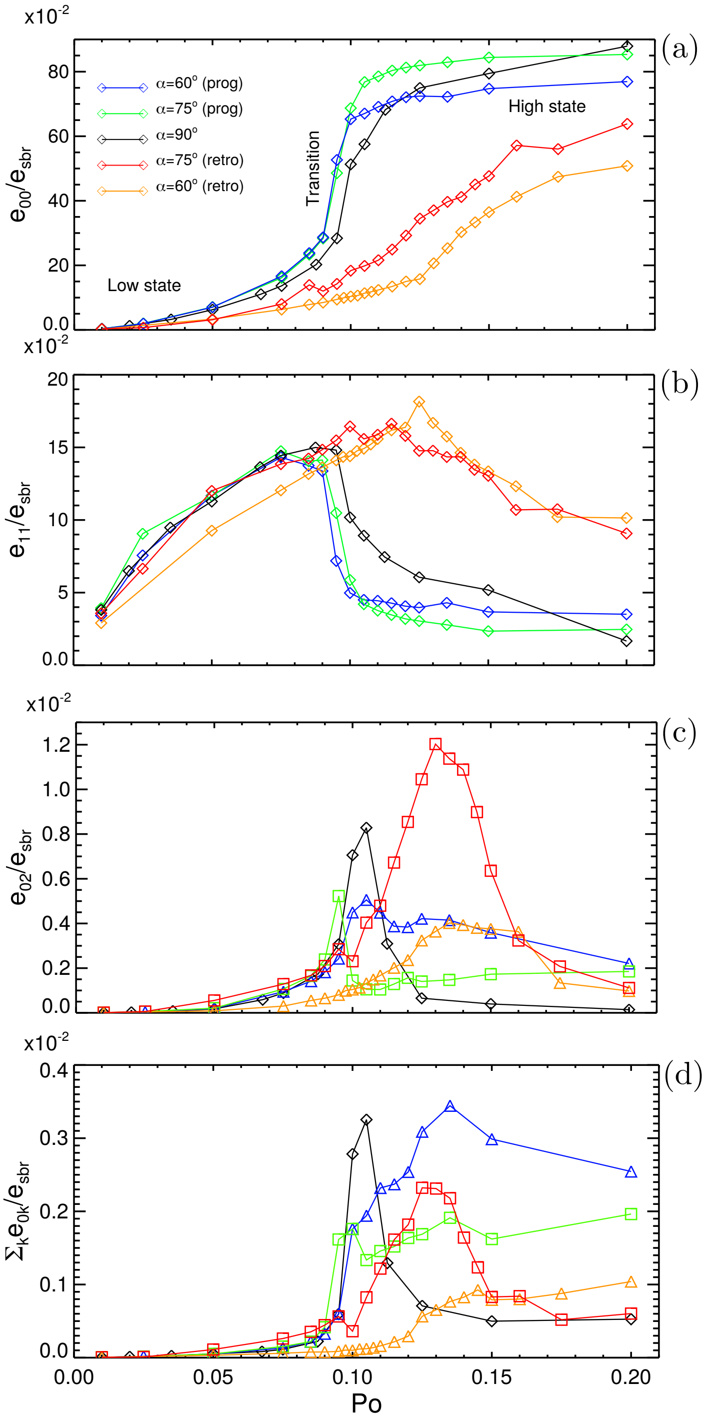

Figure 4.4. Energy content of various inertial modes versus precession ratio *Po* for different nutation angles. (a) geostrophic-axisymmetric energy e_{00}; (b) energy contained in the directly forced mode e_{11}; (c) axisymmetric poloidal energy e_{02} for the second axial wave number; (d) remaining part of the axisymmetric poloidal energy with $k \neq 2$. The energies are scaled by the solid body energy e_{sbr}, all quantities are defined in Eqs. (4.1) and (4.2).

4.5. Role of the centrifugal instability and the breakdown of the directly forced mode

We have shown that for the prograde and perpendicular cases three main regimes can be identified: (*i*) a low state dominated by the forced $m = 1$ Kelvin mode, (*ii*) a transition region and (*iii*) a high state dominated by an axisymmetric-geostrophic flow. The increase of the axisymmetric-geostrophic mode results in the dominance of an azimuthal circulation and the near-absence of axial flow in the bulk region as shown in Fig. 4.3. The strong azimuthal rotation is opposed to the container rotation leading to the braking of the original solid body rotation and, for large enough precession ratio, possibly to a centrifugally unstable flow. This topic will be our next focus.

As a common discriminant to evaluate the hydrodynamic stability of rotating flows the centrifugal stability criterion, or Rayleigh criterion, defined as

$$\frac{\partial (L)^2}{\partial r} > 0 \quad \text{with} \quad L = r\, u_\varphi^{tt} \,, \tag{4.3}$$

is employed. In Eq. (4.3), L is the angular momentum and $u_\varphi^{tt} = u_\varphi + \Omega_c r$ denotes the azimuthal velocity in the turntable reference frame. Strictly speaking this criterion holds only for purely rotational shear flows. Nevertheless, the application in the present case is supported by the prevalently azimuthal nature of the flow once the high state is achieved, and is also consistent with the description of the experimental observations by Kobine (1996).

The radial profile of the angular momentum and the radial derivative of L^2, averaged both in azimuthal and axial direction, are shown in Fig. 4.5. The left column of Fig. 4.5(a1-e1) shows the impact of the precession ratio on L. With increasing Po the flow deviates more and more from the solid body rotation (SBR) profile, eventually developing rather flat profiles in the bulk region (for $r < 0.8$, say). For prograde precession and $\alpha = 90°$, at large enough Po the angular momentum becomes negative, indicating that in this region the flow rotates opposite to the container. For large Po the deviation from SBR goes along with an emergence of a steep velocity gradient between $0.90 < r < 1.0$, owing to a marked sidewall boundary layer (Pizzi *et al.* (2021a)). The retrograde cases do not show any negative L for $Po \leq 0.20$.

The right column, Fig. 4.5 (a2-e2), shows the radial derivative of L^2. For prograde precession and $\alpha = 90°$, at large enough Po the slope of L^2 becomes negative indicating a centrifugally unstable flow. We find that for $\alpha = 60°$ (p) and $\alpha = 75°$ (p) the violation of Rayleigh's criterion occurs at $Po \approx 0.100$ (green curve in (a2) and (b2)) while for $\alpha = 90°$ the flow becomes unstable above $Po \approx 0.125$ developing a marked 'nose' shape with a positive peak at $r \approx 0.8$ and negative peak at $r \approx 0.9$.

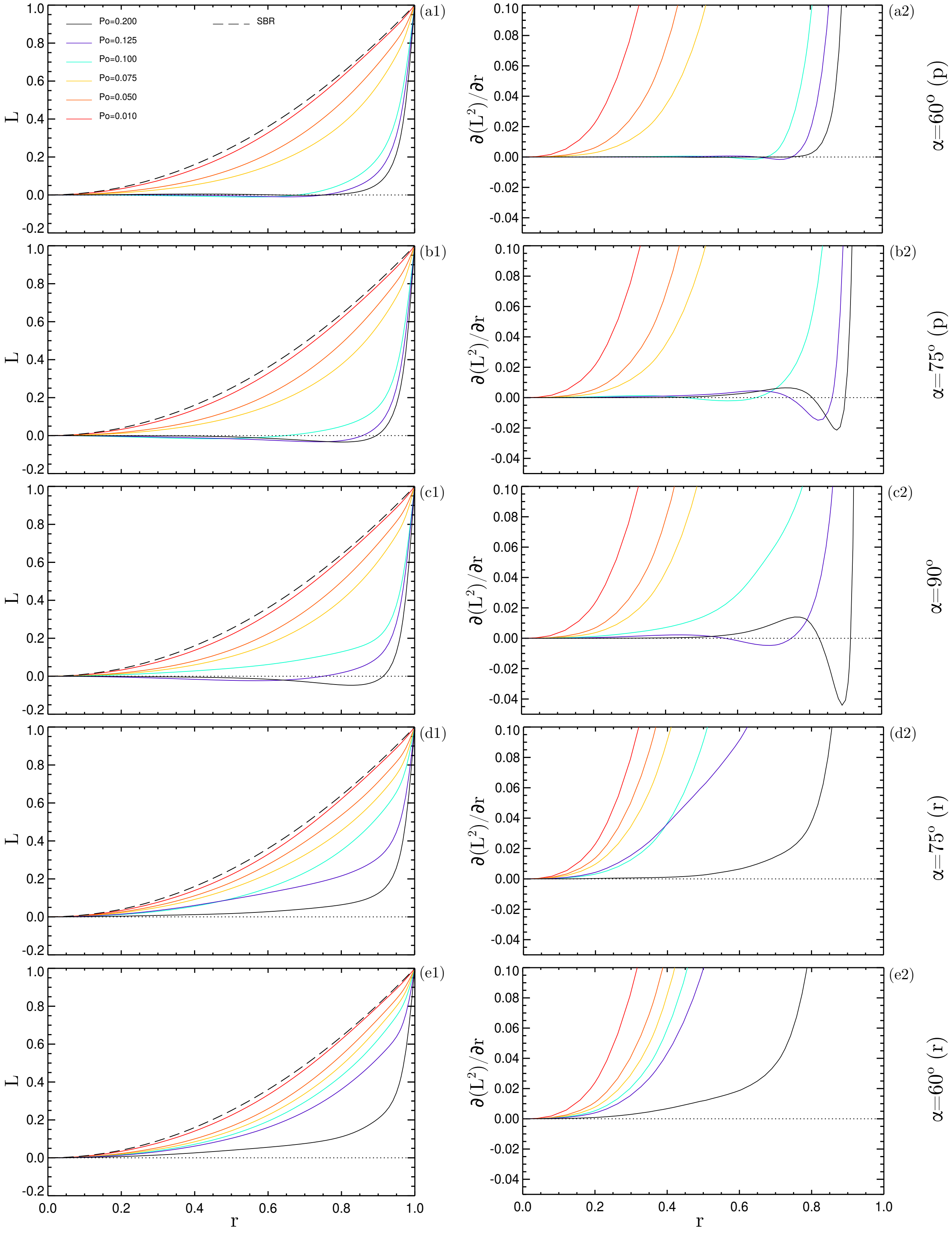

Figure 4.5. Left: radial distribution of the angular momentum for $Re = 6500$ and several configurations (a1-e1). Right: radial derivative of L^2, showing the violation of the Rayleigh's criterion for the prograde and perpendicular cases (a2-e2).

Up to this point, the analysis has been carried out for $Re = 6500$; next our goal is to extend the range to other Reynolds numbers. We begin with the study of the breakdown of the directly forced mode. In Fig. 4.6 we show the energy contained in the $(m, k) = (1, 1)$ mode as a function of Po for several Reynolds numbers. It is straightforward noticing that the steep decrease in the energy does not occur for the smallest Reynolds, i.e. $Re = 500$ and $Re = 1000$.

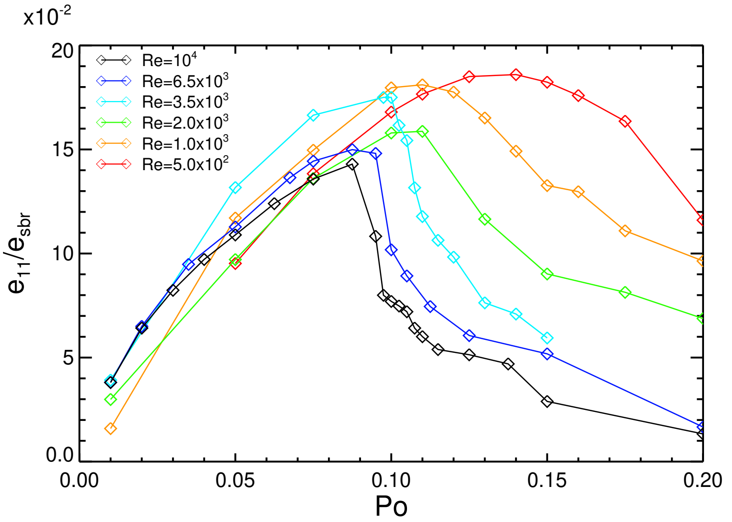

Figure 4.6. Behavior of the directly forced energy e_{11} for different Reynolds numbers and $\alpha = 90°$. Notice that the breakdown is clearly expressed only for the largest Reynolds number curves.

In Fig. 4.7, we present regime diagrams for the instabilities described so far, i.e. the breakdown of the directly forced mode and the violation of Rayleigh's criterion. Figure 4.7(a) shows the parameter space (Po, Re) that includes all cases treated in our numerical simulations. The flow is defined as stable (black symbols) or unstable (red symbols) according to the Rayleigh criterion (4.3). From the preponderance of the red symbols in the upper half plane, it is obvious that the prograde motion is substantially more prone to become unstable. It is noteworthy that in order to find an unstable flow for retrograde motion we must achieve more than twice the precession ratio of the prograde counterpart, e.g the first unstable solution at $Re = 6500$ for $\alpha = 75°$ (r) is found at $Po = 0.250$ while for prograde it is at $Po = 0.100$ (see zoom plot). This discrepancy is even more pronounced for the case $\alpha = 60°$ where no centrifugal instability is found at all for retrograde precession. In the zoom panel of Fig. 4.7(a), we observe that for the prograde cases the unstable points appear at smaller Po for smaller α, (see for instance at $Re = 6500$ and $Re = 10000$ the asterisks for $\alpha = 60°$ and the triangles $\alpha = 90°$).

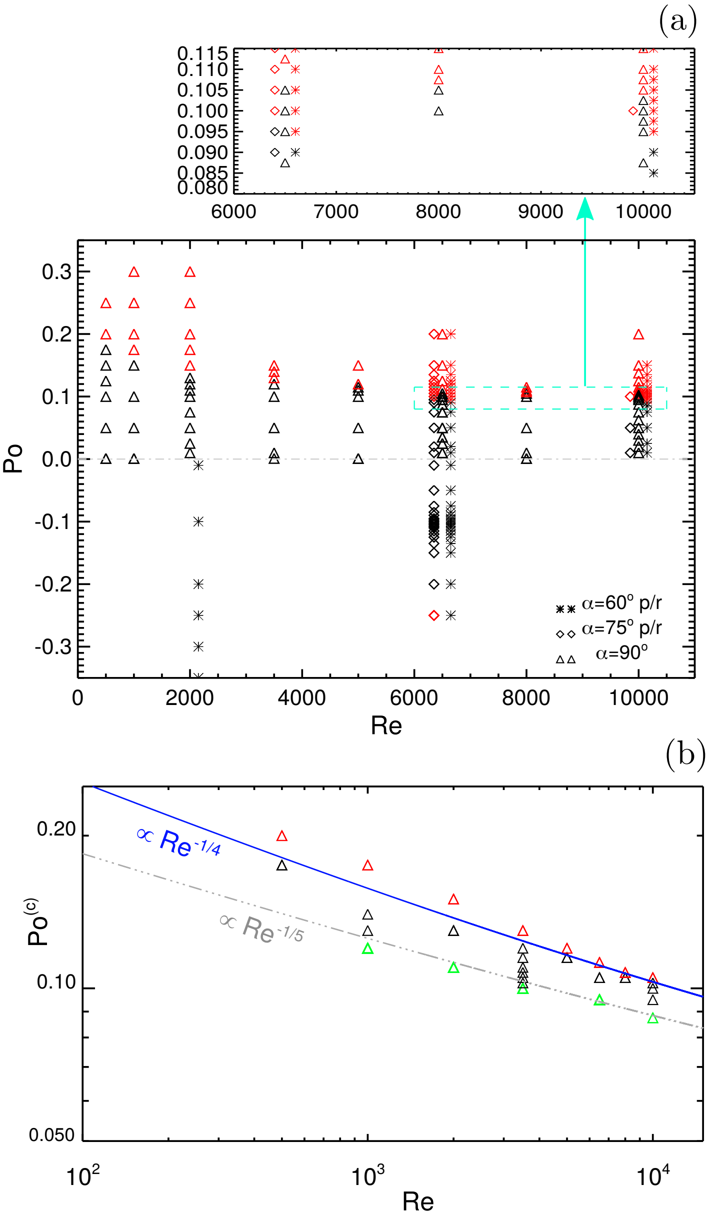

Figure 4.7. Regime diagram in the (Po, Re) space with respect to the centrifugal stability. (a) Plane showing all the simulations performed for prograde ($Po > 0$) and retrograde ($Po < 0$) precession at three different nutation angles (195 simulations). Black and red symbols represent stable and unstable solutions in the sense of Rayleigh's criterion (Eq. 4.3). The zoom plot shows a focus on larger Re to underline the impact of α for the occurrence of instability. (b) Diagram for $\alpha = 90°$. Green symbols are the stable solutions, black symbols represent the solutions already gone through the breakdown of the directly forced mode but yet centrifugally stable and red symbols denote the centrifugal unstable solutions. The grey dashed-dotted line marks the critical precession ratio $Po^{(c1)}$ for the breakdown of the $(1, 1)$ mode and the blue solid line shows the critical threshold $Po^{(c2)}$ for the violation of the Rayleigh criterion.

However, we do not find a systematic dependence of the critical precession ratio for the onset of the instability with respect to α. In particular it is not possible to unify the precession ratio and the nutation angle into a general forcing parameter $Po \sin\alpha$.

Figure 4.7(b) focuses on the case $\alpha = 90°$ for which we have simulations for several Reynolds numbers. In addition to the violation of Rayleigh's criterion we illustrate also the breakdown of the energy of the directly forced mode. For the sake of clarity we show only the last stable point where e_{11} is maximum (green symbols), the points included between the two stability curves (black symbols), and then the first centrifugally unstable point (red symbols). The grey dashed-dotted curve marks the derived scaling law for the breakdown of e_{11} whose expression is $Po^{(c1)} = 0.025 + 0.40\, Re^{-1/5}$. Note the absence of points for $Re = 500$ since this Reynolds number does not show a clear breakdown of e_{11} (see Fig. 4.6). The blue curve is the fit marking the scaling for the critical threshold, $Po^{(c2)} = 0.033 + 0.7\, Re^{-1/4}$, above which the flow is centrifugally unstable. This kind of scaling law is reminiscent of the instability threshold found by Lin *et al.* (2014) for the regime of strongly non-linear flow in a precessing cylindrical annulus.

We should remark that the parameter space studied is quite limited in terms of Reynolds numbers, therefore any extrapolation for geophysical phenomena and the DRESDYN experiment should be taken with a grain of salt. Formally, the above scaling expressions for $Po^{(c1)}$ and $Po^{(c2)}$ would cross around $Re \sim 10^{11}$, but the applicability for such large Reynolds numbers is questionable. Comparing these results with Fig. 4.4(a), we see that, for the prograde cases, the centrifugal instability appears close to the value of Po where e_{00} achieves the high state. We conclude that the emergence of the axisymmetric-geostrophic flow (essentially an azimuthal flow which counteracts the solid body rotation) is responsible for the decrease of the angular momentum L and consequently its negative radial derivative (i.e violation of Rayleigh criterion). If this is the case our results indicate a hierarchical relation between the centrifugal instability and the secondary-geostrophic instability theory proposed by Kerswell (1999) whose occurrence would scale $\propto Re^{-1/4}$.

4.6. Poloidal flow field: promising flow structures for dynamo action

In this section we focus our attention on the poloidal flow structure whose energy was plotted in Fig. 4.4(c) and Fig. 4.4(d). The interest in this particular kind of inertial modes is mainly related to their suitability for dynamo action in a precessing cylinder, as discussed in Giesecke *et al.* (2018, 2019).

Figure 4.8 shows the poloidal flow structure for various nutation angles, taken at the respective values of Po where the energy density e_{02} is maximum (see Fig. 4.4(c)). The vector field comprises the azimuthally averaged radial and axial velocities $[u_z, u_r]^{m=0}$, while the color scale represents the magnitude of the azimuthal vorticity (again azimuthally averaged) which is a measure of the rotatory behavior of $[u_r, u_z]$ in the meridional half plane:

$$(\boldsymbol{\omega} \cdot \widehat{\boldsymbol{\varphi}})^{m=0} = \omega_{\varphi}^{m=0} = \frac{1}{2\pi} \int_{\varphi} \left(\frac{\partial u_r}{\partial z} - \frac{\partial u_z}{\partial r} \right) d\varphi \,. \tag{4.4}$$

The nutation angle plays a major role both for the topology and the magnitude of the poloidal flow field. Remarkably, the prograde case with $\alpha = 60°$ (Fig. 4.8(a)) shows an opposite orientation of the double rolls compared to those in the other cases and includes smaller vortices in the corners. The colors illustrate how the azimuthal vorticity is distributed in the plane, including zones characterized by an alternation of signs. The strength and the extension of the larger rolls present an increase from $\alpha = 75°$ (p) to $\alpha = 90°$, finally achieving a maximum at $\alpha = 75°$ (r). The case $\alpha = 60°$ (r), Fig. 4.8(e), shows the weakest and smallest vortices which additionally are centered more towards the corners. This behavior is in accordance with the maximum level of e_{02} shown in Fig. 4.4(c).

In order to have a direct quantitative comparison, we plot also the axial velocity $u_z^{m=0}$ at $r = 0.5$ and the radial velocity profile $u_r^{m=0}$ at the equator $z = 0$, in Fig. 4.8(f) and Fig. 4.8(g), respectively. Again, the largest values are achieved for $\alpha = 75°$ (r) (red dashed-dotted curve) both for radial and axial velocities, while $\alpha = 60°$ (r) is the weakest case. The case $\alpha = 60°$ (p) has opposite values with respect to all other cases, consistent with the inverse rotation of the vortices in the bulk.

4.7. Transient behavior of double and quadruple rolls

In the following, we will discuss the time dependence of the poloidal rolls. Specifically, we will work out the difference between $\alpha = 90°$ (double rolls) and $\alpha = 60°$ (p) (quadruple rolls), i.e the two paradigmatic cases of double and four vortices. We choose to present the amplitude since it is directly related to the velocity and we include also the dependence on the radial wave number because it is a useful characterization of the flow field's radial distribution in the half plane.
The two cases show different evolutions of the poloidal structure as we can see in Fig. 4.9 and Fig. 4.10 where snapshots of the instantaneous flow field at different time-steps are presented together with the corresponding amplitudes.

The case $\alpha = 90°$ (Fig. 4.9) exhibits a double-vortex structure that remains rather stable during the entire period showing only a little enlargement from $t = 38$ to $t = 145$. The vortex close to the top endwall has a counterclockwise direction associated with a positive azimuthal vorticity and the opposite direction for the bottom vortex. This behavior is also reflected in the flow amplitude. Indeed, the A_{021} component is dominant and always positive while the other ones are of minor importance.

The case $\alpha = 60°$(p) (Fig. 4.10) shows a much more complex evolution. The first part of the transient (panel 1) is characterized by a double vortex structure (green arrows) analogous to the case $\alpha = 90°$. The time $t = 38$ coincides with a local peak of A_{021}, which in the subsequent period decreases while A_{022} (red curve) increases till $t = 79$ when the original double rolls are confined in the corner and a radial inward flow appears around the equator (panel 2, purple arrows). The next step (panel 3) is characterized by the organization of vortical flow around $z \approx 0$ which evolves into a clockwise vortex, denoted by the purple arrow in the blue central region, followed by the formation of another roll of opposite rotation (panel 4). At $t = 90$ (blue dashed line in the amplitude plot) we observe the crossing of A_{021} and A_{022}, which is accompanied by the formation of 4 axisymmetric vortices. In the remaining time, the central vortices migrate towards the endwalls (panel 5): the large bottom roll has acquired the final extension and inclination while the top vortex is stretched. The last panel at $t = 145$ shows the final setup where the corner rolls and bulk rolls lie next to each other with opposite rotation in a sort of 'gear' interaction. The final level of $A_{021} < 0$ denotes an opposite rotation of the larger vortices with respect to the case $\alpha = 90°$ shown in Fig 4.9.

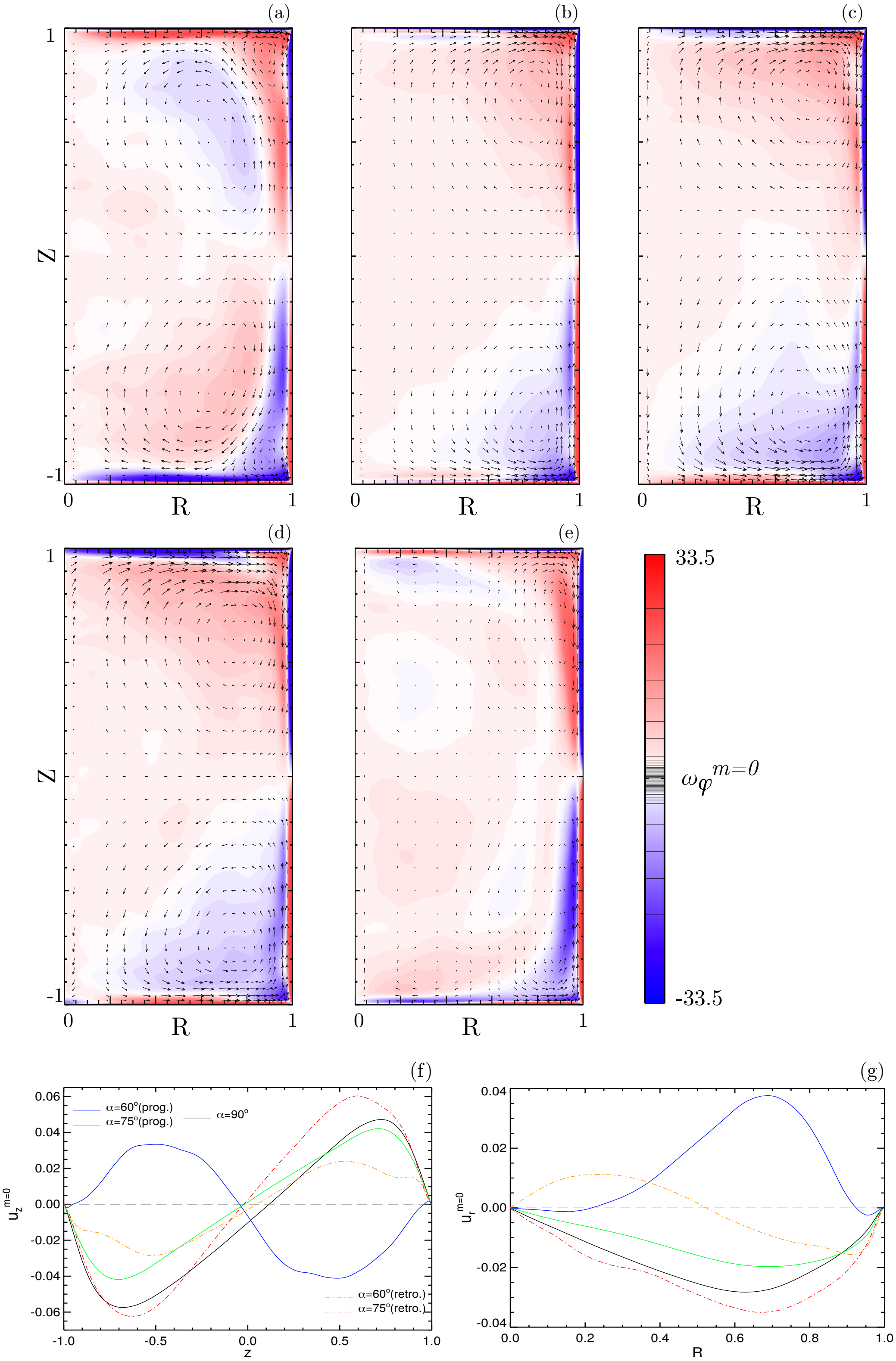

Figure 4.8. Dependence of the poloidal flow field on the nutation angle. Contours of the meridional semi-plane for $Re = 6500$ and five cases (corresponding to the maximum of e_{02} in Fig. 4.4(c)). Vector field for $[u_z, u_r]^{m=0}$ and color scheme for the azimuthal vorticity $\omega_\varphi^{m=0}$; the lines in the colorbar represent color-levels which are not uniform. (a) $\alpha = 60°$ (p), $Po = 0.105$; (b) $\alpha = 75°$ (p), $Po = 0.095$; (c) $\alpha = 90°$, $Po = 0.105$; (d) $\alpha = 75°$ (r), $Po = 0.130$; (e) $\alpha = 60°$ (r), $Po = 0.135$. (f) Velocity profiles for $u_z^{m=0}$ at $r = 0.5$ and (g) $u_r^{m=0}$ at $z = 0$.

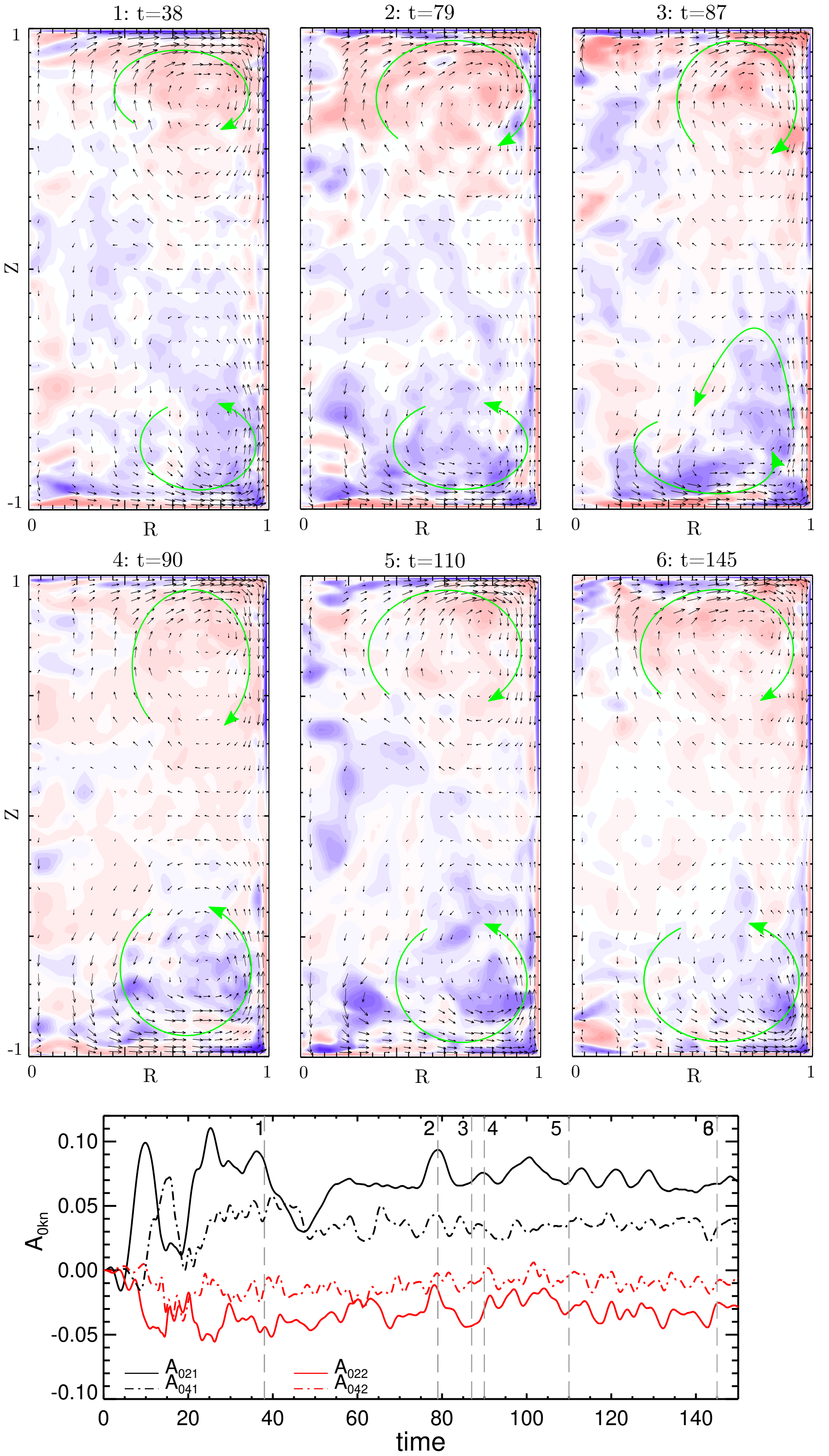

Figure 4.9. Time-evolution of double-roll topology and the amplitudes $A_{021,2}$ and $A_{041,2}$ for $\alpha = 90°$ and $Po = 0.105$. The various snapshots 1-6 represent the axisymmetric flows in correspondence with the grey dashed lines in the bottom plot. Vector field for $[u_z, u_r]^{m=0}$ and color scheme for the azimuthal vorticity $\omega_\varphi^{m=0}$.

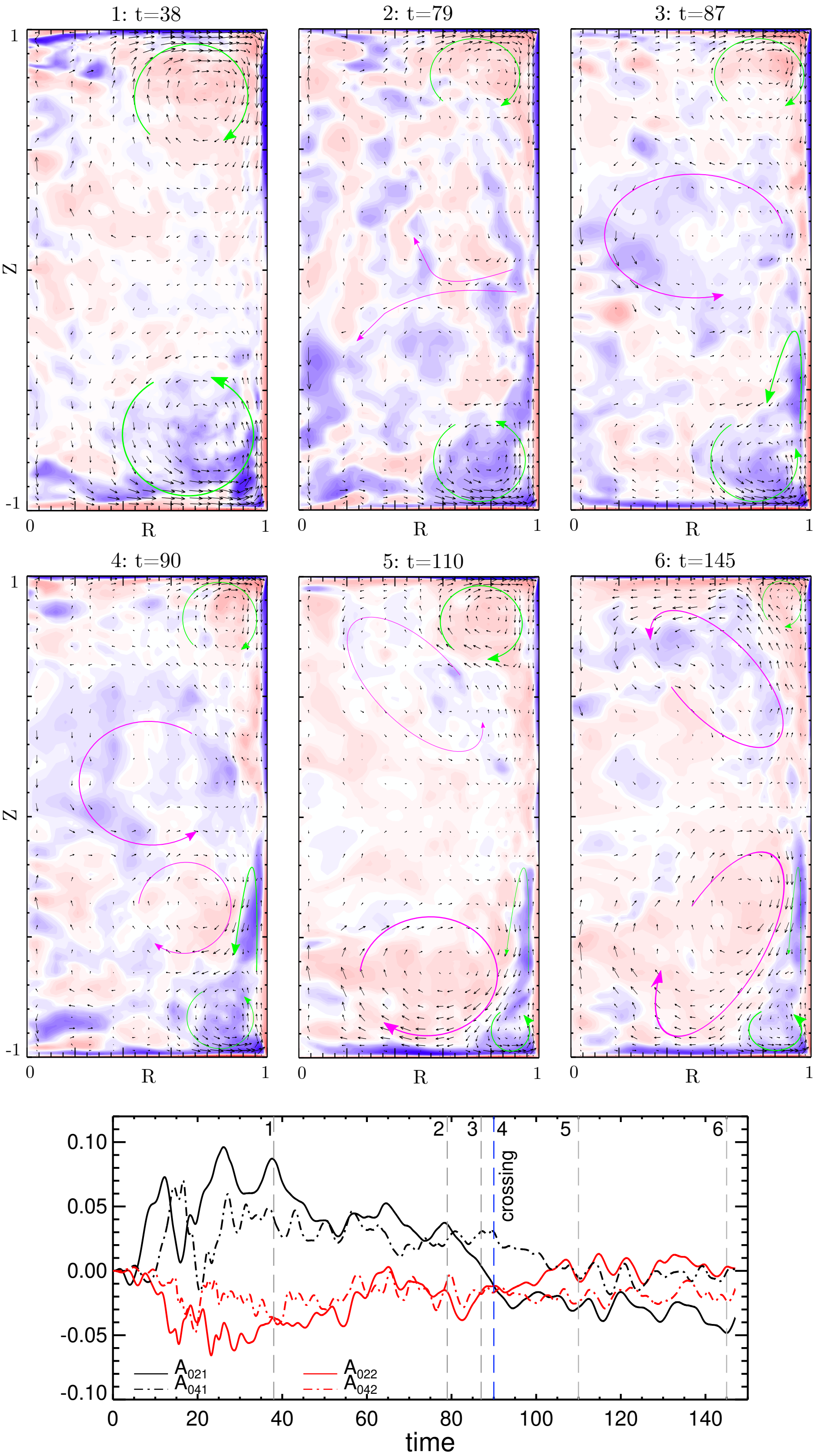

Figure 4.10. Time-evolution of quadruple-roll topology and the amplitudes $A_{021,2}$ and $A_{041,2}$ for $\alpha = 60°$(p) and $Po = 0.105$. $1-2-3$ are characterized by $A_{021} > 0$ (solid black curve) and $A_{041} < 0$ (solid red curve). Step 4 is the cross which causes the sign inversion and the emergence of the larger rolls inside the bulk. $5-6$ are the final state characterized by $A_{021} < 0$ and $A_{041} \approx 0$. Vector field for $[u_z, u_r]^{m=0}$ and color scheme for the azimuthal vorticity $\omega_{\varphi}^{m=0}$.

4.8. Summary

In this Chapter we numerically studied precession driven flows enclosed in a cylindrical geometry whose nutation angle varies between 60 and 90 degrees for prograde and retrograde precession. The two types of motion present significant differences: prograde precession shows sharp transitions between a laminar and a turbulent flow state with low and high geostrophic axisymmetric flow components. This transition is related with a centrifugal instability. By contrast, retrograde precession goes through a smooth transition between a low state and a high state. At the same time prograde and perpendicular precession show an abrupt breakdown of the flow directly excited by the forcing mechanism, which is not the case for retrograde motion. For every angle studied we observe the emergence of an axisymmetric poloidal flow which is promising for precession-driven dynamo action. This kind of flow structure resembles the Taylor vortices and they appear in a specific range of precession ratio which depends on the nutation angle.

Physical conjecture

The remarkable difference between prograde/perpendicular and retrograde precession for large forcing can be discussed in the mathematical formulation of the problem. In the turntable reference frame the rotation vector $\boldsymbol{\Omega}$ reads (Albrecht *et al.* (2021))

$$\boldsymbol{\Omega} = \underbrace{(\Omega_p \cos\alpha)\ \hat{\boldsymbol{z}}}_{background\ rotation} + \underbrace{|\Omega_p \sin\alpha|\ \hat{\boldsymbol{x}}}_{equatorial-plane\ component} \quad , \tag{4.5}$$

with $\hat{\boldsymbol{x}}$ being the equatorial coordinate, with the following specifications:

- for perpendicular precession $\rightarrow \boldsymbol{\Omega} = 0\hat{\boldsymbol{z}} + |\Omega_p|\ \hat{\boldsymbol{x}}$
- for prograde precession $\rightarrow \boldsymbol{\Omega} = (\Omega_p \cos\alpha)\ \hat{\boldsymbol{z}} + |\Omega_p \sin\alpha|\hat{\boldsymbol{x}}$
- for retrograde precession $\rightarrow \boldsymbol{\Omega} = (-\Omega_p \cos\alpha)\ \hat{\boldsymbol{z}} + |\Omega_p \sin\alpha|\hat{\boldsymbol{x}}$.

We can conclude that the combination of these two components are responsible for the difference in the flow structures (being the only difference in the Navier-Stokes equation): the equatorial component is sufficient to trigger the breakdown of the forced mode and the rising of the geostrophic zonal flow (perpendicular precession). However the background rotation can either amplify this effect if its sign is positive (prograde motion) or reduce the effect if it has a negative sign (retrograde motion).

The scenario which emerges from the present study is far from trivial. The flow field enclosed in a precessing cylinder evolves through several stages: the emergent geostrophic axisymmetric flow grows with Po modifying the distribution of the flow's angular momentum. Together with the increase of the geostrophic flow the breakdown/reduction of the directly forced mode occurs. Those two effect can be considered as the first kind of instability discussed in the present work. This process completes with the violation of Rayleigh's criterion, quite "easily" for prograde precession and hardly for retrograde. Before the onset of the centrifugal instability we observe a peak of the axisymmetric poloidal field. We argue that there is no direct cause-effect relation between the centrifugal instability and the poloidal flow, rather the rising of poloidal flow is attributed to the nonlinear self-interaction of the directly forced mode. Such a mechanism has been proposed by Waleffe (1989) and discussed in the nonlinear theory of Meunier *et al.* (2008). As shown in Fig. 4.11, the numerical results of this Chapter present good agreement with the experimental measurement conducted by Kumar *et al.* (2023).

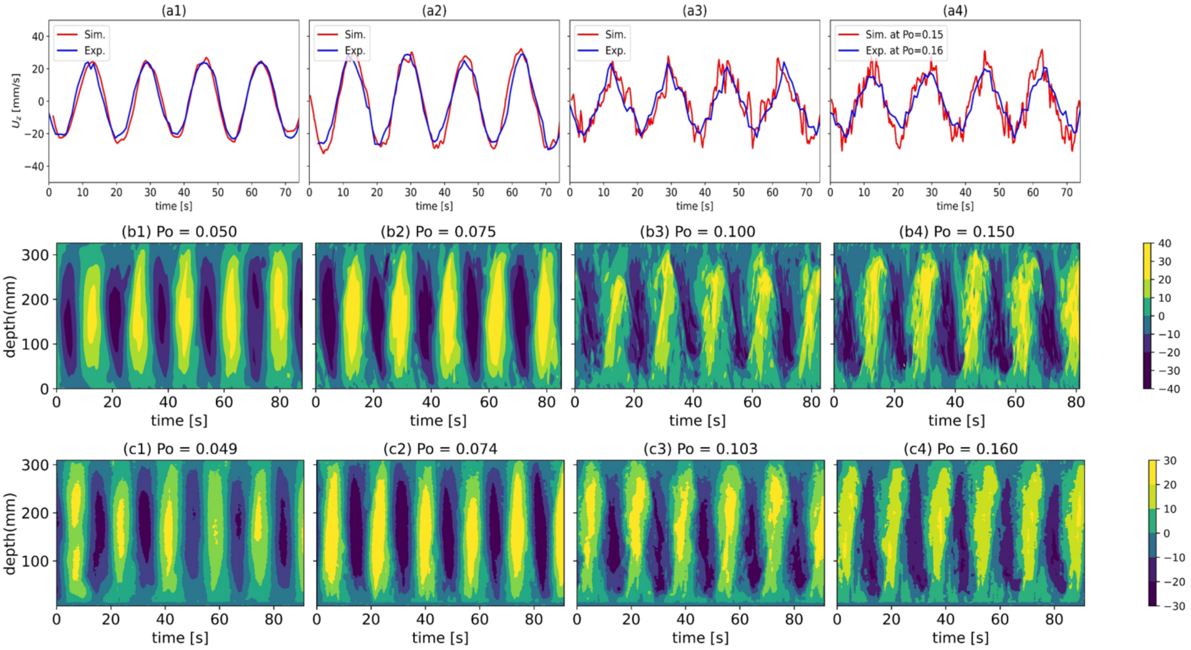

Figure 4.11. Comparison between simulations and experiments for $\alpha = 60°$, $Re = 10^4$ and different precession ratios (from Kumar *et al.* (2023)). First row shows the comparison of the axial velocity at radius $r = 0.92R$ and height $0.95H$. The other rows show the contours over time and depth of the axial velocity for different Po for simulations (b1 to b4) and experiments (c1 to c4).

5. Kinematic dynamo action in a precessing cylinder

> *Nel 1860 ebbi occasione di far costruire per conto del Gabinetto di Fisica Tecnologica dell'Universitá di Pisa un modelletto di macchina elettro-magnetica da me immaginata, e che ora mi risolvo a descrivere specialmente…*
>
> Antonio Pacinotti, Descrizione di una macchinetta elettro-magnetica

[1]In the previous Chapter 4 we have observed that precession driven flows can exhibit vigorous large scale components arising from instabilities or non-linearity effects. In this Chapter, we numerically investigate interactions between precession driven fluid flows and magnetic fields in a fluid filled cylinder whose aspect ratio is close to the first resonant one. Exploiting the hydrodynamic simulations from Chapter 4, we show precession driven dynamos in different forcing regimes. Since this represents the first step in elucidating the role of governing parameters for triggering the dynamo, our model is a rather simple. We do neither investigate the role of magnetic boundary conditions nor the back-reaction of the magnetic field on the flow due to the Lorentz force.

---

[1] The content of the present chapter comes from the journal publication *The effect of nutation angle on the flow inside a precessing cylinder and its dynamo action* by Kumar, Pizzi, Giesecke, Šimkanin, Gundrum, Ratajczak, & Stefani (2023) © 2022 (with the permission of AIP Publishing); and partly from *Numerical and theoretical framework for the DRESDYN precession dynamo experiment* by Pizzi, Giesecke, Šimkanin, Kumar, Gundrum, & Stefani (2022a) © 2022 (with the permission of Institute of Physics, University of Latvia).

5.1. Introduction

The possibility to achieve dynamo action through precession-driven motion of a fluid flow is an appealing scenario. In particular, precession represents a non-invasive way to drive the flow without using internal components such as blades or propellers. As already mentioned in the Introduction (1.1), in the last decades, with the improvements of the computer resources, the scientific community has observed precession-driven dynamos in simulations. One of the first complete studies was by Tilgner (2005) who found a dynamo in a spherical container for both laminar and turbulent flows at low Ekman number. A similar conclusion was drawn by Lin *et al.* (2016) who observed a dynamo in a full sphere for different forcing regimes proving that the magnetic field generation is due to the large scale vortices.

For cylindrical geometry the works of Nore *et al.* (2011) and Giesecke *et al.* (2018) are the keystone for the precession driven dynamo while for cube the works of Krauze (2010) and Goepfert & Tilgner (2016) are the references.

The basic approach for the numerical dynamo study is the *kinematic dynamo* approach, in which the flow velocity is prescribed and inserted in the induction equation (i.e the equation which describes the evolution of magnetic field, Eq. (2.35)). A more complicated approach is represented by *dynamically consistent dynamo models* in which the Navier-Stokes and the induction equation must be solved simultaneously and the back-reaction of Lorentz force on the flow is considered.

From a numerical point of view, in spherical geometry the MHD simulations are normally based on spectral schemes where the velocity and the magnetic field are decomposed into toroidal and poloidal components. Furthermore, the boundary conditions for the magnetic field can then be separately expressed for each degree and order of the spherical harmonics: this procedure allows to avoid the treatments of magnetic field in the exterior of the domain.

For other geometries, the implementation of magnetic boundary conditions is more complicated and several options have been chosen:

- Laplace equation method.
- Embedding method.
- BEM (Boundary Element Method).
- Integral equation method.

The Laplace method has been used, e.g., for the flow optimization of the Riga dynamo experiment (Stefani *et al.* (1997)). It consists in solving the Laplace equation for the external dynamo domain, then the results are matched with the interior solution (Gailitis *et al.* (2004), Guermond *et al.* (2003)). The drawback of this method is that it is numerically expensive.

The embedding model has been implemented for the simulations of Karlsruhe dynamo (Rädler *et al.* (2002)). The basic principle of this method is exploiting the simplicity of spherical domain for which the expansion in spherical harmonics for the boundary conditions can be used by embedding the real dynamo body inside an artificial sphere. The space between the very dynamo body and the external sphere is modeled as being filled by a medium with lower electrical conductivity than the internal of the dynamo region. Numerical convergence is then validated by decreasing the conductivity of the external medium.

The Boundary Element Method has been fully described and tested for instance in Iskakov *et al.* (2004) and by Giesecke *et al.* (2008) (coupled with a finite volume method). The main concept of this scheme is expressing the magnetic field outside the conducting region as the gradient of a scalar potential which is governed by the Laplace equation. The Laplace equation is integrated only on the boundary in the form of an algebraic set of equations by making use of the second Green's theorem.

So far we described the methods based on differential equations. However, some authors have shown the possibility to use the integral method. Roughly speaking this numerical scheme solves the Biot-Savart law in a self-consistent manner. For kinematic dynamo models, Xu *et al.* (2008) used a coupled system of equations (one for the magnetic field and the other one for the electrostatic potential) to solve the classical set up of spherical dynamo and the so called "matchbox", i.e. a rectangular box filled by electrically conducting fluid and surrounded by vacuum (Stefani *et al.* (2000)). The integral method is rather efficient allowing to achieve reasonable results with quite coarse mesh. Another positive aspect is the flexibility of this method since it is suitable for arbitrarily shaped domains.

In this work we will make use of most simple method, the pseudo-vacuum condition (known also as vertical field condition) which imposes vanishing tangential field at the wall allowing only the normal component to be non-zero.

5.2. Methodology

Here, we describe the procedure used in this thesis to approach the kinematic dynamo problem. Once the velocity field is computed (and achieves the statistically steady regime,

see for instance Fig. 3.2(a)) it is inserted into the induction equation. The time-averaged flow velocity used is characterized only by large scale structure, therefore any turbulent fluctuations are excluded. As mentioned above, the boundary condition are the *pseudo-vacuum* conditions where the tangential field components at the wall vanish.
The role of the boundary conditions are crucial for the accuracy of the model. Corresponding studies have been applied to the VKS dynamo (Ravelet *et al.* (2005), Stefani *et al.* (2006), Giesecke *et al.* (2012)), from which it is known that pseudo-vacuum boundary conditions lead to a lower threshold for the occurrence of a dynamo compared to more realistic insulator boundary conditions. For the models of the VKS dynamo, deviations in the order of 30% were found in Giesecke *et al.* (2008), and for the Riga dynamo simulations a deviation of 15% was found (Stefani, unpublished). So we should be aware that our results will show a lower threshold for the dynamo onset and further studies with more realistic boundary condition must be implemented in the future.

5.3. Results

In this section we present the results of the kinematic dynamo code applied to the flow fields as obtained in the previous section.

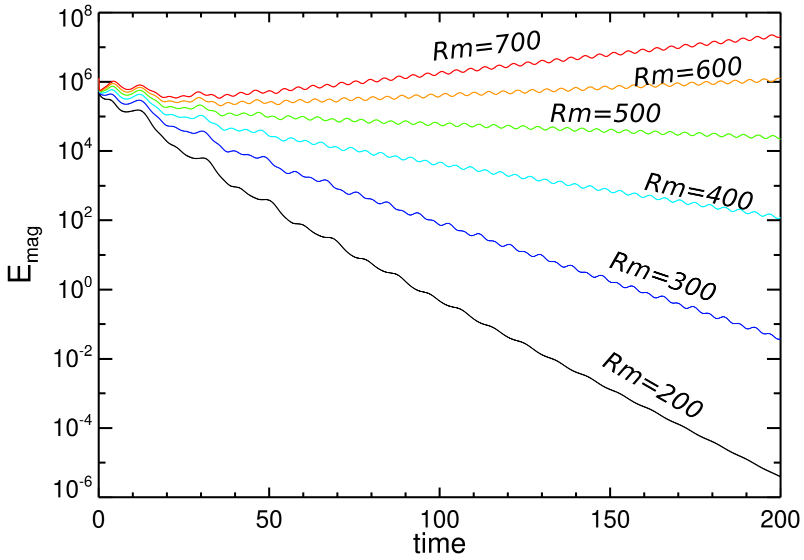

Figure 5.1. Time-evolution of the magnetic energy E_m for $Re = 6500$, $\alpha = 90°$ and $Po = 0.100$ for various magnetic Reynolds numbers Rm.

In order to clarify what we mean by "dynamo action" in our kinematic simulation, we plot in Fig. 5.1 the time evolution of the magnetic energy $E_{mag} = 1/2V \int |\boldsymbol{B}|^2 dV$. The cases for which E_{mag} exhibits a positive slope represent a dynamo effect. In the next Subsections 5.3.1, 5.3.2 we will perform this analysis for the entire data-set simulated (almost 200 simulations) to find the optimum spots.

The analysis will focus on two main points: (*i*) the influence of the nutation angle α on the ability to drive dynamo action; (*ii*) the impact of the Reynolds number for a fixed angle $\alpha = 90°$.

5.3.1. The role of the nutation angle

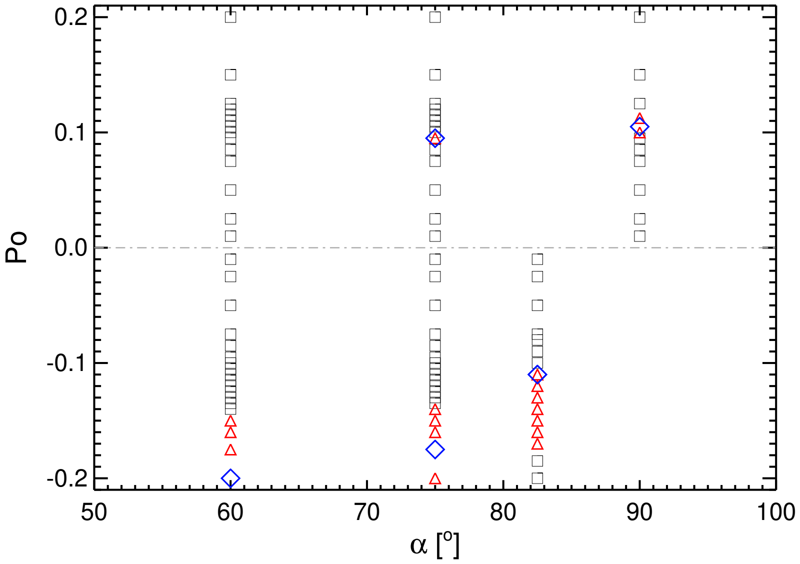

Figure 5.2. Regime diagram of the kinematic dynamo simulations in the (Po, α) parameter space with fixed $Re = 6500$. Prograde (retrograde) cases correspond to the positive (negative) region $Po > 0$ $(Po < 0)$. Red symbols indicate dynamo action; black symbols show missing dynamo action and the blue diamond show the peak of strongest dynamo for each angle. Notice that the range investigated for the dynamo occurrence is $0 \le Rm \le 1000$.

Figure 5.2 shows the regime diagram in the (α, Po) space at fixed $Re = 6500$. We find dynamo action (red symbols) for all angles except for $\alpha = 60°$ prograde. The range of the precession ratio where dynamo action occurs changes with the nutation angle: for prograde cases dynamos occur at $Po \approx 0.1$ while for retrograde they appear at $Po > 0.1$ with a more extended range. For each angle, the blue diamonds indicate the dynamo with the largest growth rate; they are plotted in Fig. 5.3 as optimum precession ratio Po^o as a function of the nutation angle. Notably the profile presents an asymmetry with respect to α since the linear trend includes also the retrograde case $\alpha = 82.5°$ and the jump does coincide with the symmetric precession i.e. $\alpha = 90°$.

We plot the growth rate of the magnetic energy $\gamma = 2\Re(\sigma)$ (where here σ is the eigenvalue)

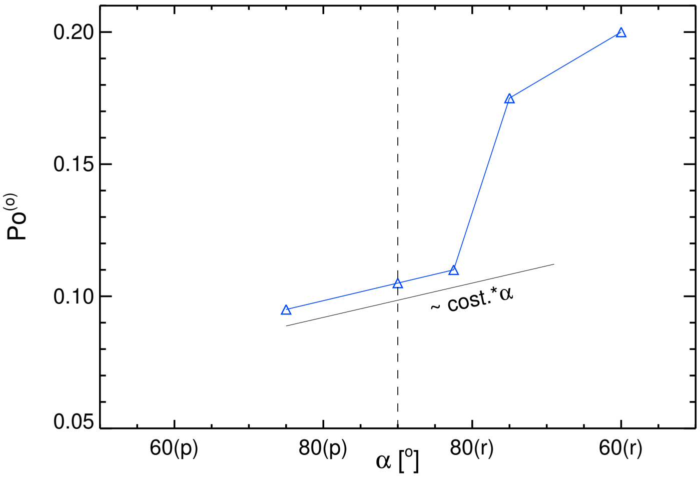

Figure 5.3. Optimum Poincaré number for the best dynamo action in dependence on the precession $Re = 6500$.

in Fig. 5.4. As already highlighted, the $\alpha = 60^\circ$ prograde shows no positive growth rate even at the largest magnetic Reynolds number considered here. The lowest critical magnetic Reynolds number occurs for $\alpha = 90^\circ$ which, therefore, turns out to be the most promising case for the later dynamo experiment.

Figure 5.5 shows the critical magnetic Reynolds number (i.e. the lowest Rm for the occurrence of dynamo action) versus the nutation angle. Clearly, the role of α is crucial in order to reduce as much as possible the threshold for the onset of dynamo, and it is clear that the optimum range is $90 < \alpha < 82.5$ retrograde. Also the magnetic field structure, for example the azimuthal component B_φ, depends on α (Fig. 5.6). The three snapshots are taken between $t = 300$ and and $t = 380$. Both cases present contours elongated along the axis and the final field shows a change in sign during the evolution.

To better observe the evolution of $\boldsymbol{B}$, we show in Fig. 5.7 the three dimensional magnetic field lines developed inside the container again for three different times (columns) for three different nutation angles. The main outcome is that α causes a substantial difference in the geometry and the time-evolution of the field. The $\alpha = 75^\circ$ retrograde case presents less dense field lines with quite chaotic shape, while the $\alpha = 90^\circ$ shows the most coherent topology characterized by two clear vortices with opposite rotations (visible as black arrows) which change over time: e.g. at t_0 the bottom large vortex is clockwise while at t_1 it becomes counterclockwise.

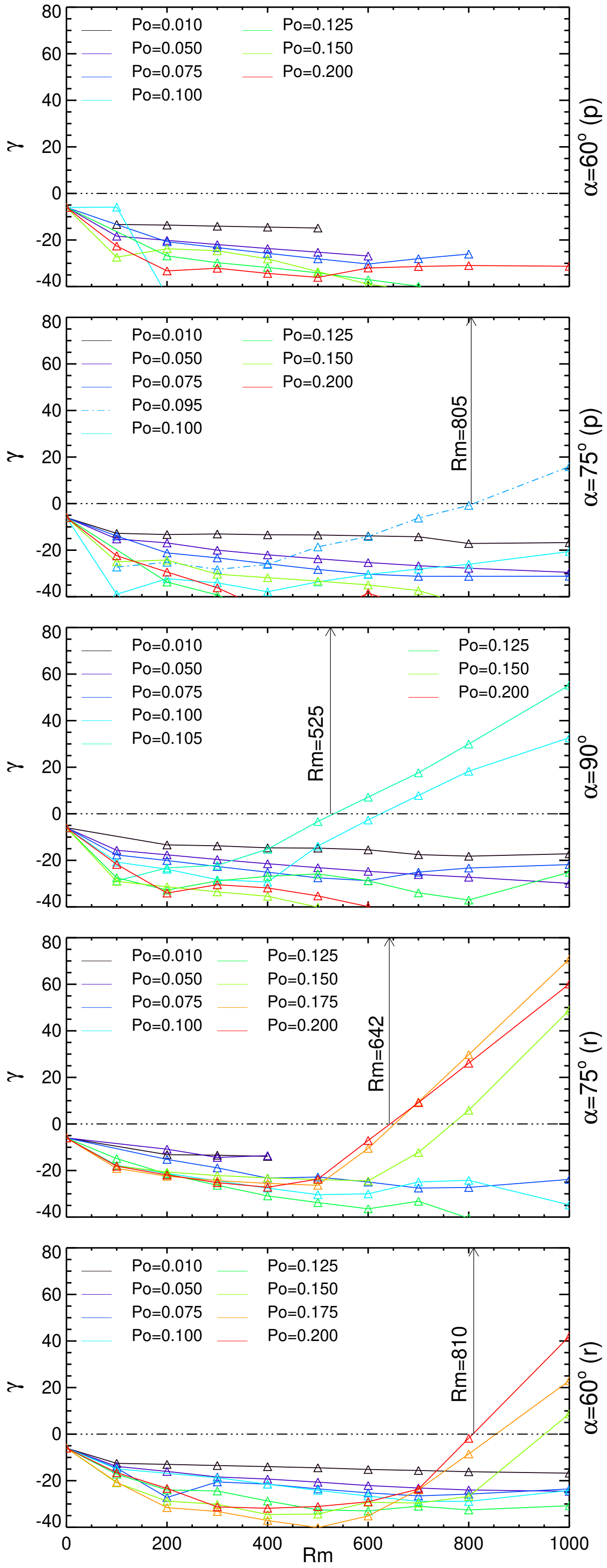

Figure 5.4. Growth rate γ of the magnetic energy as a function of the magnetic Reynolds number for five nutation angles. Various curves represent the different precession ratios and the arrows mark the dynamo onset at the critical Rm.

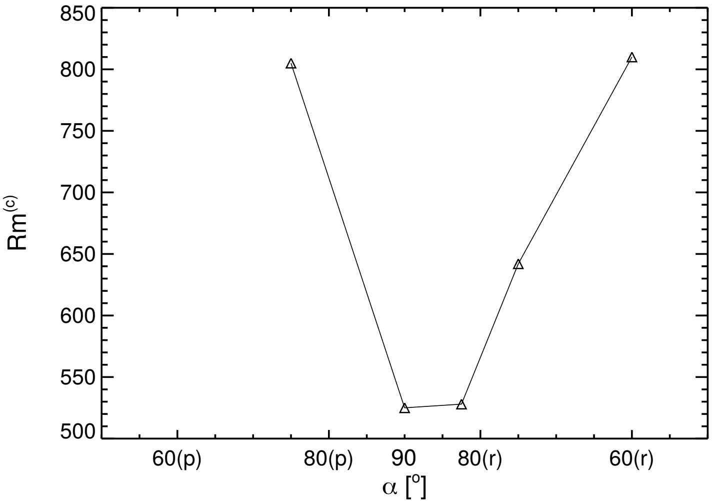

Figure 5.5. Critical magnetic Reynolds number for different nutation angles for $Re = 6500$.

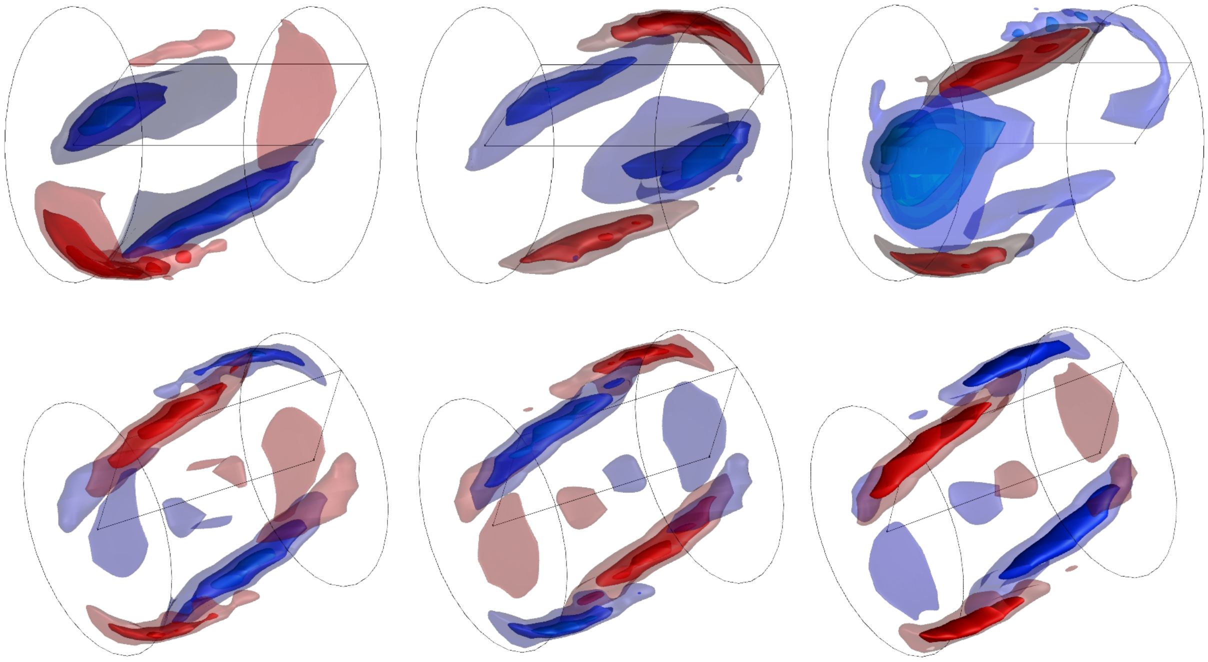

Figure 5.6. Three snapshots of the azimuthal magnetic field B_φ at $Rm = 700$: top row $\alpha = 90°$ and $Po = 0.105$; bottom row : $\alpha = 75°$ retrograde and $Po = 0.175$. Blue color denotes negative values and red color positive values with the levels of translucency denoting 30%, 50%, 70% of the field.

5.3.2. The role of the Reynolds number

In this subsection we fix the nutation angle $\alpha = 90°$ to investigate the impact of the hydrodynamic Reynolds number on the dynamo action. We select this angle since it appears to be the best angle for dynamo action, with the lowest critical magnetic Reynolds number.

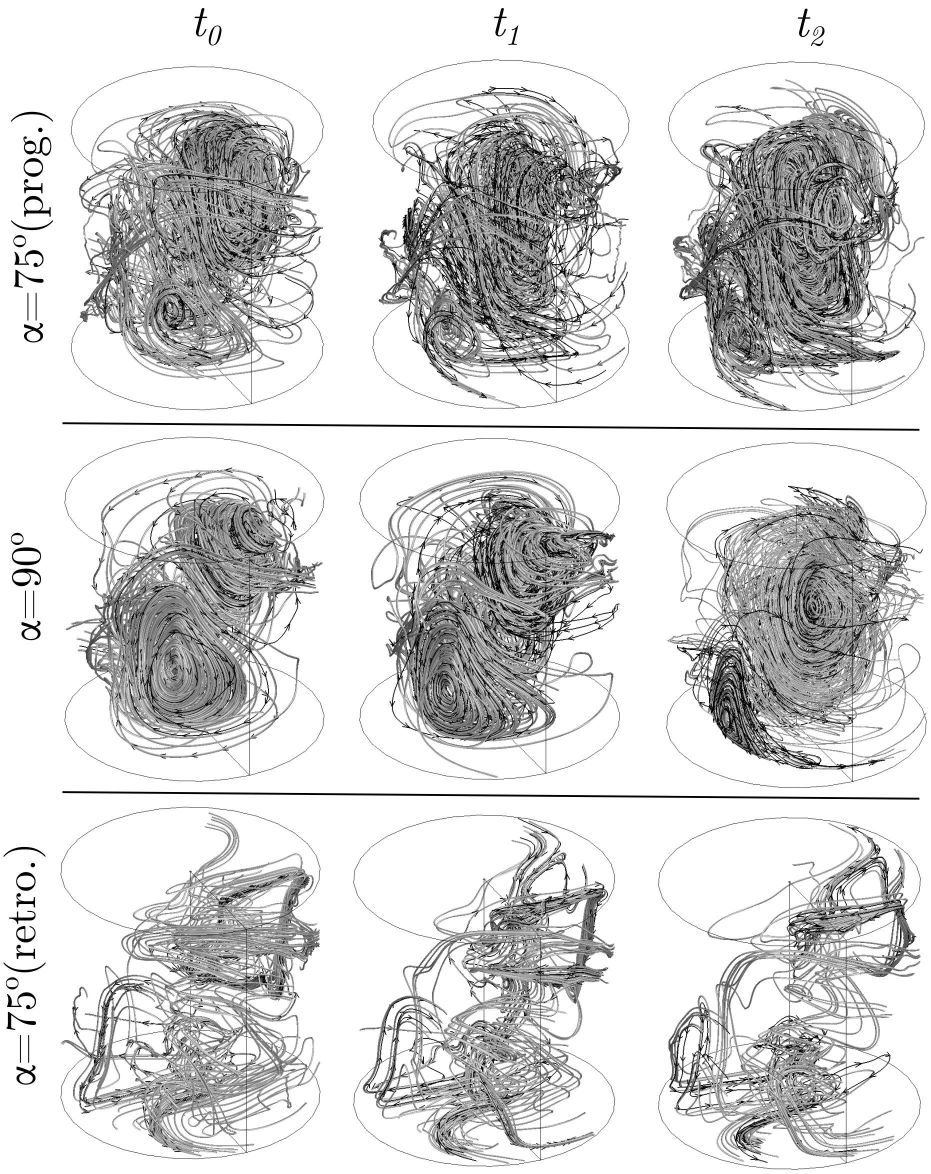

Figure 5.7. Same as Fig. 5.6 but with 3D field lines.

We start by showing the regime diagram in the (Re, Po) space where the meaning of the symbols is consistent with that of Fig. 5.2: black squares denote no dynamo action, red triangles indicate dynamo action, and blue diamonds signify the strongest dynamo action. The blue curve is a fit marking the scaling for $Po^c \approx Re^{-1/4}$. Notice that for $Re < 3500$ we observe dynamos also significantly above the threshold curve; by contrast for larger Re the dynamo action is restricted to a quite narrow range. In the next step we select the best precession ratio for every Re (the blue diamonds) and show the growth rate γ as a function of Rm in Fig. 5.9(a). The slopes of the curves seem to converge for the highest Reynolds number considered here. Collecting the points where the lines cross $\gamma = 0$ we plot the critical magnetic Reynolds number in Fig. 5.9(b). The trend is not monotonic, showing a flat maximum in the range $4000 < Re < 8000$. The smallest critical magnetic Reynolds number is found for $Re = 2000$. This might be the case since at small

Reynolds number the flow tends to remain well organized in large scale structures rather than become turbulent with the presence of small scales. More important is the apparent convergence for higher Re.

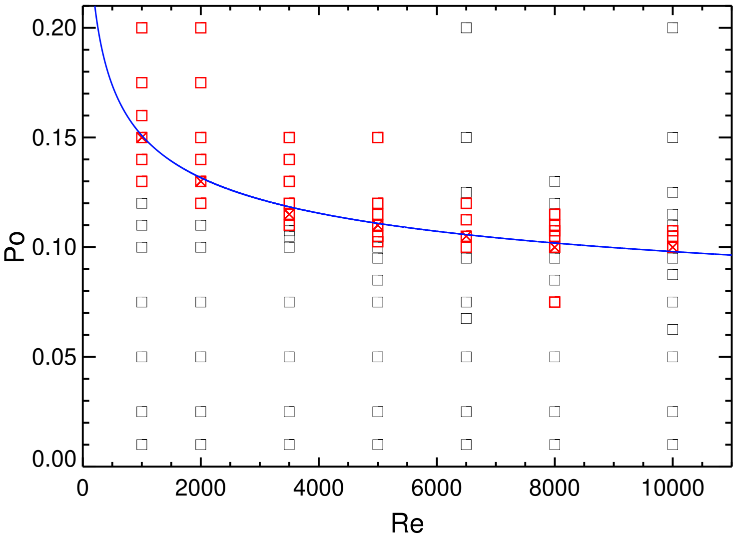

Figure 5.8. (Po, Re) parameter space with fixed $\alpha = 90°$. Black symbols represent no dynamo effect and red symbol dynamo action found in the range of $0 < Rm \leq 10^3$. Red crosses highlight the best dynamo action for each Re and the corresponding blue line is the scaling law $Po^{(c)} \sim Re^{-1/4}$.

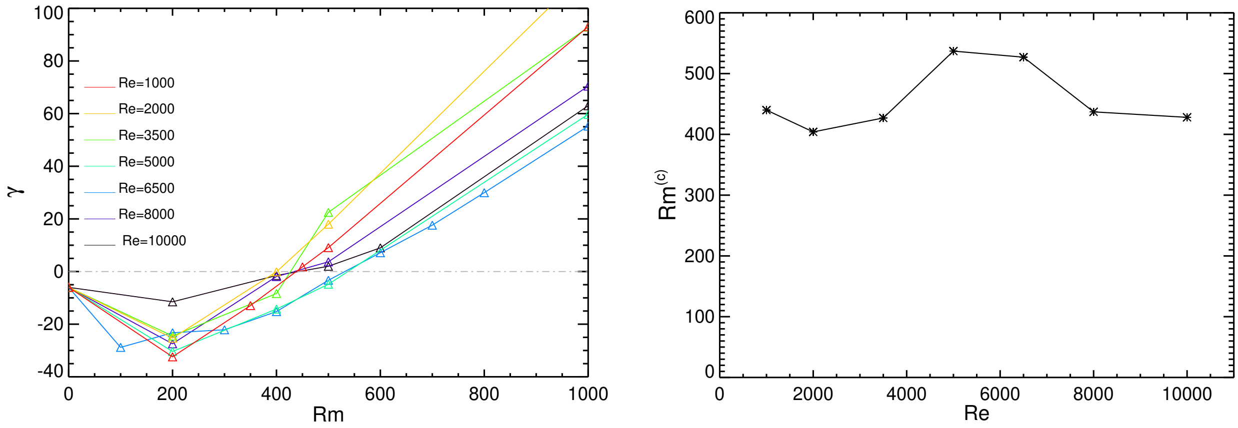

Figure 5.9. Analysis for $\alpha = 90°$. Left: Plot of the growth rate of magnetic energy for different Reynolds numbers taken at the best Po; Right: Critical magnetic Reynolds number dependent on Re.

5.4. Summary

The nutation angle is a crucial governing parameter for precession driven flows in cylindrical geometry whose role is far from trivial, especially in the nonlinear regime. It determines the flow topology and the magnitude of particular structures both for the flow and the dynamo generated magnetic field. As a consequence the possibility to achieve dynamo action is strongly influenced by the angle. The results of this Chapter give general indications about the best region in the phase space for the dynamo action: the optimum angle was found to be in the range $90° < \alpha < 82.5°$ retrograde. Future studies will focus on the extension of the analysis on other Reynolds number and to the impact of realistic magnetic boundary conditions. With view on the present results (Stefani *et al.* (2006), Giesecke *et al.* (2008)), we expect that the actual critical Rm for corrected vacuum boundary conditions to be somehow $15\% - 30\%$ larger than the ones found here.

6. A local model to study precession driven turbulence

Doue la turbolenza dell'acqua si
genera
doue la turbolenza dell'acqua si
mantiene plugho
doue la turbolenza dell'acqua si posa...

Leonardo da Vinci, Codice Atlantico

[1]This Chapter is devoted to the study of turbulence features in precessing flows. In contrast to the previous chapters, which were constrained on cylindrical geometry, we will make use of a local model (periodic box) which has several benefits:

- the possibility to focus on an unbounded flow, by removing the boundary layers, corners and other boundary condition problems.
- the possibility to achieve significantly higher Reynolds numbers than with global simulations.
- the use of a cartesian periodic box in which the application of Fourier analysis to approach the fluid flow in spectral space is straightforward.

While the following results cannot directly be applied to a cylindrical bounded flow, they are still useful to understand and explain the generation of vortices, i.e. large scale structures, which are common characteristics of all precession driven flows.

---

[1] The content of the present chapter comes from the journal publication *Interplay between geostrophic vortices and inertial waves in precession-driven turbulence* by Pizzi, Mamatsashvili, Barker, Giesecke, & Stefani (2022b) © 2022 (with the permission of AIP Publishing).

6.1. Introduction

Rotating turbulence is an ubiquitous phenomenon both in celestial objects (Barnes (2001), Cho *et al.* (2008), Knobloch & Proctor (1981), Zahn (1995)) and in industrial applications (Dumitrescu & Cardos (2004), He *et al.* (2021)). Understanding the impact of rotation on the mechanism of turbulence is far from trivial due to complexity of the behavior. In general, when a fluid is subjected to rotation, the nonlinear interactions are influenced by the Coriolis force whose strength is quantified by the Rossby number (the ratio of the advection rate to the rotation rate) and the Reynolds number (the ratio of the advection rate to the viscous rate). If the Coriolis force is strong enough the formation of coherent columnar vortices occurs inside the fluid flow. This phenomenon has been observed in experimental campaigns for several mechanisms such as oscillating grid (Hopfinger *et al.* (1982)), for decaying turbulence (Staplehurst *et al.* (2008), Lamriben *et al.* (2011)), forced turbulence (Campagne *et al.* (2014), Gallet *et al.* (2014), Campagne *et al.* (2014)), and turbulent convection (Kunnen *et al.* (2010)). Numerical simulations have been useful to analyze such tendencies in many cases (Bardina *et al.* (1985), Mansour *et al.* (1991, 1992), Hossain (1994), Yeung & Zhou (1998), Smith *et al.* (1996)) also by making use of large eddy simulations (Yang *et al.* (2004)) and turbulence models (Elena & Schiestel (1996), Spalart & Shur (1997)).

The emergence of columnar vortices is accompanied by the ubiquitous existence of inertial waves which are universal characteristics of rotating fluids. Their frequency ranges between zero and twice the rotation rate Ω of the objects (Greenspan (1968)). From this framework it is clear that the dependence on Re and Ro influences the emergence of vortices or inertial waves turbulence. However the situation is not always clearly divided since the 3D inertial waves (the so called fast modes) and the pseudo 2D vortices (also called slow modes) can coexist. Several works were devoted to the study of these two manifolds and their interactions for forced rotating turbulence (Smith & Waleffe (1999), Müller & Thiele (2007), Buzzicotti *et al.* (2018)) and also for convection rotating turbulence (Rubio *et al.*, 2014, Knobloch, 1998).

Indeed other forcing mechanisms have been shown to be characterized by this interplay, such as elliptical instabilities (Favier *et al.* (2015), Le Reun *et al.* (2017, 2019)), and tidal forcing (Barker & Ogilvie (2009, 2010), Barker & Lithwick (2013)). In this perspective the precession dynamics represents a possible candidate for the development of both three dimensional wave turbulence and rotating turbulence, but so far the studies were dedicated to approach the turbulence characteristics without focusing on slow-fast manifolds (Khlifi *et al.* (2018)). Other works were devoted to the stability analysis of the precession flows (Salhi & Cambon (2009)). Barker (2016) used a model proposed by Mason & Kerswell (2002) to study precession flows and analyze some properties such as dissipation and shell averaged spectra.

The aim of this Chapter is to answer several question such as: (*i*) how do the columnar vortices depend on the precession ratio and Reynolds number; (*ii*) what are the mechanisms for the formation of the columnar vortices in precessing driven flows, in particular if they are caused by precessing instabilities rather than nonlinear transfer; (*iii*) in the frame of nonlinear transfer what is the dominant mechanism, i.e the interaction of 2D-3D structures or the 2D-2D interaction e.g inverse cascade. (*iv*) in terms of total shell-average what type of cascade we observe and what kind of spectra characterize the precessing flows.

6.2. Results

The simulations performed in this Chapter, with the SNOOPY code (see Sec. 2.5), for different pairs of (Po, Re) are listed in Table I. All runs start with initial small random noise perturbations of velocity imposed on the basic flow.

6.2.1. 2D-3D analysis

In the present Section we follow a widely used approach in the theory of rotating anisotropic turbulence (Smith & Waleffe (1999), Rubio *et al.* (2014), Buzzicotti *et al.* (2018), Khlifi *et al.* (2018), Barker & Lithwick (2013)) and decompose the flow field into 2D and 3D modes in Fourier space to better characterize the anisotropy between horizontal and vertical motions. This choice is motivated by the observation of two main types of perturbations: vortices, which are essentially 2D structures, and 3D inertial waves in rotating turbulent flows with external forcing such as libration, elliptical instability (Le Reun *et al.* (2017), Barker & Lithwick (2013)), precession (Khlifi *et al.* (2018), Barker (2016)) and other artificial types of forcing concentrated at a particular wavenumber (Buzzicotti *et al.* (2018), Müller & Thiele (2007), Seshasayanan & Gallet (2020)). The 2D vortical modes, also called *slow* (geostrophic) modes, have dominant horizontal velocity over the vertical one and are almost uniform, or aligned along the rotation $z-$axis, i.e., their wavenumber parallel to this axis is zero, $k_z = 0$. This *slow* manifold is also referred to as 2D and three-component (2D3C) field in the literature, since it varies only in the horizontal (x, y)-plane perpendicular to the rotation axis, but still involves all three components of velocity with the horizontal one being dominant. On the other hand, 3D inertial wave modes, called *fast* (with nonzero frequency $\omega = \pm 2\Omega k_z/k$) modes, have comparable horizontal and vertical

$Re = 10^{3.5}$

Po	N	$\langle E \rangle$
0.01	64	-
0.025	64	-
0.05	64	-
0.075	64	-
0.1	64	-
0.125	64	-
0.15	64	-
0.175	64	-
0.2	64	-
0.225	64	-
0.25	64	-
0.3	64	6.09×10^{-5}

$Re = 10^{4}$

Po	N	$\langle E \rangle$
0.01	64	-
0.025	64	-
0.05	64	-
0.075	128	-
0.1	128	-
0.125	128	1.89×10^{-5}
0.15	128	6.04×10^{-5}
0.175	128	1.42×10^{-4}
0.2	128	3.54×10^{-4}
0.225	128	6.11×10^{-4}
0.25	128	9.94×10^{-4}
0.3	128	2.10×10^{-3}

$Re = 10^{4.5}$

Po	N	$\langle E \rangle$
0.01	128	-
0.025	128	-
0.05	128	-
0.075	128	3.82×10^{-5}
0.1	128	1.13×10^{-4}
0.125	128	4.93×10^{-4}
0.15	256	1.30×10^{-3}
0.175	256	2.30×10^{-3}
0.2	256	5.40×10^{-3}
0.225	256	6.20×10^{-3}
0.25	256	6.40×10^{-3}
0.3	256	9.00×10^{-3}
0.5	256	1.25×10^{-2}

$Re = 10^{5}$

Po	N	$\langle E \rangle$
0.01	256	-
0.025	256	-
0.05	256	4.55×10^{-5}
0.075	256	2.37×10^{-4}
0.1	256	1.10×10^{-3}
0.125	256	5.90×10^{-3}
0.15	256	6.80×10^{-3}
0.175	256	7.50×10^{-3}
0.2	256	8.90×10^{-3}
0.225	256	1.02×10^{-2}
0.25	256	1.14×10^{-2}
0.3	256	1.15×10^{-2}

Table 6.1. Tables of simulations for the present Chapter. Each subtable contains a specific Reynolds number with various precession ratio (second column). The second column shows the resolution N the total number of point is N^3. The other columns are respectively: the time and volume averaged kinetic energy $\langle E \rangle$.

velocities and vary along z-axis, i.e., parallel wavenumber is nonzero $k_z \neq 0$[2]. Specifically, these two mode manifolds are

$$\Psi_{2D} = \{\boldsymbol{k} \mid k_x, k_y, k_z = 0\}\,, \quad \Psi_{3D} = \{\boldsymbol{k} \mid k_x, k_y, k_z \neq 0\}\,. \tag{6.1}$$

---

[2] Due to the precessing basic flow, the $k_z(t)$ wavenumber of modes oscillates in time according to Eq. (2.21), so we classify 2D and 3D modes as having $\langle k_z(t) \rangle = k_{z0} = 0$ and $k_{z0} \neq 0$, respectively.

and the spectral velocities for 2D vortices and 3D inertial waves can be defined as

$$\bar{\boldsymbol{u}}(\boldsymbol{k}) = \begin{cases} \bar{\boldsymbol{u}}_{2D}(\boldsymbol{k}) & \text{if} \quad \boldsymbol{k} \in \Psi_{2D} \\ \bar{\boldsymbol{u}}_{3D}(\boldsymbol{k}) & \text{if} \quad \boldsymbol{k} \in \Psi_{3D}. \end{cases} \tag{6.2}$$

Note that the definition of 2D manifolds as used here differs from the Taylor-Proudman problem since it does not necessarily have a vanishing vertical flow. Indeed, velocities for both the 3D and 2D modes can be decomposed in turn into respective horizontal $\bar{\boldsymbol{u}}_h = (\bar{u}_x, \bar{u}_y, 0)$ and vertical $\bar{u}_z$ components

Using the general Eq. (2.26), separate equations can be written for the 2D and 3D mode spectral energies defined, respectively, as $E_{2D} = |\bar{\boldsymbol{u}}_{2D}|^2/2$ and $E_{3D} = |\bar{\boldsymbol{u}}_{3D}|^2/2$, (Buzzicotti *et al.* (2018), Barker & Lithwick (2013)):

$$\frac{dE_{2D}}{dt} = A_{2D} + \underbrace{NL_{2D2D} + NL_{3D2D}}_{NL_{2D}} + D_{2D}, \tag{6.3}$$

$$\frac{dE_{3D}}{dt} = A_{3D} + \underbrace{NL_{3D3D} + NL_{2D3D}}_{NL_{3D}} + D_{3D}. \tag{6.4}$$

Since injection A and dissipation D terms are of linear origin, they act for 2D and 3D modes separately, i.e.,

$$A_{2D} = A(\boldsymbol{k}), \quad D_{2D} = D(\boldsymbol{k}), \quad \text{for} \quad \boldsymbol{k} \in \Psi_{2D}$$

$$A_{3D} = A(\boldsymbol{k}), \quad D_{3D} = D(\boldsymbol{k}), \quad \text{for} \quad \boldsymbol{k} \in \Psi_{3D}.$$

However, the nonlinear transfers can act only among modes which lie respectively within the slow or the fast manifold, that is, nonlinear interactions separately among 2D-2D modes (vortex-vortex),

$$NL_{2D2D} = -\bar{\boldsymbol{u}}_{2D} \cdot \overline{(\boldsymbol{u}_{2D} \cdot \boldsymbol{\nabla} \boldsymbol{u}_{2D})},$$

and among 3D-3D modes (wave-wave),

$$NL_{3D3D} = -\bar{\boldsymbol{u}}_{3D} \cdot \overline{(\boldsymbol{u}_{3D} \cdot \boldsymbol{\nabla} \boldsymbol{u}_{3D})},$$

(long bars denote Fourier transforms) as well as between these two manifolds, that is, nonlinear cross interactions/couplings between 2D and 3D modes (vortex-wave) (Biferale *et al.* (2016), Buzzicotti *et al.* (2018)),

$$NL_{3D2D} = -\bar{\boldsymbol{u}}_{2D} \cdot \overline{(\boldsymbol{u}_{3D} \cdot \boldsymbol{\nabla} \boldsymbol{u}_{3D})}.$$

$$NL_{2D3D} = -\bar{\boldsymbol{u}}_{3D} \cdot \overline{(\boldsymbol{u}_{2D} \cdot \boldsymbol{\nabla} \boldsymbol{u}_{3D})} - \bar{\boldsymbol{u}}_{3D} \cdot \overline{(\boldsymbol{u}_{3D} \cdot \boldsymbol{\nabla} \boldsymbol{u}_{2D})}.$$

In this case, in a triad, 2D modes can receive/lose energy via nonlinear interaction of two 3D modes with opposite signs of k_z, while 3D modes can receive/lose energy via interaction of only 2D and another 3D modes (interaction between 2D and 2D modes obviously cannot feed 3D modes). The 2D-2D and 3D-3D nonlinear transfers are each conservative, $\sum_{\boldsymbol{k}} NL_{2D2D} = 0$ and $\sum_{\boldsymbol{k}} NL_{3D3D} = 0$, whereas the cross transfer terms NL_{2D3D} and NL_{3D2D}, are not, but their sum is conservative, as the net effect of these terms summed over all wavenumbers, as it should be, are equal in absolute value but have opposite signs:

$$\sum_{\boldsymbol{k}\in\Psi_{3D}} NL_{3D2D}\left(\boldsymbol{k}\right) = -\sum_{\boldsymbol{k}\in\Psi_{2D}} NL_{2D3D}\left(\boldsymbol{k}\right). \tag{6.5}$$

Below we analyze the action of these injection and transfer terms for different Po and Re (Table I).

In the following we will mostly use shell-averages of these spectra, which are defined in the standard way as:

$$\boldsymbol{f}(k) = \sum_{k\leq|\boldsymbol{k}|\leq k+\Delta k} f(\boldsymbol{k}),$$

for each spectral quantity $f \equiv (E, A, NL, D)$, where for 3D modes $\boldsymbol{k} \in \Psi_{3D}$, i.e., summation is done over spherical shells with radii $k = (k_x^2 + k_y^2 + k_z^2)^{1/2}$ and for 2D modes having $\boldsymbol{k} \in \Psi_{2D}$ over rings in the $(k_x, k_y)-$plane with radii $k = (k_x^2+k_y^2)^{1/2}$. When we plot spectra for 2D and 3D quantities, we implicitly assume each depends on its respective wavenumber magnitude k.

6.3. General features of precession-driven turbulence

The simulations performed in this paper for different pairs of (Po, Re) are listed in Table I. All runs start with initial small random noise perturbations of velocity imposed on the basic flow. In Figure 6.1, we plot the time evolution of the volume-averaged kinetic energy, which is equal to the sum of energies of 2D and 3D modes over all wavenumbers, $\langle E\rangle = \sum_{\boldsymbol{k}} E = \sum_{\boldsymbol{k}}(E_{2D} + E_{3D})$, for several precession parameters Po and at an intermediate Reynolds number $Re = 10^{4.5}$. In the initial linear regime, the energy grows exponentially corresponding to dominant 3D inertial waves being excited first by the precessional instability (Kerswell (1993), Mason & Kerswell (2002), Naing & Fukumoto (2011), Barker (2016)) (see inset in Fig. 6.1). In the given range of Po, the growth rate of the precession instability increases with Po. After about several hundreds of orbital times the exponential growth attains sufficient amplitude for nonlinearity to come into play and

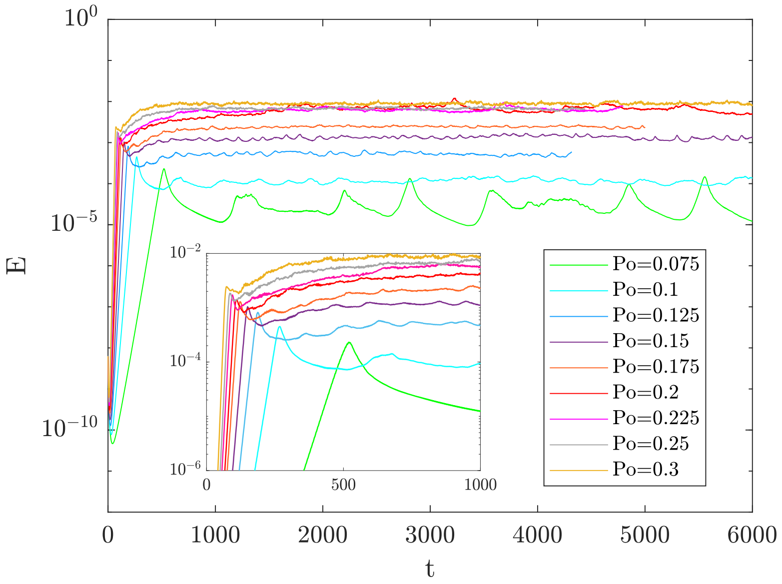

Figure 6.1. Time-evolution of the volume-averaged total (2D+3D) kinetic energy for $Re = 10^{4.5}$ and different Po. The impact of the precession parameter on the energy evolution is clearly seen, which is characterized by quasi-periodic bursts at small $Po = 0.075$ and gradually becomes statistically steady turbulence with minor fluctuations and increasing amplitude as Po increases. Inset panel zooms in the initial exponential (appearing as linear in logarithmic y-axis) growth and early saturation phases.

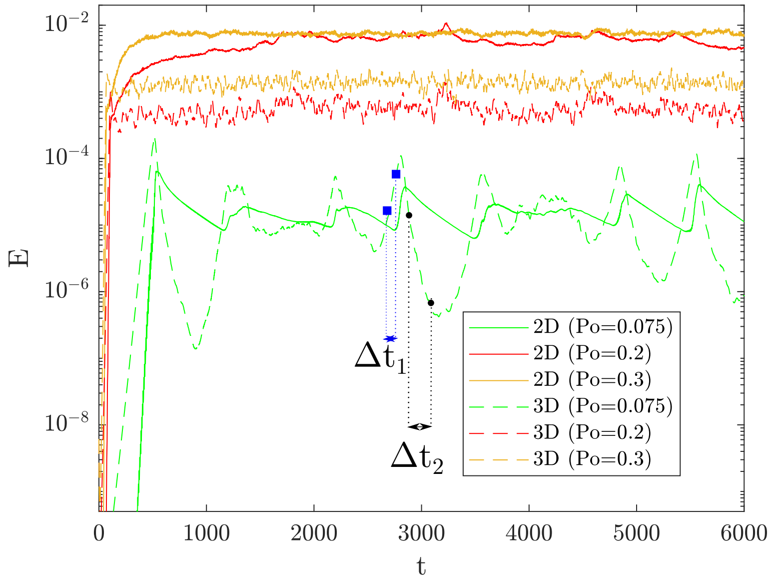

Figure 6.2. Time-evolution of the volume-averaged kinetic energies for 2D vortices, $\langle E_{2D}\rangle$ (solid), and 3D inertial waves, $\langle E_{3D}\rangle$ (dashed), for $Re = 10^{4.5}$ and three different precession parameters representative of three characteristic regimes shown in Fig. 6.1: bursts at weak ($Po = 0.075$) and quasi-steady turbulence at medium ($Po = 0.2$) and strong ($Po = 0.3$) precessions. Two intervals Δt_1 (from $t = 2690$ to $t = 2770$) in State 1 and Δt_2 (from $t = 2880$ to $t = 3080$) in State 2 denote those time intervals over which spectral analysis is performed for these two different states.

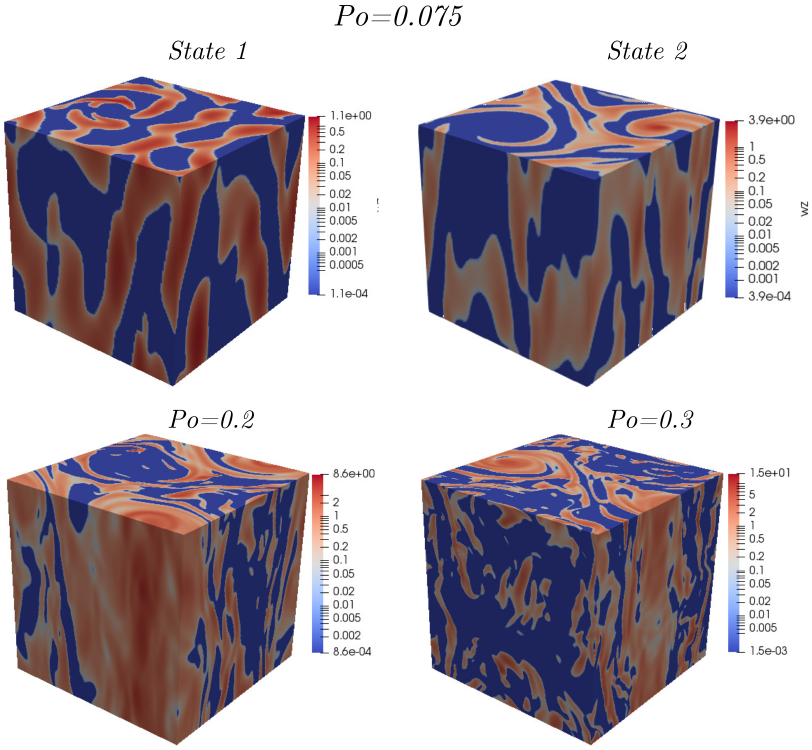

Figure 6.3. Snapshots of the vertical component of vorticity, $\omega_z = (\boldsymbol{\nabla} \times \boldsymbol{u})_z$ (log-scale), in physical space for three characteristic precession parameters: $Po = 0.075, 0.2, 0.3$ and $Re = 10^{4.5}$ in the saturated state (at $t = 3000$). The upper two boxes show the structures in State 1 (left), dominated by vertically-varying 3D inertial waves, and State 2 (right), dominated by 2D vortices nearly uniform along z-axis. Large-scale 2D columnar vortices are also evident together with a turbulent field of waves at $Po = 0.2$ and 0.3.

cause the instability to saturate with higher amplitudes and shorter saturation times for larger Po. Depending on Po, the saturated states are qualitatively different, exhibiting statistically steady turbulence at higher $Po \gtrsim 0.1$ with only minor fluctuations, whereas strong quasi-periodic oscillations (bursts) are observed at small $Po \lesssim 0.1$ with more than an order of magnitude variations in the kinetic energy. This temporal behavior of the volume-averaged kinetic energy in the nonlinear state of the precession instability with Po is consistent with previous related local studies (Barker (2016), Khlifi *et al.* (2018)). Below we interpret this temporal evolution of the total kinetic energy in terms of the dynamics of 2D vortices and 3D waves and their interplay.

A first comparison between the 2D and 3D mode dynamics is shown in Fig. 6.2 where the evolution of the total kinetic energies for 2D modes, $\langle E_{2D} \rangle$ and 3D modes, $\langle E_{3D} \rangle$, are plotted for three precession parameters. For larger $Po \gtrsim 0.1$ the energy of 2D modes is more than one order of magnitude larger than that of 3D modes. However, the saturated value of $\langle E_{3D} \rangle$ tends to increase more than that of $\langle E_{2D} \rangle$ with increasing Po, implying that the waves, as it should be, are more affected and intensified by precession than the vortices. The 2D vortices are linearly stable against precession instability and hence cannot grow

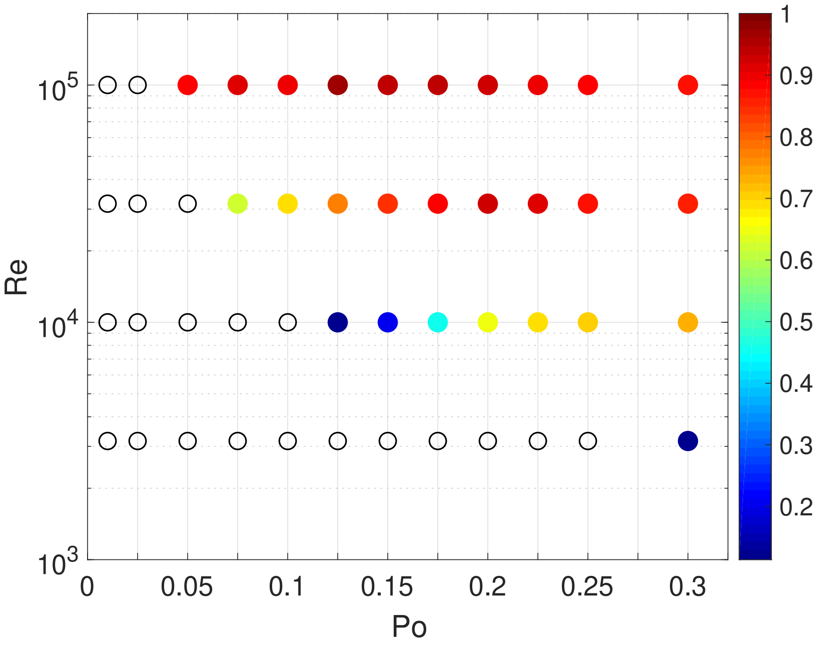

Figure 6.4. Regime diagram in the $(Po, Re)-$plane. The colors represent the ratio of time-averaged 2D to total (2D+3D) energies, $\langle E_{2D}\rangle/\langle E\rangle$, in the saturated state, while the empty points correspond to the cases stable to precessional instability when perturbations decay.

due to the latter (Kerswell (1993)). They are driven and energetically supplied by waves via nonlinear transfers (Barker (2016)), which will be examined in detail below using the spectral analysis. On the other hand, for the lowest precession parameter $Po = 0.075$, corresponding to the bursty regime, the energy of 3D waves periodically dominates over the 2D vortical mode energy during the growth (burst) phase (referred to as State 1). In this burst phase, waves excited by the elliptical instability, lose their energy to 2D vortices due to nonlinearity. As a consequence, the energy of the waves drops by about an order of magnitude (affected additionally by viscous dissipation) relative to the 2D mode energy (State 2). After that it starts to increase again due to precessional instability, closing the cycle. Although 2D mode energy also decreases at this stage, it does so much slower, on viscous time (Barker (2016)). This cyclic behavior of both components is remarkable, indicating the quasi-periodic nature of evolution due to weak precessional forcing ($Po \lesssim 0.1$), which is relevant to astrophysical and geophysical regimes (Barker (2016), Le Bars *et al.* (2015), Cébron *et al.* (2019)). This behavior will be explored in more detail in the spectral analysis section below.

Figure 6.3 shows the structure of the vorticity along the direction of the rotation z-axis, $\omega_z = (\boldsymbol{\nabla} \times \boldsymbol{u})_z$, in physical space well after the saturation for the above regimes of weak, moderate and strong precessions. The top row shows the case $Po = 0.075$ characterized by bursts. In State 1, which corresponds to the burst of 3D wave energy dominating

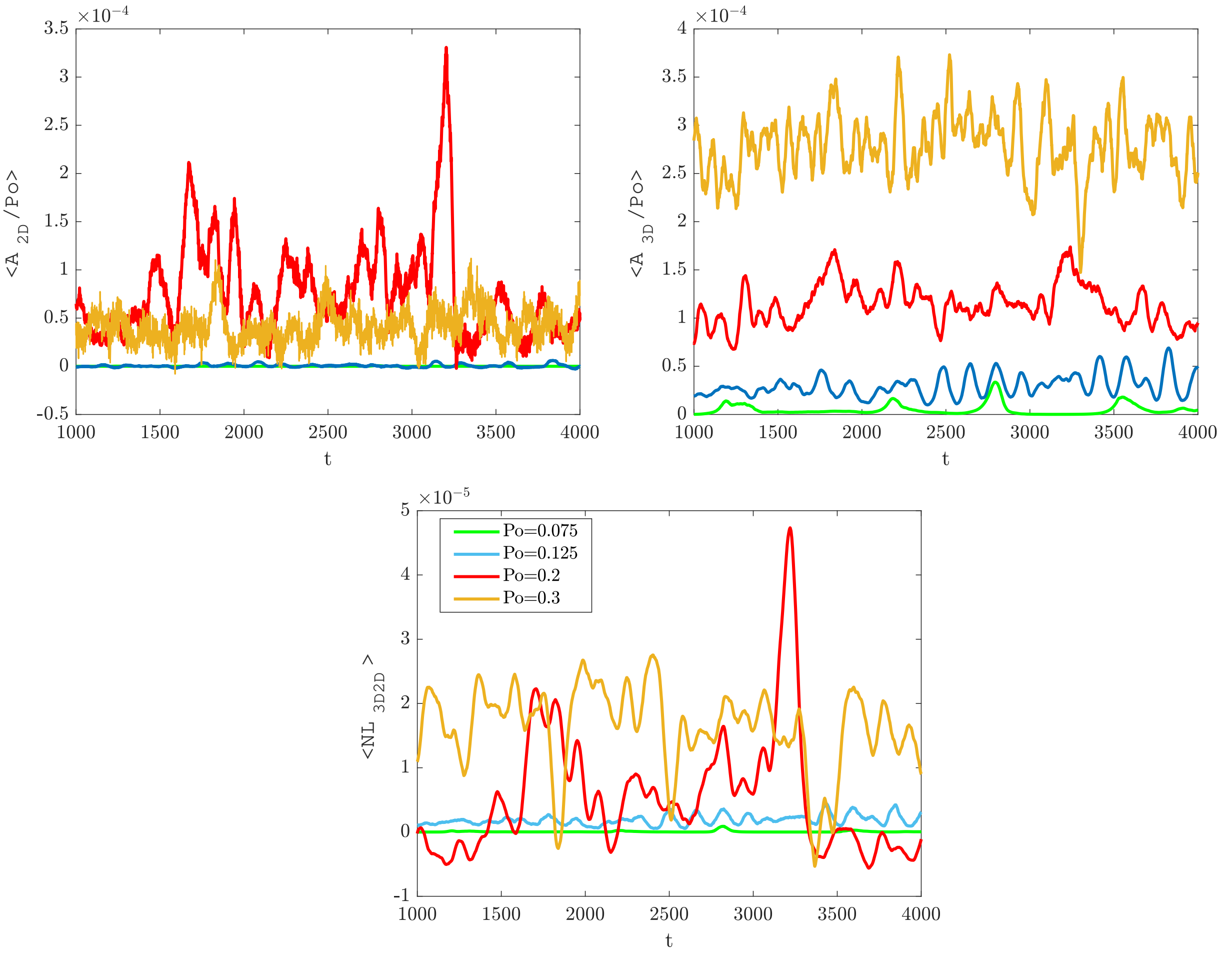

Figure 6.5. Evolution of the volume-averaged dynamical terms – energy injection $\langle A \rangle$ for 3D waves (top) and 2D vortices (bottom) together with nonlinear transfer $\langle NL_{2D3D} \rangle$ between these two modes (middle) in corresponding Eqs. 6.3 and 6.4 for different Po and given $Re = 10^{4.5}$.

over that of 2D modes in Fig. 6.2, we therefore observe pronounced 3D wave structures varying along the $z-$axis. By contrast, in the State 2, where the wave energy quickly decays afterwards and 2D modes dominate, only vertically uniform columnar vortical structures aligned with the $z-$axis are present. At larger $Po = 0.2$ and $Po = 0.3$ as shown, respectively, in bottom left and right panels of Fig. 6.3, the nonlinear states consist of vortices embedded in 3D waves, coexisting at all times. At medium $Po = 0.2$, two vertical columnar vortices with opposite vorticity (cyclonic/anticyclonic) are clearly seen in the small scale waves, whose strength with respect to vortices has increased compared to that in the above bursty regime. At even higher $Po = 0.3$, the contribution of 3D wave energy is somewhat larger (Fig. 6.2) and therefore small-scale turbulent wave structures are more pronounced with respect to a single 2D vortex.

The regime diagram in Fig. 6.4 summarizes the properties of all the runs for different

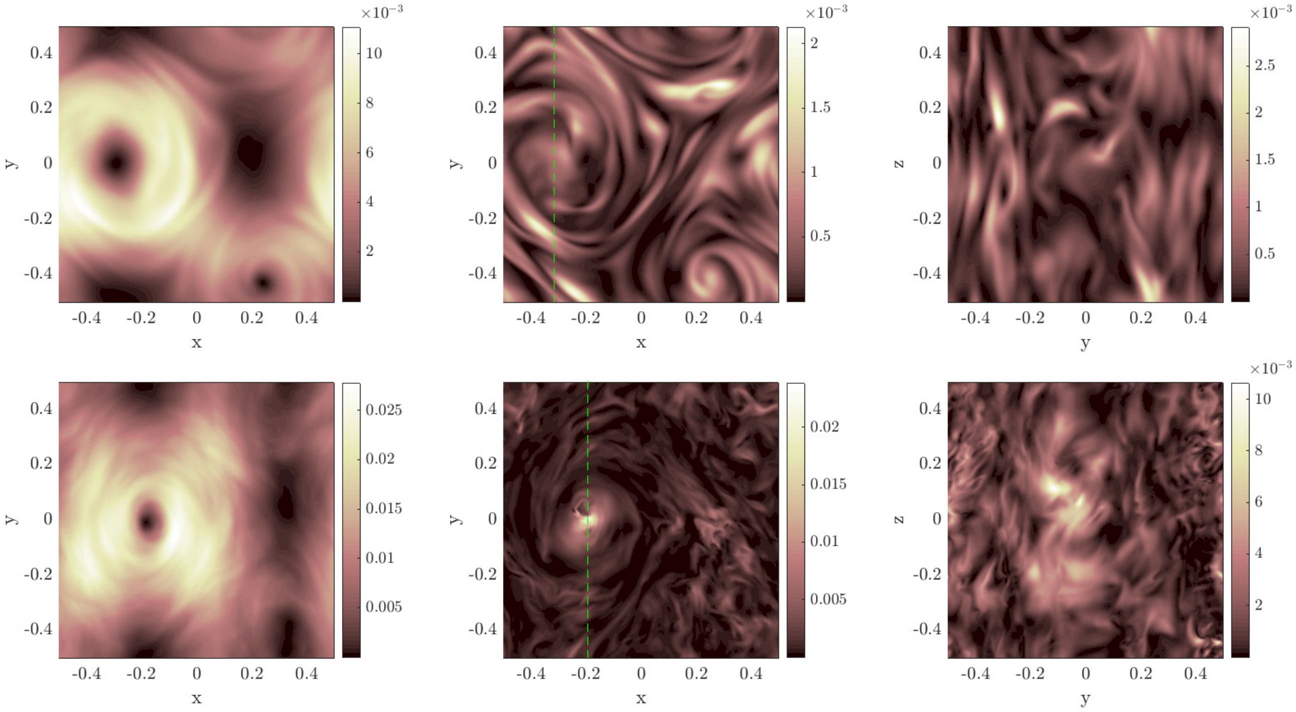

Figure 6.6. Kinetic energy density of 2D vortices (left panels) and 3D wave modes (taken at $z = 0$) in the $(x, y)-$plane (middle panels) and in $(y, z)-$plane (right panels) in the saturated state at $Po = 0.2$ (top row), $Po = 0.3$ (bottom row) and $Re = 10^{4.5}$. The green dotted line, which is at $x = -0.33$ for $Po = 0.2$ and at $x = 0.2$ for $Po = 0.3$, marks that $(y, z)-$section where 3D energy is plotted.

pairs (Po, Re). The color dots represent the ratio of the time- and volume-averaged energy of 2D vortices, $\langle E_{2D}\rangle$, to the total energy of all the modes, $\langle E\rangle$, in the statistically steady turbulent state, as shown in Figs. 6.1 and 6.2. The empty points represent the cases where the energy drops to negligible value meaning that the local flow in the box is stable against precessional instability. The colors show that at given Re, the fraction of 2D mode energy vs. total energy initially increases with Po when $Po \lesssim 0.1$, then reaches a maximum at medium precessions $Po \sim 0.1$ and decrease at larger $Po \gtrsim 0.1$. The maximum shifts towards smaller Po with increasing Re. An analysis distinguishing the latter three groups will be carried out in the following sections.

Having analyzed the time-development of the mode energies, next in Fig. 6.5 we plot the evolution of the volume-averaged (or equivalently integrated in Fourier space) dynamical terms in Eqs. 6.3 and 6.4, i.e., the energy injection, $\langle A\rangle = \sum_{\boldsymbol{k}} A$, for 3D waves (top) and 2D vortical (bottom) modes together with nonlinear transfer term between them, $\langle NL\rangle = \sum_{\boldsymbol{k}} NL$ (middle). To obtain a better visualization and a clear trend we have filtered these terms removing fast oscillations. For 3D waves, energy injection occurs due to the precession instability and hence increases with Po, it is the main energy supplier for the turbulence. As for 2D modes, they are stable against this instability (Kerswell

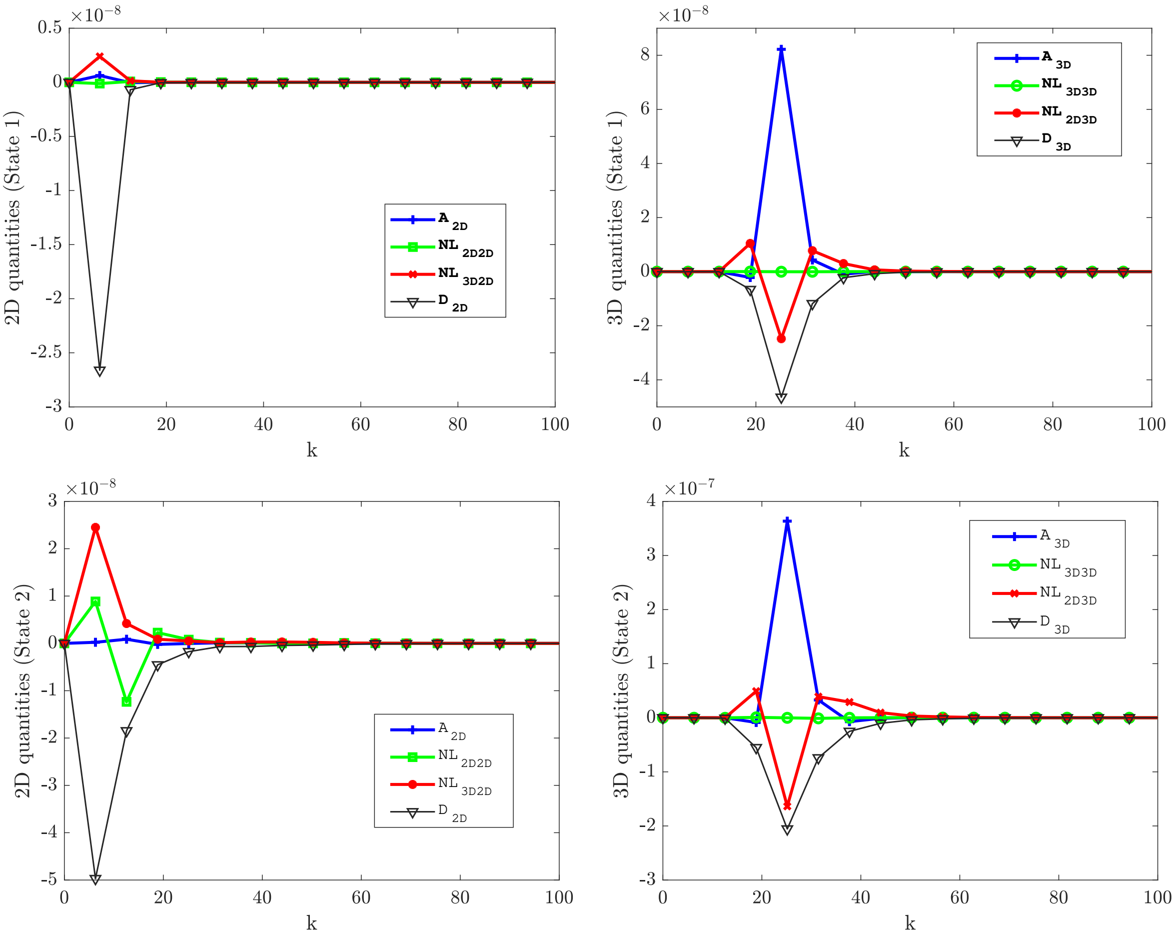

Figure 6.7. Shell-averaged spectra for the injection A (blue), viscous dissipation D (black), and nonlinear transfers among modes inside 2D manifold, NL_{2D2D} (green, left panels), inside 3D manifold NL_{3D3D} (green, right panels) and cross transfers NL_{3D2D} (red, left panels) and NL_{2D3D} (red, right panels) between the modes in these two manifolds. For 2D vortical modes (left panels) and 3D wave modes (right panels) in the State 1 (upper row) and State 2 (bottom row) at $Po = 0.075$ and $Re = 10^{4.5}$.

(1993)) and hence can be excited by the nonlinear interaction with the waves only, which is described by the term NL_{2D3D}, also increasing with Po. This term is overall positive in time, implying transfer of energy from 3D waves to 2D vortices (see also Barker & Lithwick (2013)). The excited 2D modes in turn extract energy from the basic flow via $\langle A_{2D}\rangle$. As a result, the evolution of $\langle A_{2D}\rangle$ is determined by the nonlinear transfer term $\langle NL_{2D3D}\rangle$ and hence follows the latter, as it is seen in Fig. 6.5 where the peaks of both these functions nearly coincide. For $Po = 0.2$, $\langle A_{2D}\rangle \approx \langle A_{3D}\rangle$ (red), while for $Po = 0.3$, $A_{3D} > A_{2D}$ (orange curves), indicating that the precession instability feeds the waves, while the waves in turn feed vortices via a nonlinear cascade. Below we will see how this process occurs scale by scale in Fourier space.

In Fig. 6.3 we have shown the total vorticity field including both 2D vortices and 3D waves. To better visualize these fields, we computed the inverse Fourier transforms from

$\bar{\boldsymbol{u}}_{2D}$ and $\bar{\boldsymbol{u}}_{3D}$ and showed respective energy densities in physical space in the saturated regime in Fig. 6.6. The left panels of this figure show energy of 2D modes, where now we can clearly distinguish two vortices for $Po = 0.2$ (top row) and a single vortex for $Po = 0.3$ (bottom row). The middle panels show the small-scale 3D mode energies in the $(x, y)-$plane at the central height $(z = 0)$ of the box. There is a noticeable difference between the $Po = 0.2$ and $Po = 0.3$ cases: for $Po = 0.2$ we observe larger-scale wave structures, whereas for $Po = 0.3$ the wave field is more fluctuating and rich in smaller scales, implying that increasing precession parameter intensifies first of all 3D waves and indirectly vortices due to their nonlinear coupling with the former. Note also that the 3D wave structures are concentrated around the vortices – a feature observed experimentally in precessing spherical container (Horimoto & Goto (2018)). The right panels show the vertical structure of 3D mode energy in the $(y, z)-$plane at the center of vortices (located at $x = -0.33$ and $x = -0.2$, respectively, for $Po = 0.2$ and 0.3, which are marked with green dotted line in the middle row). Again, the $Po = 0.3$ case shows a more fluctuating behavior with fine scales surrounding the column. So, the main dynamical picture consists of the coexisting columnar (geostrophic) vortices and waves whose magnitude and length-scale depend on the precession strength.

6.4. Spectral dynamics of precession-driven turbulence: vortices, waves and their interplay

So far the study has been mainly conducted in the physical (coordinate) space. However, a deeper insight into the precession-driven turbulence dynamics can be gained by investigating the dynamical processes – energy injection, nonlinear transfers and viscous dissipation – in Fourier space, where much richer dynamical picture unfolds and becomes better accessible to analysis. Following the approach of Mamatsashvili *et al.* (2014, 2016), Buzzicotti *et al.* (2018), we compute and visualize the individual injection A, viscous dissipation D and various nonlinear transfer NL terms entering spectral energy Eqs. (6.3) and (6.4) in Fourier space using the simulation data and analyze their interplay in different regimes with respect to precession parameter identified above.

6.4.1. Quasi-periodic bursts: $Po = 0.075$

As we have seen above, the case with weak precession forcing is characterized by cyclic bursts, where the system alternates between State 1 and State 2. The purpose of this section is to understand the underlying mechanisms of this behavior. With this goal, we analyze and compare the dynamics in two different intervals shown in Fig. 6.2: Δt_1 corresponding to State 1, when the energy of 3D wave modes initially increases due to precessional instability, while the energy of 2D modes is still at its minimum, and Δt_2 corresponding to State 2 when both 3D and 2D mode energies drop.

The shell-averaged spectra of the linear injection A and dissipation D terms for 2D and 3D modes as well as nonlinear transfer terms for 2D-2D, NL_{2D2D}, for 2D-3D, NL_{2D3D} and NL_{3D2D}, and for 3D-3D NL_{3D3D} mode interactions in these two states (also averaged over Δt_1 and Δt_2 time intervals, respectively) are shown in Fig. 6.7. The basic dynamical picture in this regime is the following. In State 1 (top row), the most important contribution is due to A_{3D} (blue), which injects energy into waves from the basic flow due to the initial development of precessional instability. This reaches a large peak at $k = 8\pi$ whose value is positive and larger than the comparable effects of viscous dissipation D_{3D} (black) and transfer NL_{2D3D} (red), which are both negative reaching a minimum at the same wavenumber. The effect of nonlinear transfers among waves, NL_{3D3D} (green) is relatively small at this time. This also implies that the viscosity is already important at the injection scale, that is, there is not a good scale separation (inertial range) between the injection and viscous scales. Nevertheless, $A_{3D} > 0$ is sufficiently large to overcome both these negative (sink) terms and give rise to wave growth in State 1. Since $NL_{2D3D} < 0$ at the injection wavenumbers, its counterpart for 2D modes $NL_{3D2D} > 0$, indicating that the waves nonlinearly transfer their energy to and amplify 2D vortices but at lower wavenumbers near the peak 2π of this term. These vortices additionally receive some energy from the basic flow due to the positive A_{2D} (blue) term. However, the dissipation $D_{2D} < 0$ (black curve in top left panel) for vortices is quite high, prevailing over the positive NL_{3D2D} (red) and A_{2D} and as a result vortices do not yet grow at these times.

The nonlinear transfers between waves and vortices, NL_{3D2D} and NL_{2D3D}, increase by absolute value (but retain their signs) with time and already in State 2 mostly negative NL_{2D3D}, together with dissipation $D_{3D} < 0$, dominate positive injection A_{3D} (bottom right plot in 6.7). As a result, wave energy quickly drops in State 2 (see also Fig. 6.2). On the other hand, the 2D vortices, which now receive much more energy from waves via the term $NL_{3D2D} > 0$, also develop an inverse cascade themselves described by NL_{2D2D} (bottom left panel). This is manifested in the emergence of large-scale vortices in physical space in State 2 (top right plot of Fig. 6.3). The injection A_{2D} is relatively small/insignificant at these times. However, dissipation D_{2D} is still larger than the nonlinear replenishment by NL_{3D2D} and consequently the energy of vortices slowly decreases too (Fig. 6.2). Once vortices have become weak enough, the waves can grow again due to the precessional instability and close the cycle loop. Thus, we can conclude that the bursts are caused by a quasi-periodic behavior of 3D dynamical terms which in State 1 $\sum_{\boldsymbol{k}}(A_{3D} + NL_{3D} + D_{3D}) > 0$ leading to wave energy amplification, whereas in State 2

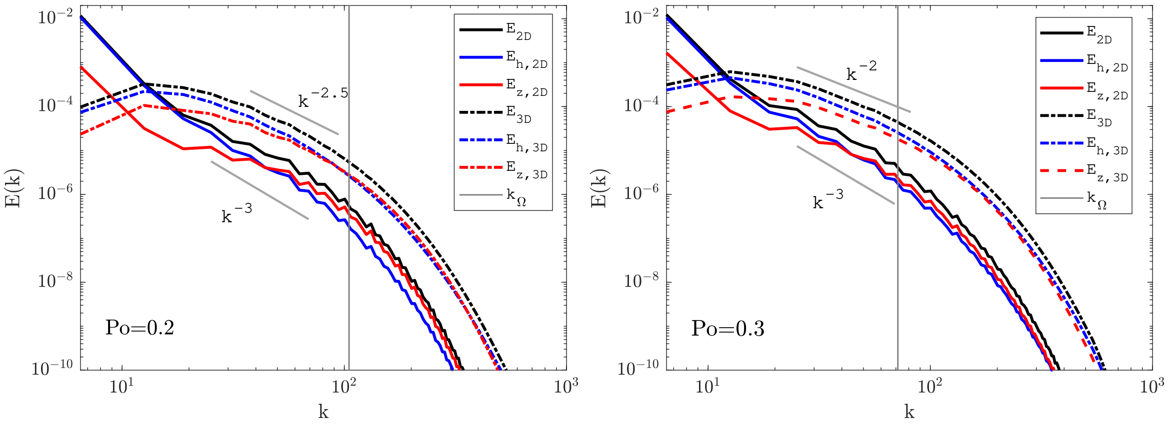

Figure 6.8. Shell-averaged energy spectra in a statistically steady turbulent state at $Po = 0.2$ (left), 0.3 (right) and $Re = 10^{4.5}$. In both cases, we distinguish between 2D mode energies (solid lines) and 3D mode energies (dashed lines), while the colors represent the total E (black), horizontal, $E_h = (|\bar{u}_x|^2 + |\bar{u}_y|^2)/2$ (blue) and vertical $E_z = |\bar{u}_z|^2/2$ (red) components. Grey vertical line shows the location of Zeman scale k_Ω.

$\sum_{\boldsymbol{k}}(A_{3D} + NL_{3D} + D_{3D}) < 0$ leading to energy decay.

6.4.2. Quasi-steady turbulence: $Po = 0.2$ and 0.3

In this Subsection we present similar analyses of the dynamical processes in Fourier space, focusing on the regime of large $Po = 0.2$ and 0.3 where the saturated state is characterized by a quasi-steady turbulence, where both 3D and 2D mode energies evolve in time with only mild fluctuations in contrast to the small-Po regime displaying quasi-periodic bursts (Fig. 6.2). We keep the Reynolds number fixed, $Re = 10^{4.5}$, to focus on the impact of an increasing precession on the spectral properties and dynamical balances of the turbulence.

Energy spectrum

Figure 6.8 shows the shell-averaged kinetic energy spectra of 2D vortices and 3D waves divided further into horizontal, $E_h = (|\bar{u}_x|^2 + |\bar{u}_y|^2)/2$, and vertical, $E_z = |\bar{u}_z|^2/2$, components at $Po = 0.2$ (left panel) and 0.3 (right panel). The time-average has been done over $\Delta t \approx 1000$ in the saturated state.[3] In this figure, the grey vertical lines mark the locations of Zeman wavenumber k_Ω defined in the presence of the energy injection due to the precessional instability as $k_\Omega = (\Omega^3/\langle A_{2D} + A_{3D}\rangle)^{1/2}$ (equal to $1/\langle A_{2D} + A_{3D}\rangle^{1/2}$ in

---

[3] As a convergence study, we have checked the robustness of the results by comparing averages over different time ranges finding very good agreement.

non-dimensional units), where $\langle A_{2D} + A_{3D} \rangle$ is the volume-averaged total injection term introduced. This definition of k_Ω differs from the usual one used in the rotating turbulence theory (Zeman (1994), Müller & Thiele (2007), Alexakis & Biferale (2018)) in that the energy injection rate, ε, due to an external forcing is replaced here by the injection due to the instability. The most remarkable aspect is the different shape and scaling of energy spectra for the 2D and 3D modes. The 2D mode energy dominates over 3D one at small wavenumbers $k \lesssim 10$ where it increases with decreasing k, reaching a maximum at the largest box scale, with its horizontal component being about an order of magnitude larger than the vertical one. This corresponds to large-scale horizontal vortical motions in physical space, as is seen in Figs. 6.3 and 6.6. At higher $10 \lesssim k \lesssim k_\Omega$, the horizontal and vertical components are comparable in the E_{2D} spectrum and its slope is close to k^{-3}, exhibiting the same power-law dependence of rotating geostrophic 2D turbulence (Smith & Waleffe (1999), Buzzicotti *et al.* (2018), Khlifi *et al.* (2018)), which does not appear to change with precession parameter Po.

The energy spectrum of 3D waves, E_{3D}, has a peak at larger $k \approx 15$ than that of E_{2D} (which approximately coincides with the peak of injection A_{3D} in Fig. 6.11). E_{3D} decreases then at lower wavenumbers, while at higher wavenumbers $15 \lesssim k \lesssim k_\Omega$ follows a scaling $\sim k^{-2\pm0.5}$ which has been typically observed in forced rotating turbulence of inertial waves in other related papers (Müller & Thiele (2007), Khlifi *et al.* (2018), Alexakis & Biferale (2018)). However, in contrast to these papers using a forcing in a very narrow wavenumber band, we do not prescribe the forced wavenumber a priori (their is no external forcing here), instead injection wavenumbers are determined by the basic flow system itself through the precessional instability and extend over a broad range (see below). Precession influences the scaling exponent of the E_{3D} spectrum: its slope seems to become shallower with increasing Po, as is seen in Figs. 6.8 (compare left and right panels) and 6.13 below. Like for 2D mode energy, also for 3D mode energy, horizontal and vertical components are comparable at higher wavenumbers, but the horizontal one dominates at lower wavenumbers.

It is seen in Fig. 6.8 that the observed power-law scalings of both 2D and 3D mode energy spectra occur at $k < k_\Omega$ and therefore are strongly influenced by rotation and precession, deviating from the classical Kolmogorov $k^{-5/3}$ spectrum. However, as is seen in this figure, with increasing precession strength Po, the Zeman wavenumber k_Ω (grey vertical lines) decreases, that is, the effect of rotation becomes increasingly weaker for lower and lower k. We will see below that in this case the energy spectrum at $k > k_\Omega$ indeed approaches Kolmogorov spectrum.

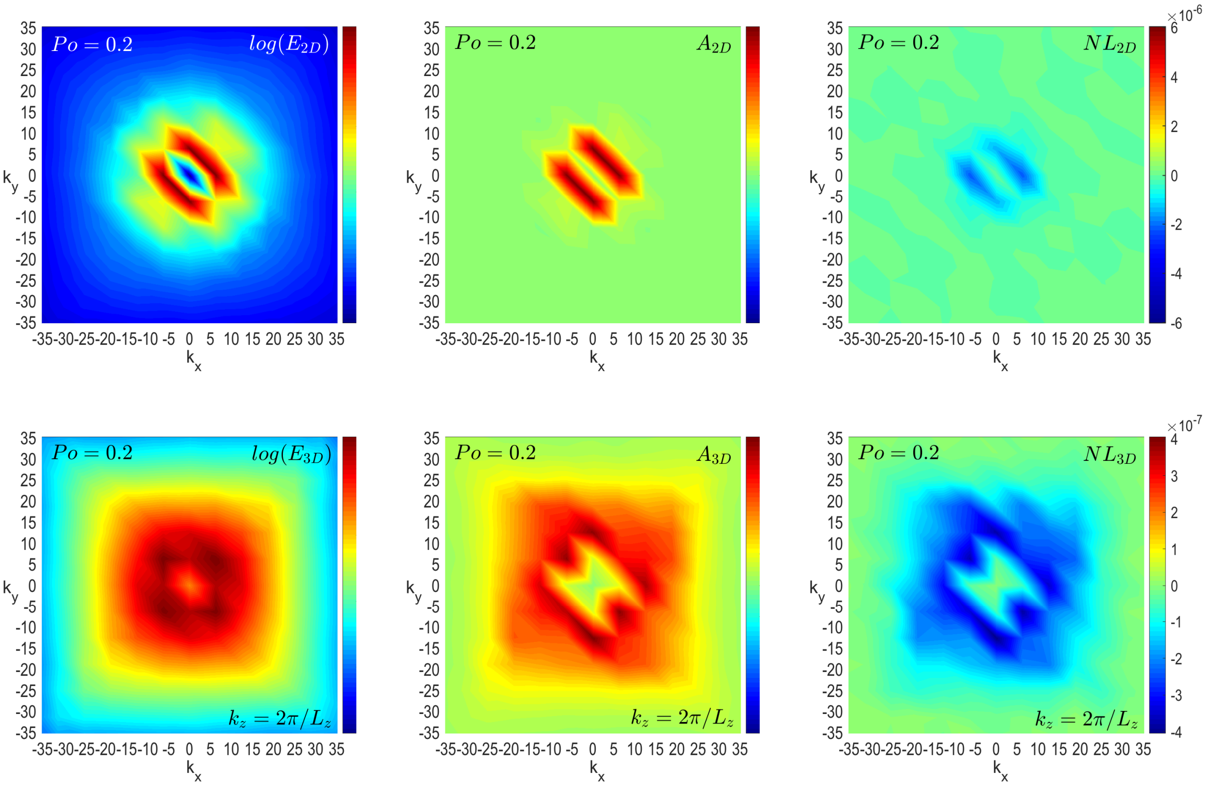

Figure 6.9. Maps of the time-averaged spectral energy E (left panels), injection A (middle panels) and the total nonlinear transfer term NL (right panels) in the $(k_x, k_y)-$plane for 2D vortical modes with $k_z = 0$ (top row) and 3D wave modes at the first $k_z = 2\pi/L_z$ in the box (bottom row) in the quasi-steady turbulent state with $Po = 0.2$ and $Re = 10^{4.5}$. Note the noticeable anisotropy of 2D manifold spectra compared with nearly isotropic spectra of 3D manifold.

Dynamical balances in Fourier space

To see the structure of spectra of energy and dynamical terms in the quasi-steady precessional turbulence, in Figs. 6.9 and 6.10 we show the time-averaged spectra of the kinetic energy E, energy injection A and the total nonlinear transfer NL in two different horizontal $(k_x, k_y)-$planes: at $k_z = 0$ for the 2D modes and at $k_z = 2\pi/L_z$ for the 3D wave modes. We have chosen here $k_z = 2\pi/L_z$ because it corresponds to the maximum injection along k_z-axis, for which therefore the precession instability reaches the largest growth rate in the box (Salhi & Cambon (2009)). The most striking observation is the anisotropic nature of the 2D manifold in Fourier space (top row), for A_{2D} and NL_{2D} and hence for the kinetic energy spectrum E_{2D} determined by the joint action of these terms, which are all localized at smaller wavenumbers, with a clear inclination towards the k_x axes. The injection term A_{2D} is always positive, implying some energy injection from the basic flow into vortices. By contrast, NL_{2D} is negative at the same wavenumbers for $Po = 0.2$, but changes sign at $Po = 0.3$. As a result, the dynamical balances for 2D modes are different for these two values of Po, which will be discussed below. In

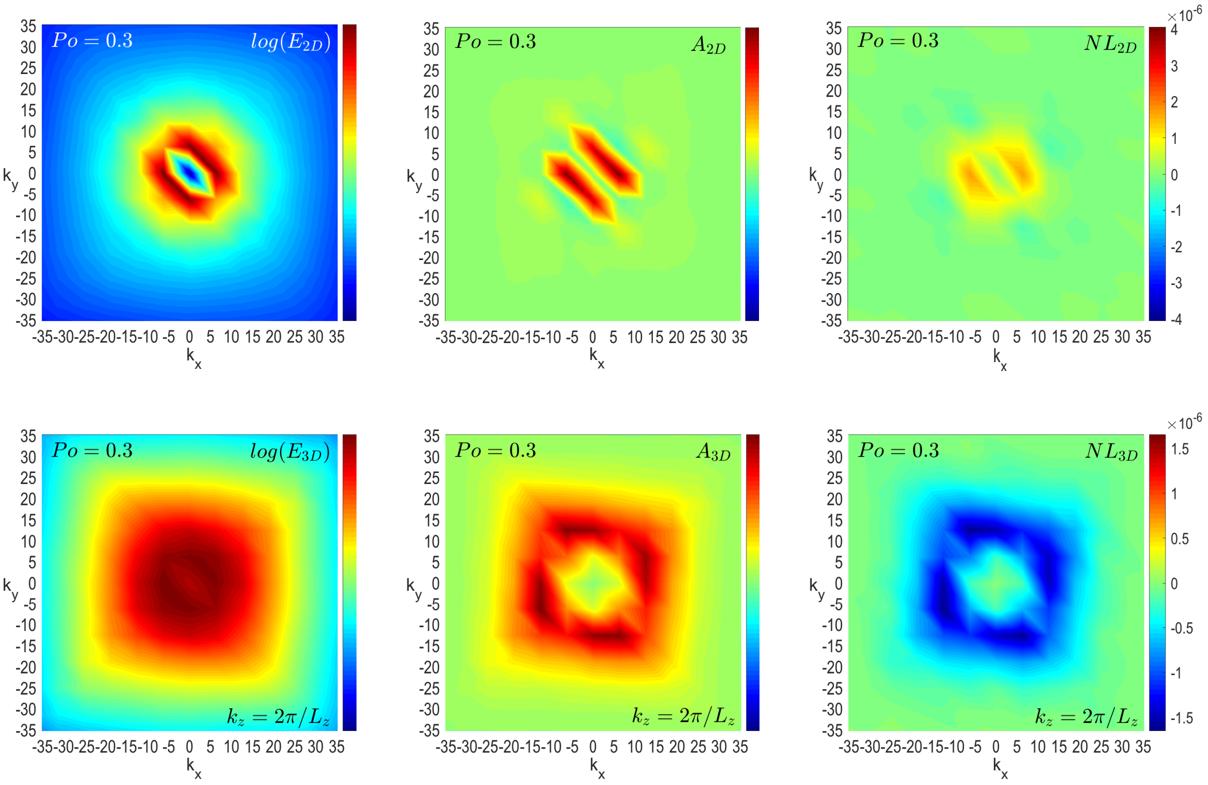

Figure 6.10. The same as in Fig. 6.9, but for $Po = 0.3$. Note the change of sign of NL_{2D} compared to the $Po = 0.2$ case.

contrast, the 3D manifold exhibits a quasi-isotropic distribution (bottom row, similarly at larger $k_z > 2\pi/L_z$ not shown here) for both $Po = 0.2$ and 0.3, whose range extends over larger wavenumbers than that of 2D quantities. Comparing the A_{3D} and NL_{3D}, the first injection term, which is due to the precessional instability, is always positive and appreciable at $5 < |k_x|, |k_y| < 25$ (yellow/red area), while the second nonlinear term is negative (blue) and also appreciable at these wavenumbers. The similar shape of these two functions in Fourier space and their comparable absolute values imply that these two processes are in balance: 3D modes receive energy from the precessional background flow predominantly in the range $5 < |k_x|, |k_y| < 25$, while nonlinearity, counteracting injection at these wavenumbers, transfer this energy to other 3D and 2D modes with different wavenumbers.

From Figs. 6.9 and 6.10, showing the distribution of total nonlinear terms NL_{2D} and NL_{3D} in Fourier space, one cannot establish specifically what kind of transfer mechanisms operate, that is, whether the cascades inside a given manifold are direct or inverse or if there are transfers of energy between these two manifolds, since these terms encapsulate nonlinear interactions among all kinds of modes. To get insight into the details of linear (energy injection) and nonlinear cascade processes in the precessional turbulence, in Fig. 6.11 we show the shell- and time-averaged spectra of all the dynamical terms – injection A,

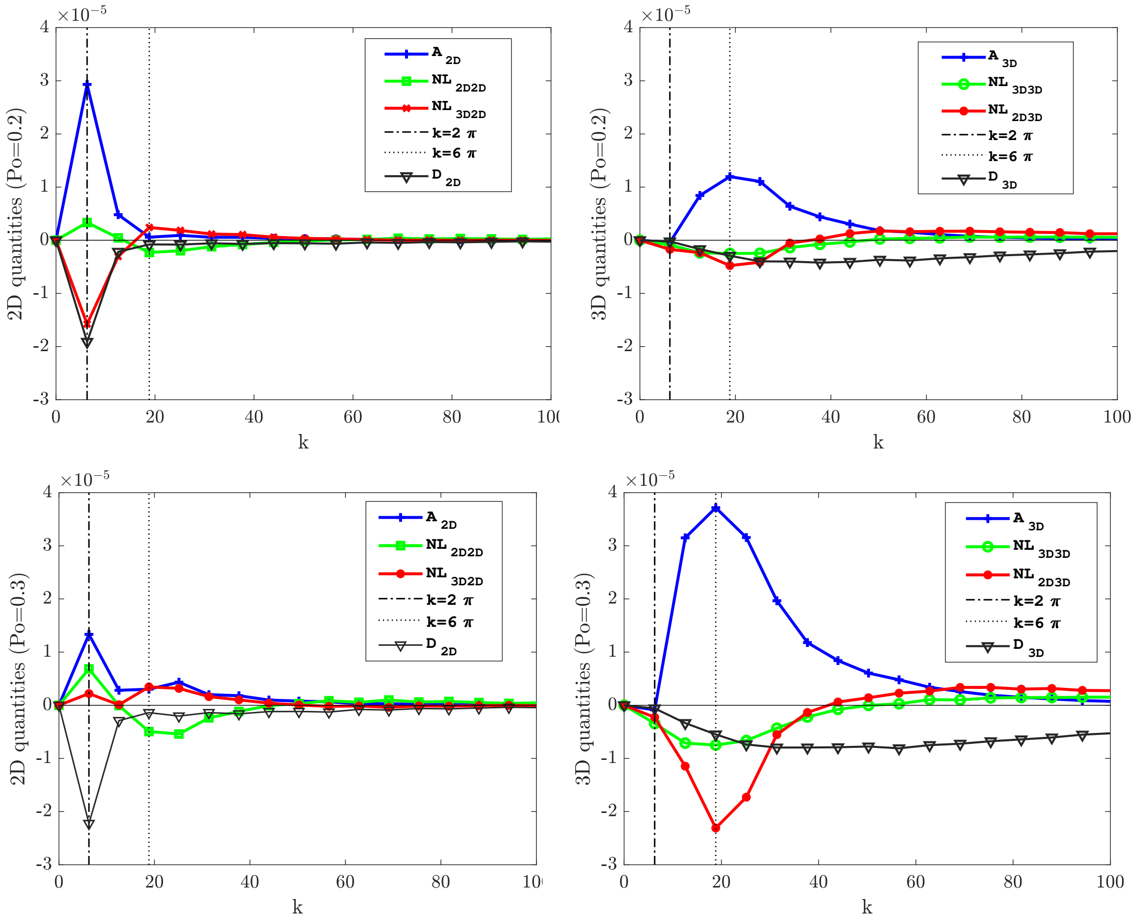

Figure 6.11. Shell-averaged spectra for the injection A (blue), viscous dissipation D (black), and nonlinear transfers among modes inside 2D manifold, NL_{2D2D} (green, left panels), inside 3D manifold NL_{3D3D} (green, right panels) and cross transfers NL_{3D2D} (red, left column) and NL_{2D3D} (red, right panels) between the modes in these two manifolds. For 2D vortical modes (left panels) and 3D wave modes (right panels) in the quasi-steady turbulent state at $Po = 0.2$ (top row), 0.3 (bottom row) and $Re = 10^{4.5}$. Dotted black vertical line marks the peak of the injection term A_{3D}, while the dash-dotted line the peak of A_{2D}.

nonlinear NL and dissipation D terms – entering Eqs. (6.3) and (6.4) again for $Po = 0.2$ and $Po = 0.3$, as we did for the bursty case $Po = 0.075$ in the above subsection.

The precession instability injects energy into 3D waves, which is described by positive A_{3D} (blue, right panels). Unlike the case of a forcing localized about certain wavenumber (Buzzicotti *et al.* (2018)), the injection due to the instability extends over a range of wavenumbers, reaching a peak at $k = 6\pi$, and increases with increasing Po. Since it is a quasi-steady state, the energy injection is balanced by nonlinear transfers, $A_{3D} + NL_{3D3D} + NL_{2D3D} \approx 0$, at those dynamically active wavenumbers where $A_{3D} > 0$ is appreciable [the role of viscous dissipation D_{3D} (black, right panels) is not important at these wavenumbers. Therefore, being negative at those injection wavenumbers, $NL_{3D3D} < 0$ (green, left panels) and $NL_{2D3D} < 0$ (red, left panels) they drain energy from the active

3D modes there and transfer it, respectively, to smaller-scale 3D waves due to positive $NL_{3D3D} > 0$ at $k > 40$ (forward/direct cascade) and to 2D vortical modes. The latter process is mediated by positive $NL_{3D2D} > 0$ (red, left panels) at $k > 18$, peaking at the same $k = 6\pi$. At these wavenumbers, 2D-2D transfer term is negative $NL_{2D2D} < 0$ (green, left panels), with a minimum also at $k = 6\pi$, and causes an inverse cascade of 2D mode energy to even smaller wavenumbers where it is positive $NL_{2D2D} > 0$ and reaches a maximum at $k = 2\pi$ that corresponds to the the largest box scale. These vortices draw some energy from the basic flow as well due to the A_{2D} term, which has a peak at the same $k = 2\pi$ as $NL_{2D2D} > 0$. It is seen that A_{2D} decreases, whereas NL_{2D2D} increases with Po and therefore this energy extraction can not be considered as a pure injection of energy into 2D modes but rather an effect induced by the "real" injection A_{3D} through nonlinearity, since the peak of A_{2D} coincides with the peak of positive NL_{2D2D}. Besides, in the linear regime, as mentioned above, idealized steady 2D vortices are stable against precessional instability (i.e., $A_{2D} = 0$). The 2D-3D nonlinear interaction term NL_{2D3D} is positive at large wavenumbers $k > 40$, redistributing part of the energy of 2D large-scale vortices back to smaller-scale 3D waves (forward cascade). Thus, as it is seen from Fig. 6.11 (left panels), similar to that for 3D modes, also for 2D modes, there is a balance among production of these modes by 2D-3D transfers, energy extraction, 2D-2D transfers, and viscous dissipation, $A_{2D}+NL_{2D2D}+NL_{3D2D}+D_{2D} \approx 0$. Note that viscous dissipation for 2D and 3D modes have completely different behavior (compare black curves in left and right panels). It is stronger and more significant for the 2D vortices: D_{2D} has a clear minimum at low wavenumber $k = 2\pi$, which coincides with the peak of A_{2D} and NL_{3D2D}, and counteracts these terms, indicating a dissipative nature of the vortices. On the other hand, for 3D modes viscosity is important only at higher $k > 40$, i.e., small scales are dissipative, in contrast to that in the bursty regime, where viscous and injection scales coincide (right panels in Fig. 6.7).

Note that the strength of all the dynamical processes depicted in Fig. 6.11 increases with increasing Po. In all cases, the peaks of energy injections into 3D wave modes due to the precessional instability are concentrated at wavenumbers smaller than the corresponding Zeman wavenumber, $k_{in,3D} = 6\pi < k_{\Omega}$ (grey vertical lines in Fig. 6.8). As we have seen in the left panels of Fig. 6.11, this injection affects the 2D-3D nonlinear transfer NL_{3D2D}, which represents the driving of 2D vortices by 3D wave modes, has a maximum at the same k_{in}. This is in agreement with the general condition for the upscale/inverse energy cascade of 2D vortices towards wavenumbers smaller than the injection one, i.e. $k < k_{in}$, in rotating turbulence (Buzzicotti *et al.* (2018)). However, in the present case of precessional driving, in the inverse cascade regime, the energy spectrum of 2D modes is slightly steeper than a k^{-3} slope (Fig. 6.8), which is usually observed in the same regime in a purely rotating case.

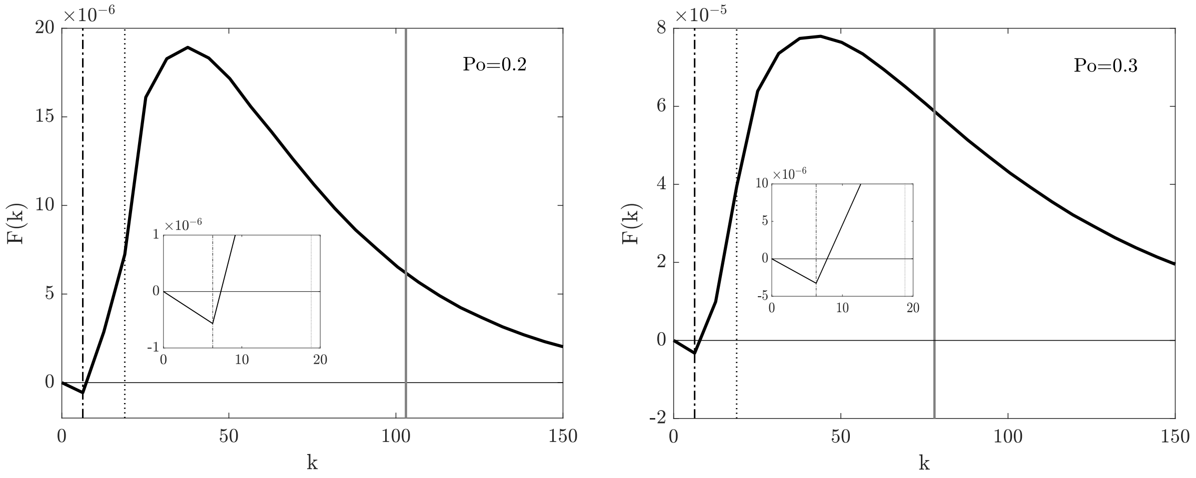

Figure 6.12. Plot of the total energy flux $F(k)$ with the vertical lines representing, for reference, the wave numbers $k_{in,2D} = 2\pi$ (dashed-dotted) and $k_{in,3D} = 6\pi$ (dotted) at the peak of the injection, respectively, for 2D and 3D modes as well as the Zeman wavenumber k_Ω (solid grey). Top panel is for $Po = 0.2$ and bottom for $Po = 0.3$. The flux is predominantly positive, $F > 0$, for larger wavenumbers $k > k_{in,2D}$ corresponding to forward cascade. The inset zoom into the inverse cascade range at small k, where $F < 0$.

Overall the above-described processes of nonlinear transfers inside the 3D manifold, inside the 2D manifold and coupling between these two manifolds are consistent with previous spectral analyses of turbulence dynamics under rotation and an imposed external forcing (Biferale *et al.* (2016), Buzzicotti *et al.* (2018), Alexakis & Biferale (2018)). In particular, in Fig. (6.11) we observe the *split* (simultaneous inverse and forward) cascade of energy typical of rotating turbulence as demonstrated in those papers, that is, forward cascade of 3D wave mode energy to high wavenumbers (small-scales) due to NL_{3D3D} and NL_{2D3D}, and inverse cascade of 2D modes to small wavenumbers (large-scales) due to NL_{2D2D}.

To confirm the overall type (direction) of the nonlinear cascades inferred above on the basis of the nonlinear transfers NL as a function of k, we also analyze shell-to-shell flux of the total energy defined as (Alexakis & Biferale (2018)):

$$F(k) = \sum_{k' \geq k} NL\,(k')\,. \tag{6.6}$$

Figure 6.12 shows the resulting flux function $F(k)$ and, for reference, the wavenumbers $k_{in,2D} = 2\pi$ and $k_{in,3D} = 6\pi$ at which the injection terms A_{2D} and A_{3D}, respectively, reach their maximum (Fig. 6.11). The grey line in this figure represents the Zeman wavenumber k_Ω. The shape of the total fluxes are qualitatively similar for $Po = 0.2$ and 0.3 and indeed display split/dual cascade: they are positive, $F > 0$, at $k > k_{in,2D}$ with a maximum value around $k \approx 50$, indicating a forward cascade of energy, and negative, $F < 0$, at small wavenumbers $k < k_{in,2D}$, indicating inverse cascade. These forward/inverse cascade

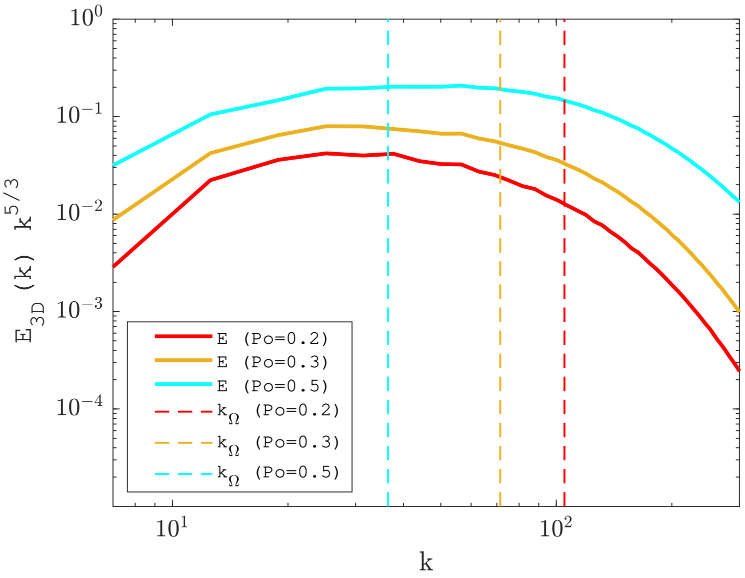

Figure 6.13. Kinetic energy spectra for 3D wave modes compensated by the Kolmogorov law $k^{-5/3}$. Solid lines represent E_{3D} for three different precession parameters $Po = 0.2$, 0.3 and 0.5 at $Re = 10^{4.5}$, while the vertical dashed lines represent the corresponding (in terms of colors) Zeman wavenumbers k_Ω. As Po is increased, k_Ω decreases and the spectrum approaches Kolmogorov scaling at $k > k_\Omega$.

regimes deduced from the behavior of the energy flux function $F(k)$ in fact confirm those found above based on the behavior of the transfer functions in Fig. 6.11. Specifically, the forward cascade at $k > k_{in,2D}$ is related to the transfer of 3D wave mode energy to higher-k, while the inverse cascade at $k < k_{in,2D}$ is related to the transfer of 2D vortical mode energy to smaller-k.

Precession forcing: a way to isotropic Kolmogorov turbulence

In this section, we draw conclusions on the properties of 3D wave modes which are the ones directly influenced and driven by the precession instability. We have already seen clear indications that these modes exhibit characteristics of isotropicity, direct cascade and decreasing the wavenumber range where the rotation is substantially dominant, that is, decreasing the Zeman wavenumber k_Ω, with increasing precession intensity. In order to confirm and generalize these concepts, we run another simulation for quite high precession parameter $Po = 0.5$ and with the same $Re = 10^{4.5}$ to check this trend.

Figure 6.13 shows the spectra of 3D mode energy for the three precession parameters. This time we compensated E_{3D} spectra with the Kolmogorov spectrum $k^{-5/3}$ to better see if the energy spectrum approaches the Kolmogorov one. Indeed, it is seen in this figure

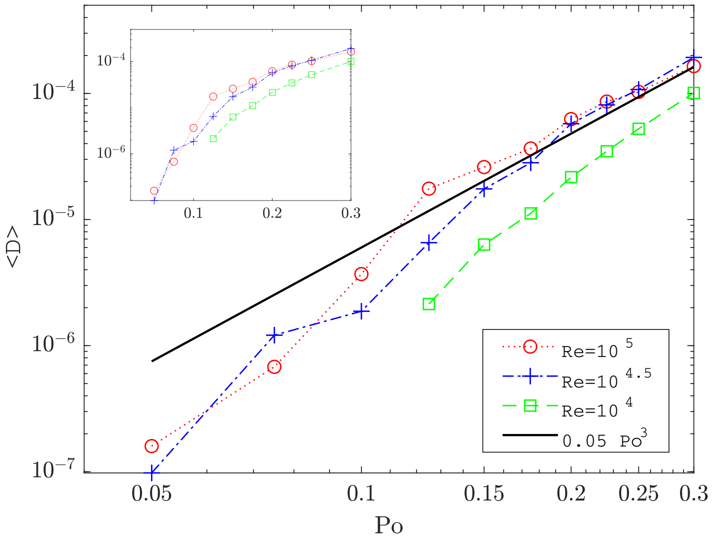

Figure 6.14. Time and volume averaged dissipation $\langle D \rangle$ as a function of the precession ratio. The various curves represent three different Reynolds numbers and the black solid line is the scaling $\sim Po^3$ given for reference. Inset plot zooms into the jump around $Po \approx 0.1$ in the linear scale associated with the transition from bursty to statistically steady turbulent regimes.

that increasing Po, the Zeman wavenumber decreases and the compensated spectrum at $k > k_\Omega$ becomes gradually flatter, indicating an approach to the Kolmogorov one $k^{-5/3}$ already at $Po = 0.5$, that is, the regime of isotropic homogeneous turbulence. Thus, we showed that the rotation-dominated range of wavenumbers $k < k_\Omega$ is narrowed as Po increases because of a dramatic decrease in Zeman wavenumbers (e.g., $k_\Omega = 103$ for $Po = 0.2$ reducing to $k_\Omega = 38$ for $Po = 0.5$). This is also reflected in the increase of Rossby number $Ro = \left(A_{2D}k_{in,2D}^2 + A_{3D}k_{in,3D}^2\right)^{1/3}/\Omega$. Specifically, we have $Ro \approx 0.176$ for $Po = 0.2$, $Ro \approx 0.24$ for $Po = 0.3$ and $Ro = 0.32$ for $Po = 0.5$.

Turbulent dissipation

We examine the dissipative nature of the precession-driven turbulent flow. Dissipation rate is an important quantity used in both experiments and numerical works to check global changes in the flow behavior such as hysteresis cycles or transition to turbulence, resulting in noticeable increase of this quantity. Figure 6.14 plots the time- and volume-averaged dissipation term $\langle D \rangle$ as a function of Po at different Re. It is seen in this figure that the turbulent dissipation more depends on Po and changes only weakly with Re. This result is in agreement with the observations by Goto *et al.* (2014) according to which turbulence properties are mainly governed by Po rather than Re. At larger $Po \gtrsim 0.1$, the turbulent dissipation scales with Po^3 in accordance with Barker (2016). Moreover, around $Po \approx 0.1$ we observe a jump which is consistent with the global simulation results in cylindrical geometry (Kong *et al.* (2015), Pizzi *et al.* (2021a), Pizzi *et al.* (2021b)) as well as with the local analysis (Barker (2016)). This jump is associated with the transition of the bursty regime at $Po \lesssim 0.1$, dominated by large-scale columnar vortices, where waves and hence turbulent dissipation are relatively weak, to the quasi-steady turbulence regime at $Po \gtrsim 0.1$, where the contribution of small-scale waves is larger leading to efficient dissipation. Therefore, the well-known transition observed in precessing fluid filled cylinder (connected with the hysteresis regime (Herault *et al.* (2015)) can be interpreted in light of those results.

6.5. Impact of Reynolds number

In this Section, we discuss how the Reynolds number affects the behavior of precession-driven turbulence. First we consider the bursty regime. For this purpose, we analyze the time-evolution of the kinetic energy for the leftmost points at a given Re of the regime diagram in Fig. 6.4. The results are shown in the top row (left and right panels) of Fig. 6.15, where we have separately put the lower $Re \leq 10^{4.5}$ and higher $Re \geq 10^5$ cases, respectively. This choice is motivated by the fact that we would like to highlight the difference in the duration of the bursts, which is basically determined by the viscous decay of vortices. Indeed, the nature of time-evolution is qualitatively similar in all these cases. The lower Reynolds number cases exhibit shorter decay periods because of relatively small viscous times compared to higher Reynolds ones where viscous time is correspondingly large (for instance the $Re = 10^{5.5}$ seems to have a period approximately between $2000 < t < 7500$). From the right-top plot it is seen that at high $Re \geq 10^5$, the time-average value of the kinetic energy seems to be more sensitive to Po and only weakly increases with Re. An analogous behavior is observed in the case of hyperviscosity where the bursty behavior is noticeably weakened due to shifting of viscous dissipation towards large wave numbers and is reduced at lower wavenumbers corresponding to vortical modes. The bottom left panel of Fig. 6.15 shows the impact of Re on the evolution of the quasi-steady turbulence at $Po = 0.3$. At all three considered values $Re = 10^4, \sim 10^{4.5}$ and 10^5, the curves are quite steady with only minor fluctuations. The level of the saturated kinetic energy increases with Re, but seems to converge at higher $Re \geq 10^{4.5}$. Therefore, the results about the spectral behaviors discussed in this paper for $Re = 10^{4.5}$ can be extended also to larger Re regimes. For a given value of Po, the evolution of the volume-averaged kinetic energy at lower Re corresponds to the bursty regime, while at higher Re to the quasi-steady regime, as is seen in Fig. 6.15 for $Po = 0.3$ where these two states are occurring, respectively, at $Re = 10^{3.5}$ (blue, top left) and $Re = 10^5$ (black, bottom

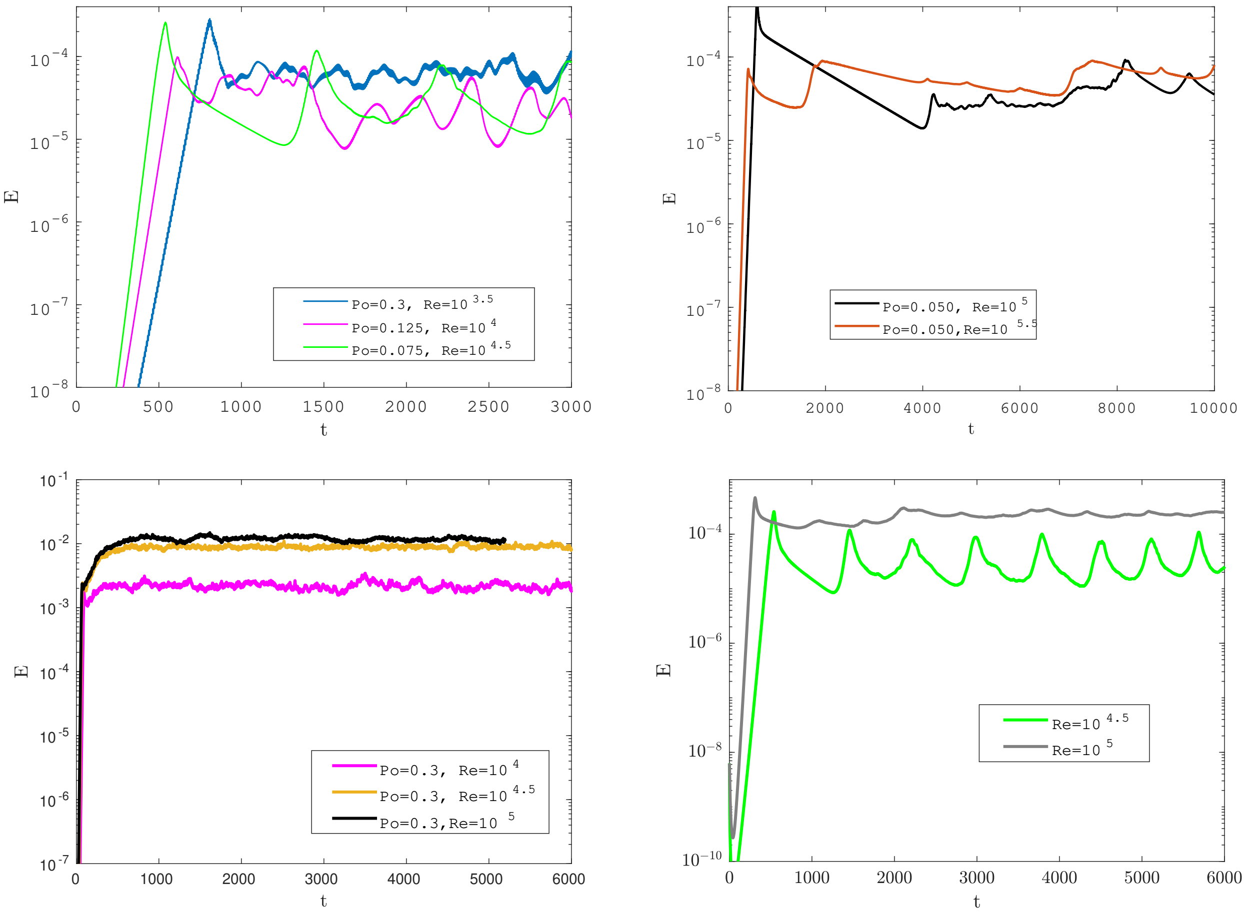

Figure 6.15. Time-evolution of the volume-averaged total kinetic energy for the bursty cases, at lower Reynolds numbers $Re \leq 10^{4.5}$ (top left) and high Reynolds numbers $Re \geq 10^5$ (top right) with different Po as well as for the quasi-steady turbulent case at $Po = 0.3$ and different Re (bottom left). Bottom right panel shows the contrast between the time-evolution of the kinetic energy for $Po = 0.075$ when it is of bursty nature at lower $Re = 10^{4.5}$ and when it is quasi-steady at higher $Re = 10^5$.

left). A similar situation is shown for $Po = 0.075$ in the bottom right panel, with bursts at $Re = 10^{4.5}$ and quasi-steady turbulence at $Re = 10^5$. From this we can conclude that the threshold value Po_c, demarcating these main two regimes in the precessional flow increases with decreasing Re, but still is of the order of $Po_c \sim 0.1$ in the chosen range of $Re \in [10^{3.5}, \sim 10^5]$.

6.6. Summary

In this Chapter, the properties of rotating turbulence driven by precession were studied using direct numerical simulations and analyses of the underlying dynamical processes in Fourier/wavenumber space. The investigation was carried out in the local rotating coordinate frame, where precession gives rise to a background shear flow, which becomes linearly unstable and breaks down into turbulence whose intensity and properties vary with strength of the precession. We observed that this precession-driven turbulence is in general characterized by coexisting 2D columnar vortices and 3D inertial waves, whose relative energies depend on the precession parameter Po. The vortices resemble the typical condensates of geostrophic turbulence, are aligned along the rotation axis (with zero wavenumber in this direction, $k_z = 0$) and are fed by the 3D waves through nonlinear transfer of energy, while the waves (with $k_z \neq 0$) in turn are directly fed by the precession instability of the background flow. The vortices themselves undergo an inverse cascade of energy and exhibit anisotropy in Fourier space. For small $Po \lesssim 0.1$ and sufficiently high Reynolds number, the typical regime for geophysical and astrophysical applications, the flow shows strongly oscillatory (bursty) evolution due to the alternation of vortices and small-scale waves. On the other hand, at larger $Po \gtrsim 0.1$ turbulence is quasi-steady with only mild fluctuations, the coexisting columnar vortices and waves in this state give rise to a split (i.e., simultaneous inverse and forward) cascade. Increasing the precession magnitude causes a reinforcement of waves and a weakening of 2D vortices with the energy spectra approaching the Kolmogorov scale. All these phenomena indicate that the precession mechanism counteracts the rotation. We quantified the nonlinear interactions between 3D waves and 2D geostrophic vortices, obtained the spectral scalings and determine the types of cascades in each manifold. We extended the study not just limiting to the shell-averaged approach, generalizing spectral analysis in Fourier space. In this way, we identified anisotropic structure of these modes. Each phenomena deserves a more extended discussion:

1. *Different states observed*: precession forcing is responsible for the appearance of a turbulent state and the Poincaré number determines the flow response. We have identified three different states: quasi-periodic states, characterized by the competition between geostrophic vortex columns and 3D inertial waves at small $Po \lesssim 0.1$; intermediate states at $Po \sim 0.1$ with coexisting 2D vortices and 3D waves with comparable amplitudes, and the state dominated by smaller scale waves with some mixture of vortices at high Po. At very small $Po \lesssim 0.01$, our models are linearly stable against precessional instability and hence turbulence has not been observed.

2. *Bursting evolution*: for small precession parameters we observed a cyclic trend of the flow where the vortices appear and disappear periodically. In this regime, the precession instability injects energy in the 3D waves which transfer directly to vortices due to nonlinearity. However, they decay due to their large dissipative character which is not counteracted by the energy taken from the 3D waves. This explanation

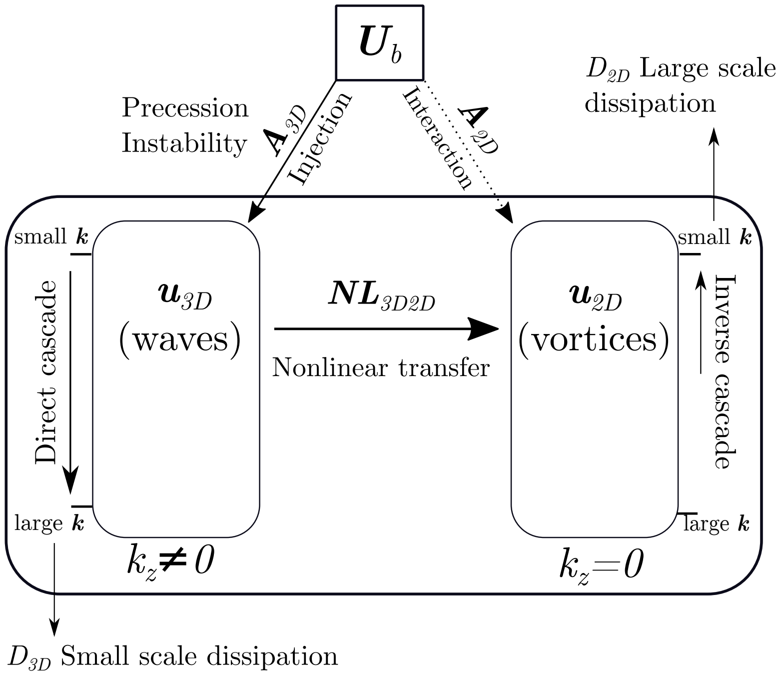

Figure 6.16. Sketch of the main mechanisms underlying precession-driven turbulence.

is consistent with the analogous behavior observed for tidal elliptical instability. Indeed the bursty nature of vortices due to viscosity disappears when a hyperviscosity model is adopted, i.e., when dissipation are concentrated only at large wavenumbers (Barker & Lithwick (2013), Barker (2016)).

3. *Quasi-steady turbulent states*: at moderate and large precession parameters the essential dynamical picture of the precessional-driven turbulence is described in Fig. 6.16 and can be summarized as follows. The precession background flow is unstable to precession instability, whose nonlinear development causes transition to sustained turbulence. In this state, the instability injects energy in the 3D waves, which in turn, is transferred partly to 2D vortices and partly dissipate through a forward cascade. The 2D vortices receive energy from 3D waves and at the same time they interact with the background flow in a sort of tuning effect. These vortices are subjected to an inverse cascade which is balanced by dissipation at large scales. Their energy spectra scale as $E(k) \sim k^{-3}$ reminiscent of the typical geostrophic turbulence while 3D waves have $E(k) \sim k^{-2\pm0.5}$, found also in several works on the forced turbulence (Müller & Thiele (2007), Salhi *et al.* (2020)). The little difference in these scalings can be attributed to the influence of precession. Overall, we observe a so called split, or dual cascade: inverse cascade for 2D vortices and direct cascade for 3D waves. The borderline between these two types of cascade occurs near the peak of energy injection for 2D vortices (see e.g., Fig. 6.12).

   In any case, the 2D vortices represent *condensates* that gain energy from smaller-

scale waves without dissipating it at the same rate. Consistent with what was observed by Smith & Waleffe (1999) the vortices are produced mainly by the energy transfer from 3D waves and grow in size by the 2D inverse cascade; this is a clear indication of strongly nonlinear phenomena at moderate Rossby numbers, $Ro \sim 0.1$. By contrast, the weakly nonlinear wave theory at small $Ro \ll 1$ prohibits the interaction of geostrophic vortical modes and waves (Galtier (2003)) allowing only resonant triads between fast 3D wave modes. This prohibition, sometimes called *Greenspan's theorem* (Greenspan (1969)), has led to the idea that the geostrophic flows in precessing cylinder can arise only by the nonlinear interaction in the Ekman layers at the endcaps, that is a purely boundary effect (Kong *et al.* (2015), Zhang & Liao (2017), Meunier *et al.* (2008)). Our local model, which by definition has no boundaries, proofs that this condition in fact is not necessary, since vortices can arise also in unbounded precessional flows for moderate Ro. In this regard, our results are also important in relation to the recent work by Le Reun *et al.* (2020) who showed that the inertial waves can excite the geostrophic mode through an instability driven by a near-resonant triadic nonlinear interactions.
The anisotropic nature of 2D vortices can be discussed on two aspects: they have a preferential direction with the substantial part of energy being horizontal; from a spectral point of view the kinetic energy, injection and nonlinear transfer have a preferential direction in $(k_x, k_y)-$plane.

4. *The role of precession parameter Po*: precession, as other forcing mechanisms, counteracts the effects of rotation. This fact has been shown through several phenomena: the larger the precession ratio the stronger the 3D waves, thereby more isotropic is the flow and at the same time the vortices are weaker. The Zeman scale decreases with the precession ratio and this means that the range of rotationally-dominated wavenumbers is reduced extending the inertial range (characterized by the direct cascade) while the range of wavenumbers where inverse cascade occurs shrinks and is reduced. Finally, the increase of precession parameter brings the spectral law for waves energy from k^{-2} to the classical Kolmogorov $k^{-5/3}$. This kind of shift was proposed initially by Zhou (1995) for the problem from strong rotation to non-rotation.

Even though our simple model is based on a local version of the Poincaré flow (which is typical of spheroidal containers), some similarities with the global cases have been found. For instance, the dissipation shows a quite steep jump around an intermediate precession parameter $Po \sim 0.1$ consistent with the transition to turbulence observed in global simulations (Goto *et al.* (2014), Kong *et al.* (2015), Cébron *et al.* (2019), Pizzi *et al.* (2021a), Pizzi *et al.* (2021b)) and experiments (Malkus (1968), Herault *et al.* (2015)). Moreover, the presence of a geostrophic flow which dominates the bulk region is a hallmark of precessing cylinders at rather large Po (Kong *et al.* (2015), Kobine (1996), Jiang *et al.* (2014)) and could correspond to 2D vortices in our local model. At large precession parameters $Po \gtrsim 0.1$, the turbulent dissipation scales as Po^3 as found already in Barker (2016).

One of the main goals of this work was to put a theoretical basis for the analysis of turbulence properties in precession-driven flows in the context of the upcoming DRESDYN (DREsden Sodium facility for DYNamo and thermohydraulic studies) precession experiment (Stefani *et al.* (2012), Stefani *et al.* (2015a), Stefani *et al.* (2015b)). This motivates the interest in the moderate to large Po regimes, which are different from the ones of geophysical and astrophysical objects. However, some speculations can be made since the different regimes observed here at $Re = 10^{4.5}$ may carry over to large-Re regime too. Because of normally weak precession of geo- and astrophysical objects, we can speculate that they would be also characterized by the bursty behavior as described in Section 6.4.1. If this is the case, it would influence the planetary evolution, producing a series of formation and destruction events (bursts) of vortices due to the nonlinear transfer between 2D and 3D flows and oscillating dissipation.

7. Conclusions

> *Ibi eam terram cognovimus non insulam, sed continentem esse, quia et longissimis producitur litoribus non ambientibus eam et infinitis habitatoribus repleta est.*
>
> Amerigo Vespucci, Mundus Novus

7.1. Summary and discussions

In this Thesis we investigated precession-driven flows, with a special focus on cylindrical geometry (whose aspect ratio is fixed to the value of the DRESDYN precession experiment). We study several fluid dynamics features of this system, such as inertial waves, boundary layers, instabilities, turbulence and dynamos, via numerical simulations.
The following points summarize the main results and accomplishments organized accordingly to the Chapters 3, 4, 5 and 6.

Bulk flow and boundary layer phenomena for $\alpha = 90°$

For weak forcing the pattern of the flow within the boundary layer reflects the structure of the precessional forcing.
For strong forcing the scenario is more complicated. It is characterized by the presence of instabilities and deviations from the laminar thickness of the Ekman layer. For a limited range of forcing magnitudes, we observed a subtle interaction between bulk flow and the endwall Ekman layers which seem to behave in a resonant-like way. However being able to run simulations with stress-free boundary condition we established a hierarchical relation:

the boundary layers reflects the bulk flow evolution with the increase of the forcing. Indeed in the distinguished parameter regime where the emergence of axisymmetric poloidal flow occurs (Giesecke *et al.* (2018)), the endwall boundary layers are influenced through a flow influx which causes the thickening of the layers themselves and a radial outflow towards the sidewalls. The poloidal rolls emerge regardless the presence of boundary layers at the endcaps as well as the emergence of geostrophic-axisymmetric circulations: they are phenomena occurring in the bulk region which then change the behavior of the boundary layers. The geostrophic flow causes the shift from an Ekman-type boundary layer to a Stewartson-like boundary layer on the cylinder sidewall.

Instabilities and turbulent Ekman layers

The close connection between boundary layers and bulk flow may also be related to the question of the transition to turbulence in the Ekman layers which, by the way, cannot be reached in our simulations.

We used four independent criteria to analyze the stability of the Ekman layers, which all show consistent results. The Ekman layer remains laminar although unstable and only the lowest Ekman numbers surpass the threshold of the first instability, the class A instability. However, we observe that the increase in thickness of the Ekman layers occurs also for the cases with larger Ek where the threshold of the A-mode instability is not crossed. In any case, our results show that the geostrophic mode is clearly preceding the B-mode instability and the threshold of turbulent boundary layers, indicating that these features are not connected.

On a first glance this is in agreement with the observation of Manasseh (1992) who found that at small nutation angle, $\alpha \leq 5°$, the transition to turbulence for the bulk flow does not depend on the thickness of the Ekman layers. In our simulations, we have found no case with fully turbulent Ekman layers since the threshold $Re_\delta \approx 150$ was not crossed. Consistently with this result, the frictional Rossby number Ro_f remains below the turbulent threshold, $\sqrt{Ro_f} \approx 10$, and the velocity ratio U_g/u_τ collapses on the relation $U_g/u_\tau = \sqrt{2 \times Ro_f}$, valid for the laminar case. At large Ro_f, corresponding to large ϵ in our simulations, U_g/u_τ lies above this line, which is clearly different from the turbulent behavior found by Sous *et al.* (2013). Regarding the law of the wall, which represents a universal criterion for turbulent boundary layers, we accordingly find that the log-layer is not well established. This also implies the minor contribution of fluctuating flow components, which is strongest for the radial component.

A linear extrapolation of our results suggests that the fully turbulent Ekman layer will be achieved somewhere in the range $Ek = [7.4 \times 10^{-5}, 5.5 \times 10^{-5}]$, for the largest precession ratio considered. For the time being this range is out of our numerical possibilities, but the result can be linked with previous experimental work (Giesecke *et al.* (2019), Herault *et al.* (2015)) in which the critical Poincaré number for the onset of bulk turbulence becomes independent of Ek for $Ek < 2 \times 10^{-5}$.

The impact of prograde/retrograde motion and the role of nutation angle

Having established that the bulk flow is the real source of instabilities and flow mechanisms, in the remaining Chapters we focused our attention on it. In Chapter 4 we analyzed the influence of the nutation angle on the precession-driven flow in cylindrical geometry with special focus on the difference between prograde and retrograde cases.

Our results show that for large precession ratio the angle and the orientation of motion (prograde/retrograde) result in different flow structures and magnitudes. Prograde and perpendicular precession show an abrupt transition of the flow state (dominance of geostrophic-axisymmetric flow together with breakdown of the directly forced mode) around a critical precession ratio; the smaller the angle the smaller is the critical precession ratio at which the transition occurs. The resulting flow structure is characterized by a bulk region with negligible axial velocity and a prevalently azimuthal circulation which nearly compensates the original solid body rotation. The transition found here is not unique for the cylinder but is also reminiscent of the steep jump between laminar and turbulent regime observed in ellipsoids or spheroids (Komoda & Goto (2019), Burmann (2020)). This process could also be related to a hysteresis cycle observed, e.g., by Malkus (1968), Vanyo (1991), but since our simulations have been performed separately for each precession ratio, it is not possible to deduce any hysteretical behavior. However, previous experimental studies (Gans (1971), Herault *et al.* (2015)) indeed found hysteresis for the transition between laminar and turbulent states in a precessing cylinder.

Retrograde precession does not exhibit a clear breakdown of the directly forced mode and it shows a smoother increase of the geostrophic-axisymmetric flow.

In all cases the growth of geostrophic-axisymmetric flow modifies the radial distribution of the angular momentum. At large precession ratio the prograde and perpendicular cases, being dominated by the zonal-geostrophic flow, show a violation of the Rayleigh criterion whereas the retrograde motion is much more stable against a centrifugal instability in the considered parameter space.

For $\alpha = 90°$ two marginal stability curves were found. The first one, related to the breakdown of the directly forced mode, seems to scale $\propto Re^{-1/5}$. This kind of phenomenon has also been investigated by Manasseh (1992) even if his experimental work was focused on small nutation angle. Remarkably, our results present commonalities with the so-called *Type A breakdown* due to its occurrence at large precession ratio with nearly no bulk motion which is indeed our case.

The second threshold, which denotes the separation between centrifugally stable/unstable flow seems to scale $\propto Re^{-1/4}$ which indicates a connection with the geostrophic instability proposed by Kerswell (1999). Moreover, this is the scaling of the sidewall boundary layer thickness of a geostrophic flow on a vertical wall, the so called Stewartson layer, as observed in Chapter 3. Even if the geostrophic and the centrifugal instabilities are two different phenomena, our results suggest that the centrifugal unstable flows are a consequence of the geostrophic instability, therefore the scaling should be the same. The difference with Kerswell's theory is that our fitting expression is asymptotic, therefore the geostrophic instability observed here could stay over certain Po for $Re \to \infty$.

The most striking connection of the centrifugal instability scaling law is with the experimental results of Lin *et al.* (2014) for precessing cylindrical annulus where the threshold for the strongly non-linear regime was found to scale as $Po^c = 0.67(\pm 0.31) Re^{-0.24(\pm 0.04)}$. From a physical point of view the fluid filled precessing cylinder studied in our work becomes analogous to a cylindrical annulus when the bulk is dominated by the zonal geostrophic flow which is similar to an internal fluid cylinder at rest.

The modification of the radial distribution of angular momentum is also related with the emergence of poloidal flow structures. Almost all cases analyzed show a double vortex dominated by the inertial mode $(m, k) = (0, 2)$. The only exception is $\alpha = 60°$ prograde which has four vortices whose formation is rather complex: we observe an evolution from double vortices to quadruple vortices with an opposite sense of rotation compared to the rolls emerging at other nutation angles. This kind of "exceptional" state can occur in strongly non-linear regimes in accordance, e.g., with the precessing cube (Goepfert & Tilgner (2016)).

The largest poloidal energy of the $(0, 2)$ mode occurs for the retrograde case with $\alpha = 75°$ which, in terms of dynamo applications, appears as quite promising because the $(1, 1)$ energy remains at high level also at large Po (no breakdown of the directly forced mode). As a consequence any violation of the Rayleigh criterion appears to be shifted to quite large precession ratios so that the flow remains centrifugally stable in an extended range (twice the width of the corresponding prograde case). Furthermore the double rolls are the strongest ones. At this precession ratio, the flow forcing is most efficient and we may speculate that it is possible to inject more energy into the flow without breaking the base state. The case $\alpha = 75°$ (r) proves that, to obtain a strong poloidal flow, it is not necessary to violate the Rayleigh criterion.

Dynamo action in a precessing cylinder

To study precession driven dynamos in a fluid filled cylinder, we have used the hydrodynamic results in a kinematic dynamo code. Even if it is a simplified model which does not take into account the Lorentz force and the effects of turbulence (no fluctuations) the lessons learned are remarkable. We summarize the outcomes in the following points:

- The nutation angle α is crucial both for the hydrodynamic flow structure and the resulting dynamo action. In the phase diagram Fig. 5.2 we have shown that (at the present state) the most efficient dynamo (with the highest growth rate γ) is found at $\alpha = 90°$. The reason for that lies in the rich and optimal flow structure for this nutation angle (as show in the Chapter 4). However, with view on Fig. 5.5 we can conclude that the best range for a lower threshold for the onset of dynamo action seems to lay somewhere between 82.5° retrograde and 90°.

- For the particular case $\alpha = 90°$ the hydrodynamic Reynolds number slightly affects the best precession ratio range where dynamo is found. This optimal precession ratio scales as $Po^c \sim Re^{-1/4}$. At low Re dynamos occur in a range of Po more extended than for larger Reynolds, e.g $0.120 < Po < 0.200$ for $Re = 2000$. The critical magnetic Reynolds number shows a weak dependence on Re with a slight increase around $Re \approx 6000$, but approaches the previously known value of 430 when going to $Re = 10000$. Given that the real dynamo experiment can achieve an Rm value of 700, there seems to be a reasonable safety margin to reach dynamo action. However the extrapolation to the hydrodynamic regime of the DRESDYN precession experiment must be considered with a grain of salt and has to be carefully checked in the larger experiment.

- The role of boundary conditions might be important. In fact switching from a pseudo-vacuum to insulator boundary conditions the critical magnetic Reynolds numbers found here could increase by $15\% - 30\%$ remaining still below the upper value achievable in the DRESDYN experiment.

Features of precessing turbulence

Having established that the boundary layers are not the cause or source of the geostrophic flow, we have studied the properties of turbulence with emphasis on the formation of geostrophic vortices by using numerical simulations in a local model with a periodic box. Through an extended data-set of simulations, new results have been obtained concerning the role of precessional forcing modeled as a background flow which injects energy into our local domain. In this case, the precession ratio, or Poincaré number, is a crucial parameter to trigger and sustain a turbulent state in the flow, as observed in global simulations (Pizzi *et al.* (2021b), Kong *et al.* (2015), Cébron *et al.* (2019)) as well as in experiments (Goto *et al.* (2007), Herault *et al.* (2015), Horimoto & Goto (2018)). Our detailed analysis was motivated mainly by the works of Barker & Lithwick (2013), Barker (2016) and it was developed both in physical and in Fourier (wavenumber $\boldsymbol{k}$-) space. Precessional turbulence is a type of rotating turbulence, where energy injection comes from the precessional instability instead of an externally imposed forcing, and shares several common features with those in the presence of other forcing mechanisms such as the concurrence of waves and geostrophic structures. We have used the 2D-3D manifold decomposition method (where 2D modes have $k_z = 0$ while 3D ones $k_z \neq 0$) to distinguish and quantify the vortices and the waves as used by several authors for other external forcings localized in a narrow band of wavenumbers (Smith & Waleffe (1999), Khlifi *et al.* (2018), Salhi *et al.* (2020), Buzzicotti *et al.* (2018), Biferale *et al.* (2016)). By contrast, precessional instability injects energy into turbulence over a broad range of wavenumbers which also modifies the character of nonlinear transfers compared with that in the case of external forcing.

We found that this precession-driven turbulence is in general characterized by coexisting two dimensional (2D) columnar vortices and three dimensional (3D) inertial waves, whose relative energies depend on the precession parameter Po. The vortices resemble the typical condensates of geostrophic turbulence, are aligned along the rotation axis (with zero wavenumber in this direction, $k_z = 0$) and are fed by the 3D waves through nonlinear transfer of energy. The waves (with $k_z \neq 0$) in turn are directly fed by the precessional instability of the background flow. The vortices themselves undergo an inverse cascade of energy and exhibit anisotropy in Fourier space. For small $Po < 0.1$ and sufficiently high Reynolds numbers, the typical regime for most geo- and astrophysical applications, the flow exhibits strongly oscillatory (bursty) evolution due to the alternation of vortices and small-scale waves. On the other hand, at larger $Po > 0.1$ turbulence is quasi-steady with only mild fluctuations, the coexisting columnar vortices and waves in this state give rise to a split (simultaneous inverse and forward) cascade. Increasing the precession magnitude causes a reinforcement of waves relative to vortices with the energy spectra approaching the Kolmogorov scaling and, therefore, the precession mechanism counteracts the effects of the rotation.

7.2. Future work and perspectives

We conclude this Thesis with some final remarks and perspectives.

The phenomena concerning the boundary layer can be further investigated in order to achieve a turbulent state. Further experimental studies are planned at the existing precession water experiment at HZDR for studying developed turbulence in the bulk and in the boundary layers with the aim to test the results here discussed.

Furthermore, the present work should be extended to more extreme regimes; for instance the stability diagram (Fig. 4.7) shows a limited range of Reynolds number due to the computational constraints. The use of experimental campaigns could help to overcome this limitations. Let us consider the scaling law $\propto Re^{-1/4}$ as guideline at what critical precession ratio $Po^{(2c)}$ the flow field in the future DRESDYN precession experiment will become centrifugally unstable. When assuming $Re \in O[10^7, 10^8]$ the braking of the base flow (followed by centrifugal instability) should occur at $Po^{(c2)} \sim [0.045, 0.040]$.

The present work can be extended in several directions. The possibility of the down-scaled water experiment to reach Reynolds numbers of up to 2 million should be utilized to confirm the $-1/4$ scaling of the critical precession ratio also for nutation angles different from $90°$.

The kinematic dynamo code should be extended to the use of vacuum boundary conditions which might still lead to some (upward) changes of the critical Rm when compared to the presently used vertical field conditions. Finally, in a more advanced study the fully coupled system of induction and Navier-Stokes equations including the back-reaction of the Lorentz forces should be performed. For our precession system, with its very sensitive dependence on various parameters, this fully non-linear system promises to show particularly interesting effects.

We conclude with some discussions related to the fully magnetohydrodynamic (MHD) dynamo effect. Within our local model, we can further investigate the properties of MHD turbulence and related dynamo action and how the magnetic field, when sufficiently strong, influences the 2D and 3D flows studied here. The work by Barker (2016) indicates that the precession instability is able in principle to drive dynamo action locally and the turbulent flow dynamics changes completely due to the back-reaction of the magnetic field. The great debate in the dynamo community about large/small scale dynamos could then be nurtured in the context of precession driven MHD.

Bibliography

Aelbrecht, D., D'Hieres, G. C., & Renouard, D. 1999 Experimental study of the Ekman layer instability in steady or oscillating flows. *Continental Shelf Research* **19**(15-16), 1851-1867, doi:10.1016/S0278-4343(99)00044-8.

Alexakis, A. & Biferale L. 2018 Cascades and transitions in turbulent flows. *Physics Reports* **767-769**, 1-101, doi:10.1016/j.physrep.2018.08.001.

Albrecht, T., Blackburn, H. M., Lopez, J. M., Manasseh, R. & Meunier, P. 2021 On the origins of steady streaming in precessing fluids. *J. Fluid Mech.* **910**, A51, doi:10.1017/jfm.2020.1041.

Avalos-Zúñiga, R. A., Priede, J., & Bello-Morales, C. E. 2017 A homopolar disc dynamo experiment with liquid metal contacts. *Magnetohydrodynamics* **53**(2), 341-347.

Avalos-Zúñiga, R. A. & Priede, J. 2023 Realization of Bullard's disc dynamo. *Proc. Royal Soc. A* **479**(2271), 20220740 doi:10.1098/rspa.2022.0740.

Backus, G. 1958 A class of self-sustaining dissipative spherical dynamos. *Ann. Phys.* **4**(4), 372-447, doi:10.1016/0003-4916(58)90054-X.

Bardina, J., Ferziger, J. H., & Rogallo, R. S. 1985 Effect of rotation on isotropic turbulence: computation and modelling. *J. Fluid Mech.* **154**, 321-336, doi:10.1017/S0022112085001550.

Barker, A. J. & Lithwick Y. 2013 Non-linear evolution of the tidal elliptical instability in gaseous planets and stars. *Mon. Not. R. Astron. Soc.* **435**(4), 3614-3626, doi:10.1093/mnras/stt1561.

Barker, A. J. & Ogilvie G. I. 2009 On the tidal evolution of Hot Jupiters on inclined orbits. *Mon. Not. R. Astron. Soc.* **395**(4), 2268-2287, doi:10.1111/j.1365-2966.2009.14694.x.

Barker, A. J. & Ogilvie G. I. 2010 On internal wave breaking and tidal dissipation near the centre of a solar-type star. *Mon. Not. R. Astron. Soc.* **404**(4), 1849-1868, doi:10.1111/j.1365-2966.2010.16400.x.

Barker, A. J. 2016 On turbulence driven by axial precession and tidal evolution of the spin-orbit angle of close-in giant planets. *Mon. Not. R. Astron. Soc.* **460**(3), 2339-2350, doi:10.1093/mnras/stw1172.

Barnes, S. A. 2001 An assessment of the rotation rates of the host stars of extrasolar planets. *The Astrophysical Journal* **561**(2), 1095-1106, doi:10.1086/323373.

Batchelor, G. K. 2000 An Introduction to Fluid Dynamics, Cambridge University Press, doi:10.1017/CBO9780511800955.

Benthuysen, J. A. & Thomas, L. N. 2012 Asymmetries in vertical vorticity and vertical velocity arising during nonlinear homogeneous spindown. *Phys. Fluids* **24**, 076601, doi:10.1063/1.4731280.

Berhanu M., Monchaux, R., Fauve, S.,Mordant, N., Pétrélis, F., Chiffaudel, A., Daviaud, F., Dubrulle, B., Marié, L., Ravelet, F., Bourgoin, M., Odier, Ph., Pinton, J. F., & Volk, R. 2007 Magnetic field reversals in an experimental turbulent dynamo. *Europhys. Lett.* **77**, 59001, doi:10.1209/0295-5075/77/59001.

Biferale, L., Bonaccorso, F., Mazzitelli, I. M., van Hinsberg, M. A. T., Lanotte, A. S., Musacchio, S., Perlekar, P. & Toschi, F. 2016 Coherent structures and extreme events in rotating multiphase turbulent flows. *Phy. Rev. X* **6**, 041036, doi:10.1103/PhysRevX.6.041036.

Blackburn, H. M., Lee, D., Albrecht, T., & Singh, J. 2019 Semtex: A spectral element-Fourier solver for the incompressible Navier-Stokes equations in cylindrical or Cartesian coordinates. *Comput. Phys. Commun.* **245**, 106804, doi:10.1016/j.cpc.2019.05.015.

Boisson, J., Cébron, D., Moisy, F., & Cortet, P. P. 2012 Earth rotation prevents exact solid-body rotation of fluids in the laboratory. *Eurphysics Letters* **98**(5), 59002, doi:10.1209/0295-5075/98/59002.

Bourgoin, M., Marié, L., Pétrélis, F.,Gasquet, C., Guigon, A., Luciani, J. B., Moulin, M., Namer, F., Burguete, J., Chiffaudel, A., Daviaud, F., Fauve, S., Odier, P., & Pinton, J. F. 2002 Magnetohydrodynamics measurements in the von Kármán sodium experiment. *Phys. Fluids* **14**, 3046-3058, doi:10.1063/1.1497376.

Bourouiba, L., Straub, D. N., & Waite, M. L. 2012 Non-local energy transfers in rotating turbulence at intermediate Rossby number. *J. Fluid Mech.* **690**, 129-147, doi:10.1017/jfm.2011.387.

Brunet, M., Gallet, B., & Cortet, P. P. 2020 Shortcut to geostrophy in wave-driven rotating turbulence: the quartetic instability. *Phy. Rev. Lett.* **124**, 124501, doi:10.1103/PhysRevLett.124.124501.

Bullard, E. C. 1949 The magnetic field within the Earth. *Proc. R. Soc. Lond. A* **197**(1051), 433-453, doi:10.1098/rspa.1949.0074.

Busse, F. H. 1968 Steady fluid flow in a precessing spheroidal shell. *J. Fluid Mech.* **33**(4), 739-751, doi:10.1017/S0022112068001655.

Busse, F. H. 1975 A Model of the Geodynamo. *Geophys. J. Int.*, **42**(2), 437-459 doi:10.1111/j.1365-246X.1975.tb05871.x.

Burmann, F. 2020 An experimental investigation of the effects of topography in planetary fluid dynamics. PhD thesis, ETH Zürich, doi:10.3929/ethz-b-000449968.

Buzzicotti, M., Aluie, H., Biferale, L., & Linkmann, M. 2018 Energy transfer in turbulence under rotation. *Phy. Rev. Fluids* **3**, 034802, doi:10.1103/PhysRevFluids.3.034802.

Caldwell, D. R. & Van Atta, C. W. 1970 Characteristics of Ekman boundary layer instabilities. *J. Fluid Mech.* **44**(1), 79-95, doi:10.1017/S0022112070001702.

Caldwell, D. R., Van Atta, C. W., & Helland, K. N. 1972 A laboratory study of the turbulent Ekman layer. *Geophys. Fluid Dyn.* **3**(2), 125-160, doi:10.1080/03091927208236078.

Campagne, A., Gallet, B., Moisy, F., & Cortet, P. P. 2014 Direct and inverse energy cascades in a forced rotating turbulence experiment. *Phys. Fluids* **26**(12), 125112, doi:10.1063/1.4904957.

Campagne, A., Gallet, B., Moisy, F., & Cortet, P. P. 2015 Disentangling inertial waves from eddy turbulence in a forced rotating-turbulence experiment. *Phys. Rev. E* **91**(4), 043016, doi:10.1103/PhysRevE.91.043016.

Cappanera L., Guermond, J. L., Léorat, J., & Nore, C. 2016 Two spinning ways for precession dynamo. *Phys. Rev. E* **93**, 043113, doi:10.1103/PhysRevE.93.043113.

Cébron, D., Laguerre, R., Noir, J., & Schaeffer, N. 2019 Precessing spherical shells: flows, dissipation, dynamo and the lunar core. *Geophys. J. Int.* **219**, S34-S57, doi:10.1093/gji/ggz037.

Cho, J. Y. K., Menou, K., Hansen, B. M. S., & Seager, S. 2008 Atmospheric circulation of close-in extrasolar giant planets. I. Global, barotropic, adiabatic simulations. *The Astrophysical Journal* **675**(1), 817-845, doi:10.1086/524718.

Christensen, U. R. & Tilgner A. 2004 Power requirement of the geodynamo from ohmic losses in numerical and laboratory dynamos. *Nature*, **429**, 169-171, doi:10.1038/nature02508.

Coleman, G. N., Ferziger, J. H., & Spalart, P. R. 1990 A numerical study of the turbulent Ekman layer. *J. Fluid Mech.* **213**, 313-348, doi:10.1017/S0022112090002348.

Coles, D. & Van Atta C. 1966 Measured distortion of a laminar circular Couette flow by end effects. *J. Fluid Mech.* **25**(3), 513-521, doi:10.1017/S0022112066000223.

Colgate, S. A., Pariev, V. I., Beckley, H. F.,Ferrel, R., Romero, V. D., & Weatherall, J. C. 2002 The New Mexico alpha-omega dynamo experiment: modeling astrophysical dynamos. *Magnetohydrodynamics* **38**, 129-142.

Consolini, G. & De Michelis P. 2003 Stochastic resonance in geomagnetic polarity reversal. *Phys. Rev. Lett.* **90**(5), 058501, doi:10.1103/PhysRevLett.90.058501.

Cowling, T. G. 1933 The magnetic field of sunspots. *Mon. Not. R. Astron. Soc.* **94**(1), 39-48, doi:10.1093/mnras/94.1.39.

Csanady, G. T. 1967 On the "Resistance Law" of a turbulent Ekman layer. *J. Atmos. Sci.* **24**(5), 467-471, doi:10.1175/1520-0469(1967)024<0467:OTLOAT>2.0.CO;2.

Davidson, P. A. 2001 An Introduction to Magnetohydrodynamics, Cambridge University Press, doi:10.1017/CBO9780511626333.

Davidson, P. A. 2013 Turbulence in rotating, stratified, and electrically conducting fluids, Cambridge University Press.

Deusebio, E., Brethouwer, G., Sclatter, P.,& Lindborg, E. 2014 A numerical study of the unstratified and stratified Ekman layer. *J. Fluid Mech.* **755**, 672-704, doi:10.1017/jfm.2014.318.

Doake, C. S. M. 1977 A possible effect of ice ages on the Earth's magnetic field. *Nature* **267**, 415-417, doi:10.1038/267415a0.

Dudley, M. L. & James, R. W. 1989 Time-dependent kinematic dynamos with stationary flows. *Proc. R. Soc. A* **425**(1869), 407-429, doi:10.1098/rspa.1989.0112.

Dumitrescu, H. & Cardos, V. 2004 Rotational effects on the boundary-layer flow in wind turbines. *AIAA* **42**(2), 408-411, doi:10.2514/1.9103.

DWYER C., A., STEVENSON, D. J. & NIMMO, F. 2011 A long-lived lunar dynamo driven by continuous mechanical stirring. *Nature* **479**, 212-214, doi:10.1038/nature10564.

EKMAN, V. W. 1905 On the influence of the Earth's rotation on ocean-currents. *Arch. Math. Astron. Phys.* **2**, 1-52.

ELENA, L. & SCHIESTEL, R. 1996 Turbulence modeling of rotating confined flows. *International Journal of Heat and Fluid Flow* **17**(3), 283-289, doi:10.1016/0142-727X(96)00032-X.

ERNST-HULLERMAN, J., HARDER, H., & HANSEN, U. 2013 Finite volume simulations of dynamos in ellipsoidal planets. *Geophys. J. Int.*, **195**(3), 1395-1405, doi:10.1093/gji/ggt303.

FARADAY, M. 1832 V. Experimental researches in electricity. *Philsophical Transactions*, **122**, 125-162, doi:10.1098/rstl.1832.0006.

FAVIER, B., GRANNAN, A. M., LE BARS, M., & AURNOU, J. M. 2015 Generation and maintenance of bulk turbulence by libration-driven elliptical instability. *Phys. Fluids*, **27**(6), 066601, doi:10.1063/1.4922085.

FALLER, A. J. & KAYLOR, R. E. 1966 A Numerical study of the instability of the laminar Ekman boundary layer. *J. Atmos. Sci.* **23**(5), 466-480, doi:10.1175/1520-0469(1966)023<0466:ANSOTI>2.0.CO;2.

FRICK, P., NOSKOV, V., DENISOV, S., KHRIPCHENKO, S., SOKOLOFF, D., STEPANOV, R. & SUKHANOVSKY, S. 2002 Non-stationary screw flow in a toroidal channel: way to a laboratory dynamo experiment. *Magnetohydrodynamics* **38**(1/2), 143-162.

FU, R. R., WEISS, B. P., SCHUSTER, D. L., GATTACCECA, J., GROVE, T. L., SUAVET, C., LIMA, E. A., LI, L., & KUAN, A. T. 2012 An ancient core dynamo in asteroid Vesta. *Science*, **338**(6104), 238-241, doi:10.1126/science.1225648.

GAILITIS, A. 1967 Self-excitation conditions for a laboratory model of a geomagnetic dynamo. *Magnetohydrodynamics*, **3**(3), 45-54.

GAILITIS, A., & FREIBERG, YA. 1976 Theory of a helical MHD dynamo. *Magnetohydrodynamics*, **12**, 127-129.

GAILITIS, A., & FREIBERG, YA. 1980 Nature of the instability of a turbulent dynamo. *Magnetohydrodynamics*, **16**, 116-121.

Gailitis, A., Karasev, B. G., Kirillov, I. R., Lielausis, O. A., Luzhanskii, S. M., Ogorodnikov, A. P. & Preslitskii, G. V. 1987 An experiment with a liquid-metal model of MHD dynamo , **23**, 349-353.

Gailitis, A. 1996 Project of a liquid sodium MHD dynamo experiment. *Magnetohydrodynamics*, **32**(1), 63-67.

Gailitis, A. 1996 Design of a liquid sodium MHD dynamo experiment. *Magnetohydrodynamics*, **32**(1), 58-62.

Gailitis, A., Lielausis, O., Dement'ev, S.,Platacis, E., Cifersons, A., Gerbeth, G., Gundrum, T., Stefani, F., Christen, M., Hänel, H., & Will, G. 2000 Detection of a flow induced magnetic field eigenmode in the Riga dynamo facility. *Phys. Rev. Lett.* **84**, 4365, doi:10.1103/PhysRevLett.84.4365.

Gailitis, A., Lielausis, O., Dement'ev, S.,Platacis, E., Cifersons, A., Gerbeth, G., Gundrum, T., Stefani, F., Christen, M., & Will, G. 2001 Magnetic field saturation in the Riga dynamo experiment. *Phys. Rev. Lett.* **86**, 3024-3027, doi:10.1103/PhysRevLett.86.3024.

Gailitis, A., Lielausis, O.,Platacis, E., Gerbeth, G., & Stefani, F. 2001 On the results of the Riga dynamo experiments. *Magnetohydrodynamics* **37**(1/2), 71-79.

Gailitis, A., Lielausis, O., Dement'ev, S.,Platacis, E., Cifersons, A., Gerbeth, G., Gundrum, T., Stefani, F., Christen, M., & Will, G. 2002 Dynamo experiments at the Riga sodium facility. *Magnetohydrodynamics* **38**, 5-14.

Gailitis, A., Lielausis, O.,Platacis, E., Gerbeth, G., & Stefani, F. 2002 On back-reaction effects in the Riga dynamo experiment. *Magnetohydrodynamics* **38**(1/2), 15-26.

Gailitis, A., Lielausis, O., Platacis, E., Gerbeth, G., & Stefani, F. 2003 The Riga dynamo Experiment. *Surveys in Geophysics*, **24**, 247-267, doi:10.1023/A:1024851818821.

Gailitis, A., Lielausis, O., Platacis, E., Gerbeth, G., & Stefani, F. 2004 Riga dynamo experiment and its theoretical background. *Physics of Plasmas*, **11**(5), 2838-2843, doi:10.1063/1.1666361.

Gailitis, A., Gerbeth, G., Gundrum, T., Lielausis, O., Lipsbergs, G., Platacis, E., & Stefani, F. 2018 Self-excitation in a helical liquid metal flow: the Riga dynamo experiments. *J. Plasma Phys.*, **84**(3), 735840301, doi:10.1017/S0022377818000363.

Gallet, B., Campagne, A., Cortet, P. P., & Moisy, F. 2014 Scale-dependent cyclone-anticyclone asymmetry in a forced rotating turbulence experiment. *Phys. Fluids* **26**(3), 035108, doi:10.1063/1.4867914.

Galtier, S. 2003 Weak inertial-wave turbulence theory. *Phys. Rev. E* **68**, 015301(R), doi:10.1103/PhysRevE.68.015301.

Gans, R. F. 1970 On the precession of a resonant cylinder. *J. Fluid Mech.* **41**(4), 865-872, doi:10.1017/S0022112070000976.

Gans, R. F. 1971 On hydromagnetic precession in a cylinder. *J. Fluid Mech.* **45**(1), 111-130, doi:10.1017/S0022112071003021.

Gans, R. F. 1984 Dynamics of a near-resonant fluid-filled gyroscope. *AIAA J.* **22**(10), 1465-1471, doi:10.2514/3.48585.

Gao, D., Meunier, P., Le Dizès, S., & Eloy, C. 2021 Zonal flow in a resonant precessing cylinder. *J. Fluid Mech.* **923**, A29, doi:10.1017/jfm.2021.574.

Giesecke, A., Stefani, F., & Gerbeth, G. 2008 Kinematic simulation of dynamo action by a hybrid boundary-element/finite-volume method. *Magnetohydrodynamics* **44**, 237-252.

Giesecke, A., Nore, C., Stefani, F., Gerbeth, G., Léorat, J., Luddens, F., & Guermond, J. L. 2010 Electromagnetic induction in non-uniform domains. *Geophys. Astrophys. Fluid Dyn.* **104**(5), 505-529, doi:10.1080/03091929.2010.507202.

Giesecke, A., Stefani, F., & Burguete, J. 2012 Impact of time-dependent nonaxisymmetric velocity perturbations on dynamo action of von Kármán-like flows. *Phys. Rev. E* **86**, 066303, doi:10.1103/PhysRevE.86.066303.

Giesecke, A., Albrecht, T., Gundrum, T., Herault, J., & Stefani, F. 2015 Triadic resonances in nonlinear simulations of a fluid flow in a precessing cylinder. *New J. Phys.* **17**, 113044, doi:10.1088/1367-2630/17/11/113044.

Giesecke A., Voigt, T., Gundrum, T., & Stefani, F. 2018 Nonlinear large scale flow in a precessing cylinder and its ability to drive dynamo action. *Phys. Rev. Lett.* **120**, 024502, doi:10.1103/PhysRevLett.120.024502.

Giesecke, A., Vogt, T., Gundrum, T., & Stefani, F. 2019 Kinematic dynamo action of a precession-driven flow based on the results of water experiments and hydrodynamic simulations. *Geophys. Astrophys. Fluid Dyn.* **113**, 235-255, doi:10.1080/03091929.2018.1506774.

Glatzmaier, G. A. & Roberts P. H. 1995 A three-dimensional self-consistent computer simulation of a geomagnetic field reversal. *Nature* **377**, 203-209, doi:10.1038/377203a0.

Goepfert, O. & Tilgner A. 2016 Dynamos in precessing cubes. *New J. Phys.* **18**, 103019, doi:10.1088/1367-2630/18/10/103019.

Goto, S., Ishii, N., Kida, S., & Nishioka, M. 2007 Turbulence generator using a precessing sphere. *Phys. Fluids* **19**(6), 061705, doi:10.1063/1.2746040.

Goto, S., Matsunaga, A., Fujiwara, M., Nishioka, M., Kida, S., Yamato, M., & Tsuda, S. 2014 Turbulence driven by precession in spherical and slightly elongated spheroidal cavities. *Phys. Fluids* **26**(5), 055107, doi:10.1063/1.4874695.

Greenspan, H. P. 1968 The Theory of Rotating Flows, Cambridge University Press.

Greenspan, H. P. 1969 On the non-linear interaction of inertial modes. *J. Fluid Mech.* **36**(2), 257-264, doi:10.1017/S0022112069001649.

Gubbins, D. 1994 Geomagnetic polarity reversals: a connection with secular variation and core-mantle interaction? *Rev. Geophysics* **32**(1), 61-83, doi:10.1029/93RG02602.

Gubbins, D. & Davies C. J. 2013 The stratified layer at the core-mantle boundary caused by barodiffusion of oxygen, sulphur and silicon. *Physics of the Earth and Planetary Interiors* **215**, 21-28, doi:10.1016/j.pepi.2012.11.001.

Guermond, J. L., Léorat, J., & Nore, C. 2003 A new finite element method for magneto-dynamical problems: two-dimensional results. *European Journal of Mechanics - B/Fluids* **22**(6), 555-579, doi:10.1016/S0997-7546(03)00054-2.

Guervilly, C., Wood, T. S., & Brummell, N. H. 2013 Effect of metallic walls on dynamos generated by laminar boundary-driven flow in a spherical domain. *Phys. Rev. E* **88**(5), 053010, doi:10.1103/PhysRevE.88.053010.

Hawley, J. F., Gammie, C. F., & Balbus, S. A. 1995 Local three-dimensional Magnetohydrodynamic simulations of accretion disks *Astrophys. Journal* **440**, 742.

He, X. Q., Bragg, A. D., Xiong, Y. L., & Fischer, P. 2021 Turbulence and heat transfer on a rotating, heated half soap bubble. *J. Fluid Mech.* **924**, A19, doi:10.1017/jfm.2021.610.

Herault, J., Gundrum, T., Giesecke, A., & Stefani, F. 2015 Subcritical transition to turbulence of a precessing flow in a cylindrical vessel. *Phys. Fluids* **27**(12), 124102, doi:10.1063/1.4936653.

Herault, J., Giesecke, A., Gundrum, T., & Stefani, F. 2019 Instability of precession driven Kelvin modes: evidence of a detuning effect. *Phys. Rev. Fluids* **4**, 033901, doi:10.1103/PhysRevFluids.4.033901.

Herzenberg, A. 1958 Geomagnetic dynamos. *Philos. Trans. R. Soc. Lond. A* **250**, 543-585.

Hopfinger, E. J., Browand, F. K., & Gagne, Y. 1982 Turbulence and waves in a rotating tank. *J. Fluid Mech.* **125**, 505-534, doi:10.1017/S0022112082003462.

Horimoto, Y. & Goto S. 2017 Sustaining mechanism of small-scale turbulent eddies in a precessing sphere. *Phis. Rev. Fluids* **2**, 114603, doi:10.1103/PhysRevFluids.2.114603.

Hossain, M. 1994 Reduction in the dimensionality of turbulence due to a strong rotation. *Phys. Fluids* **6**(3), 1077-1080, doi:10.1063/1.868278.

Iskakov, A. B., Descombes, S., & Dormy, E. 2004 An integro-differential formulation for magnetic induction in bounded domains: boundary element-finite volume method. *J. Comp. Phys.* **197**(2), 540-554, doi:10.1016/j.jcp.2003.12.008.

Jiang, J, Kong, D., Zhu, R., & Zhang, K. 2015 Precessing cylinders at the second and third resonance: turbulence controlled by geostrophic flow *Phys. Rev. E* **92**, 033007, doi:10.1103/PhysRevE.92.033007.

Jones, C. A. 2007 Thermal and Compositional Convection in the Outer Core. *Treatise on Geophysics* Chapter 8.05 **8**, 131-185, Elsevier, doi:10.1016/B978-044452748-6.00130-9.

Kaneda, Y. & Ishihara T. 2006 High-resolution direct numerical simulation of turbulence. *Journal of Turbulence* **7**, N20 , doi:10.1080/14685240500256099

Thomson, W. 1880 Vibrations of a columnar vortex. *Phil. Mag.* **10**(61), 155-168, doi:10.1080/14786448008626912.

Kerswell, R. R. 1993 The instability of precessing flow. *Geophys. Astrophys. Fluid Dyn.* **72**(1-4), 107-144, doi:10.1080/03091929308203609.

Kerswell, R. R. 1999 Secondary instabilities in rapidly rotating fluids: inertial wave breakdown. *J. Fluid Mech.* **382**, 283-306, doi:10.1017/S0022112098003954.

Kerswell, R. R. 2002 Elliptical Instability *Annu. Rev. Fluid Mech.* **34**, 83-113, doi:10.1146/annurev.fluid.34.081701.171829.

Khlifi, A., Salhi, A., Nasraoui, S., Godeferd, F., & Cambon, C. 2018 Spectral energy scaling in precessing turbulence. *Phy. Rev. E* **98**, 011102(R), doi:10.1103/PhysRevE.98.011102.

King, E. M., Stellmach, S., Noir, J., Hansen, U., & Arnou J. M. 2009 Boundary layer control of rotating convection systems. *Nature* **457**, 301-304, doi:10.1038/nature07647.

Knobloch, E. & Proctor M. R. E. 1981 Nonlinear periodic convection in double-diffusive systems. *J. Fluid Mech.* **108**, 291-316 , doi:10.1017/S0022112081002139

Knobloch, E. 1998 Rotating convection: recent developments. *International Journal of Engineering Science* **36**(12-14), 1421-1450 , doi:10.1016/S0020-7225(98)00041-X

Kobine, J. J. 1995 Inertial wave dynamics in a rotating and precessing cylinder. *J. Fluid Mech.* **303**, 233-252 , doi:10.1017/S0022112095004253

Kobine, J. J. 1996 Azimuthal flow associated with inertial wave resonance in a precessing cylinder. *J. Fluid Mech.* **319**, 387-406, doi:10.1017/S0022112096007380.

Kolmogorov, K. 1941 Local structure of turbulence in an incompressible fluid for very large reynolds numbers. *Dokl. Akad. Nauk. SSSR* **30**, 299-303, .

Kolmogorov, K. 1941 Energy dissipation in locally isotropic turbulence. *Dokl. Akad. Nauk. SSSR* **32**, 19-21, .

Komoda, K. & Goto S. 2019 Three-dimensional flow structures of turbulence in precessing spheroids. *Phis. Rev. Fluids* **4**, 014603, doi:10.1103/PhysRevFluids.4.014603.

Kong, D., Liao, X., & Zhang, K. 2014 The sidewall-localized mode in a resonant precessing cylinder *Phys. Fluids* **26**(5), 051703, doi:10.1063/1.4876924.

Kong, D., Cui, Z., Liao, X., & Zhang, K. 2015 On the transition from the laminar to disordered flow in a precessing spherical-like cylinder. *Geophys. Astrophys. Fluid Dyn.* **109**, 62-83, doi:10.1080/03091929.2014.976214.

Krauze, A. 2010 Numerical modeling of the magnetic field generation in a precessing cube with a conducting melt. *Magnetohydrodynamics* **46**(3), 271-280.

Kumar, V., Pizzi, F., Giesecke, A., Šimkanin, J., Gundrum, T., Ratajczak, M., & Stefani, F. 2023 The effect of nutation angle on the flow inside a precessing cylinder and its dynamo action. *Physics of Fluids.* **35**(1), 014114, doi:10.1063/5.0134562.

Kunnen, R. P. J., Clercx, H. J., & Geurts, B. J. 2010 Vortex statistics in turbulent rotating convection. *Phy. Rev. E* **82**(3), 036306, doi:10.1103/PhysRevE.82.036306.

Lagrange, R., Meunier, P., Nadal, F., & Eloy, C. 2011 Precessional instability of a fluid cylinder. *J. Fluid Mech.* **666**, 104-145, doi:10.1017/S0022112010004040.

LAMRIBEN, C., CORTET, P. P., & MOISY, F. 2011 Direct measurements of anisotropic energy transfers in a rotating turbulence experiment. *Phys. Rev. Lett.* **107**, 024503, doi:10.1103/PhysRevLett.107.024503.

LANDEAU, M. , FOURNIER, A., NATAF, H.C., CÉBRON, D., & SCHAEFFER, N. 2022 Sustaining Earth's magnetic dynamo. *Nature Reviews Earth and Environment* **3**, 255-269, doi:10.1038/s43017-022-00264-1.

LARMOR, J. 1919 How Could a Rotating Body Such as the Sun Become a Magnet? *British Association for the Advancement of Science* **87**, 156-160 .

LE BARS, M., CÉBRON, D. & LE GAL, P. 2015 Flows Driven by Libration, Precession, and Tides. *Ann. Rev. of Fluid Mech.* **47**, 163-193, doi:10.1146/annurev-fluid-010814-014556.

LE REUN, T., FAVIER, B., BARKER, A. J., & LE BARS, M. 2017 Inertial wave turbulence driven by elliptical instability. *Phy. Rev. Lett.* **119**, 034502, doi:10.1103/PhysRevLett.119.034502.

LE REUN, T., FAVIER, B., & LE BARS, M. 2019 Experimental study of the nonlinear saturation of the elliptical instability: inertial wave turbulence versus geostrophic turbulence. *J. Fluid Mech.* **879**, 296-326, doi:10.1017/jfm.2019.646.

LE REUN, T., GALLET, B., FAVIER, B., & LE BARS, M. 2020 Near-resonant instability of geostrophic modes: beyond Greenspan's theorem. *J. Fluid Mech.* **900**, R2, doi:10.1017/jfm.2020.454.

LÉORAT, J., RIGAUD, F., VITRY, R., & HERPE, G. 2003 Dissipation in a flow driven by precession and application to the design of a MHD wind tunnel. *Magnetohydrodynamics* **39**(3), 321-326.

LÉORAT, J. 2006 Large scales features of a flow driven by precession. *Magnetohydrodynamics* **42**, 143-151, doi:10.22364/mhd.

LESUR, G. & LONGARETTI, P. Y. 2005 On the relevance of subcritical hydrodynamic turbulence to accretion disk transport. *A & A* **444**, 25-44, doi:10.1051/0004-6361:20053683.

LIAO, X. & ZHANG K. 2012 On flow in weakly precessing cylinders: the general asymptotic solution. *J. Fluid Mech.* **709**, 610-621, doi:10.1017/jfm.2012.355.

LILLY, D. K. 1966 On the Instability of Ekman Boundary Flow. *J. Atmos. Sci.* **23**(5), 481-494, doi:10.1175/1520-0469(1966)023<0481:OTIOEB>2.0.CO;2.

Lin, Y., Noir, J., & Jackson, A. 2014 Experimental study of fluid flows in a precessing cylindrical annulus. *Phys. Fluids* **26**(4), 046604, doi:10.1063/1.4871026

Lin, Y., Marti, P., Noir, J., & Jackson, A. 2016 Precession-driven dynamos in a full sphere and the role of large scale cyclonic vortices. *Phys. Fluids* **28**(6), 066601, doi:10.1063/1.4954295

Loper, D. E. 1975 Torque balance and energy budget for the precessionally driven dynamo. *Physics of the Earth and Planetary Interiors* **11**(1), 43-60 , doi:10.1016/0031-9201(75)90074-6

Lopez, J. M. & Marques, F. 2016 Nonlinear and detuning effects of the nutation angle in precessionally forced rotating cylinder flow. *Phys. Rev. Fluids* **1**, 023602, doi:10.1103/PhysRevFluids.1.023602.

Lopez, J. M. & Marques, F. 2018 Rapidly rotating precessing cylinder flows: forced triadic resonances. *J. Fluid Mech.* **839**, 239-270, doi:10.1017/jfm.2017.922.

Lorenzani, S. & Tilgner, A. 2001 Fluid instabilities in precessing spheroidal cavities. *J. Fluid Mech.* **447**, 111-128, doi:10.1017/S002211200100581X.

Lorenzani, S. & Tilgner, A. 2003 Inertial instabilities of fluid flow in precessing spheroidal shells. *J. Fluid Mech.* **492**, 363-379, doi:10.1017/S002211200300572X.

Lowes, F. J. & Wilkinson I. 1963 Geomagnetic dynamo: a laboratory model. *Nature*, **198**, 1158-1160, doi:10.1038/1981158a0.

Lowes, F. J. & Wilkinson I. 1968 Geomagnetic dynamo: an improved laboratory model. *Nature*, **219**, 717-718, doi:10.1038/219717a0.

Malkus, W. V. R. 1968 Precession of the Earth as the cause of geomagnetism. *Science* **160**(3825), 259-264, doi:10.1126/science.160.3825.259.

Mamatsashvili, G., Gogichaishvili, D. Z., Chagelishvili, G. D., & Horton, W. 2014 Nonlinear transverse cascade and two-dimensional magnetohydrodynamic subcritical turbulence in plane shear flows. *Phys. Rev. E*, **89**, 043101, doi:10.1103/PhysRevE.89.043101.

Mamatsashvili, G., Khujadze, G., Chagelishvili, G. D., Dong, S., Jímenez, J., & Foysi, H. 2016 Dynamics of homogeneous shear turbulence: a key role of the nonlinear transverse cascade in the bypass concept. *Phys. Rev. E*, **94**, 023111, doi:10.1103/PhysRevE.94.023111.

Manasseh, R. 1992 Breakdown regimes of inertia waves in a precessing cylinder. *J. Fluid Mech.* **243**, 261-296, doi:10.1017/S0022112092002726.

Manasseh, R. 1994 Distortions of inertia waves in a rotating fluid cylinder forced near its fundamental mode resonance. *J. Fluid Mech.* **265**, 345-370, doi:10.1017/S0022112094000868.

Mansour, N. N., Cambon, C., & Speziale, C. G. 1991 Single point modeling of initially isotropic turbulence under uniform rotation. *Annual Research Briefs, CTR*, 159-167.

Mansour, N. N., Cambon, C., & Speziale, C. G. 1992 Theoretical and computational study of rotating isotropic turbulence. *Studies in Turbulence*, 159-167.

Margot, J. L., Peale, S. J., Jurgens, R. F., Slade, M. A., & Holin, I. V. 2007 Large longitude libration of Mercury reveals a molten core. *Science* **316**(5825), 710-714, doi:10.1126/science.1140514.

Marques, F. & Lopez, J. M. 2015 Precession of a rapidly rotating cylinder flow: traverse through resonance. *J. Fluid Mech.* **782**, 63-98, doi:10.1017/jfm.2015.524.

Mason, R. M. & Kerswell, R. R. 2002 Chaotic dynamics in a strained rotating flow: a precessing plane fluid layer. *J. Fluid Mech.* **471**, 71-106, doi:10.1017/S0022112002001994.

McEwan, A. D. 1970 Inertial oscillations in a rotating fluid cylinder. *J. Fluid Mech.* **40**(3), 603-640, doi:10.1017/S0022112070000344.

Merrill, R. T. & McFadden P. L. 1994 Geomagnetic field stability: Reversal events and excursions. *Earth and Planetary Science Letters*, **121**(1-2), 57-69, doi:10.1016/0012-821X(94)90031-0.

Merrill, R. T. & McFadden P. L. 1999 Geomagnetic polarity transitions. *Rev. Geophys.*, **37**(2), 201-226, doi:10.1029/1998RG900004.

Meunier, P., Eloy, C., Lagrange, R., & Nadal, F. 2008 A rotating fluid cylinder subject to weak precession. *J. Fluid Mech.* **599**, 405-440, doi:10.1017/S0022112008000335.

Miralles, S., Bonnefoy, N., Bourgoin, M.,Odier, P., Pinton, J. F., Pilhon, N., Verhille, G., Boisson, J., Daviaud, F., & Dubrulle, B. 2013 Dynamo threshold detection in the von Kármán sodium experiment. *Phys. Rev. E* **88**, 013002, doi:10.1103/PhysRevE.88.013002.

Monchaux, R., Berhanu, M., Aumaître, S.,Chiffaudel, A., Daviaud, F., Dubrulle, B., Ravelet, F., Fauve, S., Mordant, N., Pétrélis, F., Bourgoin, M., Odier, P., Pinton, J. F., Pilhon, N., & Volk, R. 2009 The von

Kármán Sodium experiment: turbulent dynamical dynamos. *Phys. Fluids* **21**, 035108, doi:10.1063/1.3085724.

Morize, C., Le Bars, M., Le Gal, P., & Tilgner, A. 2010 Experimental Determination of Zonal Winds Driven by Tides. *Phy. Rev. Lett.* **104**, 214501, doi:10.1103/PhysRevLett.104.214501.

Mouhali, W., Lehner, T., Léorat, J., , & Vitry, R. 2012 Evidence for a cyclonic regime in a precessing cylindrical container. *Exp. Fluids* **53**, 1693-1700, doi:10.1007/s00348-012-1385-2.

Müller, U., Stieglitz, R., & Horanyi, S. 2002 The Karlsruhe dynamo experiment. *Wissenschaftliche Berichte, FZKA-6756 (Oktober 2002)*, doi:10.5445/IR/270052942.

Müller, U., Stieglitz, R., & Horanyi, S. 2004 A two-scale hydromagnetic dynamo experiment. *J. Fluid Mech.* **498**, 31-71, doi:10.1017/S0022112003006700.

Müller, W. C. & Thiele M. 2007 Scaling and energy transfer in rotating turbulence. *Europhysics Letters (EPL)*, **77**(3), 34003, doi:10.1209/0295-5075/77/34003.

NASA/GSFC/SDO 2013 Raindrops Falling on the Sun. *Solar System Exploration.* 28/03/2013. National Aeronautics and Space Administration. URL: https://solarsystem.nasa.gov/resources/823/raindrops-falling-on-the-sun/?category=solar-system_sun.

NASA/GSFC/SDO 2021 Galactic Merger Warps Magnetic Fields. Composite image where the orange color shows the submillimeter wavelengths (observed by by the European Southern Observatory and Atacama Pathfinder Experiment), the blue color shows the X-ray wavelengths observed by the Chandra X-Ray observatory and the dark res shows the infrared spectrum from the Spitzer Space Telescope. *Credits: Optical: European Southern Observatory (ESO) Wide Field Imager; Submillimeter: Max Planck Institute for Radio Astronomy/ESO/Atacama Pathfinder Experiment (APEX)/A. Weiss et al; X-ray and Infrared: NASA/Chandra/R. Kraft; JPL-Caltech/J. Keene.* National Aeronautics and Space Administration. URL: https://www.nasa.gov/feature/galactic-merger-warps-magnetic-fields.

Naing, M. M. & Fukumoto, Y. 2011 Local instability of a rotating flow driven by precession of arbitrary frequency. *Fluid Dynamics Research* **43**, 055502, doi:10.1088/0169-5983/43/5/055502.

Nimmo, F. 2015 *Energetics of the Core . Treatise on Geophysics*, Chapter 8.02 **8**, 27-55, Elsevier, doi:10.1016/B978-0-444-53802-4.00139-1.

Nobili, C., Meunier, P., Favier, B., & Le Bars, M. 2021 Hysteresis and instabilities in a spheroid in precession near the resonance with the tilt-over mode. *J. Fluid Mech.* **909**, A17, doi:10.1017/jfm.2020.938.

Noir, J., Jault, D., & Cardin, P. 2001 Numerical study of the motions within a slowly precessing sphere at low Ekman number. *J. Fluid Mech.* **437**, 283-299, doi:10.1017/S0022112001004311.

Noir, J., Cardin, P., Jault, D., & Masson, J. P. 2003 Experimental evidence of non-linear resonance effects between retrograde precession and the tilt-over mode within a spheroid. *Geophys. J. Int.* **154**(2), 407-416, doi:10.1046/j.1365-246X.2003.01934.x.

Noir, J. & Cébron, D. 2013 Precession-driven flows in non-axisymmetric ellipsoids. *J. Fluid Mech.* **737**, 412-439, doi:10.1017/jfm.2013.524.

Nore, C., Léorat, J., Guermond, J. L., & Luddens, F. 2011 Nonlinear dynamo action in a precessing cylindrical container. *Phys. Rev. E* **84**, 016317, doi:10.1103/PhysRevE.84.016317.

Nornberg, M. D., Spence, E. J., Kendrick, R. D., Jacobson, C. M. & Forest, C. B. 2005 Measurements of the magnetic field induced by a turbulent flow of liquid metal. *Phys. Plasmas* **13**, 055901, doi:10.1063/1.2173614.

Pedlosky, J. 2008 On the weakly nonlinear Ekman layer: thickness and flux. *J. Phys. Oceanogr.* **38**(6), 1334-1339, doi:10.1175/2007JPO3830.1.

Peffley, N. L., Cawthorne, A. B., & Lathrop, D. P. 2000 Toward a self-generating magnetic dynamo: the role of turbulence. *Phys. Rev. E* **61**, 5287, doi:10.1103/PhysRevE.61.5287.

Pétrélis, F., Bourgoin, M., Marié, L., Burguete, J., Chiffaudel, A., Daviaud, F., Fauve, S., Odier, P., & Pinton, J. F. 2003 Nonlinear magnetic induction by helical motion in a liquid sodium turbulent flow. *Phys. Rev. Lett.* **90**, 174501, doi:10.1103/PhysRevLett.90.174501.

Pizzi, F., Giesecke, A., & Stefani, F. 2021 Ekman boundary layers in a fluid filled precessing cylinder. *AIP Adv.* **11**, 035023, doi:10.1063/5.0037922.

Pizzi, F., Giesecke, A., Šimkanin, J. , & Stefani, F. 2021 Prograde and retrograde precession of a fluid-filled cylinder. *New J. Phys.* **23**, 123016, doi:10.1088/1367-2630/ac3c0f.

Pizzi, F., Giesecke, A., Šimkanin, J., Kumar, V., Gundrum, T., & Stefani, F. 2022 Numerical and theoretical framework for the DRESDYN precession dynamo experiment. *Magnetohydrodynamics* **58**(4), 445-454.

Pizzi, F., Mamatsashvili, G., Barker, A. J., Giesecke, A., & Stefani, F. 2022 Interplay between geostrophic vortices and inertial waves in precession-driven turbulence. *Phys. Fluids* **34**, 125135, doi:10.1063/5.0131035.

Plunian, F. & Alboussière, T. 2021 Axisymmetric dynamo action produced by differential rotation, with anisotropic electrical conductivity and anisotropic magnetic permeability. *J. Plasma Phys.* **87**(1), 905870110, doi:10.1017/S0022377820001634.

Plunian, F. & Alboussière, T. 2022 Fast and furious dynamo action in the anisotropic dynamo. *J. Fluid. Mech.* **941**, A66, doi:10.1017/jfm.2022.349.

Poincaré, H. 1910 Sur la précession des corps déformables. *Bull. Astron.* **27**, 321-356.

Ponomarenko, Yu. B. 1973 Theory of the hydromagnetic generator. *Journal of Applied Mechanics and Technical Physics* **14**, 775-778, doi:10.1007/BF00853190.

Pope, S. B. 2000 Turbulent Flows. Cambridge University Press, doi:10.1017/CBO9780511840531.

Proudman, J. 1916 On the motion of solids in a liquid possessing vorticity. *Proc. R. Soc. Lond. A* **92**(642), 408-424 , doi:10.1098/rspa.1916.0026

Ravelet, F., Chiffaudel, A., Daviaud, F., & Léorat, J. 2005 Toward an experimental von Kármán dynamo: numerical studies for an optimized design. *Phys. Fluids* **17**, 117104, doi:10.1063/1.2130745.

Rädler, K. H., Rheinhardt, M., Apstein, E., & Fuchs, H. 2002 On the mean-field theory of the Karlsruhe dynamo experiment I. Kinematic theory. *Magnetohydrodynamics* **38**, 41-71

Rhines, P. B. 1979 Geostrophic Turbulence. *Ann. Rev. of Fluid Mech.* **11**(1), 401-441, doi:10.1146/annurev.fl.11.010179.002153.

Richardson, K. 1922 Weather prediction by numerical process. Cambridge University Press., doi:10.1017/CBO9780511618291.

Rincon, F. 2019 Dynamo theories. *J. Plasma Phys.* **85**(4), 205850401, doi:10.1017/S0022377819000539.

Roberts, G. O. 1972 Dynamo action of fluid motions with two-dimensional periodicity. *Philos. Trans. R. Soc. Lond. A*, **271**(1216), 411-454 doi:10.1098/rsta.1972.0015.

Roberts, P. H., Glatzmaier, G. A., & Clune, T. L. 2010 Numerical simulation of a spherical dynamo excited by a flow of von Kármán type. *Geophys. Astrophys. Fluid Dyn.* **104**(2-3), 207-220, doi:10.1080/03091920903439753.

ROBERTS, P. H. & KING, E. M. 2013 On the genesis of the Earth's magnetism. *Rep. Prog. Phys.* **76**(9), 096801, doi:10.1088/0034-4885/76/9/096801.

ROCHESTER, M. G., JACOBS, J. A., SMYLIE, D. E., & CHONG, K. F. 1975 Can precession power the geomagnetic dynamo? *Geophys. J. Int.* **43**(3), 661-678, doi:10.1111/j.1365-246X.1975.tb06186.x.

RUBIO, A. M., JULIEN, K., KNOBLOCH, E. & WEISS, J. B. 2014 Upscale energy transfer in three-dimensional rapidly rotating turbulent convection. *Phy. Rev. Lett.* **112**, 144501, doi:10.1103/PhysRevLett.112.144501.

RÜDIGER, G., HOLLERBACH, R., & KITCHATINOV, L.L. 2013 Magnetic Processes in Astrophysics: Theory, Simulations, Experiments. WILEY-VCH: Weinheim.

RÜDIGER, G. & HOLLERBACH, R. 2004 The magnetic Universe: geophysical and astrophysical dynamo theory. *Wiley-VCH, Weinheim.*

SAHOO, G., ALEXAKIS, A., & BIFERALE, L. 2017 Discontinuous transition from direct to inverse cascade in three-dimensional turbulence. *Phy. Rev. Lett.* **118**, 164501, doi:10.1103/PhysRevLett.118.164501.

SALHI, A. & CAMBON C. 2009 Precessing rotating flows with additional shear: stability analysis. *Phys. Rev. E.* **79**(3), 036303, doi:10.1103/PhysRevE.79.036303.

SALHI, A., KHLIFI, A., & CAMBON, C. 2020 Nonlinear effects on the precessional instability in magnetized turbulence. *Atmophere* **11**(1), 164501, doi:10.3390/atmos11010014.

SANSÓN, L. Z. 2001 The asymmetric Ekman decay of cyclonic and anticyclonic vortices. *Eur. J. Mech. B* **20**(4), 541-556, doi:10.1016/S0997-7546(01)01128-1.

SCHAEFFER, N., JAULT, D., NATAF, H.C., & FOURNIER, A. 2017 Turbulent geodynamo simulations: a leap towards Earth's core. *Geophys. J. Int.* **211**(1), 1-29, doi:10.1093/gji/ggx265.

SESHASAYANAN, K., GALLET, B., & ALEXAKIS, A. 2017 Transition to turbulent dynamo saturation. *Phy. Rev. Lett.* **119**, 204503, doi:10.1103/PhysRevLett.119.204503.

SESHASAYANAN, K. & GALLET B. 2020 Onset of three-dimensionality in rapidly rotating turbulent flows. *J. Fluid Mech.* **901**, R5, doi:10.1017/jfm.2020.541.

SLOUDSKY, T. 1895 De la rotation de la terre supposeé fluide á son intérieur. *Bull. Soc. Imp. Natur. Mosc.* **IX**, 285-318.

SMITH, L. M., CHASNOV, J. R., & WALEFFE F. 1996 Crossover from two- to three-dimensional turbulence. *Phys. Rev. Lett.* **77**, 2467-2470, doi:10.1103/PhysRevLett.77.2467.

Smith, L. M. & Waleffe F. 1999 Transfer of energy to two-dimensional large scales in forced, rotating three-dimensional turbulence. *Phy. Fluids*, **11**, 1608-1622, doi:10.1063/1.870022.

Smith, L. M. & Lee Y. 2005 On near-resonances and symmetry breaking in forced rotating flows at moderate Rossby number. *J. Fluid Mech.*, **535**, 111-142, doi:10.1017/S0022112005004660.

Sous, D., Sommeria, J., & Boyer D. 2013 Friction law and turbulent properties in a laboratory Ekman boundary layer. *Phys. Fluids* **25**, 046602, doi:10.1063/1.4802045.

Spohn, T. & Schubert, G. 2003 Oceans in the icy Galilean satellites of Jupiter?, *Icarus* **161**(2), 456-467, doi:10.1016/S0019-1035(02)00048-9 .

Spalart, P. R. & Schur, M. 1997 On the sensitization of turbulence models to rotation and curvature. *Aerospace Science and Technology* **1**(5), 297-302, doi:10.1016/S1270-9638(97)90051-1.

Staplehurst, P. J., Davidson, P. A., & Dalziel, S. B. 2008 Structure formation in homogeneous freely decaying rotating turbulence. *J. Fluid Mech.*, **598**, 81-105, doi:10.1017/S0022112007000067.

Steenbeck, M., Krause, F., & Rädler, K. H. 1966 Berechnung der mittleren Lorentz-Feldstärke $\overline{\mathbf{u} \times \mathbf{B}}$ für ein elektrisch leitendes Medium in turbulenter, durch Coriolis-Kräfte beeinflußter Bewegung. *Zeitschrift für Naturforschung*, **21A**, 369-376.

Steenbeck, M., Kirko, I. M., Gailitis, A., Klawina, A. P., Krause, F., Laumanis, I. J. & Lielausis, O. A. 1967 Der experimentelle Nachweis einer elektromotorischen Kraft längs eines äußeren Magnetfeldes, induziert durch eine Strömung flüssigen Metalls (α-Effekt). *Mon. ber. Dtsch Akad. Wiss. Berl.* , **9**, 714-719.

Stefani, F., Gerbeth, G., & Gailitis, A. 1997 Velocity profile optimization for the Riga dynamo experiment. *Transfer Phenomena in Magnetohydrodynamic and Electroconducting Flows* **333**, 31-44.

Stefani, F., Gerbeth, G., & Rädler, K. H. 2000 Steady dynamos in finite domains: an integral equation approach. *Astron. Nach.* **321**, 65-73.

Stefani, F., & Gerbeth, G. 2004 Asymmetric polarity reversals, bimodal field distribution, and coherence resonance in a spherically symmetric mean-field dynamo model. *Phys. Rev. Lett.* **94**, 184506, doi:10.1103/PhysRevLett.94.184506.

Stefani, F., Xu, M., Gerbeth, G., Ravelet, F., Chiffaudel, A., Daviaud, F., & Léorat, J. 2006 Ambivalent effects of added layers on steady kinematic dynamos in cylindrical geometry: application to the VKS experiment. *European Journal of Mechanics, B/Fluids* **25**(6), 894-908, doi:10.1016/j.euromechflu.2006.02.002.

Stefani, F., Eckert, S., Gerbeth, G., Giesecke, A., Gundrum, T., Steglich, C., Weier, T., & Wustmann, B. 2012 DRESDYN – a new facility for MHD experiments with liquid sodium. *Magnetohydrodynamics* **48**(1), 103-114.

Stefani, F., Albrecht, T., Gerbeth, G., Giesecke, A., Gundrum, T., Herault, J., Nore, C., & Steglich, C. 2015 Towards a precession driven dynamo experiment. *Magnetohydrodynamics* **51**(2), 275-284.

Stefani, F., Gailitis, A., Gerbeth, G., Giesecke, A., Gundrum, T., Rüdiger, G., Seilmayer, M., & Vogt, T. 2019 The DRESDYN project: liquid metal experiments on dynamo action and magnetorotational instability. *Magnetohydrodynamics* **113**, 51-70, doi:10.1080/03091929.2018.1501481.

Stewartson, K. 1957 On almost rigid rotations. *J. Fluid Mech.* **3**(1), 17-26, doi:10.1017/S0022112057000452.

Stewartson, K. 1959 On the stability of a spinning top containing liquid. *J. Fluid Mech.* **5**(4), 577-592, doi:10.1017/S0022112059000404.

Stewartson, K. & Roberts, P. H. 1963 On the motion of liquid in a spheroidal cavity of a precessing rigid body. *J. Fluid Mech.* **17**(1), 1-20, doi:10.1017/S0022112063001063.

Stieglitz, R. & Müller, U. 2001 Experimental demonstration of an homogeneous two-scale dynamo. *Phys. Fluids* **13**, 561-564, doi:10.1063/1.1331315.

Tarduno, J. A., Cottrell, R. D., Watkeys, M. K., & Bauch, D. 2007 Geomagnetic field strength 3.2 billion years ago recorded by single silicate crystals. *Nature* **446**, 657-660, doi:10.1038/nature05667.

Tatro, P. R. & Mollo-Christensen, E. L. 1967 Experiments on Ekman layer instability. *J. Fluid Mech.* **28**(3), 531-543, doi:10.1017/S0022112067002289.

Tilgner, A. 1998 On models of precession driven core flow. *Stud. Geophys. Geod.* **42**, 232-238, doi:10.1023/A:1023332115179.

Tilgner, A. 2000 Towards experimental fluid dynamos . *Physics of the Earth and Planetary Interiors*, **117**(1-4), 171-177, doi:10.1016/S0031-9201(99)00095-3.

TILGNER, A. & BUSSE, F. L. 2001 Saturation mechanism in a model of the Karlsruhe dynamo. *Dynamo and Dynamics, a Mathematical Challenge. NATO Science Series* **26**, doi:10.1007/978-94-010-0788-7_13.

TILGNER, A. 2005 Precession driven dynamos. *Phys. Fluids* **17**, 034104, doi:10.1063/1.1852576.

TILGNER, A. 2007 Kinematic dynamos with precession driven flow in a sphere. *Geophys. Astrophys. Fluid Dyn.* **101**, 1-9, doi:10.1080/03091920601045324.

TILGNER, A. 2007 Zonal wind driven by inertial modes. *Phys. Rev. Lett.* **99**, 194501, doi:10.1103/PhysRevLett.99.194501.

VAN DEN HEUVEL, E. P. J. 1966 On the precession as a cause of pleistocene variations of the Atlantic Ocean water temperatures. *Geophys. J. Int.* **11**(3), 323-336, doi:10.1111/j.1365-246X.1966.tb03086.x.

VANYO, J. P. 1991 A geodynamo powered by luni-solar precession. *Geophys. Astrophys. Fluid Dyn.* **59**, 209-234, doi:10.1080/03091929108227780.

VERMA, M. K. 2004 Statistical theory of magnetohydrodynamic turbulence: recent results. *Physics Reports* **401**(5-6), 229-380, Elsevier.

VORMANN, J. & HANSEN U. 2020 Characteristics of a precessing flow under the influence of a convecting temperature field in a spheroidal shell. *J. Fluid Mech.* **891**, A15, doi:10.1017/jfm.2020.150.

WALEFFE, F. 1989 The 3D instability of a strained vortex and its relation to turbulence. PhD thesis, MIT

WEISS, N. 2002 Dynamos in planets, stars and galaxies. *Astron. Geophys.* **43**(3), 3.9-3.14, doi:10.1046/j.1468-4004.2002.43309.x.

WICHT, J. & TILGNER A. 2010 Theory and modeling of planetary dynamos. *Space Sci. Rev.* **152**, 501-542, doi:10.1007/s11214-010-9638-y.

WILBERT, M., GIESECKE, A., & GRAUER, R. 2022 Numerical investigation of the flow inside a precession-driven cylindrical cavity with additional baffles using an immersed boundary method. *Phys. Fluids* **34**, 096607, doi:10.1063/5.0110153.

WILDE, H. 1867 Experimental researches in magnetism and electricity. *Philsophical Transactions of the Royal Society of London*, **157**, 89-107.

WILKINSON, I. 1984 The contribution of laboratory dynamo experiments to our understanding of the mechanism of generation of planetary magnetic fields. *Geophysical surveys* **7**, 107-122, doi:10.1007/BF01449179.

Wu, C-C. & Roberts P. H. 2009 On a dynamo driven by topographic precession. *Geophys. Astrophys. Fluid Dyn.* **103**(6), 467-501, doi:10.1080/03091920903311788.

Xu, M., Stefani, F., & Gerbeth, G. 2008 The integral equation approach to kinematic dynamo theory and its application to dynamo experiments in cylindrical geometry. *J. Comput. Phys.* **227**(17), 8130-8144, doi:10.1016/j.jcp.2008.05.009.

Yang, X., Andrzej Domaradzki, J. 2004 Large eddy simulations of decaying rotating turbulence. *Phys. Fluids* **16**, 4088-4104, doi:10.1063/1.1790452.

Yeung, P. K. & Zhou Y. 1998 Numerical study of rotating turbulence with external forcing. *Phys. Fluids* **10**, 2895-2909, doi:10.1063/1.869810.

Yoder, C. F. 1995 Venus' free obliquity. *Icarus* **117**(2), 250-286, doi:10.1006/icar.1995.1156.

Yoder, C. F., Konopliv, A. S., Yuan, D. N., Standish, E. M., & Folkner, W. M. 2003 Fluid core size of Mars from detection of the solar tide. *Science* **300**(5617), 299-303, doi:10.1126/science.1079645.

Zahn, J. P. 1992 Circulation and turbulence in rotating stars.. *Astronomy and Astrophysics* **265**, 115-132.

Zeman, O. 1994 A note on the spectra and decay of rotating homogeneous turbulence. *Phys. Fluids* **6**, 3221-3223. doi:10.1063/1.868053.

Zhang, K. & Liao, X. 2017 Theory and modeling of rotating fluids: convection, inertial waves and precession. Cambridge University Press., doi:10.1017/9781139024853.

Zhou, Y. 1995 A phenomenological treatment of rotating turbulence. *Phys. Fluids* **7**, 2092-2094. doi:10.1063/1.868457.

Zimmerman, D. S., Triana, S. A., Nataf, H. C., & Lathrop, D. P. 2014 A turbulent, high magnetic Reynolds number experimentalmodel of Earth's core. *J. Geophys. Res. Solid Earth* **119**(6), 4538-4557, doi:10.1002/2013JB010733.

A. Explicit derivation of vorticity for the $(1,1,1)$ mode in precessing cylinder

In the this Appendix we derive the explicit formulation of the vorticity starting from the analytical formulation by Gans (1970). Then we will compare with DNS results. Due to the linear nature of the analytical solution the results will be valid in the weak precession regime i.e $Po\sqrt{Re} < 1$.

Interior velocity:

$$\begin{aligned} u_r &= -\frac{i}{3r}|A_l| \sin\left(\frac{k_l}{\sqrt{3}}z\right) e^{i(\varphi+\varphi_{A_l})} \left(\frac{2J_1(k_l r)}{r} + k_l J_1'(k_l r)\right) , \\ u_\varphi &= \frac{1}{3r}|A_l| \sin\left(\frac{k_l}{\sqrt{3}}z\right) e^{i(\varphi+\varphi_{A_l})} \left(2k_l J_1'(k_l r) + \frac{J_1(k_l r)}{r}\right) , \\ u_z &= i|A_l|\frac{k_l}{\sqrt{3}} \cos\left(\frac{k_l}{\sqrt{3}}z\right) e^{i(\varphi+\varphi_{A_l})} J_1(k_l r) . \end{aligned} \tag{A.1}$$

The following fields are related to the boundary layers where the transformed coordinate for endwalls $\zeta = \pm(z \mp \frac{L}{D})Ek^{-1/2}$ and sidewalls $\eta = (1-r)Ek^{-1/2}$ are used.

Endwalls velocities:

$$\begin{aligned} \tilde{u}_{r-e} &= \pm i\frac{k_l|A_l|}{2} \left(J_0(k_l r) e^{\frac{\sqrt{2}}{2}\zeta} e^{(\varphi+\varphi_{A_l}-\frac{\sqrt{2}}{2}\zeta)i} + \frac{J_2(k_l r)}{3} e^{\frac{\sqrt{6}}{2}\zeta} e^{(\varphi+\varphi_{A_l}+\frac{\sqrt{6}}{2}\zeta)i}\right) , \\ \tilde{u}_{\varphi-e} &= \pm\frac{k_l|A_l|}{2} \left(-J_0(k_l r) e^{\frac{\sqrt{2}}{2}\zeta} e^{(\varphi+\varphi_{A_l}-\frac{\sqrt{2}}{2}\zeta)i} + \frac{J_2(k_l r)}{3} e^{\frac{\sqrt{6}}{2}\zeta} e^{(\varphi+\varphi_{A_l}+\frac{\sqrt{6}}{2}\zeta)i}\right) , \\ \tilde{u}_{z-e} &= 0 . \end{aligned} \tag{A.2}$$

Sidewall velocities:

$$\tilde{u}_{r-s} = 0$$

$$\tilde{u}_{\varphi-s} = J_1(k_l)|A_l|e^{(-\eta\frac{\sqrt{2}}{2})} \sin\left(\frac{k_l}{\sqrt{3}}z\right) e^{(-\eta\frac{\sqrt{2}}{2}+\varphi+\varphi_{A_l})i} \tag{A.3}$$

$$\tilde{u}_{z-s} = -iJ_1(k_l)|A_l|e^{(-\eta\frac{\sqrt{2}}{2})} \frac{k_l}{\sqrt{3}} \cos\left(\frac{k_l}{\sqrt{3}}z\right) e^{(-\eta\frac{\sqrt{2}}{2}+\varphi+\varphi_{A_l})i}$$

A is a sort of sidewall amplitude computed from boundary conditions at $r = 1$: this is why the Bessel function contains just k_l as argument. Also in this case the velocities are shifted (caused by imaginary factor i).

Now we write the gradient-tensor in cylindrical coordinate for the velocity.

$$\nabla_c(\boldsymbol{u}) = \begin{pmatrix} \frac{\partial u_z}{\partial z} & \frac{\partial u_z}{\partial r} & \frac{1}{r}\frac{\partial u_z}{\partial \varphi} \\ \frac{\partial u_r}{\partial z} & \frac{\partial u_r}{\partial r} & \frac{1}{r}(\frac{\partial u_r}{\partial \varphi} - u_\varphi) \\ \frac{\partial u_\varphi}{\partial z} & \frac{\partial u_\varphi}{\partial r} & \frac{1}{r}(\frac{\partial u_\varphi}{\partial \varphi} + u_r) \end{pmatrix}$$

Now we develop term by term.
Interior (inviscid) field:

$$\frac{\partial u_z}{\partial z} = -i|A_l|\frac{k_l^2}{3} \sin\left(\frac{k_l}{\sqrt{3}}z\right) e^{i(\varphi+\varphi_{A_l})} J_1(k_l r)$$

$$\frac{\partial u_r}{\partial z} = -\frac{i}{3}|A_l|\frac{k_l}{\sqrt{3}} \cos\left(\frac{k_l}{\sqrt{3}}z\right) e^{i(\varphi+\varphi_{A_l})} \left(\frac{2J_1(k_l r)}{r} + \frac{\partial J_1(k_l r)}{\partial r}\right)$$

$$\frac{\partial u_\varphi}{\partial z} = \frac{1}{3}|A_l|\frac{k_l}{\sqrt{3}} \cos\left(\frac{k_l}{\sqrt{3}}z\right) e^{i(\varphi+\varphi_{A_l})} \left(2\frac{\partial J_1(k_l r)}{\partial r} + \frac{J_1(k_l r)}{r}\right)$$

$$\frac{\partial u_z}{\partial r} = \frac{\partial(i\frac{\partial P_1}{\partial z})}{\partial r} = i|A_l|\frac{k_l}{\sqrt{3}} \cos\left(\frac{k_l}{\sqrt{3}}z\right) e^{i(\varphi+\varphi_{A_l})} \frac{\partial J_1(k_l r)}{\partial r}$$

$$\frac{\partial u_r}{\partial r} = -\frac{i}{3}|A_l|e^{i(\varphi+\varphi_{A_l})} \sin\left(\frac{k_l}{\sqrt{3}}z\right) \left(2\frac{\partial[J_1(k_l r)/r]}{\partial r} + \frac{\partial^2[J_1(k_l r)]}{\partial r^2}\right)$$

$$\frac{\partial u_\varphi}{\partial r} = \frac{1}{3}|A_l|e^{i(\varphi+\varphi_{A_l})} \sin\left(\frac{k_l}{\sqrt{3}}z\right) \left(\frac{\partial[J_1(k_l r)/r]}{\partial r} + 2\frac{\partial^2[J_1(k_l r)]}{\partial r^2}\right)$$

$$\frac{1}{r}\frac{\partial u_z}{\partial \varphi} = \underbrace{(i \cdot i)}_{\text{-1}}|A_l|e^{i(\varphi+\varphi_{A_l})} \frac{k_l}{\sqrt{3}} \cos\left(\frac{k_l}{\sqrt{3}}z\right) \frac{J_1(k_l r)}{r}$$

$$\frac{1}{r}\left(\frac{\partial u_r}{\partial\varphi}-u_\varphi\right)=\frac{1}{3}|A_l|e^{i(\varphi+\varphi_{A_l})}\sin\left(\frac{k_l}{\sqrt{3}}z\right)\overbrace{\frac{\left(-\frac{\partial J_1(k_lr)}{\partial r}+\frac{J_1(k_lr)}{r}\right)}{r}}^{\text{finite term in r=0}\quad -k_l^2/2}$$

$$\frac{1}{r}\left(\frac{\partial u_\varphi}{\partial\varphi}+u_r\right)=\frac{i}{3}|A_l|e^{i(\varphi+\varphi_{A_l})}\sin\left(\frac{k_l}{\sqrt{3}}z\right)\overbrace{\frac{\left(\frac{\partial J_1(k_lr)}{\partial r}-\frac{J_1(k_lr)}{r}\right)}{r}}^{\text{finite term in r=0}\quad k_l^2/2}$$

Endwalls gradients:

$$\frac{\partial\tilde{u}_{r-e}}{\partial z}=\pm\frac{k_l}{2}|A_l|Ek^{-\frac{1}{2}}(\pm)J_0(k_lr)(i+1)\frac{\sqrt{2}}{2}e^{\zeta\frac{\sqrt{2}}{2}}e^{i(\varphi+\varphi_{A_l}-\zeta\frac{\sqrt{2}}{2})}+$$

$$+\frac{J_2(k_lr)}{3}(i-1)\frac{\sqrt{6}}{2}e^{\zeta\frac{\sqrt{6}}{2}}e^{i(\varphi+\varphi_{A_l}+\zeta\frac{\sqrt{6}}{2})})$$

$$\frac{\partial\tilde{u}_{\varphi-e}}{\partial z}=\pm\frac{k_l}{2}|A_l|Ek^{-\frac{1}{2}}(\pm)(-J_0(k_lr)(1-i)\frac{\sqrt{2}}{2}e^{\zeta\frac{\sqrt{2}}{2}}e^{i(\varphi+\varphi_{A_l}-\zeta\frac{\sqrt{2}}{2})}+$$

$$+\frac{J_2(k_lr)}{3}(1+i)\frac{\sqrt{6}}{2}e^{+\zeta\frac{\sqrt{6}}{2}}e^{i(\varphi+\varphi_{A_l}+\zeta\frac{\sqrt{6}}{2})})$$

$$\frac{\partial\tilde{u}_{z-e}}{\partial z}=0$$

$$\frac{\partial\tilde{u}_{r-e}}{\partial r}=\pm\frac{i}{2}k_l|A_l|\left(e^{\zeta\frac{\sqrt{2}}{2}}e^{i(-\zeta\frac{\sqrt{2}}{2}+\varphi+\varphi_{A_l})}\frac{\partial J_0(k_lr)}{\partial r}+e^{\zeta\frac{\sqrt{6}}{2}}e^{i(+\zeta\frac{\sqrt{6}}{2}+\varphi+\varphi_{A_l})}\frac{1}{3}\frac{\partial J_2(k_lr)}{\partial r}\right)$$

$$\frac{\partial\tilde{u}_{\varphi-e}}{\partial r}=\pm\frac{1}{2}k_l|A_l|\left(-e^{\zeta\frac{\sqrt{2}}{2}}e^{i(-\zeta\frac{\sqrt{2}}{2}+\varphi+\varphi_{A_l})}\frac{\partial J_0(k_lr)}{\partial r}+e^{\zeta\frac{\sqrt{6}}{2}}e^{i(+\zeta\frac{\sqrt{6}}{2}+\varphi+\varphi_{A_l})}\frac{1}{3}\frac{\partial J_2(k_lr)}{\partial r}\right)$$

$$\frac{\partial\tilde{u}_{z-e}}{\partial r}=0$$

$$\frac{1}{r}\left(\frac{\partial\tilde{u}_{r-e}}{\partial\varphi}-\tilde{u}_\varphi\right)=(\pm)-\frac{1}{3}|A_l|k_le^{i(\varphi+\varphi_{Al}+\zeta\frac{\sqrt{6}}{2})}\frac{J_2(k_lr)}{r}e^{\zeta\frac{\sqrt{6}}{2}}$$

$$\frac{1}{r}(\frac{\partial\tilde{u}_{\varphi-e}}{\partial\varphi}+\tilde{u}_r)=(\pm)\,\frac{i}{3}|A_l|k_le^{i(\varphi+\varphi_{Al}+\zeta\frac{\sqrt{6}}{2})}\frac{J_2(k_lr)}{r}e^{\zeta\frac{\sqrt{6}}{2}}$$

$$\frac{1}{r}\frac{\partial\tilde{u}_{z-e}}{\partial\varphi}=0$$

Sidewall gradients:

$$\frac{\partial \tilde{u}_{r-s}}{\partial z} = 0$$

$$\frac{\partial \tilde{u}_{\varphi-s}}{\partial z} = J_1(k_l)|A_l|e^{i(\varphi+\varphi_{Al}-\eta\frac{\sqrt{2}}{2})}\frac{k_l}{\sqrt{3}}\cos\left(\frac{k_l}{\sqrt{3}}z\right)e^{-\eta\frac{\sqrt{2}}{2}}$$

$$\frac{\partial \tilde{u}_{z-s}}{\partial z} = iJ_1(k_l)|A_l|e^{i(\varphi+\varphi_{Al}-\eta\frac{\sqrt{2}}{2})}\frac{k_l^2}{3}\sin\left(\frac{k_l}{\sqrt{3}}z\right)e^{-\eta\frac{\sqrt{2}}{2}}$$

$$\frac{\partial \tilde{u}_{zside}}{\partial r} = J_1(k_l)|A_l|e^{i(\varphi+\varphi_{Al}-\eta\frac{\sqrt{2}}{2})}\frac{k_l}{\sqrt{3}}\cos\left(\frac{k_l}{\sqrt{3}}z\right)e^{-\eta\frac{\sqrt{2}}{2}}Ek^{-\frac{1}{2}}\frac{\sqrt{2}}{2}\left(1-i\right)$$

$$\frac{\partial \tilde{u}_{r-s}}{\partial r} = 0$$

$$\frac{\partial \tilde{u}_{\varphi-s}}{\partial r} = J_1(k_l)|A_l|e^{i(\varphi+\varphi_{Al}-\eta\frac{\sqrt{2}}{2})}\sin\left(\frac{k_l}{\sqrt{3}}z\right)Ek^{-\frac{1}{2}}\frac{\sqrt{2}}{2}\left(1+i\right)e^{-\eta\frac{\sqrt{2}}{2}}$$

$$\frac{1}{r}\frac{\partial \tilde{u}_{z-s}}{\partial \varphi} = J_1(k_l)|A_l|e^{i(\varphi+\varphi_{Al}-\eta\frac{\sqrt{2}}{2})}\frac{k_l}{\sqrt{3}}\cos\left(\frac{k_l}{\sqrt{3}}z\right)\frac{e^{-\eta\frac{\sqrt{2}}{2}}}{r}$$

$$\frac{1}{r}\left(\underbrace{\frac{\partial \tilde{u}_{r-s}}{\partial \varphi}}_{=0} - \tilde{u}_{\varphi-s}\right) = -J_1(k_l)|A_l|e^{i(\varphi+\varphi_{Al}-\eta\frac{\sqrt{2}}{2})}\sin\left(\frac{k_l}{\sqrt{3}}z\right)\frac{e^{-\eta\frac{\sqrt{2}}{2}}}{r}$$

$$\frac{1}{r}\left(\frac{\partial u_{\varphi-s}}{\partial \varphi} + \underbrace{\tilde{u}_{rside}}_{=0}\right) = iJ_1(k_l)|A_l|e^{i(\varphi+\varphi_{Al}-\eta\frac{\sqrt{2}}{2})}\sin\left(\frac{k_l}{\sqrt{3}}z\right)\frac{e^{-\eta\frac{\sqrt{2}}{2}}}{r}$$

<u>Total fields</u>:

$$\begin{aligned}\left(\frac{\partial u_z}{\partial z}\right)_{i+e+s} &= -i|A_l|\frac{k_l^2}{3}\sin\left(\frac{k_l}{\sqrt{3}}z\right)e^{i(\varphi+\varphi_{A_l})}J_1(k_l r) + 0 + \\ &+iJ_1(k_l)|A_l|e^{i(\varphi+\varphi_{Al}-\eta\frac{\sqrt{2}}{2})}\frac{k_l^2}{3}\sin\left(\frac{k_l}{\sqrt{3}}z\right)e^{-\eta\frac{\sqrt{2}}{2}}\end{aligned} \tag{A.4}$$

$$\begin{aligned}\left(\frac{\partial u_r}{\partial z}\right)_{i+e+s} &= -\frac{i}{3}|A_l|\frac{k_l}{\sqrt{3}}\cos(\frac{k_l}{\sqrt{3}}z)e^{i(\varphi+\varphi_{A_l})}\left(\frac{2J_1(k_l r)}{r} + \frac{\partial J_1(k_l r)}{\partial r}\right) + \\ &\pm\frac{k_l}{2}|A_l|(\pm)Ek^{-\frac{1}{2}}(J_0(k_l r)(i+1)\frac{\sqrt{2}}{2}e^{\zeta\frac{\sqrt{2}}{2}}e^{i(\varphi+\varphi_{A_l}-\zeta\frac{\sqrt{2}}{2})}\end{aligned}$$

$$+\frac{J_2(k_l r)}{3}(i-1)\frac{\sqrt{6}}{2}e^{\zeta\frac{\sqrt{6}}{2}}e^{i(\varphi+\varphi_{A_l}+\zeta\frac{\sqrt{6}}{2})})+0 \tag{A.5}$$

$$\left(\frac{\partial u_\varphi}{\partial z}\right)_{i+e+s} = \frac{1}{3}|A_l|\frac{k_l}{\sqrt{3}}\cos\left(\frac{k_l}{\sqrt{3}}z\right)e^{i(\varphi+\varphi_{A_l})}\left(2\frac{\partial J_1(k_l r)}{\partial r}+\frac{J_1(k_l r)}{r}\right)+$$
$$\pm\frac{k_l}{2}|A_l|(\pm)Ek^{-\frac{1}{2}}(-J_0(k_l r)(1-i)\frac{\sqrt{2}}{2}e^{\zeta\frac{\sqrt{2}}{2}}e^{i(\varphi+\varphi_{A_l}-\zeta\frac{\sqrt{2}}{2})}+$$
$$+\frac{J_2(k_l r)}{3}(1+i)\frac{\sqrt{6}}{2}e^{+\zeta\frac{\sqrt{6}}{2}}e^{i(\varphi+\varphi_{A_l}+\zeta\frac{\sqrt{6}}{2})})+J_1(k_l)|A_l|e^{i(\varphi+\varphi_{Al}-\eta\frac{\sqrt{2}}{2})}\frac{k_l}{\sqrt{3}}\cos(\frac{k_l}{\sqrt{3}}z)e^{-\eta\frac{\sqrt{2}}{2}} \tag{A.6}$$

$$\left(\frac{\partial u_z}{\partial r}\right)_{i+e+s} = i|A_l|\frac{k_l}{\sqrt{3}}\cos\left(\frac{k_l}{\sqrt{3}}z\right)e^{i(\varphi+\varphi_{A_l})}\frac{\partial J_1(k_l r)}{\partial r}+0+$$
$$J_1(k_l)|A_l|e^{i(\varphi+\varphi_{Al}-\eta\frac{\sqrt{2}}{2})}\frac{k_l}{\sqrt{3}}\cos\left(\frac{k_l}{\sqrt{3}}z\right)e^{-\eta\frac{\sqrt{2}}{2}}Ek^{-\frac{1}{2}}\frac{\sqrt{2}}{2}(1-i) \tag{A.7}$$

$$\left(\frac{\partial u_r}{\partial r}\right)_{i+e+s} = -\frac{i}{3}|A_l|e^{i(\varphi+\varphi_{A_l})}\sin\left(\frac{k_l}{\sqrt{3}}z\right)\left(2\frac{\partial[J_1(k_l r)/r]}{\partial r}+\frac{\partial^2[J_1(k_l r)]}{\partial r^2}\right)+$$
$$\pm\frac{i}{2}k_l|A_l|\left(e^{\zeta\frac{\sqrt{2}}{2}}e^{i(-\zeta\frac{\sqrt{2}}{2}+\varphi+\varphi_{A_l})}\frac{\partial J_0(k_l r)}{\partial r}+e^{\zeta\frac{\sqrt{6}}{2}}e^{i(+\zeta\frac{\sqrt{6}}{2}+\varphi+\varphi_{A_l})}\frac{1}{3}\frac{\partial J_2(k_l r)}{\partial r}\right)+0 \tag{A.8}$$

$$\left(\frac{\partial u_\varphi}{\partial r}\right)_{i+e+s} = \frac{1}{3}|A_l|e^{i(\varphi+\varphi_{A_l})}\sin\left(\frac{k_l}{\sqrt{3}}z\right)\left(\frac{\partial[J_1(k_l r)/r]}{\partial r}+2\frac{\partial^2[J_1(k_l r)]}{\partial r^2}\right)+$$
$$\pm\frac{1}{2}k_l|A_l|\left(-e^{\zeta\frac{\sqrt{2}}{2}}e^{i(-\zeta\frac{\sqrt{2}}{2}+\varphi+\varphi_{A_l})}\frac{\partial J_0(k_l r)}{\partial r}+e^{\zeta\frac{\sqrt{6}}{2}}e^{i(+\zeta\frac{\sqrt{6}}{2}+\varphi+\varphi_{A_l})}\frac{1}{3}\frac{\partial J_2(k_l r)}{\partial r}\right)+$$
$$+J_1(k_l)|A_l|e^{i(\varphi+\varphi_{Al}-\eta\frac{\sqrt{2}}{2})}\sin\left(\frac{k_l}{\sqrt{3}}z\right)Ek^{-\frac{1}{2}}\frac{\sqrt{2}}{2}(1+i)e^{-\eta\frac{\sqrt{2}}{2}} \tag{A.9}$$

$$\frac{1}{r}\left(\frac{\partial u_z}{\partial \varphi}\right)_{i+e+s} = -|A_l|e^{i(\varphi+\varphi_{A_l})}\frac{k_l}{\sqrt{3}}\cos\left(\frac{k_l}{\sqrt{3}}z\right)\frac{J_1(k_l r)}{r}+0+$$
$$+J_1(k_l)|A_l|e^{i(\varphi+\varphi_{Al}-\eta\frac{\sqrt{2}}{2})}\frac{k_l}{\sqrt{3}}\cos\left(\frac{k_l}{\sqrt{3}}z\right)\frac{e^{-\eta\frac{\sqrt{2}}{2}}}{r} \tag{A.10}$$

$$\frac{1}{r}\left(\frac{\partial u_r}{\partial \varphi}-u_\varphi\right)_{i+e+s}=\frac{1}{3}|A_l|e^{i(\varphi+\varphi_{A_l})}\sin\left(\frac{k_l}{\sqrt{3}}z\right)\frac{\left(-\frac{\partial J_1(k_l r)}{\partial r}+\frac{J_1(k_l r)}{r}\right)}{r}+$$

$$\pm\left(-\frac{1}{3}|A_l|k_l e^{i(\varphi+\varphi_{Al}+\zeta\frac{\sqrt{6}}{2})}\frac{J_2(k_l r)}{r}e^{\zeta\frac{\sqrt{6}}{2}}\right)-J_1(k_l)|A_l|e^{i(\varphi+\varphi_{Al}-\eta\frac{\sqrt{2}}{2})}\sin\left(\frac{k_l}{\sqrt{3}}z\right)\frac{e^{-\eta\frac{\sqrt{2}}{2}}}{r} \tag{A.11}$$

$$\frac{1}{r}\left(\frac{\partial u_\varphi}{\partial \varphi}+u_r\right)_{i+e+s}=\frac{i}{3}|A_l|e^{i(\varphi+\varphi_{A_l})}\sin\left(\frac{k_l}{\sqrt{3}}z\right)\frac{\left(\frac{\partial J_1(k_l r)}{\partial r}-\frac{J_1(k_l r)}{r}\right)}{r}+$$

$$\pm\frac{i}{3}|A_l|k_l e^{i(\varphi+\varphi_{Al}+\zeta\frac{\sqrt{6}}{2})}\frac{J_2(k_l r)}{r}e^{\zeta\frac{\sqrt{6}}{2}}+iJ_1(k_l)|A_l|e^{i(\varphi+\varphi_{Al}-\eta\frac{\sqrt{2}}{2})}\sin\left(\frac{k_l}{\sqrt{3}}z\right)\frac{e^{-\eta\frac{\sqrt{2}}{2}}}{r} \tag{A.12}$$

The inviscid part of the vorticity will read

$$\nabla_c\times(\boldsymbol{u})=\hat{z}(\frac{\partial u_\varphi}{\partial r}-\frac{1}{r}\frac{\partial u_r}{\partial \varphi}+\frac{u_\varphi}{r})+\hat{r}(\frac{1}{r}\frac{\partial u_z}{\partial \varphi}-\frac{\partial u_\varphi}{\partial z})+\hat{\varphi}(\frac{\partial u_r}{\partial z}-\frac{\partial u_z}{\partial r}) \tag{A.13}$$

$$\boldsymbol{\omega}=\begin{pmatrix}\omega_z\\ \omega_r\\ \omega_\varphi\end{pmatrix}=\begin{pmatrix}\frac{|A_l|}{3}e^{i(\varphi+\varphi_{A_l})}\sin\left(\frac{k_l}{\sqrt{3}}z\right)\left[(\frac{\partial(J_1(k_l r)/r)}{\partial r}+2\frac{\partial^2(J_1(k_l r))}{\partial r^2})-\frac{\left(-\frac{\partial J_1(k_l r)}{\partial r}+\frac{J_1(k_l r)}{r}\right)}{r}\right]\\ |A_l|e^{i(\varphi+\varphi_{A_l})}\frac{k_l}{\sqrt{3}}\cos\left(\frac{k_l}{\sqrt{3}}z\right)\left[\frac{2}{3}\frac{J_1(k_l r)}{r}-\frac{2}{3}\frac{\partial J_1(k_l r)}{\partial r}\right]\\ -i|A_l|\frac{k_l}{\sqrt{3}}\cos\left(\frac{k_l}{\sqrt{3}}z\right)e^{i(\varphi+\varphi_{A_l})}\left[\frac{2}{3}(\frac{J_1(k_l r)}{r})+\frac{4}{3}\frac{\partial J_1(k_l r)}{\partial r}\right]\end{pmatrix} \tag{A.14}$$

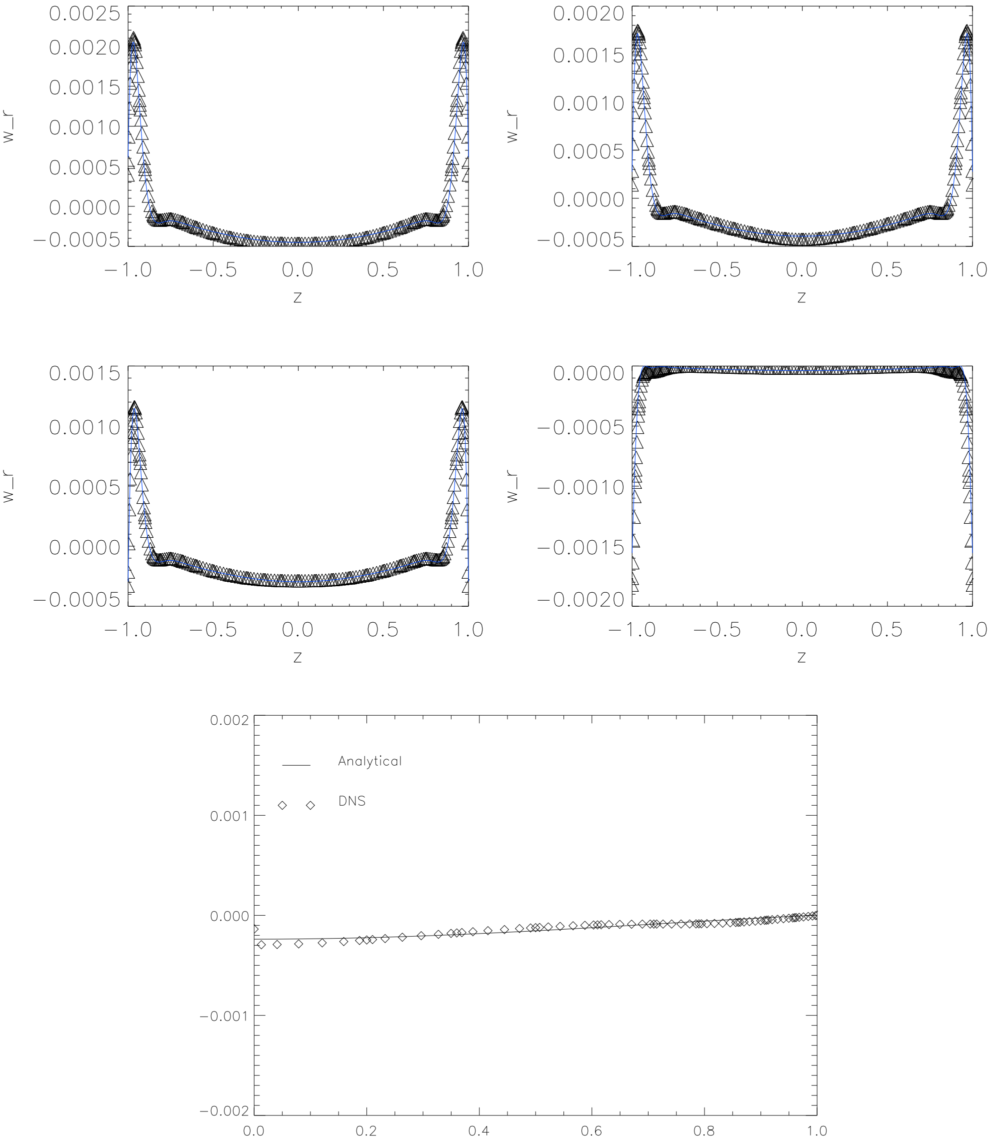

Figure A.1. Comparison between analytical (Eq. A.6, A.10) and numerical radial vorticity (in weak precession) at middle radius and four different azimuthal coordinate $\varphi = 0, \pi/2, \pi, 3/2\pi$.

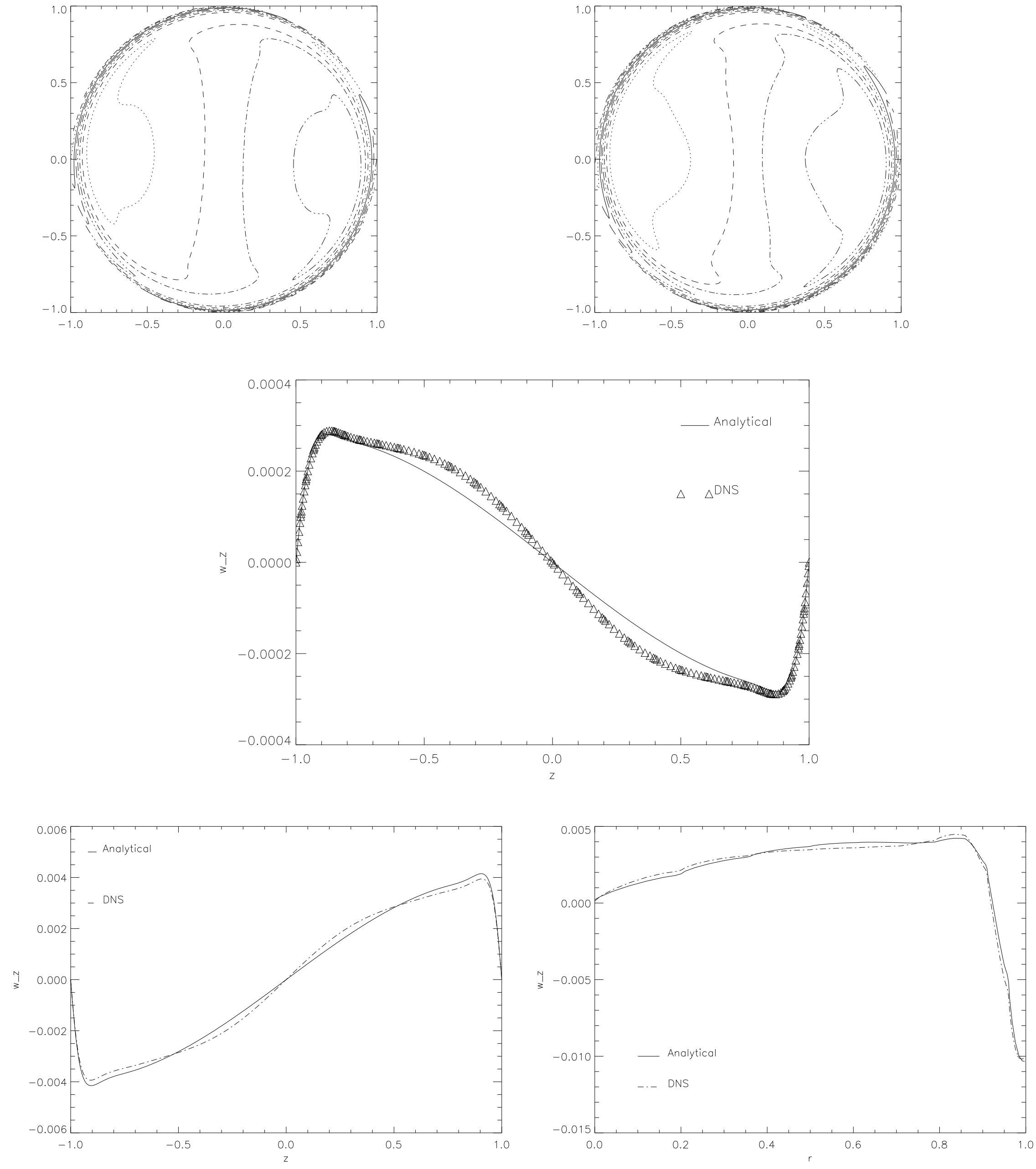

Figure A.2. Comparison between analytical computed in Eq. A.9, A.11 (left panel) and numerical (right panel) axial vorticity at equatorial plane.

B. Resolution study for the local model analysis

To check the impact of numerical resolution on the results shown in Chapter 6, we have selected one of the most explored cases with $Po = 0.3$ and $Re = 10^{4.5}$ and made additional two runs at lower 128^3 and higher 512^3 resolutions. The results of this resolution study are presented in Fig. B.1. The left plot in this figure shows the time-evolution of the volume-averaged total kinetic energy, while the right plot the shell-averaged dissipation spectra k^2E (averaged in time over the range $500 < t < 600$) at different resolutions. It is seen that both these quantities exhibit a very good agreement (convergence) with resolution, proving that the choice of the resolution 256^3 in this study is well justified. In particular, k^2E spectra coincide at wavenumbers common to these three resolutions and the zoomed-in curves in the inset show that even the lower resolution captures not just the qualitative (shape) but also the quantitative properties of the spectrum.

As a final remark, we note that the resolutions used in this work are standard ones often adopted in numerical simulations of rotating forced turbulence (Barker (2016), Barker & Lithwick (2013), Khlifi *et al.* (2018)). A good reference to check the scale of turbulent structures studied here is the Taylor microscale λ given in our non-dimensional units as (Pope (2000), Alexakis & Biferale (2018)):

$$\lambda \sim \left(\frac{\int_k E(k)dk}{\int_k k^2E(k)dk}\right)^{1/2} = \left(\frac{\nu u_{rms}^2}{\langle D\rangle}\right)^{1/2} = \left(\frac{u_{rms}^2}{Re\langle D\rangle}\right)^{1/2}$$

and the associated Reynolds number

$$Re_\lambda = \frac{u_{rms}\lambda}{\nu} = u_{rms}\lambda Re,$$

where $u_{rms} = \sqrt{\langle \boldsymbol{u}^2\rangle} = \sqrt{\langle 2E\rangle}$ is the RMS of turbulent velocity fluctuations and in our units viscosity $\nu = 1/Re$. Note that the two definitions of λ are equivalent in the sense that the first one is in spectral space while the second is in physical space. In the considered case of $Po = 0.3$ and $Re = 10^{4.5}$, the Taylor scale is $\lambda = 0.051$ and for its

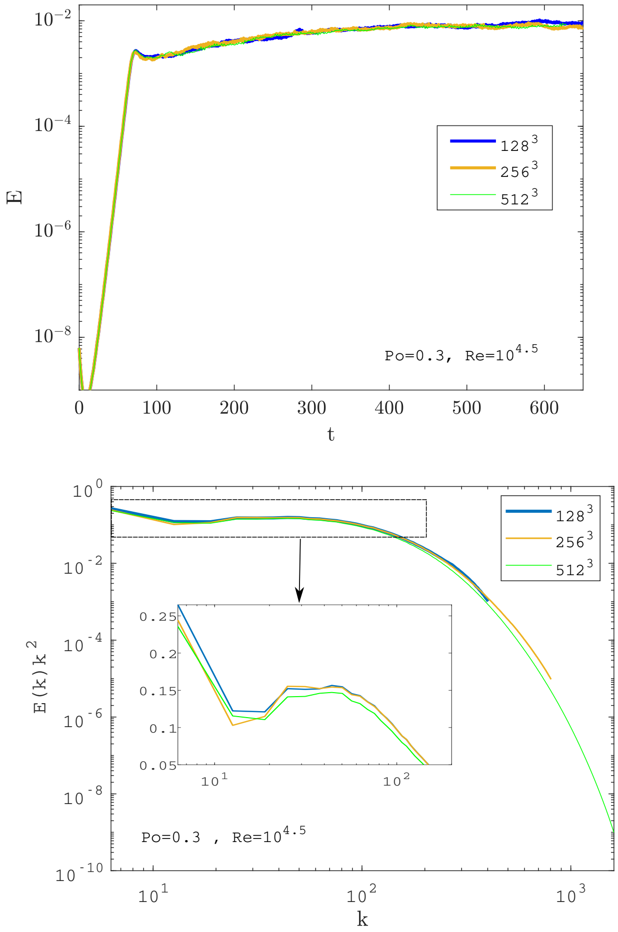

Figure B.1. Resolution study showing the comparison of the time-evolution of the volume-averaged total kinetic energy (left) and shell- and time-averaged kinetic energy spectrum $E(k)$ multiplied by k^2, which is proportional to the dissipation function D, $k^2E = Re \cdot |D|/2$ (right), for different resolutions.

ratio to the grid size $\Delta x = \Delta y = \Delta z = L/N$ we get $\lambda/\Delta x = 6,\ 12,\ 24$ at resolutions $N = 128,\ 256,\ 512$, respectively, which thus appears to be well resolved. For reference, we also give the values of Taylor microscale Reynolds number $Re_\lambda \approx 150,\ 141,\ 143$ for $N = 128,\ 256,\ 512$, respectively, which do not appear to vary much with resolution. This demonstrates that the adopted resolutions $N = 128$ and 256 are quite adequate for the present problem of precession-driven turbulence at $Po \in [0.01,\ 0.5]$ and $Re \in [10^{3.5},\ 10^5]$ (Table I) with typical $Re_\lambda \sim 150$. This resolution and value of Re_λ being consistent with the ones typically used in forced rotating turbulence studies (Bourouiba *et al.* (2012), Barker (2016), Khlifi *et al.* (2018)) are, however, much smaller than those for pure homogeneous isotropic hydrodynamic turbulence with forcing (see, e.g., Kaneda & Ishihara (2006)), where resolution as high as 4096^3 can be reached for $Re_\lambda \approx 1200$.

C. Invariance of Reynolds stress in different frames for precessing velocities

This appendix is dedicated to some algebraic steps to show that the turbulence quantities (i.e fluctuations) are not influenced by the choice of the frame of reference. This concept is particular useful in relation to the Chapter 6. We will use the tensorial notation for the sake of clarity.
We start from the definition of stress tensor of fluctuating:

$$\tau'_{ij} = \langle u'_i u'_j \rangle = \langle u_i u_j \rangle - \langle u_i \rangle \langle u_j \rangle \ . \tag{C.1}$$

The Reynolds stress tensor is a tensor of the second order and it is symmetric (Pope (2000)). Now we will use two decompositions:

- Reynolds decomposition: $u_i = \langle u_i \rangle + u'_i$ (with $\langle u_i \rangle = U_i$ being the time-averaged velocity);
- $\vec{u}_{TT} = u_{MF} + u_{SB}$ (where both are vectors. TT=turn-table, MF=mantle frame, SB=solid-body)

Starting from turn-table reference system (vectorial form and brackets for average):

$$\begin{aligned} \langle u'_{TT} u'_{TT} \rangle = \langle u_{TT} u_{TT} \rangle - \langle u_{TT} \rangle \langle u_{TT} \rangle = \\ \langle (u_{MF} + u_{SB})(u_{MF} + u_{SB}) \rangle - \langle u_{MF} + u_{SB} \rangle \langle u_{MF} + u_{SB} \rangle \end{aligned} \tag{C.2}$$

Exploiting the nature of solid body velocity (intrinsically average i.e $u'_{SB} = 0$):

$$\begin{aligned}
&\langle u'_{TT} u'_{TT} \rangle = \\
&\langle (u_{MF} + u_{SB})(u_{MF} + u_{SB}) \rangle - \langle u_{MF} + u_{SB} \rangle \langle u_{MF} + u_{SB} \rangle = \\
&\langle ((\langle u_{MF} \rangle + u'_{MF} + u_{SB})(\langle u_{MF} \rangle + u'_{MF} + u_{SB}) \rangle - \langle u_{MF} \rangle^2 + u_{SB}^2 + 2\langle u_{MF} u_{SB} \rangle = \\
&\langle \langle u_{MF} \rangle \langle u_{MF} \rangle + \langle u_{MF} \rangle u'_{MF} + \langle u_{MF} \rangle u_{SB} + u'_{MF} \langle u_{MF} \rangle + \\
&u'_{MF} u'_{MF} + u'_{MF} u_{SB} + u_{SB} \langle u_{MF} \rangle + u_{SB} u'_{MF} + u_{SB} u_{SB} \rangle - \\
&-(\langle u_{MF} \rangle^2 + u_{SB}^2 + 2\langle u_{MF} u_{SB} \rangle)
\end{aligned}$$

Because they are all summations we can apply the distributive property of the average application and also using the fundamental operation:

$$\langle \langle a \rangle a' \rangle = \langle a' \langle a \rangle \rangle = 0 \tag{C.3}$$

in this way, we obtain

$$\begin{aligned}
&\langle u'_{TT} u'_{TT} \rangle = \\
&\langle \langle u_{MF} \rangle \langle u_{MF} \rangle \rangle + \overbrace{\langle \langle u_{MF} \rangle u'_{MF} \rangle}^{=0} + \langle \langle u_{MF} \rangle u_{SB} \rangle + \overbrace{\langle \langle u'_{MF} \langle u_{MF} \rangle \rangle}^{=0} + \\
&\underbrace{\langle u'_{MF} u'_{MF} \rangle}_{\text{RS mantle}} + \underbrace{\langle u'_{MF} u_{SB} \rangle}_{=0} + \langle u_{SB} \langle u_{MF} \rangle \rangle + \underbrace{\langle u_{SB} u'_{MF} \rangle}_{=0} + \langle u_{SB} u_{SB} \rangle - \\
&-(\langle u_{MF} \rangle^2 + u_{SB}^2 + 2\langle u_{MF} u_{SB} \rangle) \, .
\end{aligned}$$

By re-organizing according to

$$\begin{aligned}
\langle u'_{TT} u'_{TT} \rangle = \langle u_{MF} \rangle^2 + 2\langle u_{MF} u_{SB} \rangle + u_{SB}^2 + \langle u'_{MF} u'_{MF} \rangle - \\
\langle u_{MF} \rangle^2 - u_{SB}^2 - 2\langle u_{MF} u_{SB} \rangle
\end{aligned} \tag{C.4}$$

We finally get:

$$\langle u'_{TT} u'_{TT} \rangle = \langle u'_{MF} u'_{MF} \rangle \, .$$

Acknowledgments

This thesis represents an attempt to condense and distill 4 years of research and training work. Many experiences and events that were essential, of course, have been excluded from it but they have been an integral part of the journey for me.
First, I would like to emphasize that this work, the published articles, and most importantly my change as a researcher and person was because of the environment in which I worked, collaborated and lived: the Magnetohydrodynamics department at HZDR and the city of Dresden.
Three people in this place have been particularly important and I would like to express my gratitude to them: Dr. André Giesecke, Dr. Frank Stefani, and Dr. George Mamatsashvili. They have not only been outstanding colleagues and supervisors but also mentors from whom I have learned so much. I feel truly fortunate to have had people of their caliber. I start by thanking André who shared with me for four years the same office. His patience and extreme attention to teach me coding and analysis tools as well as to read and correct the dozens of manuscripts I submitted to him was incredible. Some of the means used to find results were taught to me by him so I am grateful to him. Apart from work he also helped me a lot with extra-work bureaucracy and stuffs.
The second person I would like to thank is Frank. Science is many times a trial and error that "gives" frustrations... Frank's great and ubiquitous enthusiasm has always been contagious. Working with him has been stimulating because of his constant encouragement and optimism, his ability to always find positives in research, work, and generally in any situation is amazing. Over the years working with him I have known not only his scientific side but also the person himself. I remember with happiness and admiration all the stories told about the old scientists of the past generation from whom he learned, famous names related to historical events and stories about a bygone era that I had read only in history books. Dinners and events were kindled by his stories and his guitar concerts.
The third person I would like to thank is Dr. George Mamatsashvili. I really learned a lot from him especially in the last year of this journey. His great passion and motivation in investigating the phenomena have been an example; such as his deep love for science.
Another person I want to thank and who guided me along this path is Dr. Jan Šimkanin who was not only a collaborator but also a great friend. His hospitality at the Institute

of Sciences in Prague was great such as all the conversations we had. I remember with joy the workshops and conferences we attended. I also thank Dr. Adrian Barker whose collaboration was very fruitful and stimulating.

Finally I thank Prof. Uwe Harlander and Prof. Christoph Egbers very much for accepting my candidacy at BTU Cottbus and for being my thesis supervisors and Prof. Andreas Tilgner for agreeing to read this work.

Obviously couple of pages are not enough to mention all the important people in these last years so I apologize in advance if I forget anyone. I start with the guys in my department in particular Jude, Peter, Ashish and in particular Vivaswat with whom we spent hours trying to understand something about a topic as complex as precession.

The stay in Dresden would not have been the same without the group of guys and especially the coaches Marcus, Franz and Johannes from the box CrossFit DD, which has been practically a big family for me.

A final "thank you" goes out to my wonderful Ruth, friends, relatives and of course my parents who not only supported me through difficult times but passed on to me a love of discovery and exploration.

These 4 years as a Ph.D. student coincided with rather dramatic international events; between pandemics, lockdowns, and wars, science represented more than just work: it refreshed my mind. During seminars and conferences I have seen people of all beliefs and backgrounds collaborate without boundaries in what Popper would have called open society. I believe this can be taken as a paradigm for a better World. And that is why I have convinced myself that research is what I want to do when I grow up. I finish writing this last paragraph already thinking about the next scientific adventure that awaits me in other latitudes; but that is another story...